

Local and non-local thermomechanical modeling and finite-element simulation of high-speed cutting

Von der Fakultät Maschinenbau
der Technischen Universität Dortmund
zur Erlangung des Grades eines
Doktor-Ingenieurs
(Dr.-Ing.)
genehmigte Dissertation

von

Christian Hortig

Dortmund 2010

Contents

Summary	iii
1 Introduction	1
2 Simulation of chip formation during high-speed cutting	7
2.1 Introduction	7
2.2 Material modeling	8
2.3 Finite-element simulation of thermal shear-banding	12
2.4 Finite-element simulation of chip formation	17
2.5 Preliminary Summary	20
3 Adaptive FE-simulation of shear banding and high-speed cutting	23
3.1 Introduction	23
3.2 Adaptive algorithm and solution recovery	24
3.3 Error estimation at finite strain	39
3.4 Adaptive remeshing	48
3.5 Simulation of high speed cutting via adaptive remeshing	59
3.6 Preliminary summary	66
4 Local and non-local models for dynamic thermoelasticity and damage	67
4.1 Introduction	67
4.2 Continuum thermodynamic variational framework	69
4.3 Non-local modeling of thermo-viscoplasticity including ductile damage	71
4.4 Algorithmic implementation of non-local thermo-viscoplasticity including ductile damage	78
4.5 Algorithmic linearization	82
4.6 Finite-element formulation	86
4.7 Kinematics in context of adaptive remeshing	91
5 Local and non-local modeling of the cutting process	95
5.1 Implementation of local, thermo-viscoplasticity including heat conduction	95
5.2 Local, thermo-viscoplasticity including heat conduction and ductile damage	97
5.3 Non-local formulation in combination with a commercial code	100

5.4	Outlook hydrostatic/deviatoric coupling	109
5.5	CIRP Benchmark	112
6	Conclusion and Outlook	119
6.1	Conclusion	119
6.2	Outlook	120
	References	121
	Acknowledgements	127
	Curriculum Vitae	129

Summary

High-speed cutting is an important and widely-used process in modern production engineering. Considering the fundamental non-linear nature of this thermomechanical process, the finite-element method is the numerical simulation tool of choice. In this context, a realistic numerical simulation of cutting processes places high demands on accuracy and efficiency. Since large deformation and deformation localization are involved, continual remeshing and mesh adaptation are required. In the context of a finite-element analysis, localized deformation patterns, as observed in experimental observations, can be modeled using thermo-viscoplastic material models including in particular the effect of thermal softening and in general damage as well. As is well-known, such softening effects result in a loss of solution uniqueness, resulting in so-called pathological mesh-dependence of the simulation results. In the last ten to fifteen years, a number of extensions to classical local modeling of softening, damage and failure have been proposed in order to account for the inherently non-local character of many processes contributing to such failure. For example, in the case of ductile failure in metal-matrix composites as based on void development, the process of void coalescence leading to failure is inherently non-local. From the mathematical / numerical point of view, many non-local models have the additional benefit of regularizing the boundary-value problem and alleviating mesh dependence. On this basis, the intention of the work presented in the following is to develop a general finite element framework to model and simulate the process of metal cutting and related processes. Here, we deal with two key issues. To resolve the complex deformation patterns, observed in context of metal cutting, we develop an adaptive finite element framework, based on a combination of error estimation and refinement indication. Further, we present an extended thermodynamic framework, with a general non-local description of several thermodynamic quantities. In this context we also discuss the effect of ductile damage. In the context of standard isochoric plasticity, the influence of hydrostatic pressure on the development of ductile damage is usually accounted for in an indirect fashion, by defining, e.g., a pressure-dependent formulation for the rate of damage. In contrast, the current work is based on both hydrostatic stress- and deviatoric stress-driven inelastic deformation, damage, and failure. The former drives for example primarily microvoid development, while the latter is related to micro-shear-band or microcrack development. The extended non-local description allows the modeling of lengthscale-effects, in general, but also the additional benefit of further reduction of mesh dependence is important and will be discussed.

Zusammenfassung

Das Hochgeschwindigkeitsspannen ist ein wichtiger und weit verbreiteter Prozess in der modernen Produktionstechnik. Beachtet man die grundsätzlich nichtlineare Natur dieses thermomechanischen Prozesses, so bietet sich die Finite Elemente Simulation als numerisches Werkzeug an. In diesem Zusammenhang stellt eine realistische numerische Simulation hohe Anforderungen an Genauigkeit und Effizienz. Da große Deformationen und Lokalisation von plastischer Deformation auftreten, wird eine kontinuierliche Neuvernetzung sowie Netzadaptivität benötigt. Im Kontext einer Finiten Elemente Simulation können die im Experiment beobachteten lokalisierten Deformationsmuster durch ein thermo-viskoplastisches Materialgesetz unter Einbeziehung thermischer Entfestigung sowie Schädigung modelliert werden. Wie allgemein bekannt, geht mit einer solchen Entfestigung die Eindeutigkeit der Lösung verloren. Dies äußert sich in der so genannten pathologischen Netzabhängigkeit der Simulationsergebnisse. In den letzten zehn bis fünfzehn Jahren wurden eine Vielzahl von Erweiterungen der klassischen lokalen Modellierung von Entfestigung, Schädigung und Versagen vorgeschlagen, um dem von Natur aus nicht lokalen Charakter vieler entfestigender Prozesse Rechnung zu tragen. Zum Beispiel ist der Prozess des Zusammenwachsens von Hohlräumen, wie dieser bspw. beim duktilen Versagen von Metall-Matrix Verbundwerkstoffen auftritt, von Natur aus nicht lokal. Vom mathematischen und numerischen Standpunkt aus betrachtet, bringen viele dieser nicht lokalen Modelle den weiteren Vorteil, dass sie das entsprechende Randwertproblem regularisieren und netzabhängige Lösungen vermeiden. Auf dieser Basis besteht die Intention der vorliegenden Arbeit darin, einen allgemeinen Finite Elemente Rahmen zur Simulation des Zerspanens und ähnlicher Prozesse zu entwickeln. Wir beschäftigen uns hierbei mit zwei Schlüsselproblemen. Um die komplexen Deformationsstrukturen, wie sie beim Zerspanprozess auftreten, abbilden zu können, entwickeln wir zunächst ein adaptives Finite Elemente Werkzeug. Dieses basiert grundsätzlich auf einer Kombination aus Fehlerschätzung und Fehlerindikation. Weiterhin präsentieren wir eine erweiterte thermodynamische Formulierung, die eine generelle nicht-lokale Beschreibung mehrerer thermodynamischen Größen beinhaltet. In diesem Zusammenhang wird auch der Effekt duktiler Schädigung diskutiert. Im Zusammenhang der gewöhnlichen isochoren Plastizität wird der Einfluss hydrostatischer Spannungen auf die Schädigungsentwicklung für gewöhnlich in indirekter Weise, wie zum Beispiel durch eine druckabhängige Rate der Schädigung realisiert. Im Gegensatz dazu basiert die vorliegende Arbeit auf einer separaten Betrachtung von hydrostatisch und deviatorisch angetriebenen inelastischen Deformation, Schädigung und Versagen. Hydrostatische Spannungen treiben beispielsweise vorrangig die Entwicklung von Mikrohohlräumen voran. Der deviatorische Anteil wird in Zusammenhang mit Mikroscherbandentwicklung und Mikrorissen gebracht. Die erweiterte nicht-lokale Beschreibung erlaubt die Modellierung von Längenskaleneffekten im Allgemeinen. Des Weiteren ist aber auch der zusätzliche Gewinn einer weiteren Reduktion der Netzabhängigkeit wichtig, was diskutiert wird.

Chapter 1

Introduction

High-speed cutting is an important and widely-used process in modern production engineering. Considering the fundamental non-linear nature of this thermomechanical process, the finite-element method is the numerical simulation tool of choice. A variety of applications of this method in the context of high-speed cutting can be found in the recent literature, representing the state of the art. For example, in Özel and Zeren (2004), the determination of friction properties for use in finite element simulations of metal cutting is discussed. Likewise, a general discussion of thermomechanical effects playing a role in chip formation can be found in Mabrouki and Rigal (2006).

Experimental results, presented in El-Magd and Treppmann (2001); El-Wardany and Elbestawi (2001); Sievert et al. (2003); Tönshoff et al. (2005) show that shear banding represents the main mechanism of chip formation and results in reduced cutting forces. In the context of a finite-element analysis, such shear banding can be modeled using thermo-viscoplastic material models including in particular the effect of thermal softening (and in general damage as well: *e.g.*, Sievert et al. (2003)). As discussed in the work of Sievert et al. (2003) simulation results for a formulation considering only thermal softening show an overestimation of the peak temperatures. Thus, in order to decrease the mechanical power, the authors proposed an additional damage formulation. Furthermore, ductile damage has been observed for the material considered in this work (Inconel 718), in general (see *e.g.* Singh et al. (2003)).

As is well-known, such softening effects results in a loss of solution uniqueness, resulting in so-called pathological mesh-dependence of the simulation results. Usually, this dependence is expressed in terms of the size of the elements used, *i.e.*, the element edge-length. However, it is not restricted to this property of the elements. Indeed, as investigated in the current work, other properties, *e.g.*, element orientation, or interpolation order, are just as, if not more, influential in this regard. As will be shown in the current work, the influence of the mesh orientation becomes significant in the context of adiabatic shear banding, especially in connection with structured meshes.

A realistic numerical simulation of cutting processes places high demands on accuracy and efficiency. Since large deformation and deformation localization are involved, continual remeshing and mesh adaptation are required. For example, Bäker et al. (2002), use structured, quadrilateral meshes in combination with a hanging-node-based remeshing scheme to model continuous chip formation during metal cutting. In Bäker (2006), this method is applied to model chip segmentation. Marusich and Ortiz (2005) use adaptive remeshing to capture crack propagation during machining operations. In Özel and Altan (2000), unstructured quadrilateral remeshing is applied to model chip formation during high-speed flat-end milling. On the

other hand, a refinement strategy aimed in particular at accurately capturing thermomechanical localization and shear-band formation during cutting has generally not been addressed. This represents one of the goals of the current work.

In whatever context, the basic goal in any case is of course to avoid extreme element distortion. In this work, the authors investigated the strong mesh-dependence of the simulation results for the process of adiabatic shear-banding. In particular, this dependence is related to both the element size and element-mesh orientation in relation to the cutting direction. This has a significant influence of both a qualitative and quantitative nature on the results. As will be shown, adaptive remeshing can be used to significantly reduce such mesh-dependence. In particular, this involves reducing the element size below the characteristic length of material instability. A similar conclusion can also be found in Huerta and Pijaudier-Cabot (1994). In general, the element size must be small enough to resolve the material instability. And even then, pathological mesh-dependence remains.

The choice of a suitable refinement strategy for the case of adiabatic shear banding is still an open question. Most of the refinement strategies offered in literature focus on error estimation, which is technically mature for linear problems. Here, research mainly focusses on error estimation based on local residuals, as introduced by Babuska and Rheinboldt (1978) and recovery-based error estimation, as proposed by Zienkiewicz and Zhu (1987). For non-linear problems, method investigation and development is still far from complete. For example, Rodriguez-Ferran and Huerta (2000) apply residual-based error estimation in the context of a non-local damage model. Using residual-based error estimation, Huerta et al. (2002) present a general approach for the non-linear case. Application of recovery-based error estimation can be found in Boroomand and Zienkiewicz (1999), here extended to general elasto-plasticity, or in context of forging simulations in Boussetta et al. (2006).

Complementary to error-estimation methods are refinement-indicator-based methods. In particular, these facilitate a more physical interpretation of the refinement strategy. On the other hand, they are in a sense less accurate than estimation methods, heuristic in nature. Furthermore, they are application-dependent. For example, Marusich and Ortiz (2005) use the local value of the plastic power to detect the onset of localization locally. Another approach is proposed by Ortiz and Quigley (1991). Here, variations in the velocity field are chosen to act as the refinement indicator. In the present work, both error-estimation and refinement-indicator methods are investigated for application in the context of localization problems.

The use of remeshing techniques may lead to a reduction of mesh-dependence, but of course cannot eliminate it. The most simple solution, that arises intuitively, is based on enforcing simulation results to be consistent with experimental data by means of varying and limiting the minimal element size. Closely related to this approach Pietruszczak and Mroz (1981) developed an element formulation with an embedded description of the localization thickness. Here, the authors made an internal distinction between plastic active and elastic regions inside an element. In context of modeling and simulation of crack bands, a corresponding formulation can be found in the work of Bazant and Oh (1983). Following this approach, the fraction of energy, dissipated inside the plastic or cracking regime, respectively and thus, the stress strain response of the element is governed by the ratio between both regimes. Although such explicit description of

the localization thickness represent a robust and simple method to enforce a specific stress-strain response, they simply sidestep the problem. Indeed, doing this ignores the fact that an additional physical criterion is missing in the model, implicitly leading to a limited localization width.

Motivated by the fundamental work of Eringen (1966) and here especially by the *axiom of neighborhood*, various nonlocal continuum formulations have been developed with the aim to close this gap. In literature, two families of such nonlocal formulations can be identified.

Nonlocal models of *integral type* generally consist in replacing a specific variable (e.g., strain, equivalent plastic strain, damage etc.) at each point by its nonlocal counterpart obtained by weighted averaging over a neighborhood. Rather interested in the continuum based description of interacting dislocations than developing a localization limiter Eringen (1981) presented a framework based on the nonlocal counterpart of the strain tensor. Later Bazant and Lin (1988) proposed a formulation working with the nonlocal plastic strain tensor or alternatively, working with the nonlocal average of the plastic multiplier. Performing a series of simulations with different minimum element sizes, here in terms of an excavation process, Bazant and Lin (1988) successfully demonstrated the ability of this formulation to act as a localization limiter. An application of nonlocal averaging of the damage can be found, e.g., in the work of Bazant and Pijaudier-Cabot (1988) and Tvergaard and Needleman (1995). Although the interpretation of the integral type approaches is descriptive, the additional numerical effort, necessary when calculating the nonlocal average quantity for every integration point, is their main drawback. Moreover, the implementation inside a commercial finite element code is not simply to achieve.

The differential counterpart of the nonlocal integral approaches is represented by models of *gradient type*. Instead of considering the influence of the neighborhood through integrals, this family of models introduces the nonlocal character by incorporating higher order gradients into the constitutive model. Influenced by the pioneering work of Toupin (1962) and Mindlin (1964), Chambon et al. (1998) as well as Fleck and Hutchinson (1997) adapted the idea of higher order stresses, work conjugate to strain gradients, to formulate a strain gradient plasticity framework. While in the formulation of Chambon et al. (1998) the higher order stress enters only the balance of momentum, the theory of Fleck and Hutchinson (1997) considers these additional stresses in terms of the yield condition. Although physically motivated by the concept of statistically stored dislocations (SSD) and geometrically stored dislocations (GND), the essential formulation of Fleck and Hutchinson (1997) remains phenomenological. Contrarily, the group of mechanism-based strain gradient (MSG) plasticity theories is based on micromechanical effects on the flow strength of materials. An application of the MSG concept, originally formulated in Gao et al. (1999) and Huang et al. (2000), can be found, e.g., in Qiu et al. (2003), here in context of micro-indentation hardness experiments. While the above methods consider higher order displacement gradients or corresponding stress quantities, models with gradients of internal variables represent a more general concept to introduce non-locality. For example, Aifantis (1984, 1992) and Maugin (1990) consider higher gradients of the equivalent plastic strain and damage, respectively. In contrast to integral type approaches, the finite element implementation of gradient type models is, in general, straight forward. However, the higher order displacement gradients have to be considered in higher order element shape functions.

A relation between integral type and gradient type nonlocal formulations is established by applying a Taylor series expansion of the local quantity into the corresponding integral expression for the nonlocal quantity. Assuming isotropy of the used weight function, this results into an explicit gradient type approximation, including the Laplacian of the local quantity. A detailed derivation can be found, e.g., in the work of Engelen et al. (2003). As stated above, the explicit incorporation of higher order gradients requires higher order element shape functions. Thus, further improvements have been suggested by Peerlings et al. (1996). In this work the author showed, that via mathematical manipulation of the explicit nonlocal approximation an implicit formulation, including the Laplacian of the nonlocal quantity, can be established. In case of using Green's weight function, this formulation gives the exact representation of the integral formulation as has been shown by Peerlings et al. (2001). Thus, working with the weak form of the latter result, only C^0 interpolation of the corresponding quantity is required. While the explicit gradient formulation considers the dependence on the infinitely close neighborhood, the solution of the nonlocal field in terms of the implicit gradient formulation depends on the local quantity in the entire body. Thus, in the sense of Rogula (1982), explicit gradient type formulations are often referred to as *weakly nonlocal*, while implicit gradient type formulations are, in the sense of Geers et al. (2000), called *strongly nonlocal*.

The intention of the work presented in the following is to develop a general finite element framework to model and simulate the process of metal cutting and related processes. Here, we deal with two key issues. To resolve the complex deformation patterns, observed in context of metal cutting, we develop an adaptive finite element framework, based on a combination of error estimation and refinement indication. Further, we present an extended thermodynamic framework with a general non-local description of several thermodynamic quantities. In this context we also discuss the effect of ductile damage. The extended non-local description allows the modeling of lengthscale-effects, in general, but also the additional benefit of further reduction of mesh dependence is important. As basic works concerning the simulation of high speed cutting have been achieved for Inconel 718 (see Sievert et al. (2003); Singh et al. (2003)) and thus, a complete set of parameters is available, we restrict to this material throughout this work. The work is organized as follows.

Chapter 2 discusses the basic problems of material softening in context of a finite element simulation of metal cutting. Starting with a simple thermoelastic, viscoplastic material model, discussed in Section 2.2, we give an introduction to the problem of mesh dependence in context of shear band formation (Section 2.3), followed by a presentation of simulation results for the cutting process, using an established finite element model (Section 2.4). As a main outcome of these examinations we identify the problem of mesh orientation dependence, as well as the inadequately modeling of the kinematic situation inside the main deformation zone, when using standard finite element techniques. Especially the last point is relevant in context of resolving the state of the resulting cutting surface.

Based on these basic observations, we propose the application of an adequate adaptive remeshing technique, developed in **Chapter 3**. First, we give a detailed presentation of the algorithm

mic formulation of the remeshing process in Section 3.2. Possible model quantities relevant to error estimation in context of material instability are discussed in Section 3.3. Next, the error-estimation method and refinement indicators, developed in the current work, are applied to investigate different refinement strategies in the context of shear-band formation. Building on this, a complete refinement strategy is developed (Section 3.4). Finally, we apply this strategy to the simulation of the high-speed cutting process in Section 3.5. At this stage, the finite element framework allows a robust simulation of the process with an immense reduction of the influence of mesh orientation. Also, the simulation of the resulting surface is now possible.

In **Chapter 4** improvements are suggested by an extension of the material model by ductile damage and further, by a nonlocal description of the material. A detailed derivation of the extended thermodynamic framework is given in Section 4.2. The specific application to non-isochoric thermo-viscoplasticity, including ductile damage is given in Section 4.3. A detailed derivation of the algorithmic implementation and the algorithmic linearization, as needed in context of a finite element implementation, are discussed in Section 4.4 and Section 4.5, respectively. A detailed discussion of the kinematics in context of adaptive remeshing is given in Section 4.7. In context of a model with internal variables this issue is of special importance.

In **Chapter 5**, finally, the complete framework, consisting of the adaptive remeshing scheme and the extended thermodynamic formulation, is applied to the simulation of the high speed cutting process and results are discussed. Here, we start with the discussion of heat conduction, excluding damage (Section 5.1). As will be shown, thermal softening alone leads to a delayed chip segmentation and furthermore to unrealistic high temperatures inside the main deformation zone. Improvements are demonstrated in terms of an additional damage formulation, (Section 5.2). As will be shown, due to lack of any dependence on time- or lengthscale for local damage development, as e.g. given for the development of temperature in terms of the heat balance equation, simulation results show a dependence on the local element edge length for such a local formulation. Improvements by a non-local formulation of damage are discussed in Section 5.3. Here, we also discuss the implementation of the non-local formulation in a commercial code. The issue of non-isochoric plasticity and the related pressure dependent damage development are discussed in Section 5.4. This Chapter closes with the presentation of simulation results, calculated in context of a benchmark study (Section 5.5).

Chapter 2

Simulation of chip formation during high-speed cutting

Abstract– In this chapter we discuss the modeling and simulation of shear banding and chip formation during high-speed cutting. During this process, shear bands develop where thermal softening dominates strain- and strain-rate-dependent hardening. This occurs in regions where mechanical dissipation dominates heat conduction. On the numerical side, we carry out a systematic investigation of size- and orientation-based mesh-dependence of the numerical solution. The consequences of this dependence for the simulation of cutting forces and other technological aspects are briefly discussed.

2.1 Introduction

High-speed cutting is a process of great interest in modern production engineering. In order to take advantage of its potential, a knowledge of the material and structural behavior in combination with the technological conditions is essential. To this end, investigations based on the modeling and simulation of the process are necessary. Initially such investigations were analytical in nature and focused on the process of machining (*e.g.*, Lee and Shaffer (1951); Merchant (1945)). For the significantly more complex processes and geometries of today, approaches based on numerical and in particular finite-element simulation represent the state of the art, see Bäker (2003, 2006); Bäker et al. (2002); Behrens et al. (2005); Mabrouki and Rigal (2006); Özel and Altan (2000); Özel and Zeren (2004); Sievert et al. (2003). In order to account for the effects of high strain-rates and temperature on the material behavior, most of these approaches are based on thermoviscoplastic material modeling. For example, the Johnson-Cook model Johnson and Cook (1983) is used in Behrens et al. (2005); Özel and Zeren (2004); Sievert et al. (2003) and in the current work.

Experimental results of El-Magd and Treppmann (2001); El-Wardany and Elbestawi (2001); Sievert et al. (2003); Tönshoff et al. (2005) show that shear banding represents the main mechanism of chip formation and results in reduced cutting forces. In the context of a finite-element analysis such shear banding can be modeled using thermo-viscoplastic material models including in particular the effect of thermal softening (and in general damage as well: *e.g.*, Sievert et al. (2003)). As well-known this results in a loss of solution uniqueness, resulting in so-called pathological mesh-dependence of the simulation results. Usually, this dependence is expressed in terms of the size of the elements used, *i.e.*, the element edge-length. However, it is not restricted to this property of the elements. Indeed, as investigated in the current work, other properties, *e.g.*, element orientation or interpolation order, are just as, if not more, influential

in this regard. All these element properties are relevant in the context of, *e.g.*, the use of adaptive remeshing techniques, see Bäker (2003, 2006); Bäker et al. (2002); Özel and Altan (2000); Özel and Zeren (2004), to deal with large element distortion, resulting almost invariably in unstructured meshes. In the literature remeshing techniques using structured meshes can also be found. In Bäker (2006); Bäker et al. (2002), for example, an arbitrary Lagrangian-Eulerian-like approach is used to rearrange and refine a structured mesh. As will be shown in the current work, the influence of the mesh orientation becomes significant in the context of adiabatic shear banding, especially in connection with structured meshes.

The use of remeshing techniques may lead to a reduction of mesh-dependence, but of course cannot eliminate it. This can be achieved only by working with models based on additional criteria (*e.g.*, penalization of “vanishingly thin” shear-bands via regularization). As a first step in the direction of developing adaptive remeshing techniques for such regularized modeling, the purpose of the current chapter is an investigation of the effects of variable element properties such as orientation on simulation results for shear-band development and chip formation in the context of metal cutting processes. This is done here primarily for structured meshes.

2.2 Material modeling

As is well-known, metal cutting is influenced by a number of competing physical processes in the material, in particular heat conduction and mechanical dissipation. Consider, for example, the cutting of the material X20Cr12 at different cutting speeds as shown in Figure 2.1. At

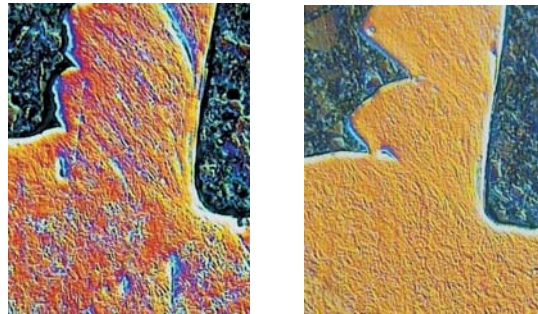


Figure 2.1: Cutting of the chrome alloy X20Cr13 at cutting speeds v_c of 8 m/min (left) and 200 m/min (right) showing the dependence of chip formation on cutting speed (courtesy of Stefan Hesterberg, Institute of Machining Technology, Dortmund University of Technology).

lower cutting speeds (left) and resulting lower strain-rates, heat conduction is sufficiently fast to prevent a temperature increase due to mechanical dissipation which would result in thermal softening. At higher speeds (right) and so higher strain-rates, however, heat conduction is too slow to prevent the temperature from increasing to the point where thermal softening occurs, resulting in shear-banding and chip formation.

The strong dependence of this process on strain-rate and temperature implies that the material behavior of the metallic workpiece is fundamentally thermoelastic and thermoviscoplastic in nature. For simplicity, isotropic material behavior is assumed here. In particular, the current model is based the assumption of constant heat capacity and isotropic thermoelasticity for small elastic strain. Further, isotropic Fourier heat conduction is assumed. In addition, a modified

form of the Johnson-Cook model for metal viscoplasticity is employed. In this case, any energy storage due to hardening is tacitly neglected. Restricting attention then to metals, small elastic strain and dynamic conditions, the free energy density in this case is assumed to be given by the thermoelastic Hooke form

$$\begin{aligned} \psi(\theta, \epsilon_H, \epsilon_D) &= \frac{1}{2} \kappa_0 \epsilon_H^2 + \mu_0 \epsilon_D^2 + 3 \kappa_0 \alpha_0 (\theta_0 - \theta) \epsilon_H \\ &+ \rho_0 c_0 \{ \theta - \theta_0 - \theta \ln(\theta/\theta_0) \}. \end{aligned} \quad (2.1)$$

Here, $\kappa_0 := \lambda_0 + \frac{2}{3} \mu_0$ represents the elastic bulk modulus, λ_0 and μ_0 are the elastic longitudinal and shear moduli, α_0 the thermal expansion, ρ_0 the density, and c_0 the heat capacity, all at the reference temperature θ_0 . In addition, θ is the absolute temperature, and

$$\begin{aligned} \epsilon_H &:= \text{tr}(\ln \mathbf{V}_E), \\ \epsilon_D &:= \text{mag}(\text{dev}(\ln \mathbf{V}_E)), \end{aligned} \quad (2.2)$$

represent scalar strain measures derived from the elastic left logarithmic stretch $\ln \mathbf{V}_E = \frac{1}{2} \ln(\mathbf{B}_E)$. In turn, this measure is determined by the elastic left Cauchy-Green deformation $\mathbf{B}_E = \mathbf{F} \mathbf{C}_P^{-1} \mathbf{F}^T$ depending on the deformation gradient \mathbf{F} and plastic right Cauchy-Green deformation \mathbf{C}_P . Here, $\text{dev}(\mathbf{A}) := \mathbf{A} - \frac{1}{3} \text{tr}(\mathbf{A}) \mathbf{I}$ is the deviatoric part, and $\text{mag}(\mathbf{A}) := \text{tr}(\mathbf{A}^T \mathbf{A})^{1/2}$ the magnitude, of any second-order tensor \mathbf{A} . In what follows, we also work with the direction $\text{dir}(\mathbf{A}) := \mathbf{A}/\text{mag}(\mathbf{A})$ of any non-zero tensor. The relations (2.1) and (2.2) determine in particular the form

$$\mathbf{K} = \partial_{\ln \mathbf{V}_E} \psi = \sigma_H \mathbf{I} + \sigma_D \text{dir}(\text{dev}(\ln \mathbf{V}_E)) \quad (2.3)$$

of the Kirchhoff stress \mathbf{K} , with

$$\begin{aligned} \sigma_H &:= \frac{1}{3} \text{tr}(\mathbf{K}) &= \partial_{\epsilon_H} \psi &= \kappa_0 \{ \epsilon_H + 3 \alpha_0 (\theta_0 - \theta) \}, \\ \sigma_D &:= \text{mag}(\text{dev}(\mathbf{K})) &= \partial_{\epsilon_D} \psi &= 2 \mu_0 \epsilon_D, \end{aligned} \quad (2.4)$$

its scalar hydrostatic and deviatoric parts, respectively. In the context of model class defined by (2.1) note that the pairs (σ_H, ϵ_H) and (σ_D, ϵ_D) are natural thermodynamic conjugates.

Neglecting any deformation-dependent damage and assuming inelastically incompressible von-Mises flow, the evolution of $\ln \mathbf{V}_E$ is given by the (objective) associated flow rule

$$- \ln \dot{\mathbf{V}}_E^* := \frac{1}{2} \ln(\mathbf{F} \dot{\mathbf{C}}_P^{-1} \mathbf{F}^T) = \dot{\alpha}_P \partial_{\mathbf{K}} \sigma_{vM} \quad (2.5)$$

in terms of the inelastic right Cauchy-Green deformation \mathbf{C}_P and accumulated equivalent inelastic deformation α_P . Here,

$$\sigma_{vM} = \sqrt{\frac{3}{2}} \sigma_D = \sqrt{6} \mu_0 \epsilon_D \quad (2.6)$$

is the von Mises effective stress measure determined by the Kirchhoff stress. In the current thermodynamic approach, this determines the evolution of α_P via the implicit evolution relation

$$\sigma_{vM} = \partial_{\alpha_P} \chi \quad (2.7)$$

as based on the dissipation potential χ , again for the case of negligible energetic hardening. The form of χ compatible with the Johnson-Cook model (Johnson and Cook (1983)) for inelastic

flow assumed here and with Fourier heat conduction is given by

$$\begin{aligned}\chi(\theta, \mathbf{F}, \alpha_P, \nabla\theta, \dot{\alpha}_P) &= (1 - C_0) \sigma_{Yd}(\theta, \alpha_P) \dot{\alpha}_P \\ &+ C_0 \sigma_{Yd}(\theta, \alpha_P) \dot{\alpha}_{P0} (1 + \dot{\alpha}_P/\dot{\alpha}_{P0}) \ln(1 + \dot{\alpha}_P/\dot{\alpha}_{P0}) \\ &+ \frac{1}{2} \theta^{-1} k_0 \mathbf{F}^{-T} \nabla\theta \cdot \det(\mathbf{F}) \mathbf{F}^{-T} \nabla\theta.\end{aligned}\quad (2.8)$$

Here, k_0 represents the coefficient of thermal conductivity, and $\nabla\theta$ is the referential temperature gradient. Further, the material parameter C_0 mediates the strain-rate dependence of hardening and

$$\sigma_{Yd}(\theta, \alpha_P) := \{A_0 + B_0 \alpha_P^{n_0}\} \{1 - [\langle\theta - \theta_0\rangle/(\theta_{M0} - \theta_0)]^{m_0}\} \quad (2.9)$$

represents the temperature- and strain-dependent part of the effective yield stress. This yield stress is determined by the initial yield stress A_0 , the isotropic hardening parameters B_0 and n_0 , as well as the melting temperature θ_{M0} and thermal softening exponent m_0 . In addition, $\langle x \rangle = \frac{1}{2} (x + |x|)$ is the ramp function.

The current thermomechanical model formulation is completed by the field relation

$$\rho_0 c_0 \dot{\theta} = \omega - \operatorname{div} \mathbf{q} \quad (2.10)$$

for the temperature θ . Here, ω represents the rate of heating, and

$$-\mathbf{q}/\theta = \partial_{\nabla\theta} \chi \quad (2.11)$$

the heat flux, here given by the Fourier model. Assuming no external supplies and the Taylor-Quinney approximation, ω takes the form

$$\omega = \beta_0 \sigma_{vM} \dot{\alpha}_P - 3 \kappa_0 \alpha_0 \theta \mathbf{F}^{-T} \cdot \dot{\mathbf{F}}, \quad (2.12)$$

determined in particular by the Taylor-Quinney coefficient β_0 . In Rosakis et al. (2000), it has been shown that β_0 is in fact not a constant but rather depends on strain and strain-rate to varying degrees. In the following, this coefficient will be treated as constant as there is no experimental data relevant to the determination of β_0 for the material (Inconel 718) considered in this study.

Consider next the algorithmic formulation of the above model relations. Backward-Euler integration of the flow rule (2.5) over a time interval $[t_n, t_{n+1}]$ with time-step $t_{n+1,n} := t_{n+1} - t_n$ yields its algorithmic form

$$\ln \mathbf{V}_{En+1} + \sqrt{\frac{3}{2}} \alpha_{P_{n+1,n}} \operatorname{dir}(\operatorname{dev}(\ln \mathbf{V}_{En+1})) = \ln \mathbf{V}_{En+1}^{\operatorname{tr}}. \quad (2.13)$$

Here, $\alpha_{P_{n+1,n}} := \alpha_{P_{n+1}} - \alpha_{P_n}$,

$$\ln \mathbf{V}_{En+1}^{\operatorname{tr}} = \frac{1}{2} \ln(\mathbf{F}_{n+1} \mathbf{C}_{P_n}^{-1} \mathbf{F}_{n+1}^T) = \frac{1}{2} \ln(\mathbf{F}_{n+1,n} \mathbf{B}_{E_n} \mathbf{F}_{n+1,n}^T) \quad (2.14)$$

represents the trial value of the elastic left logarithmic stretch, $\mathbf{B}_E := \mathbf{F}_E \mathbf{F}_E^T$ is the elastic left Cauchy-Green deformation, and $\mathbf{F}_{n+1,n} := \mathbf{F}_{n+1} \mathbf{F}_n^{-1}$ the relative deformation gradient. In an analogous fashion, backward-Euler integration of the rate of heating (2.12) yields

$$\omega_{n+1} = \beta_0 \sigma_{vM_{n+1}} \alpha_{P_{n+1,n}}/t_{n+1,n} - 3 \kappa_0 \alpha_0 \theta_{n+1} \ln(\det(\mathbf{F}_{n+1,n}))/t_{n+1,n}. \quad (2.15)$$

In the special case of adiabatic conditions, this determines the algorithmic update

$$\theta_{n+1} = \frac{\rho_0 c_0 \theta_n + \beta_0 \sigma_{vMn+1} \alpha_{Pn+1,n}}{\rho_0 c_0 + 3 \kappa_0 \alpha_0 \ln(\det(\mathbf{F}_{n+1,n}))} \quad (2.16)$$

for the temperature from (2.10). Returning to (2.13), it implies the updates

$$\begin{aligned} \sigma_{Hn+1} &= \kappa_0 \{ \epsilon_{Hn+1}^{\text{tr}} + 3 \alpha_0 (\theta_0 - \theta_{n+1}) \}, \\ \sigma_{Dn+1} &= 2 \mu_0 \epsilon_{Dn+1}^{\text{tr}} - \sqrt{6} \mu_0 \alpha_{Pn+1,n}, \end{aligned} \quad (2.17)$$

of σ_H and σ_{Dn+1} via (2.4). Note also that

$$\text{dir}(\text{dev}(\ln \mathbf{V}_{En+1})) = \text{dir}(\text{dev}(\ln \mathbf{V}_{En+1}^{\text{tr}})) \quad (2.18)$$

follows from (2.13). On the other hand, backward-Euler integration of (2.7) yields

$$\begin{aligned} \sigma_{vMn+1}^{\text{tr}} &= 3 \mu_0 \alpha_{Pn+1,n} \\ &+ \sigma_{Yd}(\theta_{n+1}, \alpha_{Pn+1}) \left\{ 1 + C_0 \ln \left(1 + \frac{\alpha_{Pn+1,n}/t_{n+1,n}}{\dot{\alpha}_{P0}} \right) \right\} \end{aligned} \quad (2.19)$$

via (2.8) and (2.13) to solve for α_{Pn+1} . As usual, this is done on a predictor-corrector basis here. In particular, if $\sigma_{vMn+1}^{\text{tr}} \leq \sigma_{Yd}(\theta_{n+1}, \alpha_{Pn})$ holds for $[t_n, t_{n+1}]$, this is a thermoelastic step. Otherwise, we have a corrector step based on the numerical solution of the implicit relation (2.19) for α_{Pn+1} . From this, one obtains the update (2.17)₂ for σ_D . Together with (2.17)₁ and (2.18), this determines \mathbf{K}_{n+1} via (2.3).

The local behavior of the above model can be illustrated with the help of the adiabatic special case and neglecting elastic strain. In this case, set $\epsilon \equiv \alpha_P$. One obtains the simple coupled system

$$\begin{aligned} \sigma(\theta, \epsilon, \dot{\epsilon}) &= \sigma_{Yd}(\theta, \epsilon) \{ 1 + C_0 \ln(1 + \dot{\epsilon}/\dot{\alpha}_{P0}) \}, \\ \theta(\sigma, \dot{\epsilon}) &= \theta_0 + \beta_0 \sigma \dot{\epsilon} / c_0, \end{aligned} \quad (2.20)$$

from (2.16) and (2.19). At fixed strain-rate $\dot{\epsilon}$, for example, these determine the stress and temperature as a function of strain. For all calculations to follow, we work with the parameter values for the material Inconel 718. These have been identified in Sievert et al. (2003) and are summarized in Table 5.1. Now, when the material deforms plastically, the part of inelastic mechanical

θ_0 [K]	λ_0 [MPa]	μ_0 [MPa]	α_0 [K ⁻¹]	ρ_0 [kg/ m ³]	c_0 [J/kg K]		
300	110476	80000	4.3 10 ⁻⁶	8.19325 10 ³	435		
A_0 [MPa]	B_0 [MPa]	n_0	θ_{M0} [K]	m_0	C_0	$\dot{\alpha}_{P0}$ [s ⁻¹]	β_0
450	1700	0.65	1570	1.3	0.017	0.001	0.9

Table 2.1: Johnson-Cook model parameters for Inconel 718 (partly from Sievert et al. (2003)).

dissipation transformed into heat (as determined by β_0) results in a temperature rise. On the basis of (2.20) and the above parameters, the temperature increase can be calculated. It is shown as a function of equivalent strain in Figure 2.2 (left). In contrast to accumulated inelastic strain, an increase of temperature results in softening. At points of maximal mechanical dissipation in the material, softening effects may dominate hardening (Figure 2.2, right), resulting in material instability, deformation localization and shear-band formation.

This completes the summary of the model. Next, we turn to the finite-element simulations and the issue of mesh-dependence.

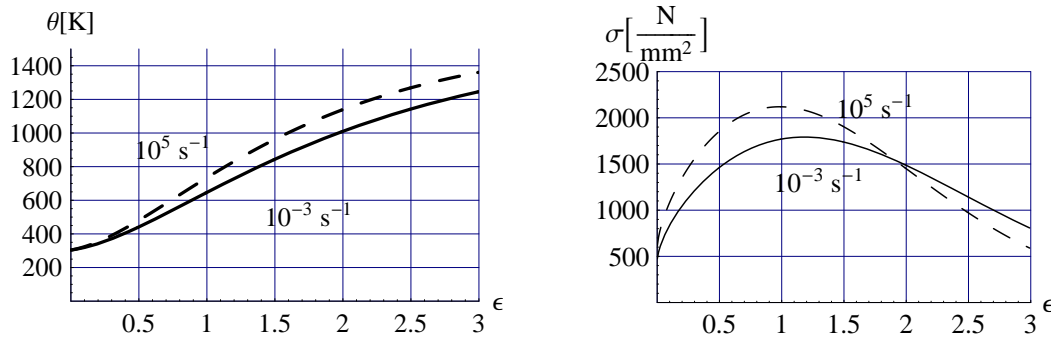


Figure 2.2: Temperature (left) and yield stress (right) as a function of equivalent strain in dynamic uniaxial tension at two different strain-rates as based on (2.20).

2.3 Finite-element simulation of thermal shear-banding

Since chip formation begins with the onset of shear-banding, we begin by looking at this process. For comparison with the following results, consider the cutting process idealized as a simple shear of the material in the shear zone as shown in Figure 2.3. Cutting of the region enclosed in the dashed box is carried out at an assumed shear angle of $\phi = 40^\circ$ and a cutting depth of 0.25 mm. The deformation is assumed to be plane strain. The applied shear velocity v_{shear} corresponds to a cutting velocity v_c in the shear zone of about 1000 m/min.

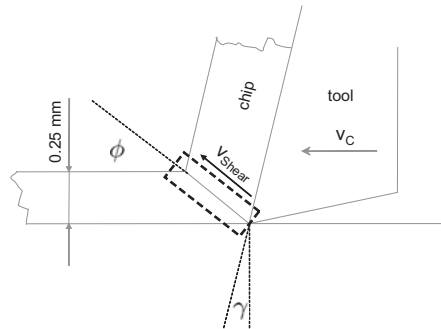


Figure 2.3: Cutting zone idealized as a shear zone in the material undergoing simple shear.

Roughly speaking, a shear band begins to form in the material at a point where the behavior changes from hardening to softening. In particular, in a material deforming initially homogeneously, this will occur in regions of stress concentration, *i.e.*, at geometric or material inhomogeneities. In the technological context of chip formation, the contact of the tool edge with the work piece and the subsequent loading results in such an inhomogeneity. In the context of real materials, of course, material heterogeneity often plays a role as well.

As we have seen in Figure 2.1 for the material X20Cr13, the cutting speed plays a role in whether or not shear-band and chip formation occurs during cutting. To look at this briefly in the context of the simulation, consider the idealized notched specimen shown in Figure 2.4. Except where otherwise indicated, the simulations in this work have been carried out in ABAQUS/Explicit using bilinear quadrilateral elements with reduced integration (CPE4R). The reduced integration scheme is based on the *uniform strain formulation*, as introduced by Flanagan and Belytschko (1981). In this method, the element strain is assumed to be given by the

average strain over the element.

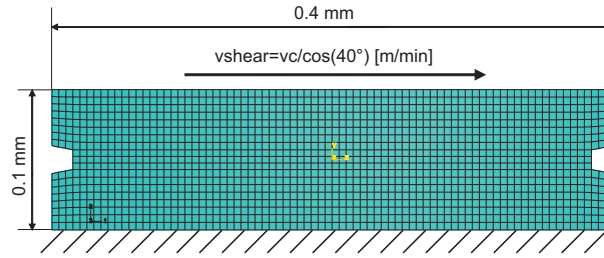


Figure 2.4: Idealized notched structure discretized with bilinear elements oriented in the predicted shear-band direction. Average element edge-length here is 0.005 mm.

The notch in the idealized specimen represents a geometric inhomogeneity where stress concentrates upon loading. Consequently, the material yields there first, inelastic deformation accumulates there the fastest, and the temperature increase due to inelastic dissipation is the greatest. From the point of view of the material behavior as shown in Figure 2.2, the notch regions will consequently be the first to soften, concentrating further inelastic deformation there and resulting in band formation.

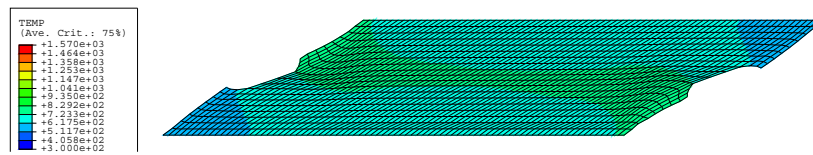


Figure 2.5: Temperature distribution inside the notched structure from Figure 2.4 subject to a shearing rate equivalent to a cutting speed v_c of 10 m/min. At this “slow” speed, thermal conduction is sufficiently fast to prevent any increase of temperature in the structure to the point where thermal softening begins and leads to shear-band formation.

Using this geometry, consider first the influence of strain-rate on shear-band formation. In the technological context, the strain-rate is correlated with the cutting speed. Consider now the shear deformation of the structure in Figure 2.4 at rates representing cutting speeds of 10 m/min and 1000 m/min, respectively. As shown in Figure 2.5, at 10 m/min, heat conduction in Inconel 718 has sufficient time to prevent any significant temperature rise in the material due to mechanical dissipation which could result in thermal and shear-band formation. On the other hand, at 1000 m/min, thermal conductivity is simply too slow in comparison to the rate of mechanical dissipation to prevent a sufficient temperature rise for thermal softening and shear-banding to occur, as shown in Figure 2.6. For the case of Inconel 718, in the context of the Johnson-Cook model, note that the temperature varies between the melting temperature (1570 K) and room temperature (300 K). In the above simulations, the thermal conductivity is fixed at $k_0=20$ [Wm⁻¹K⁻¹]. A temperature dependent description of this quantity is given in Pottlacher et al. (2002).

Clearly, for Inconel 718 subject to a shearing rate corresponding to a cutting speed of 1000 m/min, mechanical dissipation dominates thermal conduction leading to thermal softening, shear-band development and chip formation. Restricting now attention to this “high” cutting speed, one can reasonably assume adiabatic conditions for simplicity. In this case, the spatial

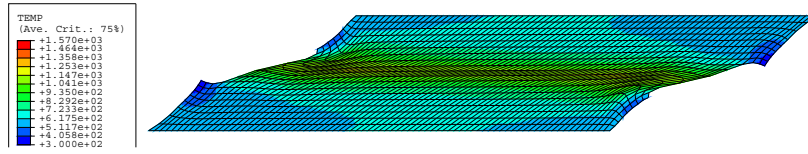


Figure 2.6: Temperature distribution inside the notched structure in Figure 2.4 subject to a shearing rate equivalent to a cutting speed v_c of 1000 m/min. In contrast to the case at low cutting speeds in Figure 2.5, here thermal conduction is too slow to prevent thermal softening and shear-band formation.

distribution of the temperature and the (equivalent) strain-rate are correlated, and either can be used to display shear-band development.

Now, as discussed in the introduction, shear-band formation due to thermal softening in the context of the local material model being used here is inherently dependent on the properties of the mesh. Firstly, consider a change of element orientation at constant element edge length for the structure from Figure 2.4. In particular, rotation of all elements in the corresponding mesh at an angle of 45° to the expected (*i.e.*, horizontal) shear-band orientation yields the alternative discretization shown in Figure 2.7. For simplicity, we will refer in what follows to the discretization parallel to the shear direction (Figure 2.4) as being “parallel”, and that in Figure 2.7 as “rotated”. In what follows, we assume adiabatic conditions.

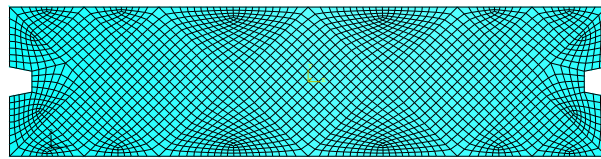


Figure 2.7: Idealized structure with elements oriented at 45° to the direction of shearing. As before, the average element edge length here is 0.005mm.

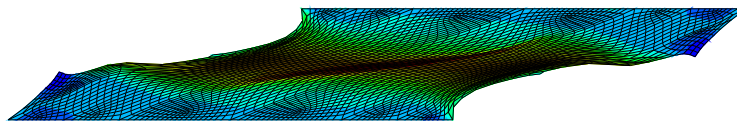


Figure 2.8: Temperature distribution in the mesh from Figure 2.7 after shearing at a rate equivalent to a cutting speed of 1000 m/min. Temperature contours are the same as in Figure 2.6. See text for an explanation and details.

Corresponding to the case shown in Figure 2.6, the structure in Figure 2.7 is sheared at a rate equivalent to a cutting speed of 1000 m/min. The resulting temperature field is shown in Figure 2.8. In contrast to the case of the mesh parallel to the direction of shearing in Figure 2.6, the rotated mesh shows no shear-band formation in the expected direction. The material instability proceeds, contrary to physical expectations, slanted across the structure.

To understand why the orientation of the mesh influences shear-band development in this fashion, consider the situation shown in Figure 2.9.

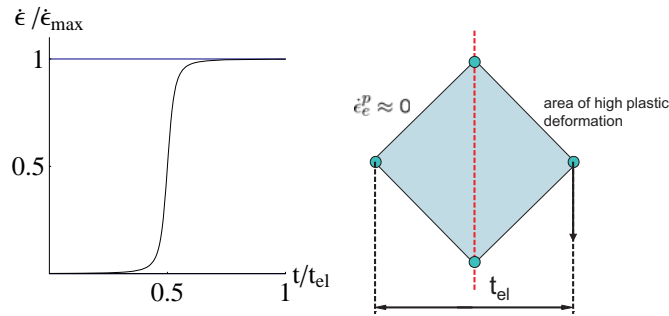


Figure 2.9: Lack of shear-band formation for rotated elements due to the incapacity of the elements to resolve corresponding strain gradient.

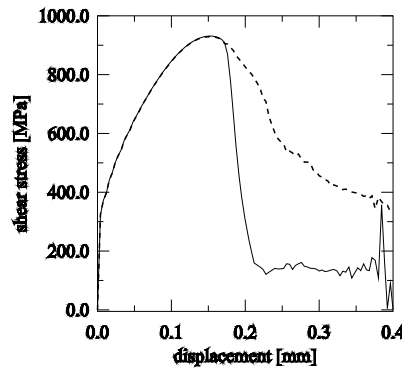


Figure 2.10: Averaged shear stress along upper, sheared edge of structure in the parallel mesh (Figure 2.6; continuous curve) and rotated mesh (Figure 2.8; dashed curve) as a function of the displacement of the upper edge of the structure.

In a coarse, rotated mesh such as that in Figure 2.8, any nucleating shear-band, which physically “wants” to form in the direction of shearing, would have to cross the element interior. Since the elements involved are constant-strain elements, however, they are unable to resolve the corresponding strain gradient in their interiors (see Figure 2.9). In contrast, the strain field can vary from one to the next across the element boundary, facilitating the resolution of strain gradients associated with shear-band formation in the case of the parallel mesh. This is also reflected in the development of the respective shear stresses as shown in Figure 2.10. The inability of the rotated coarse mesh to resolve the shear-band leads to a stiffer behavior than in the parallel case with shear band. On the other hand, if we increase the number of elements (in the process decreasing the element edge-size down to 0.0025 mm), a sufficient number of elements becomes available for the shear-band to form over multiple rotated elements which together can resolve the strain gradient. This is shown in detail in Figure 2.11.

Since in the rotated case, many more elements are required to resolve the same strain-gradient, the shear-band in this case is much wider and “smeared-out” than in the parallel case. Because of this, the development of the shear band in the rotated mesh is also much more sensitive to a change of element edge-length than in the parallel mesh.

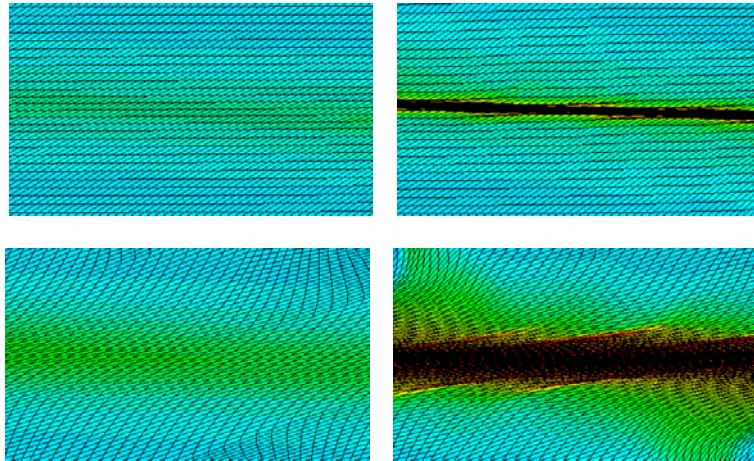


Figure 2.11: Shear-band development in a finely-discretized parallel (above) and rotated (below) mesh at constant element edge-length of 0.0025 mm.

Up to this point, we have fixed the average element edge-length to 0.005 mm. Reducing this size to 0.0025 mm, one obtains the results shown in Figure 2.12 for the parallel case and in Figure 2.13 for the rotated case. In the case of the parallel mesh with constant strain elements, the usual pathological mesh-dependence is evident. In this case, the shear-band volume tends to zero as the number of elements tends to infinity. On the other hand, in the case of the rotated mesh with such elements, the constant-strain constraint clearly prohibits this and would lead to the attainment of a minimum shear-band width. Again, these tendencies are also reflected in the corresponding ones for the shear stress as a function of upper-edge displacement as shown in Figure 2.14. As expected, the coarser mesh in both cases, and the rotated mesh in general, behave more stiffly, resulting in “delayed” shear-band development.

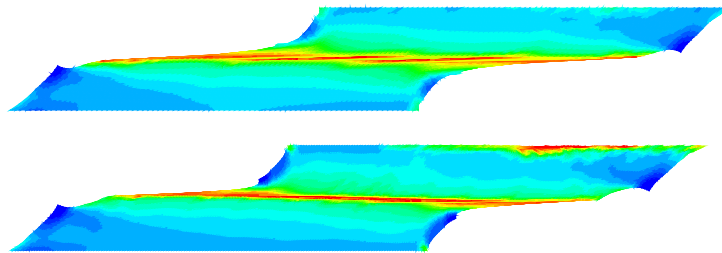


Figure 2.12: Temperature distribution in the notched structure discretized parallel to the shear direction using different element edge lengths: 0.005 mm (above), 0.0025 mm (below). Temperature contours are the same as in Figure 2.6.

Up to this point, we have worked with a fixed element formulation. For completeness, consider now the use of (i) 4-node bilinear elements, and (ii) 8-node biquadratic elements, both having an average element edge-length of 0.005 mm. Figure 2.15 displays the results obtained for the average shear-stress as a function of displacement. These can be compared with the analogous results for the 4-node reduced integration elements from Figure 2.10.

In both cases, the average element edge length remains constant. For the parallel mesh, simulations yield comparable results, as again, the shear-band localizes on aligned element bound-

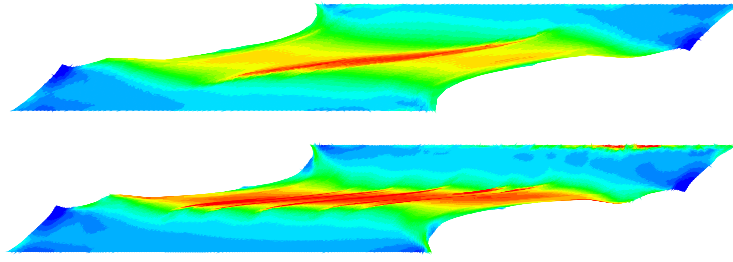


Figure 2.13: Temperature distribution in the notched structure discretized at a 45° angle to the shear direction using different element edge lengths: 0.005 mm (above), 0.0025 mm (below). Temperature contours are the same as in Figure 2.6.

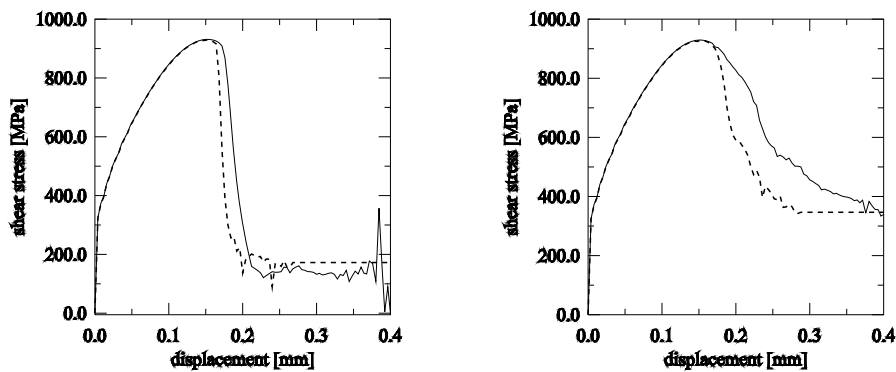


Figure 2.14: Averaged shear stress along upper, sheared edge of structure as a function of the displacement of the top of the structure for the parallel mesh (left) and for the rotated mesh (right) with average element edge-lengths of 0.005 mm (continuous curve) and 0.0025 mm (dashed curve).

aries. As expected for the rotated mesh, an increase in interpolation order and the possibility of resolving strain-gradients within the element results in an accelerated shear-band formation and a slightly faster drop of the shear stress with displacement.

2.4 Finite-element simulation of chip formation

Based on the insight gained into the mesh-dependence of shear-band formation from the previous section, we now turn to the modeling and simulation of the cutting process and chip formation. To this end, we work with the finite-element idealization of the tool / work-piece system shown schematically in Figure 2.16, consistent with the model of Sievert et al. (2003).

For the simulations, the work piece (in blue) is discretized using 4-node bilinear elements with reduced integration (CPE4R). Further, plane strain conditions are assumed. The mesh is oriented at an angle δ to the cutting plane. Initially, we work with a 60×10 element mesh for the work piece. The tool is treated here for simplicity as an analytical rigid body. Also indicated in Figure 2.16 are the contact pairs between the tool and work piece surfaces as well as the fixed nodes. The friction coefficient between tool and workpiece has been estimated and is fixed at μ

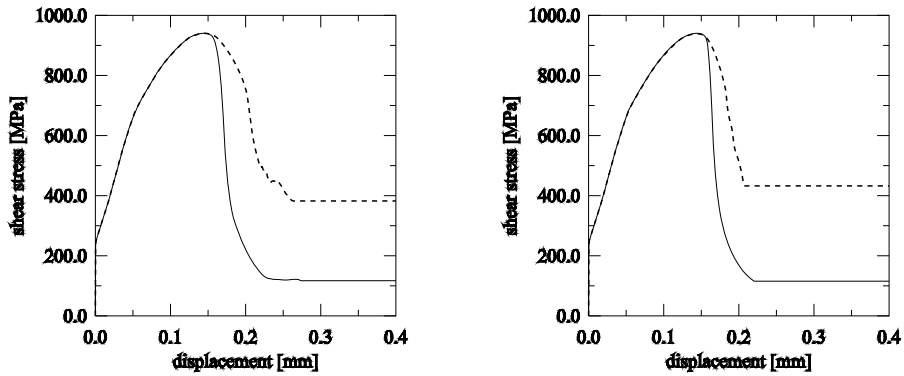


Figure 2.15: Averaged shear stress along the sheared (upper) edge of structure as a function of the displacement of the top of the structure for the 4-node bilinear element case (left) and for the 8-node biquadratic element case (right). The continuous line represents the case of the parallel mesh, and the dashed line that of the rotated mesh. Average element edge-length for all meshes is 0.005 mm.

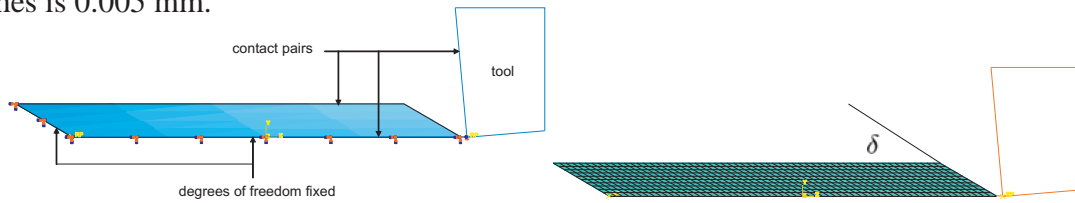


Figure 2.16: Finite-element model for the work-piece / tool system used for the cutting simulation. Mesh orientation relative to the cutting plane is represented here by the angle δ .

= 0.1. All simulations to follow have been carried out using ABAQUS/Explicit.

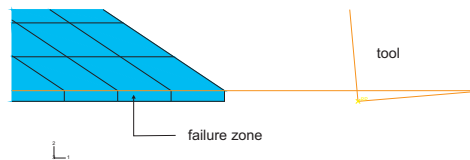


Figure 2.17: Failure zone in the work piece defined by the critical value ϵ_{Pf} of the accumulated equivalent inelastic deformation. The result is a controlled separation of the chip at a defined distance from the tool tip.

The separation of the chip from the work piece is modeled with the help of a failure zone (Figure 2.17). Up to failure, this zone behaves according to the current Johnson-Cook-based model described in Section 2.2. The failure of this zone takes place at a critical value ϵ_{Pf} of the accumulated equivalent inelastic deformation ϵ_P set to a value of 2. Between failure zone and the rest of the work piece, a rigid contact layer is used to avoid penetration of the work piece into the area of the failure zone. This ensures a continuous shear deformation of the failure zone and thus a controlled separation of the chip from the surrounding work piece in a defined distance from the tool tip.

On this basis, consider now the simulation of cutting and chip formation in relation to the

discretization. To begin, attention is focused on the relation between the shear angle ϕ and the mesh discretization angle δ . Since there is no information about the value of ϕ , we begin by considering the well-known models of Merchant (1945) and Lee and Shaffer (1951). In the context of the Merchant model, the relation

$$\phi = \frac{\pi}{4} - \frac{1}{2} (\arctan \mu - \gamma) \quad (2.21)$$

between ϕ and the tool rake angle γ holds, with μ the coefficient of friction between chip and tool. Assuming, for example, $\gamma = -5^\circ$ and $\mu = 0.1$, one obtains $\phi = 40^\circ$. Alternatively, in the model of Lee and Shaffer, one derives the relation

$$\phi = \frac{\pi}{4} \arctan \mu + \gamma \quad (2.22)$$

for ϕ . For the same values of γ and μ , it predicts a smaller shear angle $\phi = 35^\circ$ than the Merchant model.

In the current adiabatic context, the shear angle is determined in the simulations on the basis of the “orientation” of the temperature field within the chip (*i.e.*, normal to the temperature gradient, see Figure 2.18). Determined in this fashion, ϕ varies between 30° and 35° . For discretization angles δ equal to ϕ , one obtains effectively the case of parallel discretization from the last section. Analogously, for δ larger than ϕ , the case of rotated discretization holds. Indeed, as shown by the simulation results in Figure 2.18, chip formation becomes increasingly inhibited and diffuse as δ increases beyond ϕ .

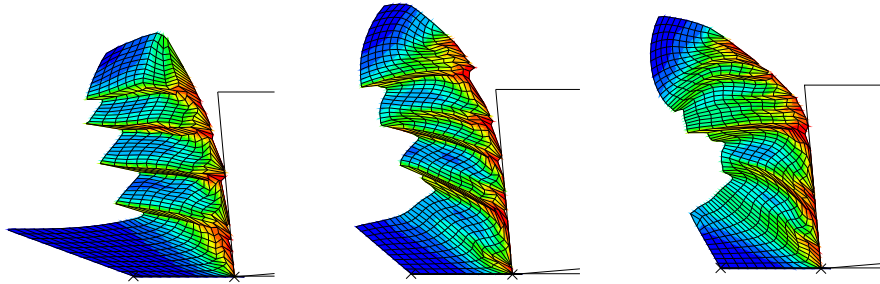


Figure 2.18: Chip formation and temperature field development for different mesh orientation angles δ : $\delta = 20^\circ$ (left), $\delta = 40^\circ$ (middle), $\delta = 60^\circ$ (right). Temperature contours here, and in the following are the same as in Figure 2.6

Also shown in Figure 2.18 (left), as well as close-up in Figure 2.19 (left), is the case $\delta < \phi$. In essence, this also represents the case of the rotated mesh in that shear-band formation is distorted and more diffuse. This is in contrast to the case shown in Figure 2.19 (right), representing in essence the case of the parallel mesh. The shear band is resolved by exactly one layer of elements and there is practically no rotation of the elements. The primary deformation is shear parallel to the element edges.

Turning next to the issue of element edge-length, consider the results shown in Figure 2.20. As discussed above, a reduction of the characteristic element length causes an accelerated formation of the shear band with, globally considered, smaller deformation. For the chip formation

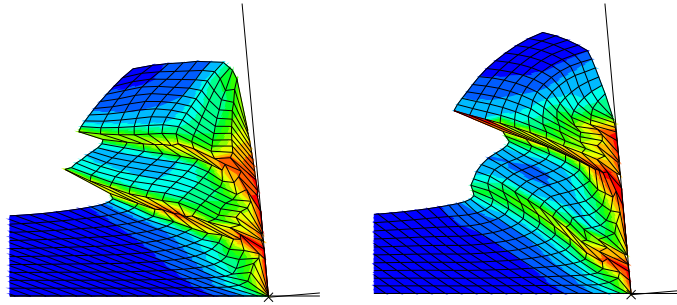


Figure 2.19: Shear-band development during chip formation. Left: $\delta = 20^\circ$. Right: $\delta = 35^\circ$.

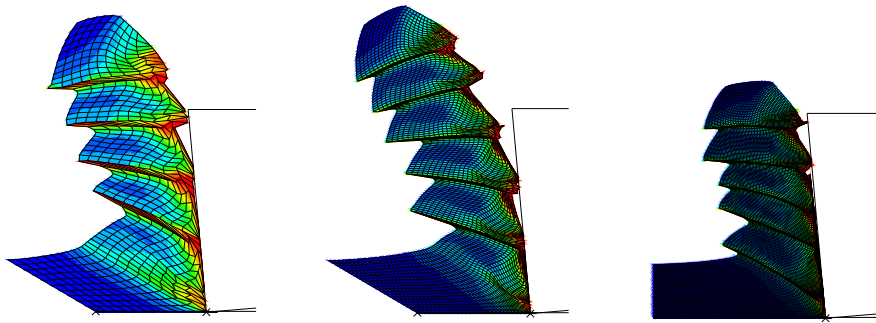


Figure 2.20: Chip formation with $\gamma = -5^\circ$ and $\delta = 30^\circ$ for different discretizations. Left: 60x10 elements; middle: 150x20 elements; right: 250x30 elements. Note the mesh-dependence of segmentation, *i.e.*, an increase in segmentation frequency with mesh refinement.

process, this implies that shear-band formation takes place at a smaller total deformation. As usual, increasing the fineness of the mesh also makes it softer, leading to the tendency shown for the cutting forces in Figure 2.21.

A reduction of the element size results in a reduction in cutting forces with increased segmenting frequency. As discussed above, a reduction of the element size causes stronger deformation localization. This results in an increase of the local deformation-rate to the point where the numerical simulation becomes unstable, as shown in Figure 2.21 (right; solid curve).

As discussed in detail in the previous sections, the finite-element simulation of shear banding and chip formation is strongly dependent not only on mesh size but also on mesh orientation. In light of this, the practice of using the mesh to fit the orientation and thickness of simulated shear bands to experimental results is somewhat questionable and in any case must be done with great care.

2.5 Preliminary Summary

A major issue in the numerical modeling of shear-banding and chip formation during high-speed cutting is the strong dependence of the results on the choice of element size and orientation. As shown in the current work, this choice can have a major influence on the prediction of, for example, chip geometry and cutting forces. The common practice of using the choice of element geometry to adjust simulation results to be in agreement with experimental results (*e.g.*, Sievert

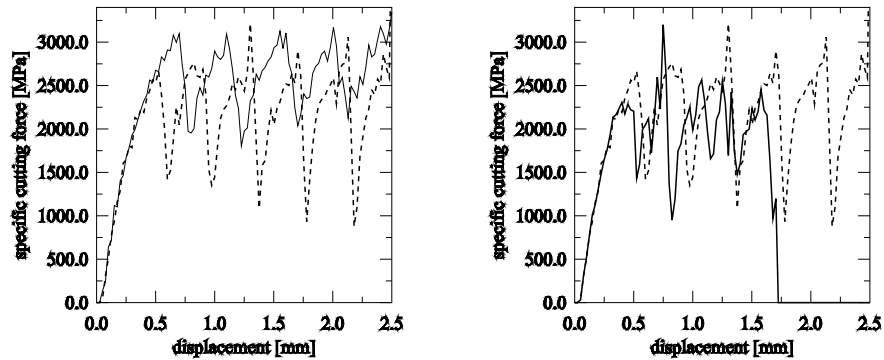


Figure 2.21: Influence of the discretization on the specific cutting force for $\gamma = -5^\circ$; left: 60x10 elements, 150x20 elements (dashed); right: 150x20 elements (dashed), 250x30 elements. Note that the specific cutting force is defined as the cutting force divided by the cutting cross section (cutting depth times cutting feed). Again, note the increase in segmentation frequency with mesh refinement.

et al. (2003)) simply sidesteps the problem. Indeed, doing this simply ignores the fact that an additional physical criterion is missing in the model, the application of which would result in a unique solution to the boundary-value problem in the softening regime. Various possibilities exist, including variational (*e.g.*, Yang et al. (2005)) and non-local approaches also involving damage (*e.g.*, Reusch et al. (2003)). In addition, error control and adaptive mesh-refinement methods (also for variational and non-local models) are being implemented for efficient and robust finite-element simulations of deformation localization (*e.g.*, Comi and Perego (2004)). In this context, the above results clearly show, that the application of adaptive remeshing must primarily ensure the resolution of the gradients of internal variables. This has to be considered, when discussing, *e.g.*, reasonable remeshing criteria.

Chapter 3

Adaptive FE-simulation of shear banding and high-speed cutting

Abstract– The purpose of this chapter is to extend the finite element framework in terms of an adaptive remeshing scheme. In this context, possible model quantities relevant to error estimation in context of material instability are discussed. After a detailed presentation of the algorithmic formulation and implementation, the error-estimation method and refinement indicators, developed in the current work, are applied to investigate different refinement strategies in the context of shear-band formation. Building on this, a complete refinement strategy is developed. Finally, we apply this strategy to the simulation of the high-speed cutting process. At this stage, the finite element framework allows a robust simulation of the process with an immense reduction of the influence of mesh orientation. Also, the simulation of the resulting surface is now possible.

3.1 Introduction

In whatever context, the basic goals of adaptive remeshing are (i) to avoid extreme element distortion and (ii) to ensure the appropriate resolution of the underlying boundary value problem at any time and thus, avoiding mesh dependent results. As will be shown, adaptive remeshing can be used to significantly reduce mesh-dependence. In context of adiabatic shear banding, this involves reducing the element size below the characteristic length of material instability. A similar conclusion can also be found in Huerta and Pijaudier-Cabot (1994). In general, the element size must be small enough to resolve the material instability. And even then, pathological mesh-dependence remains.

The choice of a suitable refinement strategy for the case of adiabatic shear banding is still an open question. Most of the refinement strategies offered in literature focus on error estimation, which is technically mature for linear problems. Here, research mainly focuses on error estimation based on local residuals, as introduced by Babuska and Rheinboldt (1978) and recovery-based error estimation, as proposed by Zienkiewicz and Zhu (1987). For non-linear problems, method investigation and development is still far from complete. For example, Rodriguez-Ferran and Huerta (2000) apply residual-based error estimation in the context of a non-local damage model. Using residual-based error estimation, Huerta et al. (2002) presents a general approach for the non-linear case. Application of recovery-based error estimation can be found in Boroomand and Zienkiewicz (1999), here extended to general elasto-plasticity, or in context of forging simulations in Boussetta et al. (2006).

Complementary to error-estimation methods are refinement-indicator-based methods. In par-

ticular, these facilitate a more physical interpretation of the refinement strategy. On the other hand, they are less accurate than estimation methods, as heuristic in nature. Furthermore, they are application-dependent. For example, Marusich and Ortiz (2005) use the local value of the plastic power to detect the onset of localization locally. Another approach is proposed by Ortiz and Quigley (1991). Here, variations in the velocity field are chosen to act as the refinement indicator. In the present work, both error-estimation and refinement-indicator methods are investigated for application in the context of localization problems.

3.2 Adaptive algorithm and solution recovery

As stated above, the application of adaptive remeshing and mesh refinement is needed to ensure the resolution of a developing material instability. In this section, we discuss the algorithmic framework of our implementation, the theoretical background of the recovery technique used for error estimation, as well as data transfer, in detail. These components form the basis for the adaptive strategy. Error estimation and error indication, which control the process of remeshing and in particular mesh refinement, will be discussed separately below in Section 3.3 and Section 3.4, respectively.

The finite element program Abaqus offers the opportunity to manage and combine all tasks necessary for custom adaptive mesh refinement together using Python scripting. The current adaptive strategy has been implemented in Abaqus/CAE and is shown in Figure 3.1. A detailed outline of the general components is given in Table 3.1. The use of Python, or more gener-

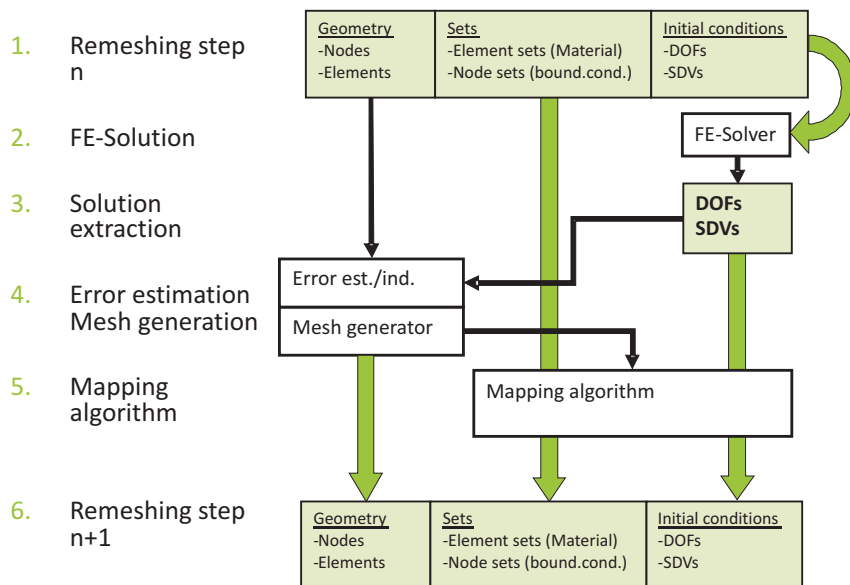


Figure 3.1: Adaptive remeshing scheme based on object-oriented (Python) scripting.

ally scripting, in this way is not limited to Abaqus. It can be, and has been, exploited to “glue together” a wide variety of numerical simulation tools. After the successful completion of a given timestep, all information needed is contained in the nodes and integration points of the current mesh. In particular, the structural degrees-of-freedom (DOF) are contained in the nodes, and the state-dependent variable (SDV) information is stored in the integration points. The error estimator/indicator procedure uses this information, especially the SDV values, to provide

Adaptive algorithm (general overview)
<p>1. Information to run a finite element analysis:</p> <p><u>Geometry</u> $Nodes = \{\{1, x_1, y_1\}, \dots, \{n_N, x_{n_N}, y_{n_N}\}\},$ $Elements = \{\{1, N_{11}, N_{12}, N_{13}\}, \dots, \{1, N_{n_E1}, N_{n_E2}, N_{n_E3}\}\},$</p> <p><u>Sets</u> $Nodesets = \{Nset_1, \dots, Nset_{n_{NS}}\}$ (boundary conditions, contact) with $Nset_i$ lists of corresponding node numbers $Elementsets = \{Elset_1, \dots, Elset_{n_{ES}}\}$ (material assignments) with $Elset_i$ lists of corresponding node numbers</p> <p><u>Initial/boundary conditions, degrees of freedom</u> $DOFs = \{\{q_{11}, \dots, q_{1n_N}\} \dots \{\{q_{n_{DOF1}}, \dots, q_{n_{DOFn_N}}\}\}$</p> <p><u>Initial conditions, state dependent variables at integration points</u> $SDVs = \{\{q_{11}, \dots, q_{1n_{int}}\} \dots \{\{q_{n_{SDV1}}, \dots, q_{n_{SDVn_{int}}}\}\}$</p> <p>2. Generate inputfile, run analysis</p> <p>3. Extract information (see 1.)</p> <p>4. Solution recovery (enhanced representation of SDVs in Nodes) $SDVsNodes = \{\{q_{11}, \dots, q_{1n_N}\} \dots \{\{q_{n_{SDV1}}, \dots, q_{n_{SDVn_N}}\}\}$</p> <p>5. Error estimation (see Section 3.3 for details) Input: FE values $SDVs$, enhanced solution $SDVsNodes$ Output: list of adapted element sizes, given at nodes $ElementSizes = \{h_1, \dots, h_{n_N}\}$</p> <p>6. Mesh generation Output: $Nodes, Elements$</p> <p>7. Data mapping Output: $Nodesets, Elementsets, DOFs, SDVs$</p> <p>Continue with 2. . . .</p>

Table 3.1: Adaptive algorithm, general overview

the mesh generator with the information about the desired mesh density. After remeshing, the SDVs have to be retransferred/mapped from the old mesh to the new one. Both the error estimator/indicator procedure and the mapping algorithm are based on a recovery procedure that provides a smoothed field of information at the integration points stored in the nodes. The main aspects of the adaptive scheme include (i) the finite element solver, (ii) the recovery procedure, (iii) error estimation/indication, (iv) mesh generation, and (v) the data mapping algorithm. In the current work, the finite-element solver being used is commercial (Abaqus). Further, the mesh generator is a modified version of a source code developed by Topping et al. (2004), or

the mesh generator in Abaqus. The routines for recovery, error estimation and the data mapping algorithm have been developed by the author.

As the recovery procedure has a direct influence on the quality of both, error estimation and mapping algorithm, we will now take a closer look into this component. A detailed discussion of the point wise error estimation is given in Section 3.3. For now it is sufficient to point out that a smoothed field of the inner quantities, contained in the nodes, can be used to perform an error estimation and further allows a mapping of information from the old to the new mesh. In the latter case, independently from the used recovery procedure, the values are retransferred to the integration points with the usual finite element interpolation ansatz

$$q(\xi) = \mathbf{q}_E \cdot \mathbf{h}(\xi) \quad . \quad (3.1)$$

Here, \mathbf{q}_E is the vector of nodal values for element E , $\mathbf{h}(\xi)$ is the shape function vector and ξ is the vector of local element coordinates.

A standard method to recover a solution to the nodes is simple nodal averaging. This method is simple to implement and, from the numerical point of view, very efficient. Many commercial finite element codes, such as ABAQUS have implemented it. Here, to display a continuous representation of the gausspoint values. The problem with simple nodal averaging is the strong effect of numerical diffusion when performing a large number of remeshing steps.

More advanced recovery procedures are based on polynomial smoothing techniques as, e.g., the well known superconvergent patch recovery method, introduced by Zienkiewicz and Zhu (1992a,b) or local projection techniques. Hinton and Campbell (1974), e.g., use standard finite element shape functions, to extrapolate the gauss point values of the 2×2 gauss point element to the nodes. All these methods are based on the existence of certain points at the interior of the element, where the finite element values are closer to the exact solution than elsewhere. These superconvergent or best-fit points are used as sampling points to determine a patch field in the considered neighborhood $P \subset B$ of a point. In the context of a finite element approximation we have

$$B \approx \bigcup_{e=1}^{n_{\text{elem}}} B^e \quad . \quad (3.2)$$

In this work, attention is restricted to three-node (i.e., lowest-order) two-dimensional triangular elements B^e , $e = 1, \dots, n_{\text{elem}}$. In this context, the Cartesian components $\chi_i^e(t, \mathbf{x}_r^e)$, $i = x, y$, of the element position field, or the temperature field $\theta^e(t, \mathbf{x}_r^e)$, represent time-dependent scalar fields on B^e . Such element fields take the algorithmic form

$$s^e(t, \mathbf{x}_r) = s_1^e(t) + s_2^e(t) x_r^e + s_3^e(t) y_r^e \quad (3.3)$$

in terms of $s_i^e(t)$, $i = 1, 2, 3$, the combinations of the nodal values of this field and the element referential position coordinates $\mathbf{x}_r^e = (x_r^e, y_r^e)$. Consequently, the corresponding gradient field

$$\nabla_r^e s^e(t, \mathbf{x}_r^e) = (s_2^e(t), s_3^e(t)) \quad (3.4)$$

is constant in B_r^e . In the adiabatic case, the element temperature itself is spatially-constant. Since the Kirchhoff stress depends non-linearly on the temperature (thermal softening) in the

constitutive model from Section 2.2, the element Kirchhoff stress field

$$\mathbf{k}^e(t, \mathbf{x}_r^e) = (K_{xx}^e(t, \mathbf{x}_r^e), K_{yy}^e(t, \mathbf{x}_r^e), K_{xy}^e(t, \mathbf{x}_r^e)) \quad (3.5)$$

is in general non-linear in \mathbf{x}_r^e . In the adiabatic case, however, it will be spatially-constant in the element. For three-node triangular elements, the element heat flux as based on the Fourier model is in any case spatially-constant in the element. For simplicity, attention is restricted to adiabatic conditions unless otherwise stated.

Consider next the patch field

$$\mathbf{k}^p(t, \mathbf{x}_r) = \mathbf{k}_1^p(t) + \mathbf{k}_2^p(t) x_r + \mathbf{k}_3^p(t) y_r \quad (3.6)$$

linear in \mathbf{x}_r . Assume that \mathbf{k}^e and \mathbf{k}^p are weakly equal over B^e , i.e.,

$$\langle \mathbf{k}^e(t, \mathbf{x}_r^e) \rangle_r^e = \langle \mathbf{k}^p(t, \mathbf{x}_r) \rangle_r^e = \mathbf{k}_1^p(t) + \mathbf{k}_2^p(t) \langle x_r \rangle_r^e + \mathbf{k}_3^p(t) \langle y_r \rangle_r^e, \quad (3.7)$$

where

$$\langle f \rangle_r^e := \frac{1}{v_r^e} \int_{B_r^e} f_r^e dv_r^e \quad (3.8)$$

represents the element volume average. The optimal sampling point in each element B_r^e is then given by the centroid

$$\mathbf{x}_r^s := \langle \mathbf{x} \rangle_r^e \quad (3.9)$$

of the element. Although this formulation has been carried out with respect to the stress field and here in combination with a linear patch field, we assume that this represents an analogous optimal sampling point for other dependent constitutive fields (e.g., the state-dependent variables) and also for higher order patch fields in what follows.

Using the finite element value at the position of the centroid or gauss point, respectively, we can now perform, e.g., a superconvergent node patch recovery (Zienkiewicz and Zhu (1992a,b)) to obtain a smoothed field of derivatives contained inside the nodes. To determine the patch field in the neighborhood B^p of the corresponding node, one works with the representation

$$q^*(\mathbf{x}, \mathbf{a}) = \mathbf{p}(\mathbf{x}) \cdot \mathbf{a} \quad (3.10)$$

in terms of a set $\mathbf{p}(\mathbf{x})$ of polynomials and an array \mathbf{a} of parameters to be determined via least-squares minimization of the objective function

$$\phi(\mathbf{a}) = \frac{1}{2} \sum_{i=1}^n (q(\mathbf{x}_i^s) - q^*(\mathbf{x}_i^s, \mathbf{a}))^2, \quad (3.11)$$

with $q(\mathbf{x}_i^s)$ the value of the finite element solution at the position of the sampling points (See Figure 3.2). As usual, minimization of this with respect to \mathbf{a} yields the system

$$\left\{ \sum_{i=1}^n \mathbf{p}(\mathbf{x}_i^s) \otimes \mathbf{p}(\mathbf{x}_i^s) \right\} \mathbf{a} = \sum_{i=1}^n q(\mathbf{x}_i^s) \mathbf{p}(\mathbf{x}_i^s), \quad \mathbf{x}_i^s \in P \subset B \quad (3.12)$$

of equations to solve for \mathbf{a} . Among other things, the condition κ of the matrix $\sum_{i=1}^n \mathbf{p}(\mathbf{x}_i^s) \otimes \mathbf{p}(\mathbf{x}_i^s)$

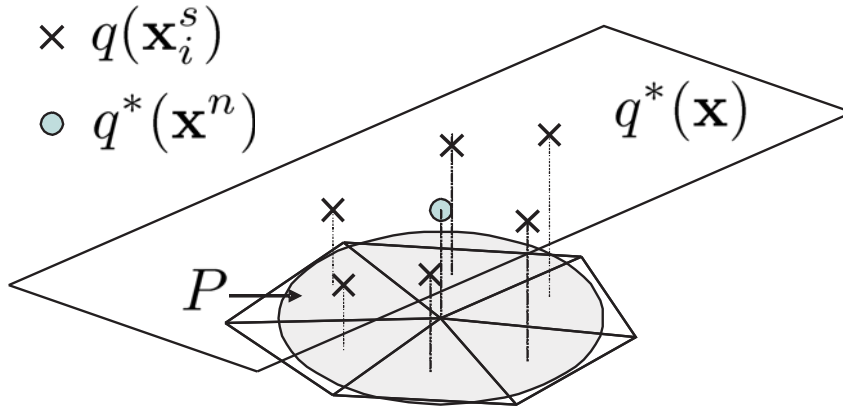


Figure 3.2: SNPR: The patch field $q^*(\mathbf{x})$ is determined via a least square fit to the given sampling point values $q(\mathbf{x}_i^s)$. The value at the position of the corresponding node is then calculated as $q^*(\mathbf{x}^n)$.

in (3.12) is influenced by the number and distribution of sampling points available. Consider the standard situation in a triangular mesh as given in Figure 3.3_a. An investigation on the influence of the position of the sampling points on the condition κ , when employing, e.g., the quadratic ansatz

$$\mathbf{p}(\mathbf{x}) = (1, x, y, x^2xy, y^2), \quad (3.13)$$

reveals the ill-conditioning of the problem for this or situations alike. As shown in Figure 3.3_c, positions of the sampling point in an exactly regular mesh even cause the problem to be ill-posed ($\kappa = \infty$). Here, the orientation of the mesh hardly effects the condition (see Figure 3.3_{b,d}).

The cause for this fact is revealed when optimizing the condition number for the given number of surrounding sampling points. Figure 3.4 shows the positions of the sampling point for an optimal condition, found by an evolution strategy implemented by the author. Obviously the lack of information inside the patch causes the ill-conditioning. Thus, when performing a superconvergent node patch recovery with higher order ansatz functions, a sufficiently wide area for the sampling points must be considered. Additionally, the dimensions of the problem should be normalized, as suggested from the results, shown in Figure 3.4.

In contrast to superconvergent node patch recovery techniques, that interpolate the nodal value from neighboring elements and integration points, respectively, extrapolation techniques perform a local, elementwise extrapolation (see Figure 3.5) with subsequent averaging

$$\mathbf{q}_n = k^{-1} \sum_{i=1}^k \mathbf{q}_i \quad . \quad (3.14)$$

In the case of linear triangular elements, element field gradients are constant. As such, this averaging is equivalent to simple nodal averaging. To go beyond this, additional sampling points are utilized for extrapolation. Motivated by the work of Levine (1985), who demonstrated that the average stress value is superconvergent at the midpoint of element edges for structured triangular meshes, we can, again making use of (3.7), derive the position of these points for the general case of unstructured meshes. In this case, the position of the optimal sampling point is

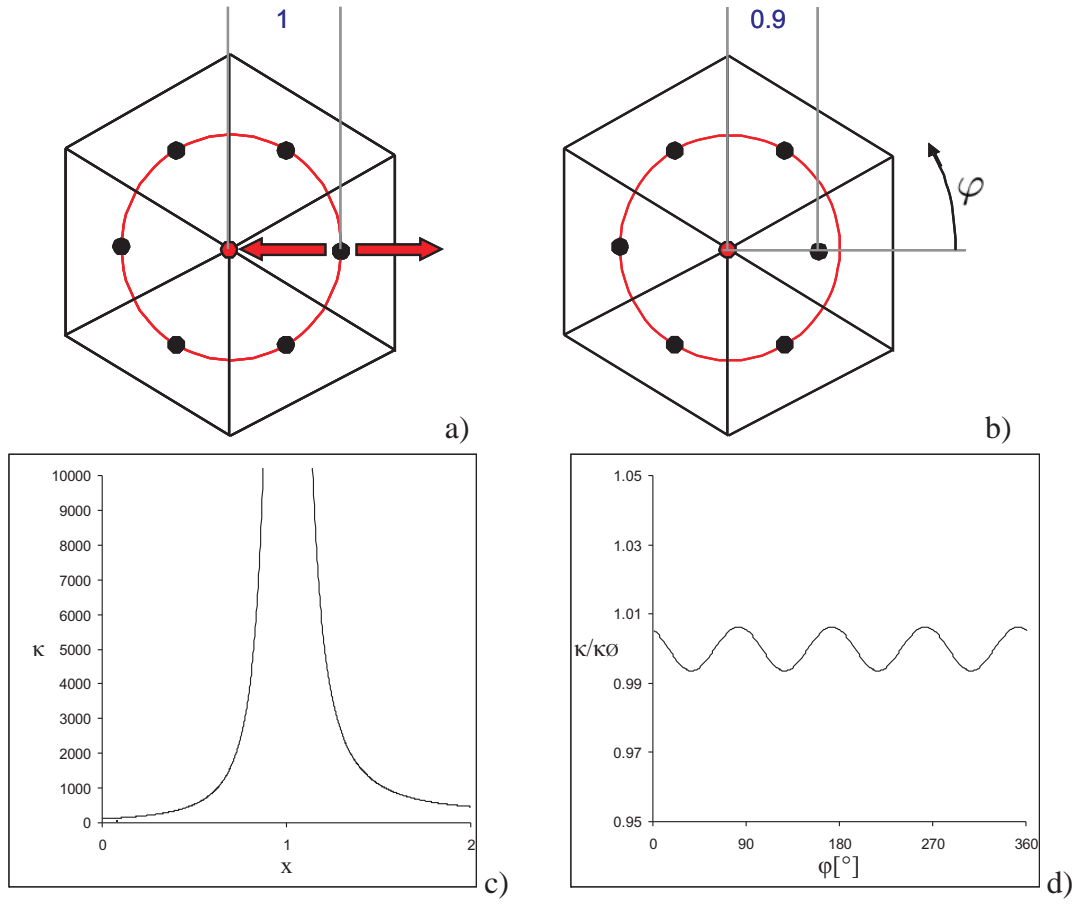


Figure 3.3: Influence of the position of the sampling points on the condition of the matrix $\sum_{i=1}^n \mathbf{p}(\mathbf{x}_i) \otimes \mathbf{p}(\mathbf{x}_i)$.

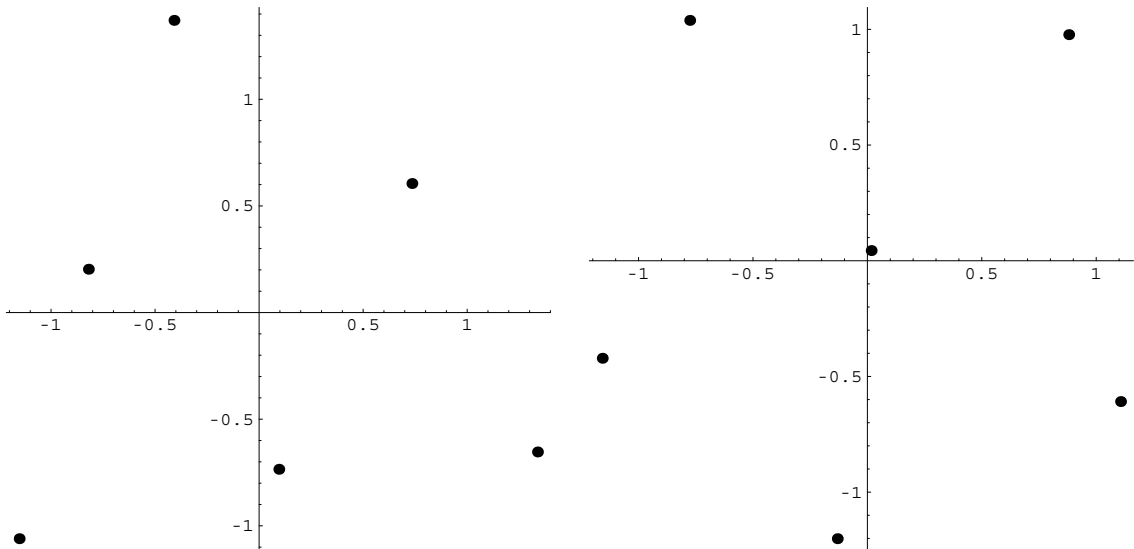


Figure 3.4: Position of the sampling points for an optimal condition κ of the matrix $\sum_{i=1}^n \mathbf{p}(\mathbf{x}_i) \otimes \mathbf{p}(\mathbf{x}_i)$, found by an evolution strategy.

assumed to be given by the average position of the corresponding centers, i.e.,

$$\mathbf{x}_r^s = \frac{1}{2} (\langle \mathbf{x} \rangle_r^{e_1} + \langle \mathbf{x} \rangle_r^{e_2}) . \quad (3.15)$$

Using the notation for a two-element patch as shown in Figure 3.6, we have in particular

$$\begin{bmatrix} x_r^s \\ y_r^s \end{bmatrix} = \frac{1}{6} \begin{bmatrix} x_{r1} + 2x_{r2} + 2x_{r3} + x_{r4} \\ y_{r1} + 2y_{r2} + 2y_{r3} + y_{r4} \end{bmatrix} \tag{3.16}$$

for the corresponding sample point. Having now three sampling points for every neighboring element, we can perform a linear extrapolation as demonstrated in Figure 3.7

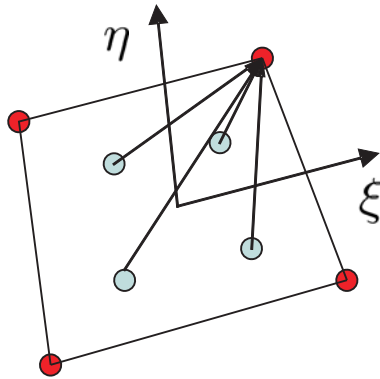


Figure 3.5: Extrapolation of finite element derivatives.

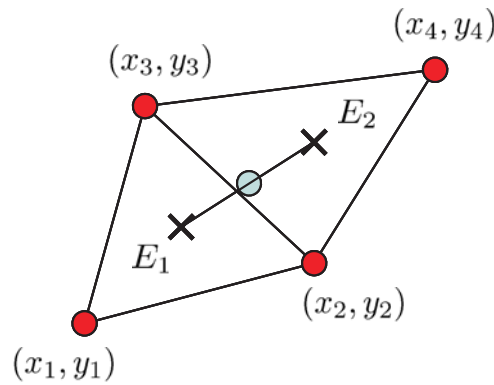


Figure 3.6: Optimal patch sampling point for a patch consisting of two neighboring elements.

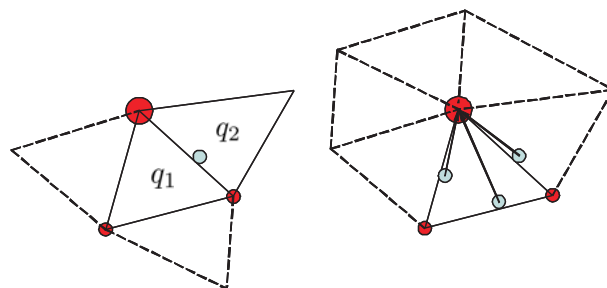


Figure 3.7: Extrapolation of finite element derivatives in linear triangular elements. Here, the additional sampling points (blue) allow linear extrapolation.

Now we turn to a comparison of simple nodal averaging (NA), superconvergent node patch

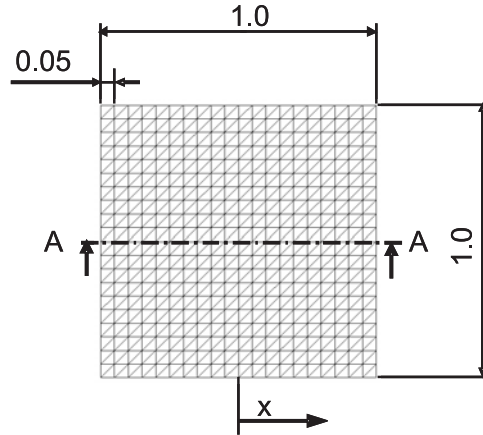


Figure 3.8: Reference mesh for data mapping investigation, in particular along the cross-section AA.

recovery (SNPR), and extrapolation with additional sampling points (EAS). For simplicity, we start with the fixed mesh as shown in Figure 3.8. Three different prescribed “solution” fields in the integration points are examined, i.e.,

$$\begin{aligned} q(x) &= x, \\ q(x) &= x^2, \\ q(x) &= \sin(2\pi x). \end{aligned} \tag{3.17}$$

The data mapping operation consists of solution projection (i.e., recovery) onto the nodes and subsequent transfer to the integration points via shape function interpolation. A detailed description of the mapping algorithm is given in Table 3.2. The distribution of the result as a function of the method used will be examined along the cross-section AA shown in Figure 3.8. Consider first the results for the linear case (3.17)₁ after 100 mapping operations as shown in Figure 3.9.

Since the shape functions are linear themselves, the SNPR method, based on a linear polynomial, results in exact recovery of the initial field independent of the number of mapping operations. This is also true for the EAS approach. The small deviations observed in the EAS case are due to the fact that, for elements with edges lying on the boundary, the lack of neighboring elements is dealt with by choosing the integration point value as midpoint value. The percentage of affected elements for boundary node patches is high in comparison to that for elements in interior node patches. To avoid numerical diffusion, then, linear polynomial smoothing is used for boundary node patches. This effect of numerical diffusion is also quite evident for the NA method. In the case of an increasing gradient at the boundary, for example, the recovered value is always smaller than the maximum value of the surrounding elements. This results in an artificial decrease of the results when mapped back to the integration points.

We turn next to the quadratic case (3.17)₂ with comparison in Figure 3.10. As expected, the SNPR method based on linear polynomials is incapable of resolving the quadratic field. The usual remedy is to increase the polynomial degree p . To avoid an ill conditioned system matrix in (3.12), a sufficient number of sampling points must be used. Thus we expand the node patch to neighboring elements for interior node patches and use linear interpolation for boundary node

<p>Solution recovery and transfer (nodal based)</p> <ol style="list-style-type: none"> 1. Solution field $q(\mathbf{x})$ known everywhere on B. 2. Structural nodal positions $\mathbf{x}_i^n, i = 1, \dots, n_n$ on B are known. 3. Sampling point positions $\mathbf{x}_i^s, i = 1, \dots, n_s$ on B are known. 4. Determination of the corresponding subsets (patch regions) $P^i, i = 1, \dots, n_n$, discretized by n_e^i elements. 5. Project solution field onto structural nodes $*$. 6. Retransfer of the field quantities to any point via shape function interpolation : $q(\xi) = \mathbf{q}_E \cdot \mathbf{h}(\xi)$.
<p><i>* recovery procedure</i></p> <p>nodal averaging (NA)</p> $q^*(\mathbf{x}_i^n) = \frac{1}{n_s^i} \sum_{j=1}^{n_s^i} q(\mathbf{x}_j^s) \quad , \quad \mathbf{x}_j^s \in P^i$ <p>superconvergent node patch recovery (SNPR)</p> $q^*(\mathbf{x}_i^n) = \mathbf{p}(\mathbf{x}_i^n) \cdot \mathbf{a}_i \quad \text{with } \mathbf{a}_i \text{ determined via}$ $\left\{ \sum_{j=1}^{n_s^i} \mathbf{p}(\mathbf{x}_j^s) \otimes \mathbf{p}(\mathbf{x}_j^s) \right\} \mathbf{a}_i = \sum_{j=1}^{n_s^i} q(\mathbf{x}_j^s) \mathbf{p}(\mathbf{x}_j^s) \quad , \quad \mathbf{x}_j^s \in P^i$ <p>extrapolation with additional sampling points (EAS)</p> $q^*(\mathbf{x}_i^n) = \frac{1}{n_e^i} \sum_{j=1}^{n_e^i} q_j(\mathbf{x}_i^n)$ <p>with $q_j(\mathbf{x})$ a suitable extrapolation function, defined on $B_j^e \in P^i$</p>

Table 3.2: Algorithm of solution mapping combining nodal recovery and subsequent shape function projection.

patches. The remaining deviation of the SNPR with $p = 2$ stems from the retransfer via linear interpolation functions (Figure 3.10) and from the mentioned use of linear interpolation for boundary node patches.

Accepting the additional computational costs, the mapping transfer can be improved by separating it from the recovery procedure and perform a superconvergent element patch recovery (SEPR, see Figure 3.11 and Table 3.3 for further details) to enable a direct transfer between integration points of different meshes. Using, e.g., an ansatz function of order $p = 2$, at least for quadratic fields, no deviations are detected. Lastly, we have the case (3.17)₃ and the results in Figure 3.12. As shown, both the SNPR with polynomial order $p = 2$ and the EAS method perform well. The most exact mapping can be stated for the SEPR method but again, the additional numerical costs have to be considered.

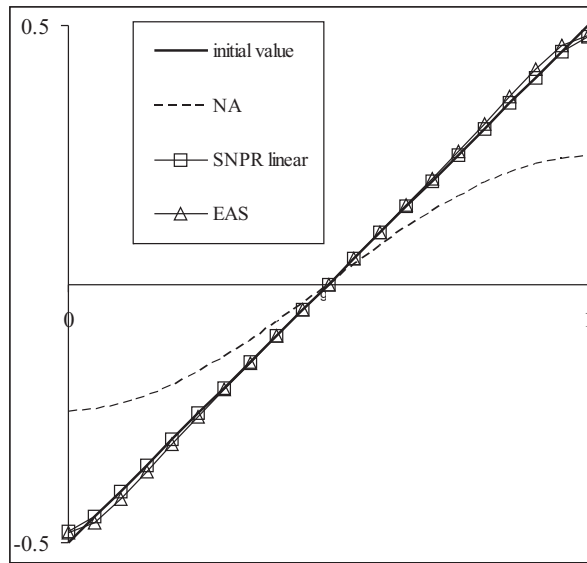


Figure 3.9: Distribution of $(3.17)_1$ in the cross section AA after 100 mapping operations. Initial distribution (continuous curve), nodal averaging (NA: dashed curve), polynomial smoothing (SPR: quadrilaterals), extrapolation method (EAS: triangles).

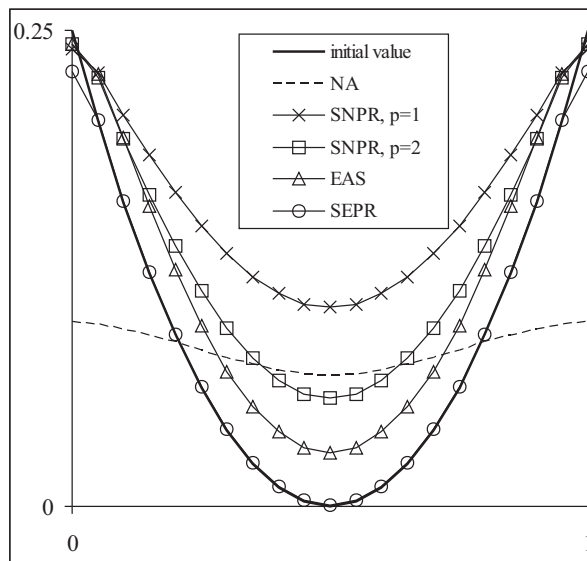


Figure 3.10: Distribution of $(3.17)_2$ in the cross section AA after 100 data mappings. Given are the initial distribution (continuous) together with the mappings results based on nodal averaging (dashed), linear polynomial smoothing (cross), quadratic polynomial smoothing (quad), extrapolation (triangle), and superconvergent element patch recovery (circle).

In the following, a short description of the complete approach used to transfer integration-point and nodal quantities from the old mesh to the new mesh is now given. As usual, this is based on determining the locations of the new integration points and nodes with respect to the old elements. To do this, we first need to determine in which old elements these new points lie.

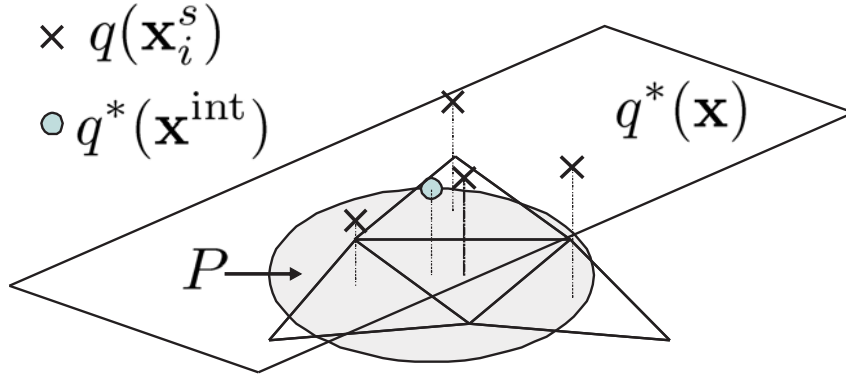


Figure 3.11: SEPR: The patch field $q^*(\mathbf{x})$ is determined via least square fit to the given sampling point values $q(\mathbf{x}_i^s)$. The value at the position of the corresponding new gausspoint is then calculated as $q^*(\mathbf{x}^{int})$.

Direct solution transfer

1. Solution field $q(\mathbf{x})$ known everywhere on B .
2. Integration point positions of target mesh (new mesh) $\mathbf{x}_i^{int}, i = 1, \dots, n_{int}$ on B are known.
3. Sampling point positions $\mathbf{x}_i^s, i = 1, \dots, n_s$ on B are known.
4. Determination of the corresponding subsets (patch region) $P^i, i = 1, \dots, n_{int}$, discretized by n_e^i elements.
5. Direct projection of the solution field onto integration points *.

* transfer procedure

superconvergent element patch recovery (SEPR)

$$q^*(\mathbf{x}_i^{int}) = \mathbf{p}(\mathbf{x}_i^{int}) \cdot \mathbf{a}_i \quad \text{with } \mathbf{a}_i \text{ determined via}$$

$$\left\{ \sum_{j=1}^{n_s^i} \mathbf{p}(\mathbf{x}_j^s) \otimes \mathbf{p}(\mathbf{x}_j^s) \right\} \mathbf{a}_i = \sum_{j=1}^{n_s^i} q(\mathbf{x}_j^s) \mathbf{p}(\mathbf{x}_j^s) \quad , \quad \mathbf{x}_j^s \in P^i$$

Table 3.3: Algorithm of solution mapping using a direct transfer between integration points of different meshes

Given this knowledge, the usual interpolation relation

$$\mathbf{x}_p = \sum_{i=1}^m h_i(\boldsymbol{\xi}) \mathbf{x}_i \quad (3.18)$$

can be solved for the corresponding master element coordinates $\boldsymbol{\xi}$. Here, \mathbf{x}_p represent the coordinates of any such point in the new mesh, $\mathbf{x}_1, \dots, \mathbf{x}_m$ are the coordinates of the nodes of the old element, and $h_1(\boldsymbol{\xi}), \dots, h_m(\boldsymbol{\xi})$ are the element shape-functions. In case of, e.g., linear triangular elements, a point is inside an element if $0 \leq \xi \leq 1$ and $0 \leq \eta \leq 1 - \xi$ hold. This is shown in Figure 3.13. To increase efficiency, the search for such elements can

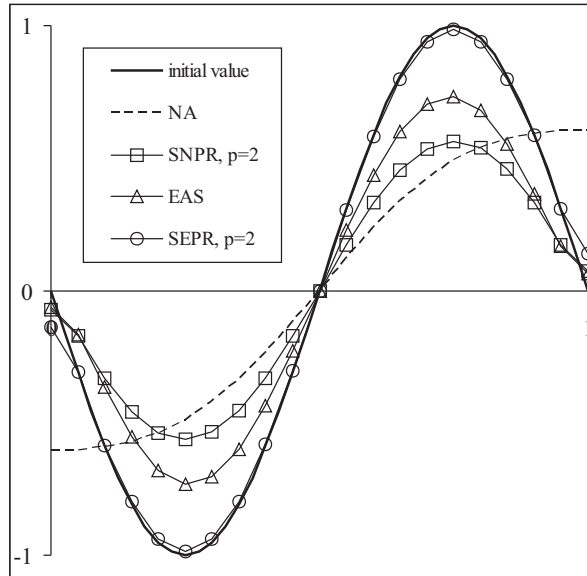


Figure 3.12: Distribution of $(3.17)_3$ in the cross-section AA after 50 mappings. Given are the initial distribution (continuous) together with the mappings results based on nodal averaging (dashed), linear polynomial smoothing (cross), quadratic polynomial smoothing (quad), extrapolation (triangle), and superconvergent element patch recovery (circle).

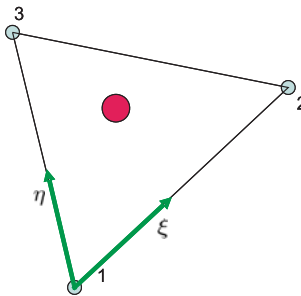


Figure 3.13: Determination of local coordinates during the data mapping process (see text for further details).

be restricted to subdomains of the entire mesh as follows. The entire mesh is divided into such subdomains by a grid (see Figure 3.14). The assignment of elements to subdomains of the grid is determined by the size (edge coordinates) of a rectangle, enclosing the corresponding element (see Figure 3.14 below right). The search is then reduced to that subdomain and corresponding set of elements containing the point in question (Figure 3.15). A detailed formulation of the above searching algorithm is given in Table 3.4 and Table 3.5, respectively. The size of the subdomains is of special importance. Figure 3.16 shows the influence of the size of the subdomains on the computational costs. The given reference calculation has been performed with a rectangular background mesh, discretized by 2500 elements. As shown, setting the subdomain size to that of the average element minimizes the computational costs (see Figure 3.16). To emphasize this further, the mesh is shown in the background. The second type of information that has to be transferred is that for the boundary and contact conditions. The determination of the corresponding boundary node sets is based on the distance of a given node from the boundary. For simplicity, consider the 2D case shown in Figure 3.17. Here, a node is

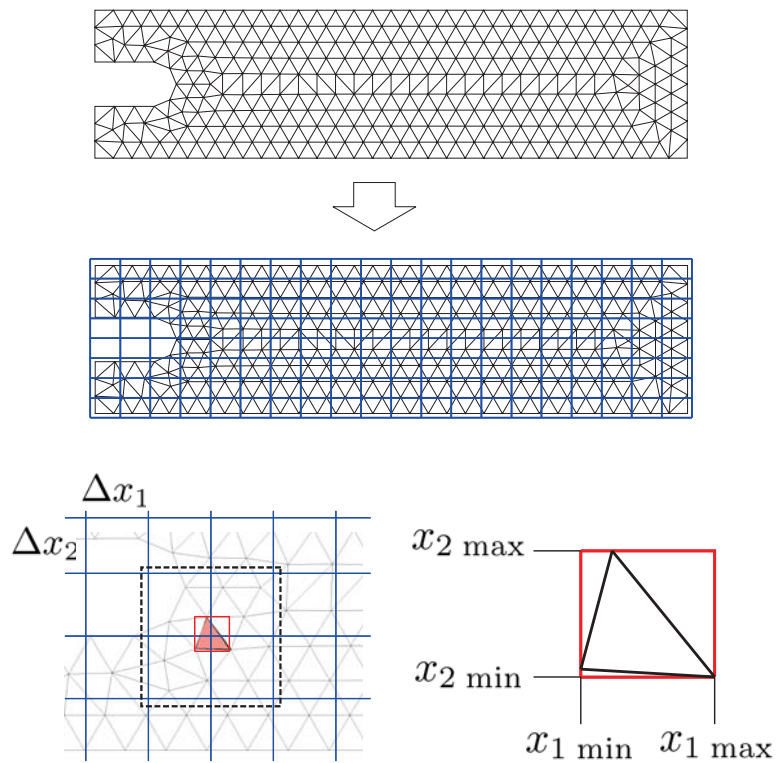


Figure 3.14: Division of the entire mesh into subdomains via a grid for the data transfer process. The assignment of elements to subdomains of the grid is determined by the size (edge coordinates) of a rectangle, enclosing the corresponding element.

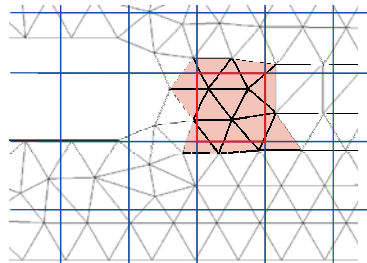


Figure 3.15: Subdomain and corresponding elements for the data mapping process.

on the boundary if its position is inside the enclosing rectangle marking a boundary node set. To reduce the node sets to be searched, use is made of the information from the previous data transfer. Since the position of every point is known, the relevant node set reduces to the nodes which are positioned inside the neighboring elements of the corresponding subdomain of the surface.

Determination of the background element for an arbitrary point

1. Determine the list of possible background elements \mathbf{E} .
In general, we have $\mathbf{E} = \{1, \dots, n_e\}$.
Using the additional algorithm, as given in Table 3.5, we can work with the reduced set $\mathbf{E} = \mathbf{E}^R$.
2. Having the coordinates of the point \mathbf{x}_p , solve
$$\mathbf{x}_p = \sum_{i=1}^m h_i(\boldsymbol{\xi}) \mathbf{x}_i^e, \quad \forall e \in \mathbf{E}$$

in terms of the reference element coordinates $\boldsymbol{\xi}$.
3. In case of, e.g., linear triangular elements, a point is inside an element if
 $0 \leq \xi \leq 1$ and $0 \leq \eta \leq 1 - \xi$.

Determination of the corresponding background element allows:

1. Transfer of element sets.
2. Data mapping via shape function projection (upstream solution recovery presupposed, see Table 3.2).
3. Direct solution transfer. (see Table 3.3).

Table 3.4: Determination of background elements.

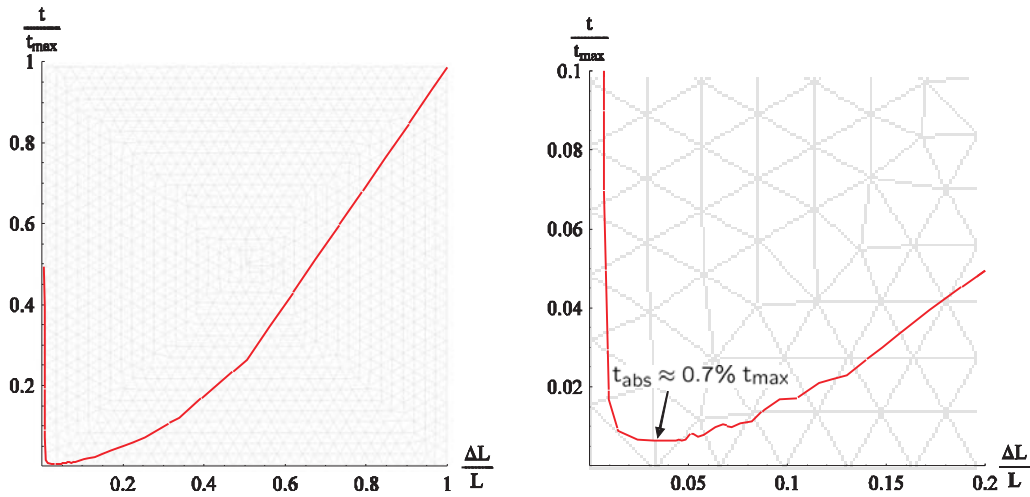


Figure 3.16: Computational costs to identify the local coordinates of points (nodes and integration points) inside a background mesh. Setting the grid size of the subdomains comparable to that of the average element size, minimizes the computational costs. To illustrate this fact, the mesh is printed in the background of the diagrams.

Allocation of reduced sets of possible background elements (optional)	
1. Determine the limit coordinates $x_{min}^B, x_{max}^B, y_{min}^B, y_{max}^B$ of the domain B .	
2. Define the rectangular domain $B^\square \supset B$, bounded by the limit coordinates $x_{min}^B, x_{max}^B, y_{min}^B, y_{max}^B$.	
3. Define $n_x n_y$ rectangular subdomains $B_{ij}^\square \subset B^\square$, bounded by the limit coordinates	
	$x_{min}^{ij} = x_{min}^B + (i-1) \frac{x_{max}^B - x_{min}^B}{n_x}, \quad x_{max}^{ij} = x_{min}^B + i \frac{x_{max}^B - x_{min}^B}{n_x},$ $y_{min}^{ij} = y_{min}^B + (j-1) \frac{y_{max}^B - y_{min}^B}{n_y}, \quad y_{max}^{ij} = y_{min}^B + j \frac{y_{max}^B - y_{min}^B}{n_y}.$
4. Generate a table (matrix) \mathbf{B}^\square containing $n_x n_y$ empty lists $\mathbf{B}_{ij}^\square = \{\}$. In the following process, the components \mathbf{B}_{ij}^\square will collect the element numbers e of the elements, assigned to the subdomains B_{ij}^\square .	
5. Assign background elements to the subdomains B_{ij}^\square :	
	For every background element with element number $e \in \{1, \dots, n_e\}$:
5.1 Determine its limit coordinates $x_{min}^e, x_{max}^e, y_{min}^e, y_{max}^e$.	
5.2 Determine the indexes of the occupied subdomains	
	$I^e = \left\{ \left\lceil \frac{x_{min}^e - x_{min}^B}{x_{max}^B - x_{min}^B} n_x \right\rceil \right\} \cup \left\{ \left\lceil \frac{x_{max}^e - x_{min}^B}{x_{max}^B - x_{min}^B} n_x \right\rceil \right\}$ $J^e = \left\{ \left\lceil \frac{y_{min}^e - y_{min}^B}{y_{max}^B - y_{min}^B} n_y \right\rceil \right\} \cup \left\{ \left\lceil \frac{y_{max}^e - y_{min}^B}{y_{max}^B - y_{min}^B} n_y \right\rceil \right\}.$
	5.3 $\mathbf{B}_{ij}^\square = \{e\} \cup \mathbf{B}_{ij}^\square, \forall i \in I^e \wedge \forall j \in J^e$
Having an arbitrary point with coordinates \mathbf{x}_p , the set of possible background elements is given by	
$\mathbf{E}^R = \mathbf{B}_{ij}^\square$ with	
$i = \left\{ \left\lceil \frac{x_p - x_{min}^B}{x_{max}^B - x_{min}^B} n_x \right\rceil \right\}, j = \left\{ \left\lceil \frac{y_p - y_{min}^B}{y_{max}^B - y_{min}^B} n_y \right\rceil \right\}$	

Table 3.5: Algorithm for the allocation of reduced sets of possible background elements.

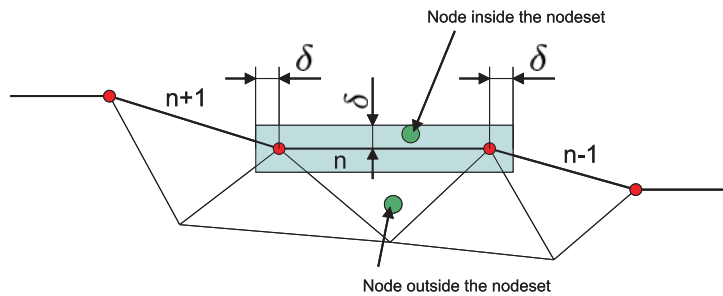


Figure 3.17: Mapping of node sets. To detect all nodes which are inside the domain of a node set, the distances from the nodes to the subdomain in question are determined. The set of nodes to be tested can be reduced to the nodes positioned in the neighboring elements of the corresponding subdomain.

3.3 Error estimation at finite strain

As stated above, an adequate discretization of the boundary value problem has to be guaranteed at any time. As this requirement holds of course for any problem solved by means of a finite element analysis, an appropriate error analysis shall be the basis for our adaptive strategy. In the literature, the focus of attention is on residual based error estimation and recovery based methods. The residual based methods were originally introduced by Babuska and Rheinboldt (1978). The idea here is to investigate residuals occurring in a single element (interior estimation) and in a patch of elements (patch estimation). This is generally carried out by comparing the current finite step solution to a reference solution obtained solving a series of local problems defined on fine patches. A detailed explanation and a general overview can be found, e.g., in Rodriguez-Ferran and Huerta (2000) and Huerta et al. (2002). The general drawback of the residual based methods is the comparatively high numerical effort due to the additional finite element computations.

A robust and easy to implement alternative was introduced by Zienkiewicz and Zhu (1987) with the recovery method. In general, the error of a finite element solution can locally be expressed by

$$\mathbf{e}_q = \mathbf{q} - \hat{\mathbf{q}} \quad (3.19)$$

where \mathbf{q} is the array of exact solution values for any quantity (e.g., stresses, strains, temperature) and $\hat{\mathbf{q}}$ is the finite element approximation. As a substitute for the exact solution, recovery methods are often used to calculate a higher-accuracy approximation \mathbf{q}^* and then define the error as

$$\mathbf{e}_q = \mathbf{q}^* - \hat{\mathbf{q}}. \quad (3.20)$$

Originally, \mathbf{q}^* was obtained by simple nodal averaging (see Zienkiewicz and Zhu (1987)). In later works, further advances were made by introducing the so called superconvergent patch recovery (see Table 3.2), which replaced simple nodal averaging (Zienkiewicz and Zhu (1992a,b)). In the following error estimation based on recovery methods will be favored due to the following facts. Although both, the recovery methods and residual based methods have proven their worth, investigations of Babuska et al. (1994) show higher robustness for the recovery procedures. Further, the implementation of recovery based procedures is, as recovery procedures in form of transfer algorithms are generally part of an adaptive algorithm, comparatively effortless.

The main objective of adaptive mesh refinement strategies is to provide a finite element solution with a prescribed level of error in a norm with a specific physical meaning. In context of linear elastic problems, the standard norm to express the error is traditionally the elastic energy norm

$$\|\mathbf{e}_e\| = \left(\int_{\Omega} \mathbf{e}_\sigma^T \mathbf{C}^{-1} \mathbf{e}_\sigma d\Omega \right)^{1/2} \quad (3.21)$$

or

$$\|\mathbf{e}_e\| = \left(\int_{\Omega} \mathbf{e}_\varepsilon^T \mathbf{C} \mathbf{e}_\varepsilon d\Omega \right)^{1/2} \quad (3.22)$$

respectively, as it considers both the accurate resolution of the stresses and the strains. Noting

that the elastic tangent \mathbf{C} is only a weighting factor, the so called L_2 norm

$$\|\mathbf{e}_q\| = \left(\int_{\Omega} \mathbf{e}_\varepsilon^T \mathbf{e}_\varepsilon d\Omega \right)^{1/2} \quad (3.23)$$

represents a direct measure for the error in strains. Here and in the following, ε can be any strain measure linked by the operator \mathbf{C} to a conjugate stress measure.

The field of interest considered in the elastic energy norm is that for the strains, or more general, the derivatives of the degrees of freedom (current positions or displacements). The stresses are directly connected via the elastic tangent to the strains. This dependence allows a direct capturing of both the error in the strains and, what is of course more relevant in engineering applications, the error in stresses with the same quality.

In context of large plastic deformations, the linear dependence between the derivatives of the displacements and stresses is lost. In fact, due to the history dependence there is no explicit dependence at all. Thus, only a separate calculation of the error for the history dependent quantities (e.g., plastic strains, stresses) is possible. Even for monotonic loadings working with the elastic energy error norm leads to poor results. From Figure 3.18 the underestimation of the error in the derivatives with increasing deformation is easily to establish. Here, large variations in total strains and plastic strains respectively cause only small variations of the elastic energy and the stress, respectively. In the case of large plastic deformation the problem is, as

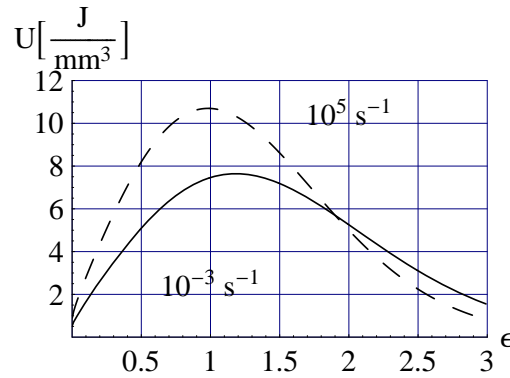


Figure 3.18: Elastic energy density U as a function of equivalent strain in dynamic uniaxial-tension at two different strain rates as based on the Johnson-Cook model. Note $\epsilon_p \approx \epsilon$ for large plastic deformations.

mentioned, the state dependent tangent. An error norm, analogous to the energy error norm, can only be defined incrementally, if at all. Thus, we define the incremental energy error norm

$$\|\Delta_e\| = \left(\int_{\Omega} \mathbf{e}_{\Delta\varepsilon}^T \mathbf{C} \mathbf{e}_{\Delta\varepsilon} d\Omega \right)^{1/2}. \quad (3.24)$$

Here, we chose an explicit dependence of ε , as the strains are the only quantity directly connected to our solution field (e.g., displacements). Noting again, that the tangent \mathbf{C} is only a weighting factor, we use the L_2 norm to express the error

$$\|\mathbf{e}_{\Delta\varepsilon}\| = \left(\int_{\Omega} \mathbf{e}_{\Delta\varepsilon}^T \mathbf{e}_{\Delta\varepsilon} d\Omega \right)^{1/2}. \quad (3.25)$$

Due to the history dependence of the tangent \mathbf{C} , the error in total strains reveals nothing about the error in stresses. Furthermore, the application of the tangent \mathbf{C} even leads to an underestimation of the error in total strains with increasing plastic deformation. Thus, if our goal is to ensure the resolution of the field for the derivatives (total strain) and beyond the resolution of the state-dependent quantities (stresses, plastic strains etc.), we are forced to perform a separate calculation of the error for every single quantity of interest. The use of an incremental error norm is no longer necessary and can therefore be replaced by using, e.g., the L_2 norm in general

$$\|\mathbf{e}_q\| = \left(\int_{\Omega} \mathbf{e}_q^T \mathbf{e}_q d\Omega \right)^{1/2}. \quad (3.26)$$

Here q can be identified with any quantity of interest (strains, stresses, temperature etc.).

The general refinement strategy when working with an integral form of the error norm, as these defined above, is to obtain an equal distribution of the error in every subdomain and element respectively. In the context of linear elasticity, it is a proven fact that, especially in connection with the energy error norm, this strategy leads to optimal meshes (see, e.g., Babuska and Rheinboldt (1979)). The resulting meshes are optimal in the sense, that they provide the lowest number of elements for a fixed amount of global error. Noting that the square of (3.26) can be obtained by summing the corresponding element values

$$\|\mathbf{e}_q\|^2 = \sum_{i=1}^n \|\mathbf{e}_q\|_i^2. \quad (3.27)$$

the equal distribution of the error can be achieved by postulating

$$\|\mathbf{e}_q\|_i^2 = \frac{\|\mathbf{e}_q\|^2}{n} \forall \Omega_i \quad (3.28)$$

where subindex i indicates the element number and n the total number of elements, respectively.

Although this method leads to optimal meshes in the above sense, it produces a concentration of errors in the zones with maximum element density. Normally, these are the zones where attention is focused. In the context of simulating the process of adiabatic shear banding, a concentration of errors in the area of the shear band is expected.

An alternative mesh refinement criterion based on the equal distribution of the density of the error was proposed by Onate and Bugeda (2007). With the corresponding averages on the whole domain Ω and on the element subdomain Ω_i the equal distribution of the error density can be achieved by postulating

$$\left(\frac{\|\mathbf{e}_q\|_i^2}{\Omega_i} \right) = \left(\frac{\|\mathbf{e}_q\|^2}{\Omega} \right) \forall \Omega_i. \quad (3.29)$$

For the same amount of global error, this strategy produces more expensive meshes than the classical method, but these meshes ensure a more reasonable distribution of error in the quantities of interest.

It is well known that for linear elements such as used in the current work, the derivative of the finite element solution has the highest local error at interelement nodes (see Zienkiewicz and

Zhu (1992a,b)). Further, the average of the error in the nodes is strongly related to the average error for an element. Thus, Bugeda (2002) proposes a pointwise error estimation in the nodes. This approach avoids evaluating the integral formulation of the error. Here, the error norm is defined by

$$\|\mathbf{e}_q\| = \|\mathbf{q} - \hat{\mathbf{q}}\| \quad (3.30)$$

and refinement in the neighborhood of a node n takes place to ensure

$$\|\mathbf{e}_q\|_n < \|\mathbf{e}_q\|_{\max} . \quad (3.31)$$

The following arguments suggest the application of a point-wise recovery-based error estimator:

- No more concentration of the error in sensitive areas, as with equal error distribution
- direct and physically reasonable capturing of the errors and gradients, respectively, for any quantity
- low numerical costs, as in comparison to standard norms the evaluation of the integral formulation is avoided.

In the context of modeling and simulation of material instabilities we are mainly interested to ensure the resolution of the gradients of our solution field and in particular the gradients of the field of plastic deformation. Actually, the pointwise error estimation allows the estimation of gradients in a numerical effective manner and will thus be used in the following investigations.

To guarantee the resolution in any of the surrounding elements k , we define the nodal error

$$\|\mathbf{e}_q\|_n = \max(\|\mathbf{q}_n^* - \hat{\mathbf{q}}_k\|) . \quad (3.32)$$

A projection method is, at least for linear elements, not needed, as the error of derivatives can be evaluated directly from integration point values (see Figure 3.19). The error estimation is merely the basis for our adaptive procedure. The information about the desired mesh density is supplied by the remeshing criterion. Following the criterion of equal distribution of the error density as proposed by Onate and Bugeda (2007) the criterion of equal distribution of the error in every node seems to be consistent for a pointwise error estimation (see Bugeda (2002)).

To decide whether mesh refinement or mesh coarsening is needed, we define the refinement parameter

$$\xi = \frac{\|\mathbf{e}_q\|_n}{\|\mathbf{e}_q\|_{\max}} , \quad (3.33)$$

which provides a measure for the derivation of the pointwise error from the desired and maximum error, respectively.

The refinement strategy has to be completed by a rule for the new local mesh size \bar{h} , to satisfy the requirement of the refinement criterion. In general this requirement is achieved in an iterative process. To ensure maximum effectiveness, we have to consider the convergence of the error with respect to the element size. At least for linear elasticity it is fact that the error in stresses at each point behaves as h^p . In this case, having again the direct relation between stresses and strains, we can assume this dependence for the derivatives of the solution field, in

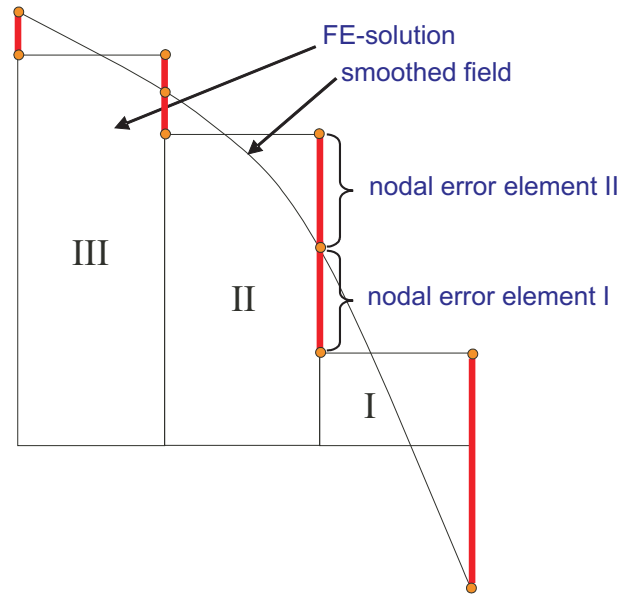


Figure 3.19: The pointwise error estimation in combination with nodal averaging allows the capturing of gradients in a numerical effective manner, as the recovery procedure and the evaluation of the error can be combined in a single step.

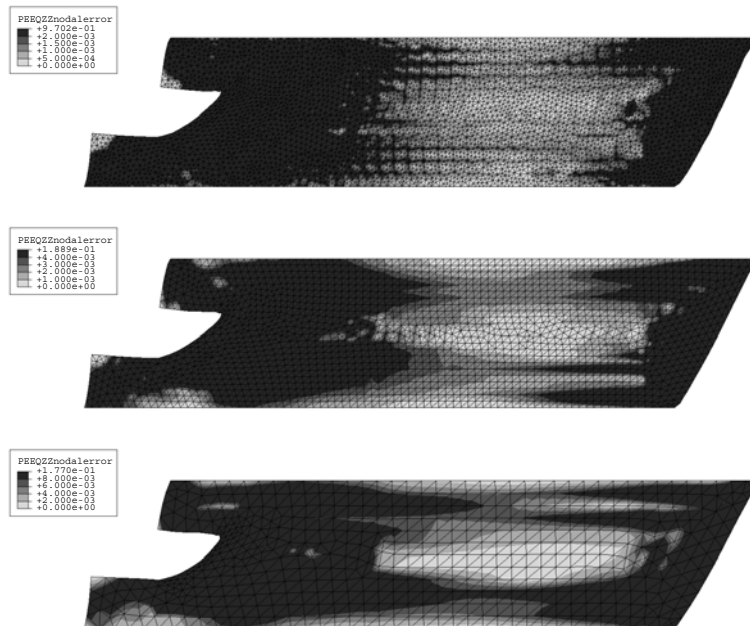


Figure 3.20: Distribution of the pointwise error in ϵ_p inside a notched shear specimen (Figure 3.25) at an early stage of deformation. As we are dealing with large plastic deformations and small elastic deformations ($\epsilon \approx \epsilon_p$) the h^p dependence of the error in the derivatives, can also be stated for ϵ_p . The simulations had been carried out with elementsize $h=0.0025$ mm (above), $h=0.005$ mm (middle) and $h=0.01$ mm (below). Note the different scaling of the error.

general. A numerical certification for the equivalent assumption for the error in plastic strains is presented in Figure 3.20. Considering the convergence behavior of the error

$$\left(\frac{h}{\bar{h}}\right)^p = \frac{\|\mathbf{e}_q\|_n}{\|\mathbf{e}_q\|_{\max}} = \xi, \quad (3.34)$$

the new local mesh size can now be defined using the expression

$$\bar{h} = \frac{h}{\xi^{1/p}}. \quad (3.35)$$

In addition, a description of the maximum error $\|\mathbf{e}_q\|_{\max}$ in terms of a prescribed number of new elements n_p will be given. This approach ensures constrained computational costs. Assuming that the number of new elements in the region of an old element is given by

$$n_i = \left(\frac{h_i}{\bar{h}_i}\right)^d, \quad (3.36)$$

with d the dimension, we can calculate the total number of new elements by

$$n_p = \sum_{i=1}^n \left(\frac{h_i}{\bar{h}_i}\right)^d = \sum_{i=1}^n \bar{\xi}_i^{\frac{d}{p}} = \sum_{i=1}^n \left(\frac{1}{k} \sum_{j=1}^k \frac{\|\mathbf{e}_q\|_{ij}}{\|\mathbf{e}_q\|_{\max}}\right)^{\frac{d}{p}} = \|\mathbf{e}_q\|_{\max}^{-\frac{d}{p}} \sum_{i=1}^n \overline{\|\mathbf{e}_q\|_i^{\frac{d}{p}}}. \quad (3.37)$$

Here, n is the total number of old elements, $\bar{\xi}_i$ and $\overline{\|\mathbf{e}_q\|_i}$ are the elemental averages of the corresponding nodal quantities for one element and k is the number of nodes per element. Rearranging leads to

$$\|\mathbf{e}_q\|_{\max} = \left(\frac{1}{n_p} \sum_{i=1}^n \overline{\|\mathbf{e}_q\|_i^{\frac{d}{p}}}\right)^{\frac{p}{d}}. \quad (3.38)$$

If desired, the latter result can be used within (3.34) and (3.35) to calculate the new local mesh size in terms of a prescribed number of new elements.

With this rule the formulation of our error estimator is completed and we can now turn to the investigation of its behavior in context of the analysis of localized material instabilities.

Before we apply the developed adaptive procedure on the problem of deformation localization, a short comparison between the different recovery procedures in context of error estimation should be given. For this purpose recall the numerical testing environment as given in Figure 3.8 (see Section 3.2). Again, we will set the initial distribution of the derivative by the distribution functions

$$q(x) = x, \quad q(x) = x^2, \quad q(x) = \sin(2\pi x). \quad (3.39)$$

Defining the average error

$$\|\mathbf{e}\|_a = \frac{1}{n} \sum_{i=1}^n \|\mathbf{e}_q\|_i \quad (3.40)$$

and the effectivity index

$$\Theta = \frac{\|\mathbf{e}\|_a}{\|\mathbf{e}_e\|_a}, \quad (3.41)$$

with $\|\mathbf{e}_e\|_a$ the averaged exact error, a comparison between the different recovery procedures is possible. In the following, we treat the artificial distribution as the exact solution. Thus, $\|\mathbf{e}_e\|_a$ is calculated by comparing the finite element element values (integration point values) with the distribution function.

Figures 3.21-3.24 show the error and the effectivity index for the different recovery procedures for different distribution functions with varying element sizes. The reference element size is set to $h_0=0.05$ mm. First of all, the results for the average exact error (Figures 3.21-3.24 left) approve the stated convergence rule (3.34). Starting with a linear distribution function, the discussed problems with boundary elements, when using the NA or EAS method, are revealed. With increasing element size, the fraction of boundary elements increases which leads to an increasing deviation from the exact error using this methods. The SNPR method gives an exact representation of the error for any element size ($\Theta = 1$, Figure 3.21 left). Here and in the following, the SNPR is performed with polynomial order $p = 2$, as described in Section 3.2. Comparing the results in the center point and thus, without any influence of the boundary elements, all methods provide the exact error (see Figure 3.22). The results for the quadratic distribution are shown in Figure 3.23. Obviously, the EAS method shows a stronger mesh-size sensitivity than the SNPR method. Similar results can be observed for the trigonometric distribution function (see Figure 3.24). Based on this results, we favor the SNPR method, in terms of error estimation.

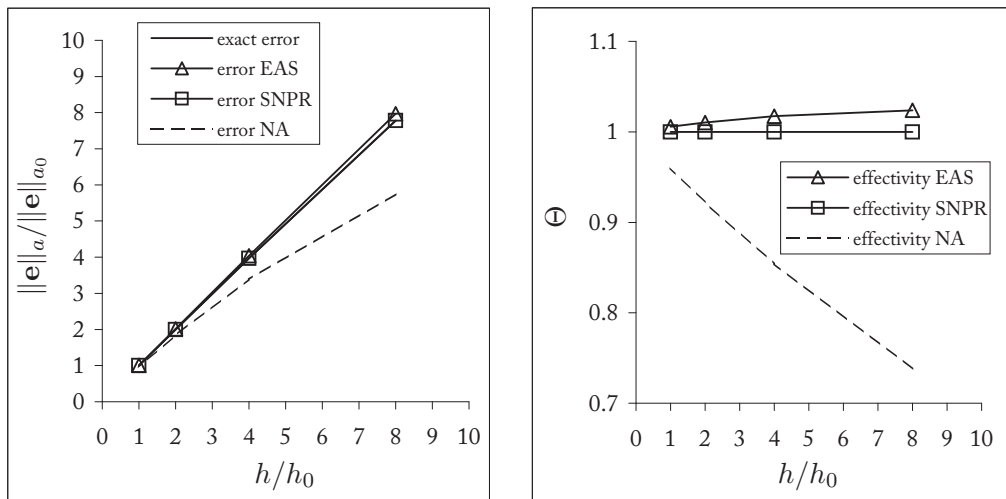


Figure 3.21: Average error (left) and effectivity index (right) for the linear distribution function for different element sizes.

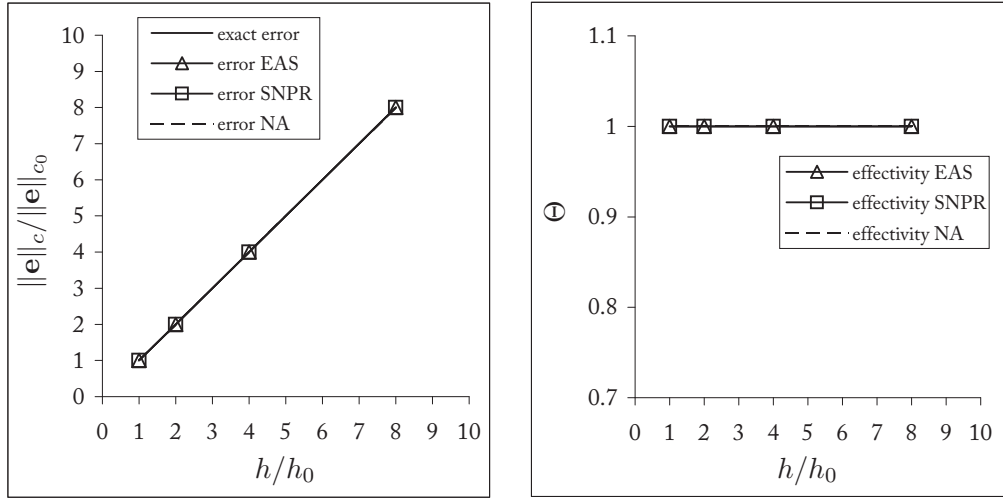


Figure 3.22: Error in the center point of the mesh (left) and effectivity index at the center point (right) for the linear distribution function for different element sizes.

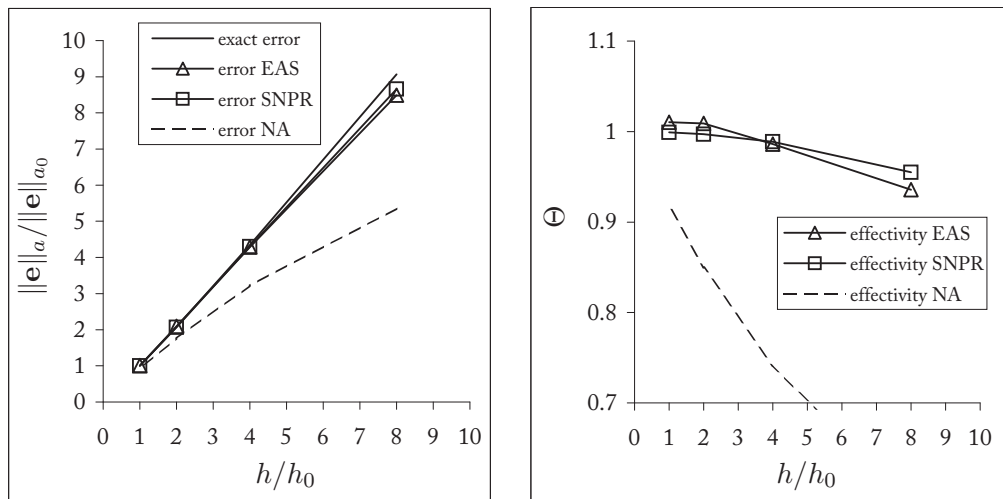


Figure 3.23: Average error (left) and effectivity index (right) for the quadratic distribution function for different element sizes.

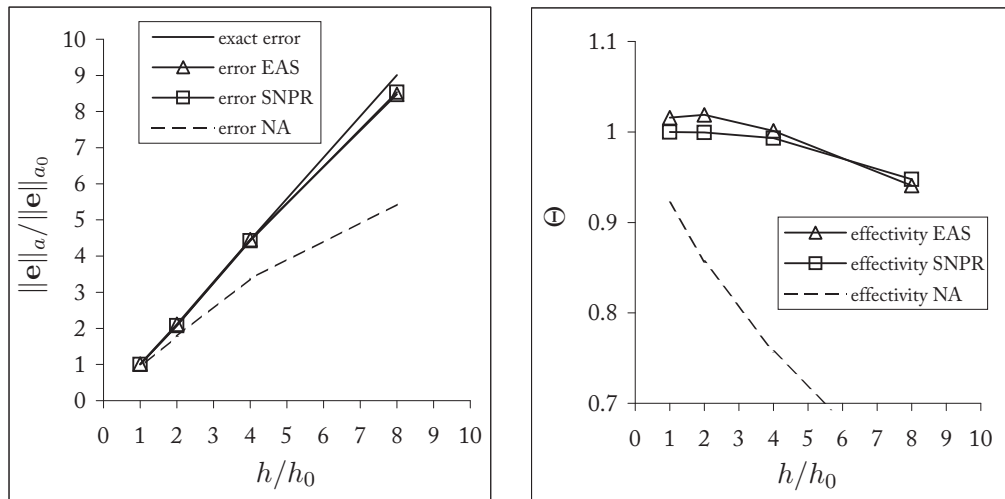


Figure 3.24: Average error (left) and effectivity index (right) for the trigonometric distribution function for different element sizes.

3.4 Adaptive remeshing

Since chip formation begins with the onset of shear-banding, we start by looking at this process more closely. As shown in Figure 3.25, for simplicity, one can start by idealizing the cutting process as a simple shear of the material in the shear zone. Cutting of the region enclosed in the

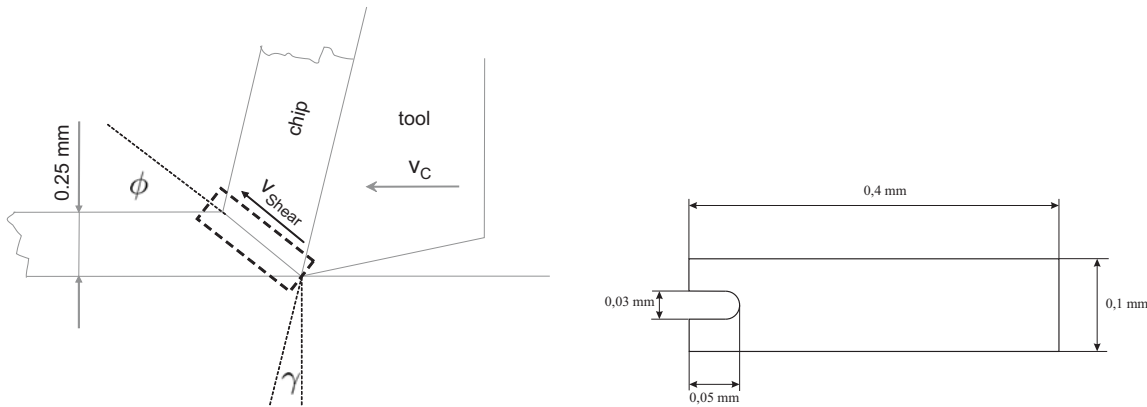


Figure 3.25: Cutting zone idealized as a region in the material undergoing simple shear.

dashed box is assumed to take place at a shear angle of $\phi = 40^\circ$ and a cutting depth of 0.25 mm. The deformation is assumed to be plane strain. The applied shear velocity v_{shear} corresponds to a cutting velocity v_c in the shear zone of about 1000 m/min. Since the shear specimen is notched on only one side, the shear band can develop independent of the geometry.

The determination of the accuracy of any given finite-element approximation in general requires a knowledge of the exact solution. Since this is generally not possible, one instead compares a given finite-element solution with one of higher accuracy serving as the reference approximation or numerical solution. In the current context of shear-band formation, such a reference approximation is based on a fine discretization of the specimen. In a first step the specimen is discretized with triangular elements oriented in the predicted shear-band direction. In a second step the same analysis is carried out with continuous remeshing of an initially coarser mesh. A constant element size is utilized throughout. The remeshing procedure yields an unstructured mesh with no preferred direction for shear banding. Here and in the following, all calculations have been carried out with linear triangular elements. Considering the pathological mesh dependence (see Section 2.3) and thus, to ensure comparability, the average element edge length is fixed at 0.0025 mm for the simulations to follow.

Figure 3.26 shows the result for the oriented mesh. Due to the strong mesh dependence, the shear band develops horizontally in the direction of the orientation of the mesh. Since for the oriented mesh, the width of the shear band is determined by the local element length, only a small amount of material has to be deformed beyond the critical point. This is also reflected by the sharp decrease of the shear stress after passing the critical point of deformation as shown in Figure 3.28. In contrast to the oriented mesh, the simulation with continuous remeshing shows a more diffuse and wider shear band (Figure 3.27). Since the elements involved are constant-strain elements, they are unable to represent a strain gradient in their interiors. Thus, in the oriented case, the shear band can localize along element edges, the strain gradient is approximated as a strain jump at the element boundaries, and the resulting shear band is sharp.

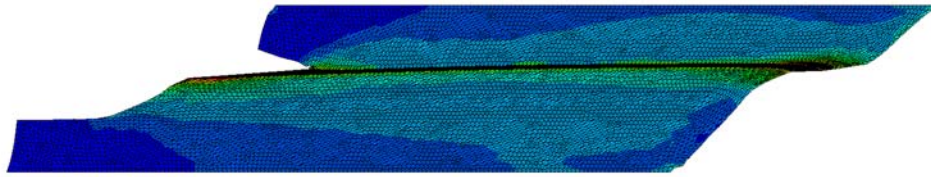


Figure 3.26: Shear-band development in the notched structure of Figure 3.25 finely-discretized parallel to the shear direction.

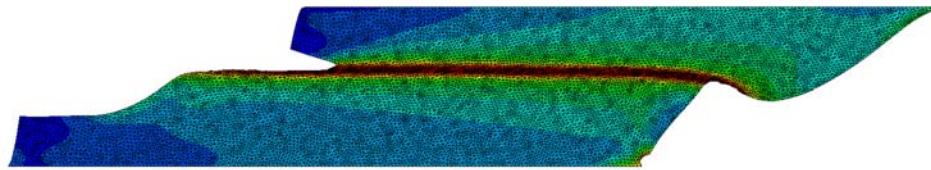


Figure 3.27: Shear-band development in the notched structure of Figure 3.25 during continuous remeshing. See text for details.

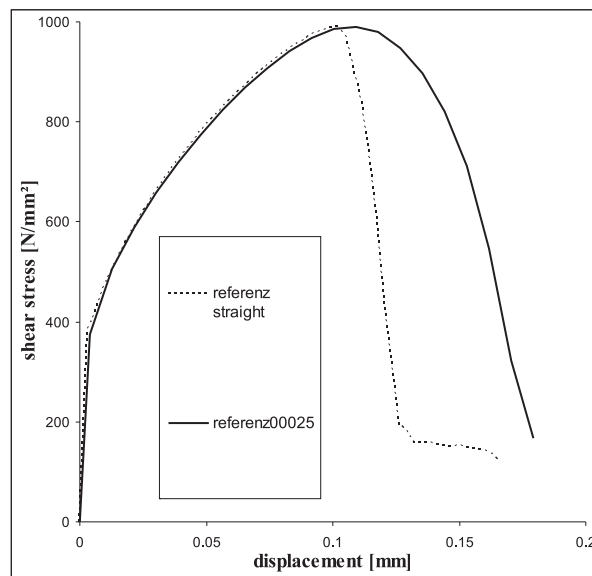


Figure 3.28: Averaged shear stress along upper edge of structure as a function of displacement there. Dashed curve: Oriented fine mesh (Figure 3.26). Continuous curve: Continuous remeshing (Figure 3.27).

On the other hand, in the non-oriented case, no element edges are available and the shear-band is forced to spread out over more than one element layer. As shown in Figure 3.27, this results in a more diffuse shear-band. With increasing shear-band thickness, the amount of material that has to be deformed beyond the critical point increases as well. This fact is represented by delayed shear-band development as well as by an initially gradual decrease in the shear stress after passing the critical point (see Figure 3.28).

In comparison to the approach of orienting the mesh, the simulation with remeshing demands a higher number of elements to resolve the same thickness of the shear band. Nevertheless, in

terms of simulating the process of cutting, remeshing allows a more realistic simulation of the process as the orientation of the shear band is no longer affected by the orientation of the mesh. Also the modeling of the separation of chip and workpiece is now possible without introducing an artificial failure zone (see, e.g., Hortig and Svendsen (2007)). Keeping these results in mind we will now turn to the investigation of suitable remeshing criteria.

As the choice of the maximum error $\|\mathbf{e}_q\|_{\max}$ has a significant influence on both the accuracy and the effectiveness of the adaptive strategy, we consider a reference simulation to determine useful bounds for this quantity. Due to the h^p dependence of the error, a transfer of results between different mesh sizes is generally possible, but we have to consider variations caused by the mesh dependence. To allow a sufficiently trusted transfer of the results in both directions (coarser and finer meshes), we chose an element size between h_{\max} and h_{\min} . Starting from a mesh size of $h_{\max} = 0.01$ mm and working with a minimum size of $h_{\min} = 0.0025$ mm as chosen for the reference simulations above, we set the mesh size to $h = 0.005$ mm. A transfer to the maximum and minimum mesh size is now possible by simply multiplying and dividing, respectively with the factor $h^1 = 2$ ($p = 1$, linear elements) (see also Figure 3.20).

Figure 3.29 and Figure 3.30 show the distribution of the error in ϵ_p and the distribution of the equivalent plastic deformation ϵ_p , respectively. The scaling in Figure 3.34 is set from $\epsilon_p = 0.0$ to $\epsilon_p = 1.0$ to display the areas of potentially shear-band formation. From Figure 2.2 it can be stated, that for an adiabatic deformation, the critical point, where the material enters the softening regime is nearly independent from the strain rate. For the given material this point is identified by $\epsilon_p \approx 1.0$. To ensure a sufficient resolution of the shear band, at least the area of potential shear band formation has to be discretized with the highest mesh density. For the given problem and the given mesh size of $h = 0.005$ mm the critical area shows an error of $\|\mathbf{e}_{\epsilon_p}\| > 0.1$ (see Figure 3.29). Now, choosing the light grey areas in Figure 3.29 ($\|\mathbf{e}_{\epsilon_p}\| < 0.025$) to be discretized with the maximum element size of $h_{\max} = 0.01$ mm the allowable error has to be set to

$$\|\mathbf{e}_{\epsilon_p}\|_{\max} = 0.025 \frac{0.01 \text{ mm}}{0.005 \text{ mm}} = 0.05, \quad (3.42)$$

to give the maximum element size in this area.

Comparing the distribution of the error and the distribution of the equivalent plastic deformation itself (Figure 3.30), error estimation is suspected to lead to a delayed refinement of the critical areas. This observation suggests the demand for an additional indicator. As stated above, the critical point, when the material enters the softening regime is strongly connected to ϵ_p . Thus, a direct use of ϵ_p as an refinement indicator is generally possible.

In the following we will apply the discussed strategy based on pointwise error estimation. Additionally, we will test the applicability of ϵ_p as a direct refinement indicator. Therefore we will link the new mesh size by a linear relation to ϵ_p (see Figure 3.31). In the following simulation the refinement starts at $\epsilon_{p1} = 0.3$ and ends at $\epsilon_{p2} = 0.9$. An algorithmic overview for the process of error estimation/indication is given in Table 3.6.

Figure 3.32 to Figure 3.34 show the results for both strategies in comparison to the reference simulation with continuous remeshing and constant element size. As expected, the error estimation leads to a delayed refinement (Figure 3.33). This results in a delayed shear band

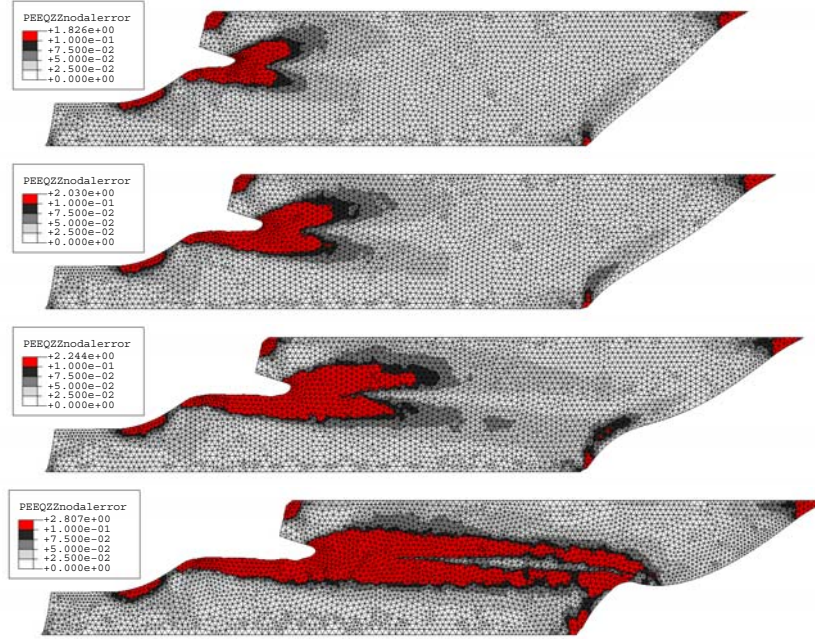


Figure 3.29: Distribution of the pointwise error in ϵ_p inside the notched shear specimen (Figure 3.25) for an element size of $h = 0.005$ mm

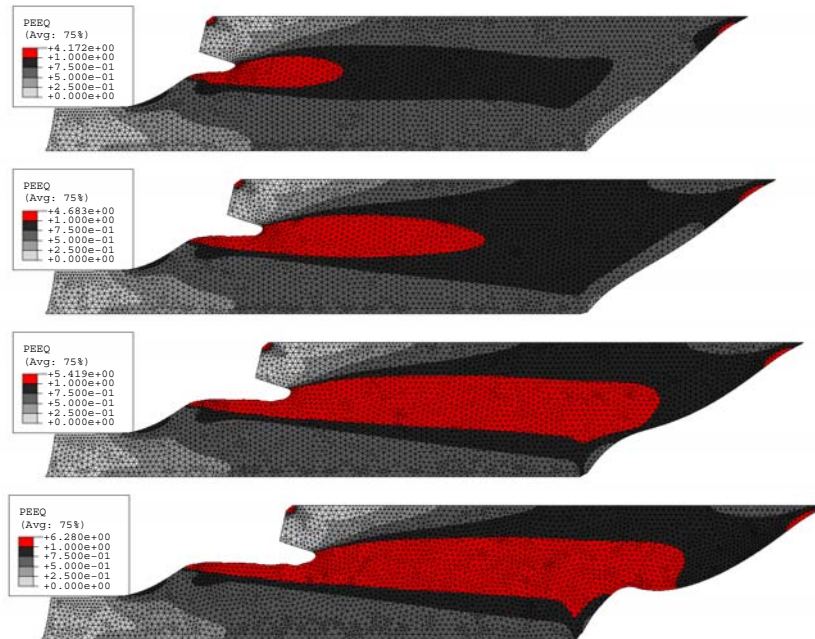


Figure 3.30: Distribution of equivalent plastic deformation ϵ_p inside the notched shear specimen (Figure 3.25) for an element size of $h = 0.005$ mm

development and also, in comparison to the reference simulation, in a more gradual reduction corresponding shear stress after passing the critical point of deformation (Figure 3.32). This behavior can be directly explained by the kinematics of a developing material instability. Here, the steepest gradients are situated at the boundary and not in the interior. The resulting coarse mesh at the tip of the developing shear band (see last stage of Figure 3.33) inhibits its devel-

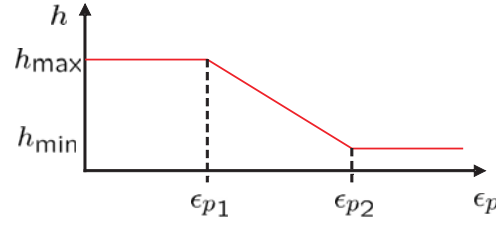


Figure 3.31: Refinement function $h(\epsilon_p)$. Here, ϵ_{p1} and ϵ_{p2} allow the adjustment of the adaptive strategy.

Error estimation/indication

1. Calculate the pointwise error:

$$\|\mathbf{e}_q\|_n = \max(\|\mathbf{q}_n^* - \hat{\mathbf{q}}_k\|), \quad \forall n \in \{1, \dots, n_N\}$$

2. Calculate the refinement parameter in terms of the pointwise error:

$$\xi_n = \frac{\|\mathbf{e}_q\|_n}{\|\mathbf{e}_q\|_{\max}}, \quad \forall n \in \{1, \dots, n_N\}$$

3. Calculate the new local mesh size in terms of the pointwise error:

$$\bar{h}_e^n = \frac{h_n}{\xi_n^{1/p}}, \quad \forall n \in \{1, \dots, n_N\}$$

4. Calculate the new mesh size in terms of the refinement indicators r_i (linear ansatz):

$$\text{if } r_{i1} \leq r_i^n \leq r_{i2}: \bar{h}_{r_i} = h_{\max} - \frac{h_{\max} - h_{\min}}{r_{i2} - r_{i1}} (r_i^n - r_{i1}), \quad \forall n \in \{1, \dots, n_N\}$$

3. Calculate the new local mesh size:

$$\bar{h}_n = \min(\bar{h}_e^n, \bar{h}_{r_1}^n \dots \bar{h}_{r_{\text{ind}}}^n), \quad \forall n \in \{1, \dots, n_N\}$$

Table 3.6: Error estimation/indication, general overview.

oping. The strategy with refinement indication shows a better performance. The results nearly coincide with the results for the reference simulation (Figure 3.32). The good performance of the refinement indicator method is explained by the early and extensive remeshing behavior. In contrast, the error estimation method is much more economical.

Considering the distribution of the equivalent plastic deformation, and in particular the area of $\epsilon_p > 0.9$ in Figure 3.33, a strategy combining the anticipatory character of the refinement indicator method and the economy of the error estimation method suggests itself. The result for a combined strategy is given in Figure 3.35 and Figure 3.36. As we are mainly interested in a pre refinement of the critical area (see Figure 3.33), the refinement indicator method starts to refine at a later point, at $\epsilon_p = 0.7$. Thus, the basis of the combined approach is still the error estimation. The influence of the refinement indicator is activated when it indicates a smaller element size than the error estimator.

As a preliminary result for this section, it can be stated that error estimation without any anticipatory refinement indicator is not capable to indicate a developing material instability. On the other hand, refinement indication without error estimation is generally possible. But only the combination ensures both a sufficiently fine discretization of the critical areas and the reliability of the results.

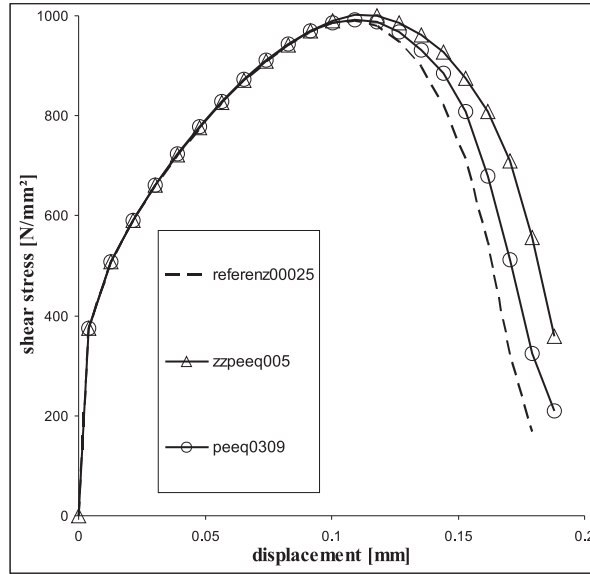


Figure 3.32: Averaged shear stress along upper, sheared edge of structure as a function of the displacement of the upper edge of the structure for different remeshing strategies. Reference simulation with continuous remeshing and constant element size (dashed), refinement basing on error estimation (triangle) and direct use of ϵ_p as refinement indicator (circle).

For the additional refinement indicator any meaningful quantity is possible. The onset of shear banding is not only restricted to a critical amount of plastic deformation. Also, a locally increased strain rate and a locally increased rate of plastic work, respectively, indicate the possible zone of deformation localization. In contrast to the equivalent plastic deformation, which critical amount is directly given by the corresponding stress strain diagram, the refinement boundaries for strain rate or plastic power are not given in advance. These have to be determined for any specific problem. In this regard, working with quantities normalized to the mean value, increases the expressiveness. For the given shear specimen, refinement between $\bar{\epsilon}_{p1} = 1$ and $\bar{\epsilon}_{p2} = 2$ for the normalized rate of plastic deformation and between $\bar{p}_{p1} = 1$ and $\bar{p}_{p2} = 2$ for the normalized plastic power, respectively, lead to an early and localized refinement of the critical region, when used in combination with the error estimation (see Figure 3.37 and Figure 3.38).

Comparing the stress displacement diagrams (see Figure 3.39), as well as the development of the meshes for the different additional refinement indicators, plastic power and equivalent plastic strain rate, respectively, seem to be most effective to indicate the developing material instability. But again, the refinement boundaries for these quantities are problem dependent.

In the following section we will test the discussed refinement strategies on the simulation of the high speed cutting process. The allowable error of $\|\mathbf{e}_{\epsilon_p}\|_{\max} = 0.05$, identified by considering a virtual reference specimen will be used further on.

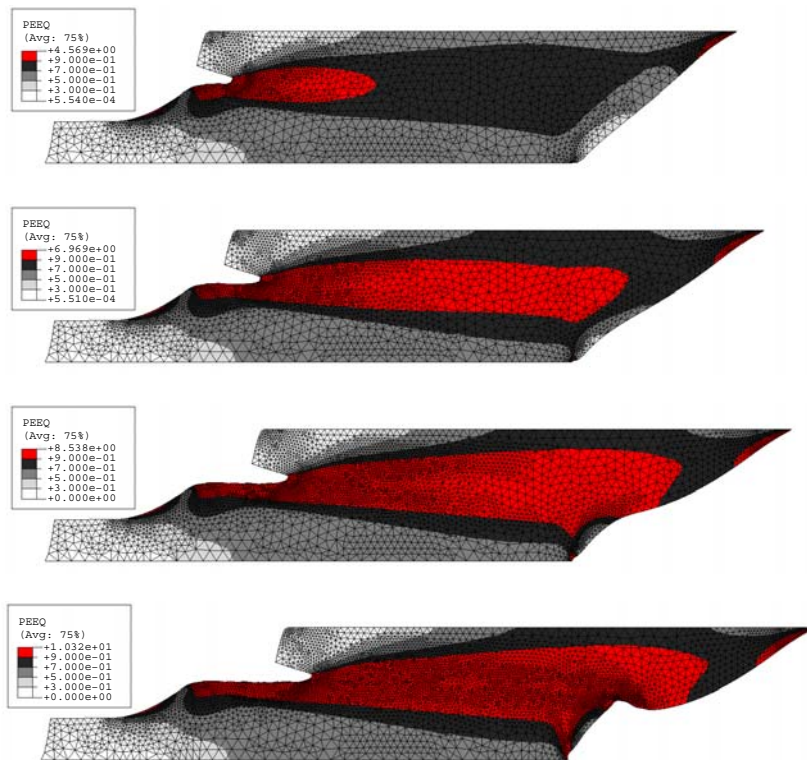


Figure 3.33: Distribution of the equivalent plastic deformation inside the notched specimen for the refinement strategy based on error estimation. Here, the allowable error is set to $\|e_{\epsilon_p}\|_{\max} = 0.05$. Note the late refinement of the interior of the critical area. As the steepest gradients are situated at the boundaries of a developing material instability, these areas are refined first. Inside the developing shear band the gradients are quite smooth. The resulting coarse discretization has a blocking effect on the development of the shear band.

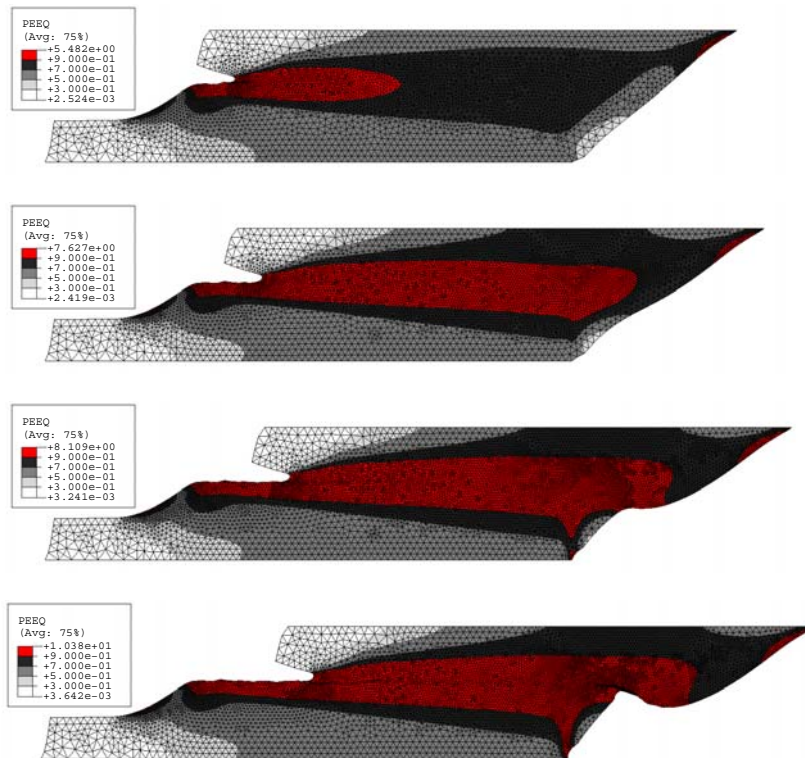


Figure 3.34: Distribution of the equivalent plastic deformation inside the notched specimen for the refinement strategy based on refinement indication. Here, the element size is linearly reduced between $\epsilon_p = 0.3$ and $\epsilon_p = 0.9$.

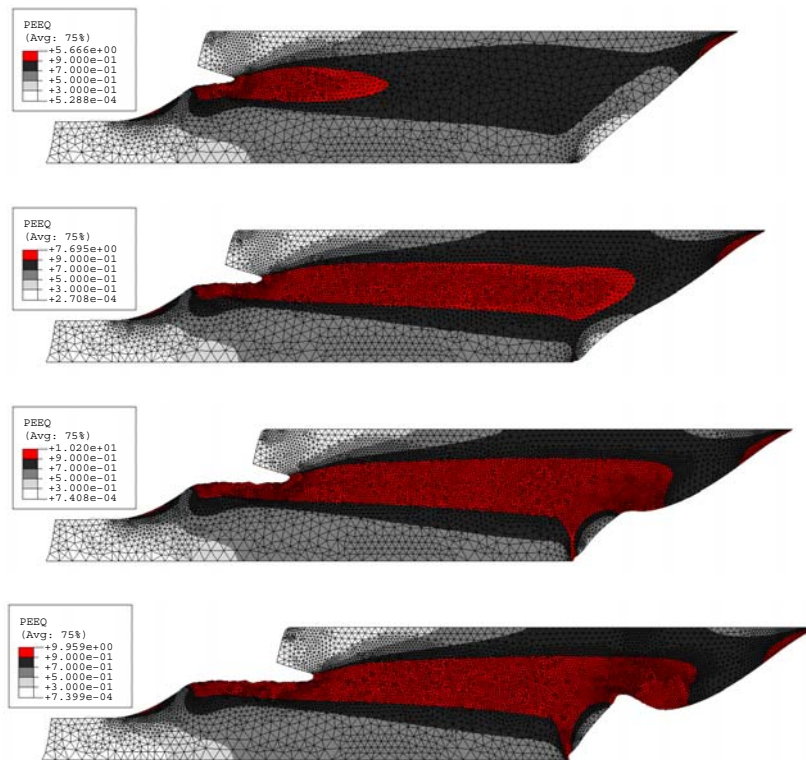


Figure 3.35: Distribution of the equivalent plastic deformation inside the notched specimen for the refinement strategy based on a combination of error estimation and refinement indication. Here, the allowable error is set to $\|e_{\epsilon_p}\|_{\max} = 0.05$. The additional refinement indicator triggers the refinement between $\epsilon_p = 0.7$ and $\epsilon_p = 0.9$.

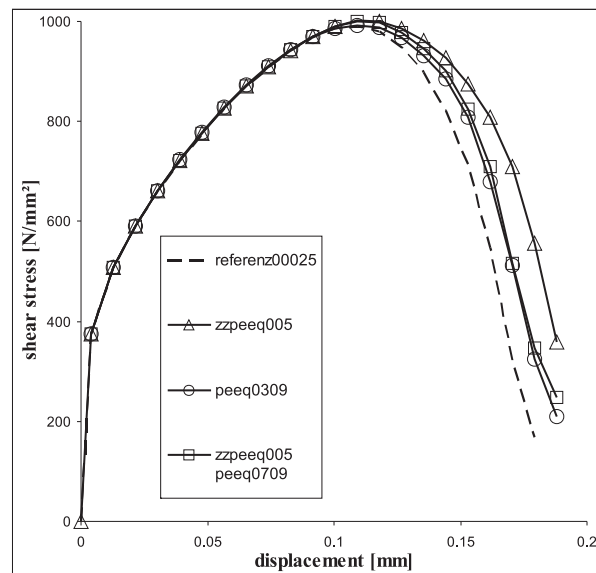


Figure 3.36: Averaged shear stress along upper, sheared edge of structure as a function of the displacement of the upper edge of the structure for different remeshing strategies. Reference simulation with continuous remeshing and constant element size (dashed), refinement basing on error estimation (triangle), direct use of ϵ_p as refinement indicator (circle) and a combination of error estimation and refinement indication (quad).

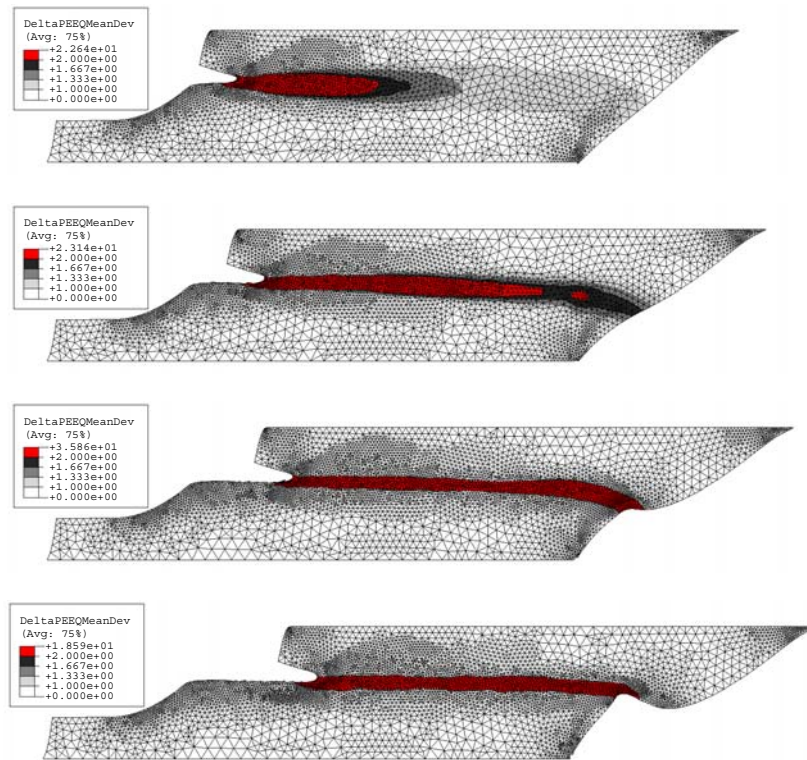


Figure 3.37: Distribution of the normalized rate of plastic deformation inside the notched specimen for the refinement strategy based on a combination of error estimation and refinement indication. Here, the allowable error is set to $\|e_{e_p}\|_{\max} = 0.05$. The additional refinement indicator triggers the refinement between $\bar{\epsilon}_{p1} = 1$ and $\bar{\epsilon}_{p2} = 2$.

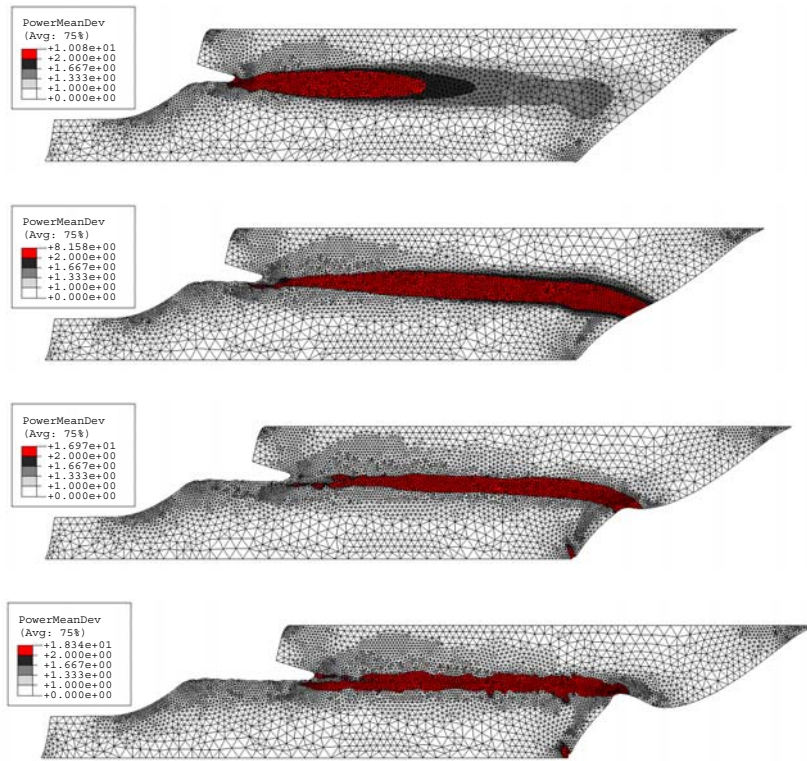


Figure 3.38: Distribution of the normalized plastic power inside the notched specimen for the refinement strategy based on a combination of error estimation and refinement indication. Here, the allowable error is set to $\|e_{\epsilon_p}\|_{\max} = 0.05$. The additional refinement indicator triggers the refinement between $\bar{p}_{p1} = 1$ and $\bar{p}_{p2} = 2$.

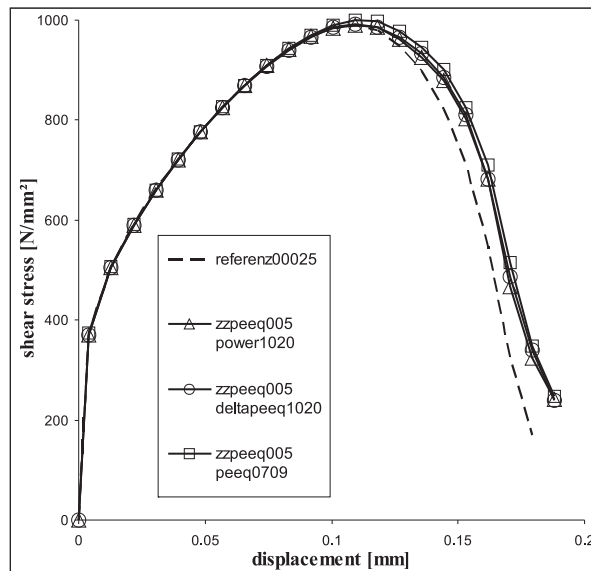


Figure 3.39: Averaged shear stress along upper, sheared edge of structure as a function of the displacement of the upper edge of the structure for different remeshing strategies. Reference simulation with continuous remeshing and constant element size (dashed) and refinement basing on error estimation in combination with different refinement indicators. Plastic power (triangle), rate of plastic deformation (circle), plastic deformation (quad).

3.5 Simulation of high speed cutting via adaptive remeshing

The finite element model of the cutting process is given in Figure 3.40. During the simulation the workpiece is subjected to permanent remeshing. Modeling of the separation of the chip from the workpiece is, thus, possible only by means of plastic flow and without an additional failure zone. The tool is modeled as analytically rigid and moves with a constant velocity into the workpiece. The implemented material model is the discussed Johnson-Cook model with parameters for *IN718* (see Section 2.2). Enforcing adiabatic conditions, the cutting velocity is set to $v_c=1000$ m/min. The tool rake angle, the cutting depth and the tool edge radius are fixed at $\gamma=-5^\circ$, $t=0.25$ mm and $r=20$ μm , respectively. The friction coefficient between tool and chip has been estimated and is fixed at $\mu=0.1$. The above results for error estimation and error indication have been carried out in a general manner. Thus, lacking any detailed experimental data at the moment, the intention of the simulation results to follow, based on this generic situation, is mainly to test and to demonstrate the developed adaptive scheme.

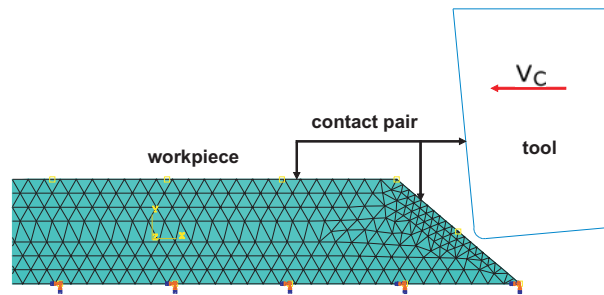


Figure 3.40: Finite element model of the cutting process

To determine meaningful parameters for the additional refinement indicator, we start with the refinement strategy, controlled only by means of error estimation. Figure 3.41 shows the error distribution for this strategy at an early stage of chip formation. As a first result, we can confirm the observations gained from the reference specimen. Again, we detect a refinement, beginning at the boundaries of the developing instability. As Figure 3.41 and Figure 3.42 show, areas of advanced equivalent plastic deformation as well as areas of highest plastic power and equivalent plastic strain rate, respectively remain at a coarse level of refinement, which again suggests these quantities to be acting as additional refinement indicators.

In contrast to the reference shear specimen, which deals with a potential zone of strain localization, more or less fixed in space, the problem of metal cutting confronts with a moving zone, not known in advance. Here, the different indicators give more differentiated results, concerning the areas of maximum refinement. Again, the equivalent plastic deformation appears as a robust indicator, that gives reasonable results for the potential areas of localization. The parameters ε_{p1} and ε_{p2} are directly given by the corresponding, adiabatic stress-strain diagram and are thus independent from the specific application. As a drawback, in case of multiple and moving localization zones, this quantity leads to a massive and irreversible refinement, as the equivalent plastic deformation behaves monotonically nondecreasing. Here, the plastic power and the equivalent plastic strain rate, respectively, seem attractive, as these quantities capture the highly dynamic deformation field.

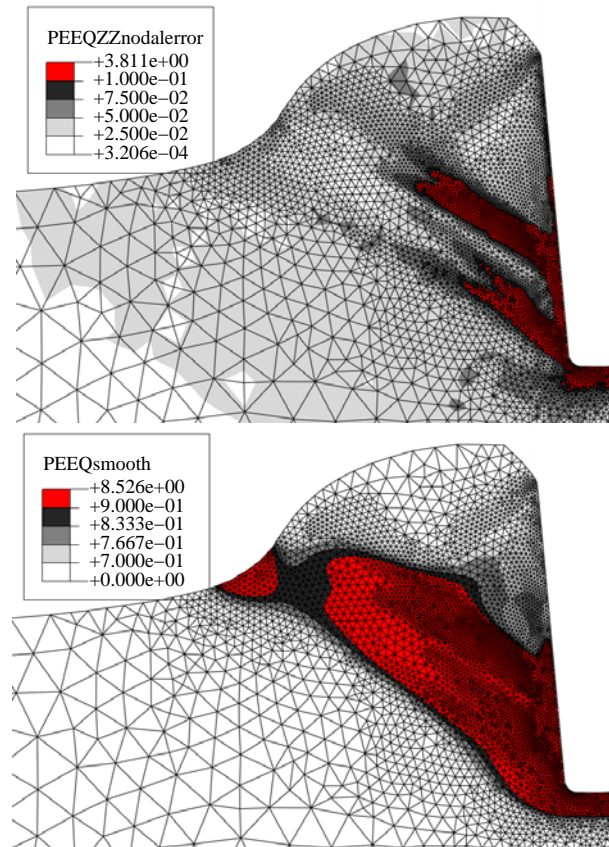


Figure 3.41: Distribution of the error in equivalent plastic deformation (above) and equivalent plastic deformation (below) at an early stage of chip formation.

The following figures demonstrate the process of chip formation, calculated with the developed adaptive remeshing scheme. Here, the additional refinement indicator is the equivalent plastic strain rate (Figure 3.43) and the plastic power (Figure 3.44), respectively. Both figures show the field of the corresponding indicator quantity, scaled to the adjusted lower and upper boundary of refinement. Although the results for both indicators show good agreement, the plastic power leads to an earlier indication of the potential zone of localization. This is explained by the fact that, in this zone, not only accelerated deformation takes place, also the stress state is increased. On the other hand, the plastic power ignores the fully developed shear band as the stress state is decreased, although strain rates are increased. This is no drawback as, at this stage, the resolution of the shear band is ensured by the error estimation. Figure 3.45 compares the results for different quantities at the stage of chip formation as given in Figure 3.43 e) and Figure 3.44 e), respectively. The plots for the von Mises stress (first line) and the equivalent plastic strain (second line) show very good agreement. Differences in the progression of the developing shear band at the tip of the cutting tool can be explained by the earlier indication of the shear band with the plastic power. The results reveal, that only an adaptive remeshing scheme is capable of resolving the complex deformation field, especially in the primary deformation zone at the tool tip. As can be seen in Figures 3.43 and 3.44, besides the primary shear bands that develop under a specific shear angle, also secondary shear bands, perpendicular to the primary ones, can be detected. Running a simulation without any remeshing and working instead with

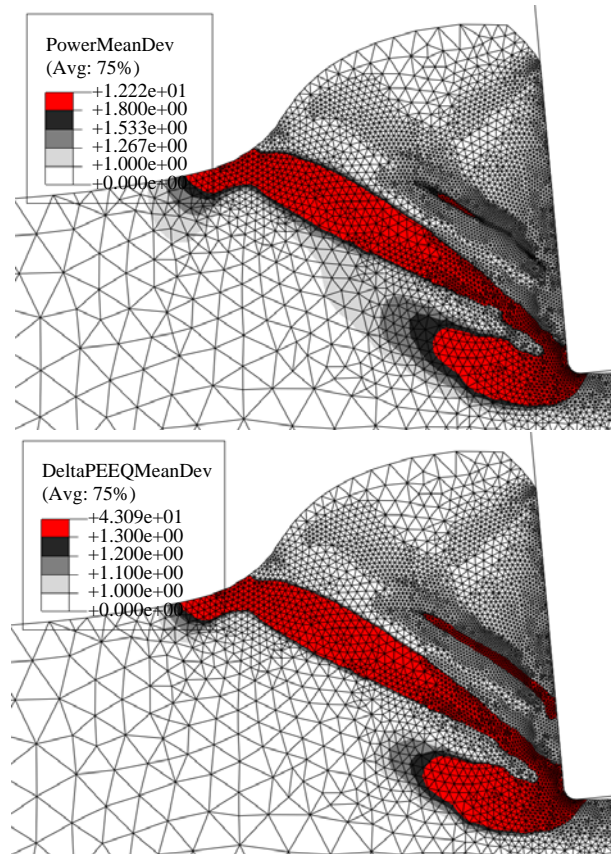


Figure 3.42: Distribution of the plastic power (above) and equivalent plastic strain rate (below), normalized to the corresponding mean value. The scale has been adjusted, to give comparable refined areas. (below) at an early stage of chip formation.

an oriented mesh, chip formation is still possible, as shown in Hortig and Svendsen (2007). However, the complex deformation field will inevitably lead to massively distorted elements, and finally to doubtful results, especially in the primary deformation zone (see Figure 3.46).

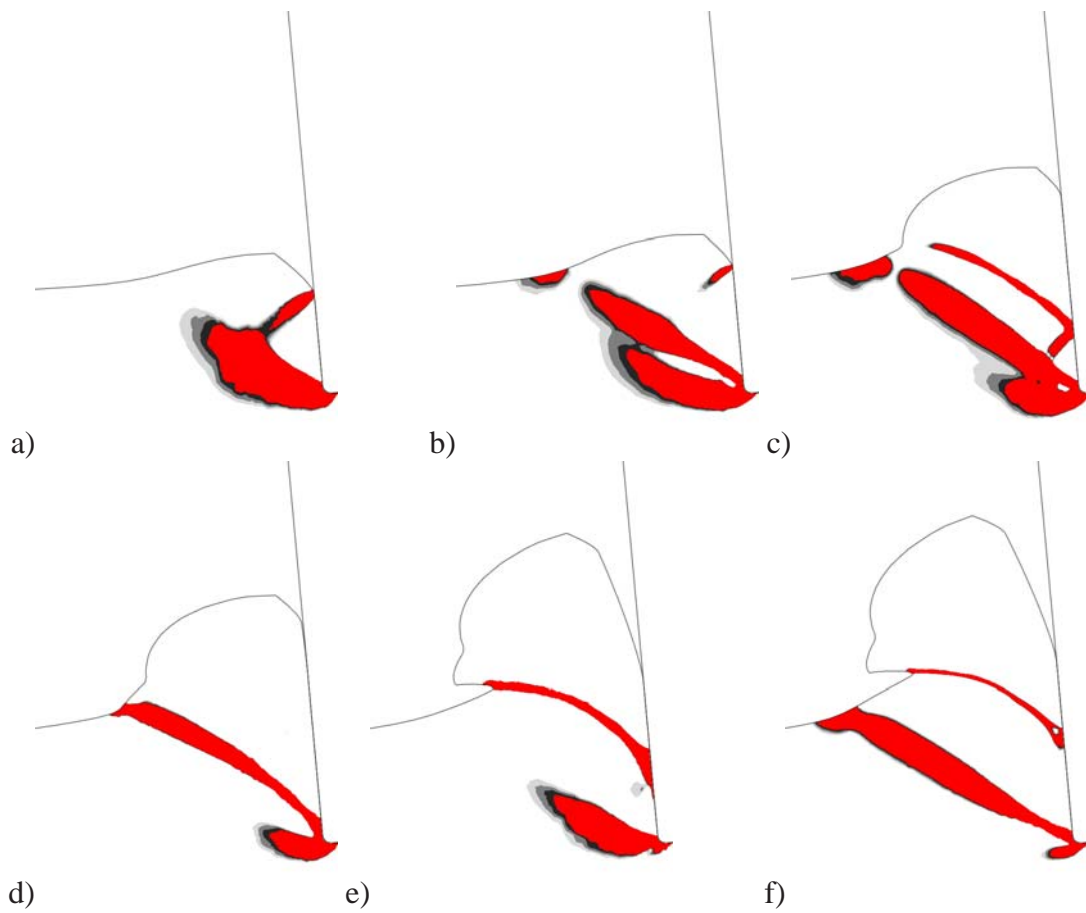


Figure 3.43: Process of chip formation. Here, the additional refinement indicator is the equivalent plastic strain rate, normalized to the corresponding mean value. The figures show the field of the indicator quantity, scaled to the adjusted lower and upper boundary of refinement.

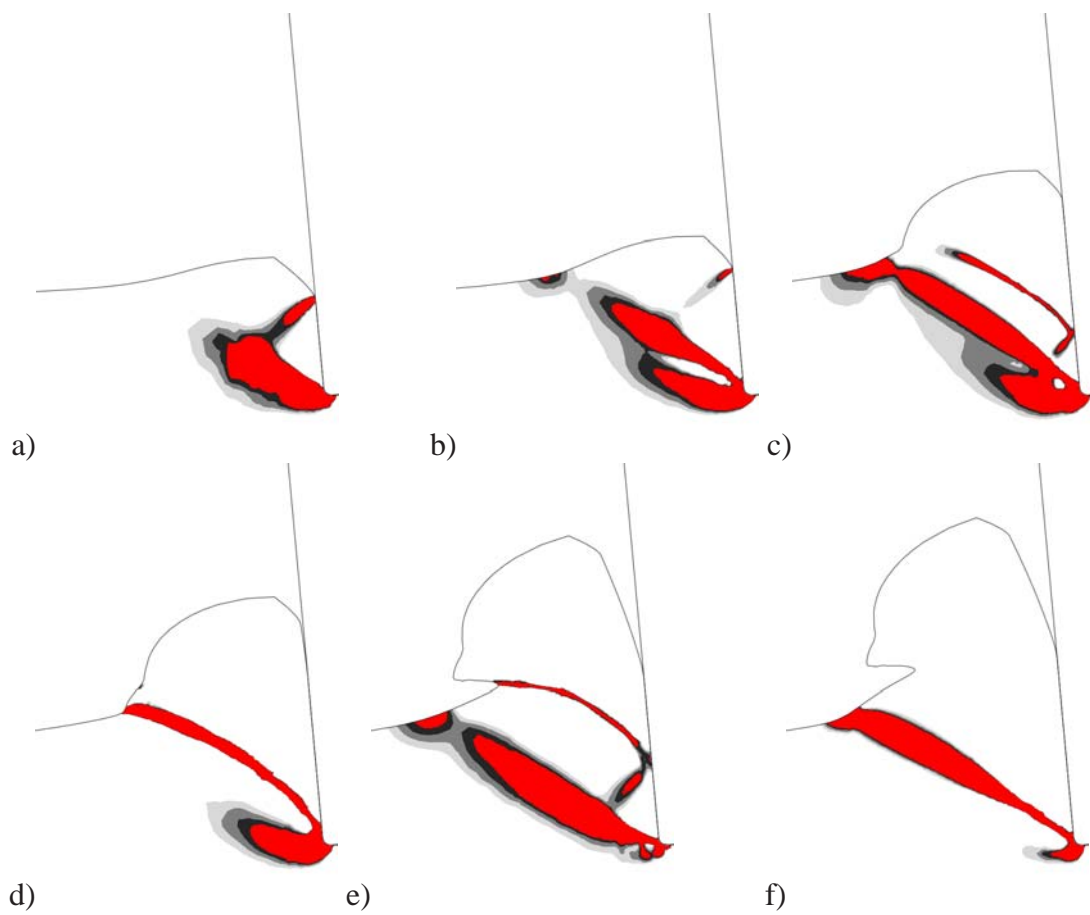


Figure 3.44: Process of chip formation. Here, the additional refinement indicator is the plastic power, normalized to the corresponding mean value. The figures show the field of the indicator quantity, scaled to the adjusted lower and upper boundary of refinement.

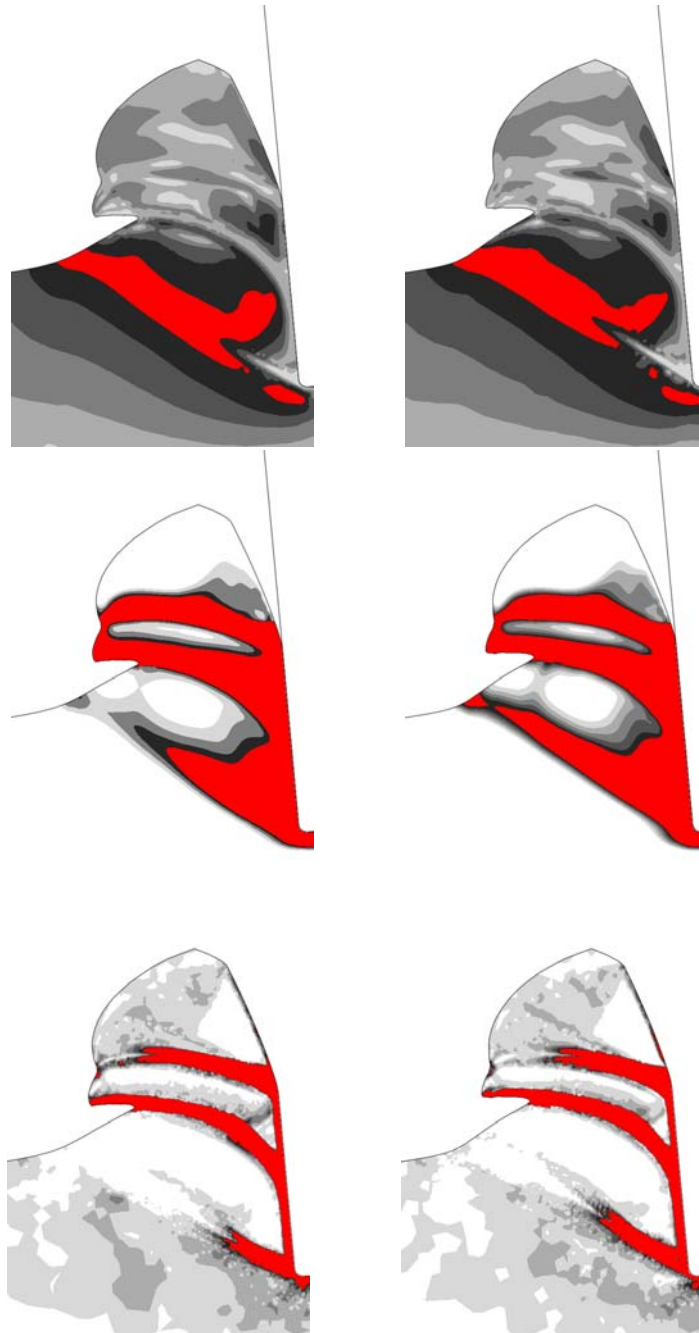


Figure 3.45: Influence of different refinement indicators on the formation of shear bands. Here, the left column shows the results for the equivalent plastic strain rate and the right column the results for the plastic power. The first line shows the distribution of the von Mises stress, the second line shows the distribution of the equivalent plastic deformation and the third line shows the distribution of the error in equivalent plastic deformation.

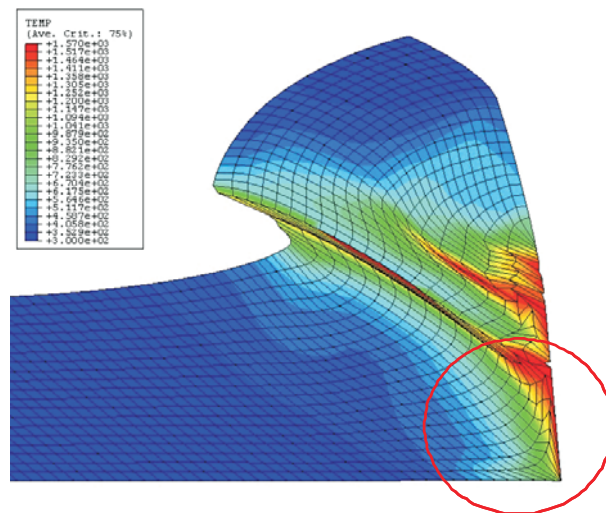


Figure 3.46: Chip formation without adaptivity. Here, the mesh has been oriented in the direction of the predicted shear angle. The complex deformation field in the region of the tool tip leads to massive distorted elements, and finally to doubtful results.

3.6 Preliminary summary

The application of error estimation and refinement indication on problems dealing with localization phenomena has been discussed and tested. It has been shown that classical error estimation is not capable of detecting critical areas of deformation. On the other hand, by using refinement indicator methods only, we suffer a loss in accuracy. Especially in context of sophisticated applications, such as the simulation of the process of high speed cutting, only a combination of error estimation and refinement indication ensures both, a control of accuracy and a pre-determining character of the strategy, essential when dealing with localization problems. The presented method of point wise error estimation is robust, easily implemented and is capable of identifying the magnitude of gradients with a minimum of numerical cost. For the mapping of internal variables, it has been shown that the classical finite element projection of the recovered values leads to numerical diffusion. Here, a separated, direct transfer should be established. The physical meaning of ϵ_p in context of localization phenomena has been shown and a possible application as a refinement indicator has been demonstrated through numerical examples. In context of detecting material instabilities, also the rate of equivalent plastic strain as well as the plastic power have turned out to work very well. Here, in contrast to ϵ_p , the parameters for the refinement strategy are problem dependent and cannot be determined in advance. Simulation results reveal that only an adaptive remeshing scheme is capable of resolving the complex deformation field, especially in the primary deformation zone at the tool tip. Moreover, having no more predefined separation zone, the modeling of the resulting surface becomes possible. With these adaptive tools at hand the first part of our work is complete and we will now turn to the discussion of an extended non-local material model.

Chapter 4

Local and non-local models for dynamic thermoelasticity and damage

Abstract– In this chapter the thermomechanical formulation is improved by an extension of the material model by ductile damage and further, by a nonlocal description of the material. After the derivation of the extended thermodynamic framework, we present a specific application to non-isochoric thermo-viscoplasticity including ductile damage. In this context a detailed derivation of the algorithmic implementation and the algorithmic linearization, as needed in terms of a finite element implementation, is given. Additionally, we discuss the kinematics in context of adaptive remeshing. In regards to a model with internal variables this issue is of special importance.

4.1 Introduction

Failure in metals during processes like metal cutting is influenced by a number of competing physical processes in the material. For example, heat conduction and mechanical dissipation play a strong role here in the sense of thermal softening. At lower cutting speeds and resulting lower strain-rates, heat conduction is sufficiently fast to prevent a temperature increase due to mechanical dissipation which would result in thermal softening. At higher speeds and accordingly higher strain-rates, however, heat conduction is too slow to prevent the temperature from increasing to the point where thermal softening occurs, resulting in shear-banding and chip formation. Beyond thermal softening, other softening effects, such as damage are also present. The strong dependence of this process on strain-rate and temperature implies that the material behavior of the metallic workpiece is fundamentally thermoelastic and thermoviscoplastic in nature. The material model presented in section 2.2 for thermoelastic viscoplasticity is restricted to deformation behavior and adiabatic conditions. In the current work, the model is extended to account for non-local inelastic deformation and damage processes as well as heat conduction. In particular, isotropic Fourier heat conduction is assumed here for simplicity. Motivated by the fundamental work of Eringen (1966) and here especially by the *axiom of neighborhood*, various nonlocal continuum formulations have been developed with the aim to close this gap. In literature, two families of such nonlocal formulations can be identified.

Nonlocal models of *integral type* generally consist in replacing a specific variable (e.g., strain, equivalent plastic strain, damage etc.) at each point by its nonlocal counterpart obtained by weighted averaging over a neighborhood. Rather interested in the continuum based description of interacting dislocations than developing a localization limiter Eringen (1981) presented a framework based on the nonlocal counterpart of the strain tensor. Later Bazant and Lin

(1988) proposed a formulation working with the nonlocal plastic strain tensor or alternatively, working with the nonlocal average of the plastic multiplier. Performing a series of simulations with different minimum element sizes, here in terms of an excavation process, Bazant and Lin (1988) successfully demonstrated the ability of this formulation to act as a localization limiter. An application of nonlocal averaging of the damage can be found, e.g., in the work of Bazant and Pijaudier-Cabot (1988) and Tvergaard and Needleman (1995). Although the interpretation of the integral type approaches is descriptive, the additional numerical effort, necessary when calculating the nonlocal average quantity for every integration point, is their main drawback. Moreover, the implementation inside a commercial finite element code is not simply to achieve.

The differential counterpart of the nonlocal integral approaches is represented by models of *gradient type*. Instead of considering the influence of the neighborhood through integrals, this family of models introduces the nonlocal character by incorporating higher order gradients into the constitutive model. Influenced by the pioneering work of Toupin (1962) and Mindlin (1964), Chambon et al. (1998) as well as Fleck and Hutchinson (1997) adapted the idea of higher order stresses, work conjugate to strain gradients, to formulate a strain gradient plasticity framework. While in the formulation of Chambon et al. (1998) the higher order stress enters only the balance of momentum, the theory of Fleck and Hutchinson (1997) considers these additional stresses in terms of the yield condition. Although physically motivated by the concept of statistically stored dislocations (SSD) and geometrically stored dislocations (GND), the essential formulation of Fleck and Hutchinson (1997) remains phenomenological. Contrarily, the group of mechanism-based strain gradient (MSG) plasticity theories is based on micromechanical effects on the flow strength of materials. An application of the MSG concept, originally formulated in Gao et al. (1999) and Huang et al. (2000), can be found, e.g., in Qiu et al. (2003), here in context of micro-indentation hardness experiments. While the above methods consider higher order displacement gradients or corresponding stress quantities, models with gradients of internal variables represent a more general concept to introduce non-locality. For example, Aifantis (1984, 1992) and Maugin (1990) consider higher gradients of the equivalent plastic strain and damage, respectively. In contrast to integral type approaches, the finite element implementation of gradient type models is, in general, straight forward. However, the higher order displacement gradients have to be considered in higher order element shape functions.

A relation between integral type and gradient type nonlocal formulations is established by applying a Taylor series expansion of the local quantity into the corresponding integral expression for the nonlocal quantity. Assuming isotropy of the used weight function, this results into an explicit gradient type approximation, including the Laplacian of the local quantity. A detailed derivation can be found, e.g., in the work of Engelen et al. (2003). As stated above, the explicit incorporation of higher order gradients requires higher order element shape functions. Thus, further improvements have been suggested by Peerlings et al. (1996). In this work the author showed, that via mathematical manipulation of the explicit nonlocal approximation an implicit formulation, including the Laplacian of the nonlocal quantity, can be established. In case of using Green's weight function, this formulation gives the exact representation of the integral formulation as has been shown by Peerlings et al. (2001). Thus, working with the weak form of the latter result, only C^0 interpolation of the corresponding quantity is required. While the explicit gradient formulation considers the dependence on the infinitely close neighborhood,

the solution of the nonlocal field in terms of the implicit gradient formulation depends on the local quantity in the entire body. Thus, in the sense of Rogula (1982), explicit gradient type formulations are often referred to as *weakly nonlocal*, while implicit gradient type formulations are, in the sense of Geers et al. (2000), called *strongly nonlocal*.

For the development of the current non-local framework, we follow the continuum thermodynamic rate variational approach developed in Svendsen (2004), which results in particular in an implicit gradient type formulation for the thermodynamic field quantities. The dynamic thermoviscoplastic flow behavior of the material is modeled with the help of a modified form of the model of Johnson and Cook (1983) for metal thermoviscoplasticity with isotropic damage. For simplicity, attention is restricted in this work to the evolution of inelasticity due to (i) the motion of dislocations, and (ii) the deformation (dilatation / shear) of voids. As usual, the former is assumed to be initiated and driven primarily by deviatoric loading. On the other hand, the latter may in general be initiated and driven by both hydrostatic and deviatoric loading. Both (i) and (ii) are in general modeled non-locally. The current model formulation is continuum thermodynamically in nature and is summarized briefly in the following section.

4.2 Continuum thermodynamic variational framework

Let B_r be a reference configuration of the material in question with boundary ∂B_r and outward unit normal \mathbf{n}_r . In the current extended thermomechanical context, the unknown continuum fields are the deformation χ , the temperature θ , and a set $\boldsymbol{\kappa} = \{\kappa_1, \kappa_2, \dots\}$ of scalar-valued non-local fields related to dislocation-based (e.g., hardening) and defect-based (e.g., softening) processes. From the thermodynamic point of view, such processes are assumed to result in energy storage and / or energy dissipation (i.e., energy loss). For simplicity, we neglect any body forces or supply-rate densities, as well as any moving or stationary singular surfaces, in what follows.

Energy storage in the current model class is represented by the general form

$$\psi_r = \psi_r(\theta, \nabla^r \chi, \mathbf{F}_P, \boldsymbol{\kappa}, \nabla^r \boldsymbol{\kappa}) \quad (4.1)$$

of the referential free energy density in terms of the deformation gradient $\mathbf{F} = \nabla^r \chi$ and local inelastic deformation \mathbf{F}_P . The evolution of \mathbf{F}_P takes the form

$$\dot{\mathbf{F}}_P = \mathbf{F}_E^{-1} \mathbf{L}_{Pc} \mathbf{F}_E \mathbf{F}_P, \quad (4.2)$$

$$\dot{\mathbf{F}}_P = \mathbf{L}_{Pi} \mathbf{F}_P, \quad (4.3)$$

with

$$\mathbf{L}_{Pi} = \sum_a \dot{\kappa}_a \mathbf{N}_{Pia}(\theta, \nabla^r \chi, \mathbf{F}_P, \boldsymbol{\kappa}, \nabla^r \boldsymbol{\kappa}) \quad (4.4)$$

for \mathbf{L}_{Pi} linear in $\dot{\kappa}$. These yield the constitutive form¹

$$\begin{aligned} \zeta_r &= \partial_\theta \psi_r \dot{\theta} + \partial_{\nabla^r \chi} \psi_r \cdot \nabla^r \dot{\chi} \\ &+ \sum_a (\partial_{\kappa_a} \psi_r + \partial_{\mathbf{F}_P} \psi_r \mathbf{F}_P^T \cdot \mathbf{N}_{Pia}) \dot{\kappa}_a + \partial_{\nabla^r \kappa_a} \psi_r \cdot \nabla^r \dot{\kappa}_a \end{aligned} \quad (4.5)$$

¹The notation $\dot{\psi}_r$ used for ζ_r in earlier work Svendsen (2004) is unfortunately confusing at best. Indeed, as just discussed, ζ_r depends on multiple constitutive relations. Because of this, in contrast to $\dot{\psi}_r$, ζ_r is generally non-integrable.

for the energy storage rate density. Note that this density is linear in the rates $\dot{\boldsymbol{\kappa}}$ and $\nabla^r \dot{\boldsymbol{\kappa}}$ associated with inelastic processes. Kinetics-based processes, e.g., dislocation activation, however, generally depend non-linearly on such rates. Consequently, the influence of these on the material behavior is accounted for in the current formulation by a second potential, i.e., the dissipation potential

$$\chi_{\text{vr}} = \chi_{\text{vr}}(\dots, \nabla^r \theta, \dot{\boldsymbol{\kappa}}, \nabla^r \dot{\boldsymbol{\kappa}}). \quad (4.6)$$

As shown elsewhere (e.g., Svendsen, 2004), in the direct continuum thermodynamic approach corresponding to the variational one being employed here, the dissipation principle (e.g., Silhavy, 1997, Chapter 9) is satisfied sufficiently when χ_{vr} is non-negative and separately convex in its non-equilibrium arguments $\dot{\boldsymbol{\kappa}}$, $\nabla^r \dot{\boldsymbol{\kappa}}$ and $\nabla^r \theta$. In this case, the dissipation-rate density

$$\delta_r = \partial_{\nabla^r \theta} \chi_{\text{vr}} \cdot \nabla^r \theta + \sum_a \partial_{\dot{\kappa}_a} \chi_{\text{vr}} \dot{\kappa}_a + \partial_{\nabla^r \dot{\kappa}_a} \chi_{\text{vr}} \cdot \nabla^r \dot{\kappa}_a \geq \chi_{\text{vr}} \geq 0 \quad (4.7)$$

is bounded below by χ_{vr} .

With the basic constitutive relations in hand, we are now in a position to carry out the continuum thermodynamic variational formulation of the evolution-field relations of the model following Svendsen (2004). For simplicity, the following is restricted to a loading environment for the material under consideration of the generalized deformation-traction type² generalized to the current setting, i.e., applying to $(\boldsymbol{\chi}, \boldsymbol{\kappa})$. On this basis, the formulation begins with the rate functional³

$$R := \int_{B_r} r_{\text{vr}} + \int_{\partial B_r} r_{\text{sr}} \quad (4.8)$$

as based on the volume

$$r_{\text{vr}} := \zeta_r + \chi_{\text{vr}} \quad (4.9)$$

and surface r_{sr} rate densities, respectively, the latter determining the boundary flux densities

$$\begin{aligned} -\mathbf{p}_r &= \partial_{\dot{\boldsymbol{\chi}}} r_{\text{sr}}, \\ -\varphi_{ar} &= \partial_{\dot{\kappa}_a} r_{\text{sr}} \end{aligned} \quad (4.10)$$

associated with $\boldsymbol{\chi}$ and each $\kappa_a \in \boldsymbol{\kappa}$, respectively. In particular, \mathbf{p}_r represents the boundary traction vector field. For the current constitutive class, the form of r_{vr} is determined by (4.1) and (4.6). From an abstract point of view, R represents a functional on the tangent bundle of the (infinite-dimensional) manifold of all admissible fields $(\boldsymbol{\chi}, \boldsymbol{\kappa})$. The first variation of R in the rates $\dot{\boldsymbol{\chi}}$ and $\dot{\kappa}_a$ together with partial integration and the divergence theorem then yield

$$\begin{aligned} \delta R &= \int_{B_r} \delta_{\dot{\boldsymbol{\chi}}} r_{\text{vr}} \cdot \delta \dot{\boldsymbol{\chi}} + \int_{\partial B_r} (\partial_{\nabla^r \dot{\boldsymbol{\chi}}} r_{\text{vr}} \mathbf{n}_r + \partial_{\dot{\boldsymbol{\chi}}} r_{\text{sr}}) \cdot \delta \dot{\boldsymbol{\chi}} \\ &+ \int_{B_r} \sum_a \delta_{\dot{\kappa}_a} r_{\text{vr}} \delta \dot{\kappa}_a + \int_{\partial B_r} \sum_a (\partial_{\nabla^r \dot{\kappa}_a} r_{\text{vr}} \mathbf{n}_r + \partial_{\dot{\kappa}_a} r_{\text{sr}}) \delta \dot{\kappa}_a, \end{aligned} \quad (4.11)$$

where

$$\delta_x f := \partial_x f - \text{div}_r(\partial_{\nabla^r x} f) \quad (4.12)$$

²Other such environments, e.g., unilateral or bilateral contact (Silhavy, 1997, §13.3), are also possible.

³For notational simplicity, we dispense with the volume element dv and area element da notation in volume and area integrals here and in what follows.

represents the variational derivative. Stationarity of δR with respect to all $\delta \dot{\chi}$ vanishing on that part $\partial B_{r\dot{\chi}}$ of $\partial B_r = \partial B_{r\dot{\chi}} \cup \partial B_{rp}$ where $\dot{\chi}$ is specified determines the variational form

$$\begin{aligned} \delta_{\dot{\chi}} r_{vr} &= \mathbf{0} && \text{on } B_r, \\ \partial_{\nabla^r \dot{\chi}} r_{vr} \mathbf{n}_r + \partial_{\dot{\chi}} r_{sr} &= \mathbf{0} && \text{on } \partial B_{rp}, \end{aligned} \quad (4.13)$$

of the evolution-field relations and boundary conditions associated with $\dot{\chi}$. This is simply the linear momentum balance in variational form, i.e.,

$$\begin{aligned} \delta_{\dot{\chi}} r_{vr} &= -\text{div}_r(\partial_{\nabla^r \dot{\chi}} \psi_r), \\ \partial_{\nabla^r \dot{\chi}} r_{vr} \mathbf{n}_r + \partial_{\dot{\chi}} r_{sr} &= \partial_{\nabla^r \dot{\chi}} \psi_r \mathbf{n}_r - \mathbf{p}_r, \end{aligned} \quad (4.14)$$

from (4.5), (4.6), (4.9), (4.10)₁ and (4.12), again for quasi-static conditions and no body forces. In an analogous fashion, stationarity of δR with respect to all $\delta \dot{\kappa}_a$ vanishing on that part $\partial B_{r\dot{\kappa}_a}$ of $\partial B_r = \partial B_{r\dot{\kappa}_a} \cup \partial B_{r\varphi_a}$ where $\dot{\kappa}$ is specified yields the variational evolution-field relations and boundary conditions

$$\begin{aligned} \delta_{\dot{\kappa}_a} r_{vr} &= 0 && \text{on } B_r, \\ \partial_{\nabla^r \dot{\kappa}_a} r_{vr} \cdot \mathbf{n}_r + \partial_{\dot{\kappa}_a} r_{sr} &= 0 && \text{on } \partial B_{r\varphi_a}, \end{aligned} \quad (4.15)$$

associated with each $\kappa_a \in \boldsymbol{\kappa}$. The particular form of these latter relations for the purpose at hand, i.e., the modeling of non-local hardening and softening processes, is contingent on the further model development, to which we now turn.

4.3 Non-local modeling of thermo-viscoplasticity including ductile damage

The strong dependence of the deformation and failure of metals on the loading-rate and temperature during dynamic loading is accounted for by modeling the behavior as thermoelastic and thermoviscoplastic. In particular, the dynamic thermoviscoplastic flow behavior is modeled with the help of a modified form of the model of Johnson and Cook (1983) for metal thermoviscoplasticity with isotropic damage. For simplicity, attention is restricted in this work to the evolution of inelasticity due to (i) the motion / glide / climb of dislocations, and (ii) the deformation (dilatation / shear) of voids. As usual, the former is assumed to be initiated and driven primarily by deviatoric loading. On the other hand, the latter may in general be initiated and driven by both hydrostatic and deviatoric loading. In particular, we distinguish in this work between hydrostatic ($I = H$) and deviatoric ($I = D$) stress states and loading processes. Corresponding local damage processes are likewise modeled here via a local damage variable d_I ($I = H, D$). As discussed in the introduction, dynamic processes like high-speed cutting generally involve heat conduction. In particular, isotropic Fourier heat conduction is assumed here for simplicity.

In context of the continuum thermodynamic rate variational approach developed presented above, the deformation χ , the temperature θ , as well as the the non-local accumulated equivalent inelastic deformation $\bar{\alpha}_I$ and non local damage \bar{d}_I (due to, e.g., coalescence), with respect to some reference configuration B_r of the material in question, represent the fields of interest. Further, let F_p represent the inelastic local deformation, $F = \nabla^r \chi$ the total local deformation

or deformation gradient, and $\mathbf{F}_E = \mathbf{F} \mathbf{F}_P^{-1}$ the local elastic deformation. Since the model of Johnson and Cook (1983) includes local hardening effects on the inelastic flow behavior directly in the flow rule, energetic hardening is tacitly neglected. In the current non-local context, however, GND-based hardening is assumed to be energetic and lengthscale-dependent. In this case, the form of the free energy density generalizes to

$$\psi_r(\theta, \nabla^r \chi, \mathbf{F}_P, \boldsymbol{\kappa}, \nabla^r \boldsymbol{\kappa}) = \psi_{Er}(\theta, \mathbf{F}_E) + \frac{1}{2} \mu_0 \ell_{E0}^2 \det(\mathbf{F}) |\mathbf{F}^{-T} \nabla^r \bar{\alpha}_D|^2. \quad (4.16)$$

Besides the elastic part ψ_{Er} , we now have a non-local hardening contribution. The latter depends only on dislocation-process-based (i.e., deviatoric) inelasticity and the corresponding energetic lengthscale ℓ_{E0} . The specific form of the gradient part of (4.16) is chosen in analogy to the fourier type heat flux

$$\mathbf{q}_{Cr} = -\det(\mathbf{F}) \mathbf{F}^{-1} \mathbf{F}^{-T} k_0 \nabla^r \theta, \quad (4.17)$$

assumed in the following model formulation, with k_0 , the coefficient of thermal conductivity. Here, we defined

$$\mathbf{q}_{Er} := -\det(\mathbf{F}) \mathbf{F}^{-1} \mathbf{F}^{-T} \ell_{E0}^2 \nabla^r \bar{\alpha}_D = -\mu_0^{-1} \partial_{\nabla^r \bar{\alpha}_D} \psi_r. \quad (4.18)$$

This in turn determines the thermoelastic forms

$$\begin{aligned} \mathbf{K} &= \partial_{\mathbf{F}} \psi_r \mathbf{F}^T = \partial_{\mathbf{F}_E} \psi_{Er} \mathbf{F}_E^T, \\ -\eta_r &= \partial_{\theta} \psi_r = \partial_{\theta} \psi_{Er}, \end{aligned} \quad (4.19)$$

for the Kirchhoff stress \mathbf{K} and the referential entropy density η_r .

Besides isotropy, attention is restricted here to metals and to small elastic strain. In this case, the elastic left logarithmic stretch $\ln \mathbf{V}_E = \frac{1}{2} \ln(\mathbf{B}_E)$ becomes relevant. $\mathbf{B}_E = \mathbf{F}_E \mathbf{F}_E^T = \mathbf{F} \mathbf{C}_P^{-1} \mathbf{F}^T$ is the elastic left Cauchy-Green deformation, and $\mathbf{C}_P = \mathbf{F}_P^T \mathbf{F}_P$ is the plastic right Cauchy-Green deformation. Besides isotropy, we assume that the heat capacity of the material is approximately constant. The process of energy storage in the material can then be modeled by the thermoelastic Hooke form

$$\begin{aligned} \psi_{Er}(\theta, \mathbf{F}_E) &= \psi_{El}(\theta, l_H, l_D) \\ &= \frac{1}{2} \kappa_0 l_H^2 + \mu_0 l_D^2 + 3 \kappa_0 \alpha_0 (\theta_0 - \theta) l_H \\ &\quad + c_0 \{ \theta - \theta_0 - \theta \ln(\theta/\theta_0) \} \end{aligned} \quad (4.20)$$

at small elastic strain. In this relation, $\kappa_0 := \lambda_0 + \frac{2}{3} \mu_0$ represents the elastic bulk modulus, λ_0 and μ_0 are the elastic longitudinal and shear moduli, respectively, α_0 is the thermal expansion, and c_0 represents the heat capacity. All of these material properties are at the reference temperature θ_0 , θ being the absolute temperature. Further,

$$\begin{aligned} l_H &:= \text{tr}(\ln \mathbf{V}_E), \\ l_D &:= \text{tr}(\text{dev}(\ln \mathbf{V}_E)^2)^{1/2}, \end{aligned} \quad (4.21)$$

represent the first invariant of $\ln \mathbf{V}_E$, and minus twice the second invariant of $\text{dev}(\ln \mathbf{V}_E)$, respectively. The relations (4.20) and (4.21) determine in particular the form

$$\mathbf{K} = (\partial_{\mathbf{F}_E} \psi_{Er}) \mathbf{F}_E^T = \partial_{\ln \mathbf{V}_E} \psi_{El} = k_H \mathbf{I} + k_D \text{dir}(\text{dev}(\ln \mathbf{V}_E)) \quad (4.22)$$

of the Kirchhoff stress \mathbf{K} , with

$$\begin{aligned} k_{\text{H}} &:= \frac{1}{3} \text{tr}(\mathbf{K}) , \\ k_{\text{D}} &:= \text{tr}(\text{dev}(\mathbf{K})^2)^{1/2} , \end{aligned} \quad (4.23)$$

the hydrostatic part and deviatoric magnitude, respectively, of \mathbf{K} . Here, $\text{tr}(\mathbf{A}) := \mathbf{I} \cdot \mathbf{A}$, $\text{dev}(\mathbf{A}) := \mathbf{A} - \frac{1}{3} \text{tr}(\mathbf{A}) \mathbf{I}$, $\text{mag}(\mathbf{A}) := \text{tr}(\mathbf{A}^T \mathbf{A})^{1/2}$ and $\text{dir}(\mathbf{A}) := \partial_{\mathbf{A}} \text{mag}(\mathbf{A}) = \mathbf{A} / \text{mag}(\mathbf{A})$ represent the trace, deviatoric part, magnitude, and direction, respectively, of any second-order tensor \mathbf{A} . Note that

$$\begin{aligned} k_{\text{H}} &= \partial_{l_{\text{H}}} \psi_{\text{El}} = \kappa_0 \{l_{\text{H}} + 3\alpha_0(\theta_0 - \theta)\} , \\ k_{\text{D}} &= \partial_{l_{\text{D}}} \psi_{\text{El}} = 2\mu_0 l_{\text{D}} , \end{aligned} \quad (4.24)$$

via (4.23). On this basis, then, in the context of the model class defined by (4.20), then, the pairs $(k_{\text{H}}, l_{\text{H}})$ and $(k_{\text{D}}, l_{\text{D}})$ are natural thermodynamic conjugates. In what follows, we will also work with the von Mises equivalent stress

$$k_{\text{M}} := \sqrt{\frac{3}{2}} k_{\text{D}} \quad (4.25)$$

determined by k_{D} .

Consider next the inelastic constitutive relations. Following standard metal plasticity, assume that dislocation glide is driven by deviatoric stress k_{D} alone. On the other hand, for dynamic shear processes such as machining and cutting, assume that microvoid development is driven by both hydrostatic k_{H} and deviatoric k_{D} stress. Furthermore, under the assumption that (at least) the respective initiation processes are (at least partly) distinct, accumulated inelastic deformation α_{D} driven by deviatoric loading is assumed distinct from that α_{H} due to hydrostatic loading. In particular, these considerations bear on the constitutive form of the inelastic “velocity gradient”

$$\begin{aligned} \mathbf{L}_{\text{Pi}} &:= \dot{\mathbf{F}}_{\text{P}} \mathbf{F}_{\text{P}}^{-1} , \\ \mathbf{L}_{\text{Pc}} &:= \mathbf{F}_{\text{E}} \mathbf{L}_{\text{Pi}} \mathbf{F}_{\text{E}}^{-1} . \end{aligned} \quad (4.26)$$

On this basis, we work with the constitutive forms

$$\begin{aligned} \text{tr}(\mathbf{L}_{\text{Pc}}) &= \dot{\alpha}_{\text{H}} n_{\text{H}} , \\ \text{dev}(\mathbf{L}_{\text{Pc}}) &= \dot{\alpha}_{\text{D}} \mathbf{N}_{\text{D}} , \end{aligned} \quad (4.27)$$

for \mathbf{L}_{Pc} in terms of the respective directions

$$\begin{aligned} n_{\text{H}} &= \partial_{k_{\text{H}}} \phi_{\text{Hr}} , \\ \mathbf{N}_{\text{D}} &= \partial_{k_{\text{D}}} \phi_{\text{Dr}} \text{dev}(\partial_{\mathbf{K}} k_{\text{D}}) , \end{aligned} \quad (4.28)$$

and inelastic potentials

$$\begin{aligned} \phi_{\text{H}}(\dots, k_{\text{H}}, k_{\text{D}}) &= k_{\text{H}} = \frac{1}{3} \text{tr}(\mathbf{K}) , \\ \phi_{\text{D}}(\dots, k_{\text{H}}, k_{\text{D}}) &= k_{\text{M}} = \sqrt{\frac{3}{2}} k_{\text{D}} = \sqrt{\frac{3}{2}} \text{mag}(\text{dev}(\mathbf{K})) , \end{aligned} \quad (4.29)$$

given in the simplest possible case by the hydrostatic stress and von Mises equivalent stress, respectively, both with respect to \mathbf{K} . As implied by the dependence of ϕ_{H} on k_{H} , both positive and negative hydrostatic stresses are relevant here, related for example to void growth and closure or healing, respectively. In particular, the above formulations determine

$$\mathbf{L}_{\text{Pc}} = \dot{\alpha}_{\text{H}} \frac{1}{3} \mathbf{I} + \dot{\alpha}_{\text{D}} \sqrt{\frac{3}{2}} \text{dir}(\text{dev}(\mathbf{K})) . \quad (4.30)$$

Then

$$\begin{aligned}\zeta_r &= \partial_\theta \psi_r \dot{\theta} + \partial_{\nabla^r \chi} \psi_r \cdot \nabla^r \dot{\chi} \\ &- \sigma_D \dot{\bar{\alpha}}_D - \sigma_H \dot{\bar{\alpha}}_H + \partial_{\nabla^r \bar{\alpha}_D} \psi_r \cdot \nabla^r \dot{\bar{\alpha}}_D\end{aligned}\quad (4.31)$$

follows for the energy storage rate density via (4.30) and (4.5), in terms of the thermodynamic conjugate

$$\begin{aligned}\sigma_D &:= \mathbf{K} \cdot \partial_{\mathbf{K}} \phi_{Dr} = k_M \\ \sigma_H &:= \mathbf{K} \cdot \partial_{\mathbf{K}} \phi_{Hr} = k_H\end{aligned}\quad (4.32)$$

to $\bar{\alpha}_I$ for $I = D, H$.

Assume that both dilatation (i.e., void growth) and deviatoric (i.e., shear banding) loading drive damage development under dynamic conditions. In this context, consider the saturation form

$$\dot{d}_I = r_I \langle \bar{\alpha}_I - \alpha_{Id} \rangle (s_I - \bar{d}_I) \dot{\bar{\alpha}}_I \quad (4.33)$$

of the local damage production for $I = D, H$. These relations depend on the initial amount $\bar{d}_{I0} := \bar{d}_I(\bar{\alpha}_I = 0)$ of microcracks / microvoids, the saturation rates r_I , the saturation values s_I , the critical accumulated inelastic shear deformation $\bar{\alpha}_{Id}$ for damage activation. Although, the above form for the evolution of the local d_I in terms of $\bar{\alpha}_I$ makes the failure process non-local in general, the detailed determination of the specific effects, causing non-local interaction, is still work in progress. Thus, we can generally assume an additional non-local development of the different populations of damage d_I , with the development of the corresponding non-local quantities \bar{d}_I , driven by the d_I . A specific relation for the \bar{d}_I will be developed below. For the moment, just recognize, that \bar{d}_I is a quantity, representing macroscopically detected softening due to microstructural development (voids, defects etc.). The constitutive relations, determining the influence of this damage quantities (voids, defects etc.) on the thermodynamic stresses σ_I , are derived in a framework, motivated from the concept of homogenization. Without going so far as to formulate and solve the corresponding homogenization and boundary-value problem for an RVE, which represents work in progress, consider now a possible framework as based on the effective microscopic stress

$$\sigma_{Im} := \sigma_I / f_I(\bar{d}). \quad (4.34)$$

Here, the function $f_I(\bar{d})$ determines how the specific microstructure (e.g. voids, defects etc.) transforms effective microscopic stresses σ_{Im} (e.g., in the matrix) in a model-dependent, phenomenological, effective fashion to the macroscopic one σ_I . For simplicity we work with the mixed quantity \bar{d} instead of working with \bar{d}_H and \bar{d}_D , separately. Here, we simply assume

$$\dot{\bar{d}} := \dot{\bar{d}}_H + \dot{\bar{d}}_D. \quad (4.35)$$

Further, we define the undamaged state for $\bar{d} = 0$ and the totally damaged state for $\bar{d} = 1$. Consistently, we work with

$$\dot{d}_I = r_I \langle \bar{\alpha}_I - \alpha_{Id} \rangle (s_I - \bar{d}) \dot{\bar{\alpha}}_I, \quad (4.36)$$

instead of (4.33). Since we have assumed plastic incompressibility for the undamaged material, it makes sense to assume an infinite hydrostatic activation stress for the undamaged material and zero activation stresses for the totally damaged state. These assumptions imply $f_D(\bar{d} = 0) = 1$,

$f_H(\bar{d} = 0) = \infty$ and $f_D(\bar{d} = 1) = 0$. Again, lacking further information on the specific form of $f_I(\bar{d})$ for the moment, we work with the simple relations

$$f_D(\bar{d}) = (1 - \bar{d}) \quad (4.37)$$

and

$$f_H(\bar{d}) = D_1 (1 - \bar{d})/\bar{d}^{D_2} \quad (4.38)$$

for these functions satisfying the given requirements. In any case, note that $f_I(\bar{d})$ transforms the microscopic stress σ_{Im} into the macroscopic stress states represented by $\sigma_H = k_H$ and $\sigma_D = k_M$, respectively. This issue becomes relevant again, when specifying the constitutive relation for the σ_I . Keeping this in mind, we now discuss the non-local description of the relevant thermodynamic quantities.

In the current non-local context, the activation of dislocation motion and of defect-based processes is dissipative and assumed to be lengthscale-dependent. Further, defect development is assumed to be purely dissipative (i.e, result in energy loss). Thus, in terms of the extended thermomechanical framework presented above, we have $\boldsymbol{\kappa} := (\bar{\alpha}_D, \bar{\alpha}_H, \bar{d})$, the corresponding field quantities of the accumulated devatoric and spherical plastic deformation, as well as an additional scalar valued softening quantity, henceforth referred to as damage. These imply the form

$$\begin{aligned} \chi_r(\dots, \dot{\bar{\alpha}}_D, \dot{\bar{\alpha}}_H, \nabla^r \dot{\bar{\alpha}}_D, \nabla^r \dot{\bar{\alpha}}_H, \nabla^r \theta) \\ = \chi_{\text{Dr}}(\dots, \dot{\bar{\alpha}}_D, \nabla^r \dot{\bar{\alpha}}_D) + \chi_{\text{Hr}}(\dots, \dot{\bar{\alpha}}_H, \nabla^r \dot{\bar{\alpha}}_H) + \chi_{\text{d}}(\dots, \dot{\bar{d}}, \nabla^r \dot{\bar{d}}) + \chi_{\text{Cr}}(\dots, \nabla^r \theta) \end{aligned} \quad (4.39)$$

of (4.6), embodying the dependence of the activation of non-local inelastic deformation and non-local failure on kinetics-controlled processes which are dissipative. Here,

$$\begin{aligned} \chi_{\text{Ir}}(\dots, \dot{\bar{\alpha}}_I, \nabla^r \dot{\bar{\alpha}}_I) &= \chi_{\text{Irl}}(\dots, \dot{\bar{\alpha}}_I) + \frac{1}{2} \chi_{\text{I}0} \ell_{\text{I}0}^2 \det(\mathbf{F}) |\mathbf{F}^{-\text{T}} \nabla^r \dot{\bar{\alpha}}_I|^2, \\ \chi_{\text{dr}}(\dots, \dot{\bar{d}}, \nabla^r \dot{\bar{d}}) &= \frac{1}{2} \chi_{\text{d}0} (\dot{\bar{d}} - \dot{\bar{d}}_D - \dot{\bar{d}}_H)^2 + \frac{1}{2} \chi_{\text{d}0} \ell_{\text{d}0}^2 \det(\mathbf{F}) |\mathbf{F}^{-\text{T}} \nabla^r \dot{\bar{d}}|^2, \\ \chi_{\text{Cr}}(\dots, \nabla^r \theta) &= \frac{1}{2} \theta^{-1} k_0 \det(\mathbf{F}) |\mathbf{F}^{-\text{T}} \nabla^r \theta|^2, \end{aligned} \quad (4.40)$$

for $I = D, H$. Again, choosing a form analogous to the potential, which defines the fourier type heat flux

$$\mathbf{q}_{\text{Cr}} = -\det(\mathbf{F}) \mathbf{F}^{-1} \mathbf{F}^{-\text{T}} k_0 \nabla^r \theta = -\theta \partial_{\nabla^r \theta} \chi_r \quad (4.41)$$

we defined

$$\begin{aligned} \mathbf{q}_{\text{Ir}} &:= -\det(\mathbf{F}) \mathbf{F}^{-1} \mathbf{F}^{-\text{T}} \ell_{\text{I}0}^2 \nabla^r \dot{\bar{\alpha}}_I = -\chi_{\text{I}0}^{-1} \partial_{\nabla^r \dot{\bar{\alpha}}_I} \chi_r, \\ \mathbf{q}_{\text{dr}} &:= -\det(\mathbf{F}) \mathbf{F}^{-1} \mathbf{F}^{-\text{T}} \ell_{\text{d}0}^2 \nabla^r \dot{\bar{d}} = -\chi_{\text{d}0}^{-1} \partial_{\nabla^r \dot{\bar{d}}} \chi_r \end{aligned} \quad (4.42)$$

The damage terms in (4.40) are analogous to the models for non-local ductile damage developed by Reusch et al. (2008, 2003). Here, $\chi_{\text{I}0}$, $I = D, H$, $\chi_{\text{d}0}$, represent characteristic dissipation levels associated with the nucleation and activation of dislocation and damage processes, respectively. Further, $\ell_{\text{I}0}$, $I = D, H$, $\ell_{\text{d}0}$ are the corresponding characteristic material lengthscales associated with the nucleation and activation of these as non-local processes. In addition, k_0 is the coefficient of thermal conductivity. Specialising the variational approach Svendsen (2004)

to the specific forms for ζ_r (4.31) and χ_r (4.40), one derives in particular the forms

$$\begin{aligned}
\delta_{\dot{\alpha}_D} r_{vr} &= \partial_{\dot{\alpha}_D} \chi_{Dr} - \bar{\sigma}_D + \chi_{D0} \operatorname{div}_r(\mathbf{q}_{Dr}), \\
\partial_{\nabla^r \dot{\alpha}_D} r_{vr} \cdot \mathbf{n}_r + \partial_{\dot{\alpha}_D} r_{sr} &= -\mu_0 \mathbf{q}_{Er} \cdot \mathbf{n}_r - \chi_{D0} \mathbf{q}_{Dr} \dot{\alpha}_D \cdot \mathbf{n}_r + \partial_{\dot{\alpha}_D} r_{sr}, \\
\delta_{\dot{\alpha}_H} r_{vr} &= \partial_{\dot{\alpha}_H} \chi_{Dr} - \bar{\sigma}_H + \chi_{H0} \operatorname{div}_r(\mathbf{q}_{Hr}), \\
\partial_{\nabla^r \dot{\alpha}_H} r_{vr} \cdot \mathbf{n}_r + \partial_{\dot{\alpha}_H} r_{sr} &= -\chi_{H0} \mathbf{q}_{Hr} \cdot \mathbf{n}_r + \partial_{\dot{\alpha}_H} r_{sr}, \\
\delta_{\dot{d}} r_{vr} &= \partial_{\dot{d}} \chi_{dr} + \chi_{d0} \operatorname{div}_r(\mathbf{q}_{dr}), \\
\partial_{\nabla^r \dot{d}} r_{vr} \cdot \mathbf{n}_r + \partial_{\dot{d}} r_{sr} &= -\chi_{d0} \mathbf{q}_{dr} \cdot \mathbf{n}_r + \partial_{\dot{d}} r_{sr},
\end{aligned} \tag{4.43}$$

from (4.15) for $\bar{\alpha}_I \in \boldsymbol{\kappa}$, $I = D, H$ via (4.32), (4.18) and (4.42), with

$$\begin{aligned}
\bar{\sigma}_D &:= -\partial_{\dot{\alpha}_D} \zeta_r + \operatorname{div}_r(\partial_{\nabla^r \dot{\alpha}_D} \zeta_r) = k_M - \mu_0 \operatorname{div}_r(\mathbf{q}_{Er}), \\
\bar{\sigma}_H &:= -\partial_{\dot{\alpha}_H} \zeta_r + \operatorname{div}_r(\partial_{\nabla^r \dot{\alpha}_H} \zeta_r) = k_H
\end{aligned} \tag{4.44}$$

from (4.32) and (4.31). Then

$$\begin{aligned}
\bar{\sigma}_D &= \partial_{\dot{\alpha}_D} \chi_{Dr} + \chi_{D0} \operatorname{div}_r(\mathbf{q}_{Dr}), \\
\mu_0 \mathbf{q}_{Er} \cdot \mathbf{n}_r + \chi_{D0} \mathbf{q}_{Dr} \cdot \mathbf{n}_r &= 0, \\
\bar{\sigma}_H &= \partial_{\dot{\alpha}_H} \chi_{Dr} + \chi_{H0} \operatorname{div}_r(\mathbf{q}_{Hr}), \\
\chi_{H0} \mathbf{q}_{Hr} \cdot \mathbf{n}_r &= 0, \\
0 &= \partial_{\dot{d}} \chi_{dr} + \chi_{d0} \operatorname{div}_r(\mathbf{q}_{dr}), \\
\chi_{d0} \mathbf{q}_{dr} \cdot \mathbf{n}_r &= 0,
\end{aligned} \tag{4.45}$$

follow for the case of zero-flux boundary conditions $\partial_{\dot{\alpha}_I} r_{sr} = 0$, $I = D, H$ and $\partial_{\dot{d}} r_{sr} = 0$. Via generalized Legendre transformation, note that (4.45)_{1,3,6} can be expressed in the conjugate forms

$$\begin{aligned}
\partial_{\bar{\sigma}_D} \varphi_{Dr} &= \dot{\alpha}_D + \operatorname{div}_r(\mathbf{q}_{Dr}), \\
\partial_{\bar{\sigma}_H} \varphi_{Hr} &= \dot{\alpha}_H + \operatorname{div}_r(\mathbf{q}_{Hr}), \\
\dot{d}_D + \dot{d}_H &= \dot{d} + \operatorname{div}_r(\mathbf{q}_{dr}).
\end{aligned} \tag{4.46}$$

In the limits $\ell_{E0} \rightarrow 0$ and $\ell_{D0} \rightarrow 0$, note that the non-local relation (4.45)₁, (4.46)₁ reduces to the analogous local relation $\bar{\sigma}_D \rightarrow \sigma_D$, $\bar{\alpha}_D \rightarrow \alpha_D$. Likewise, as $\ell_{H0} \rightarrow 0$, (4.45)₂, (4.46)₁ reduces to $\bar{\sigma}_H \rightarrow \sigma_H$, $\dot{\alpha}_H \rightarrow \dot{\alpha}_H$. Analogously, as $\ell_{d0} \rightarrow 0$, the non-local relation (4.46)₃ reduces to the local relation $\dot{d} \rightarrow \dot{d}$. The current thermomechanical model formulation is completed by an evolution-field relation for the temperature. This is derived here from the Clausius-Duhem dissipation balance

$$\theta \dot{\eta}_r = \delta_r - \partial_{\nabla^r \theta} \chi_r \cdot \nabla^r \theta + \operatorname{div}_r(\theta \partial_{\nabla^r \theta} \chi_r) \tag{4.47}$$

assuming no external supplies. Using (4.20), (4.7), (4.16), (4.41), this reduces to

$$c_0 \dot{\theta} = \omega_r - \operatorname{div}_r(\mathbf{q}_{Cr}), \tag{4.48}$$

in terms of the volumetric rate of heating

$$\begin{aligned}
\omega_r &:= \sum_a (\partial_{\dot{\kappa}_a} \chi_r - \mathbf{K}_\eta \cdot \mathbf{N}_{Pc_a} - \theta \partial_{\kappa_a} \eta_r) \dot{\kappa}_a \\
&+ \sum_a (\partial_{\nabla^r \dot{\kappa}_a} \chi_r - \theta \partial_{\nabla^r \kappa_a} \eta_r) \cdot \nabla^r \dot{\kappa}_a \\
&+ \mathbf{K}_\eta \mathbf{F}^{-T} \cdot \dot{\mathbf{F}}
\end{aligned} \tag{4.49}$$

for the current non-local class, with

$$\mathbf{K}_\eta := -\theta \partial_{\mathbf{F}} \eta_r \mathbf{F}^T \quad (4.50)$$

the entropic part of the Kirchhoff stress. Further, having

$$-\partial_{\mathbf{F}} \eta_r = \partial_\theta \mathbf{K} \mathbf{F}^{-T} \quad (4.51)$$

the volumetric rate of heating can be rewritten as

$$\begin{aligned} \omega_r &:= \sum_a (\partial_{\dot{\kappa}_a} \chi_r - \theta \partial_{\kappa_a} \eta_r) \dot{\kappa}_a \\ &+ \sum_a (\partial_{\nabla^r \dot{\kappa}_a} \chi_r - \theta \partial_{\nabla^r \kappa_a} \eta_r) \cdot \nabla^r \dot{\kappa}_a \\ &+ \theta \partial_\theta \partial_{\ln \mathbf{V}_E} \psi_{Er} \mathbf{F}_E^{-T} \cdot \dot{\mathbf{F}}_E \\ &= \omega_{Pr} + \theta \partial_\theta \partial_{\ln \mathbf{V}_E} \psi_{Er} \mathbf{F}_E^{-T} \cdot \dot{\mathbf{F}}_E \end{aligned} \quad (4.52)$$

In order to simplify the algorithmic implementation, neglect the effect of elastic heating and approximate the plastic part of the rate of volumetric heating by the Taylor-Quinney form

$$\omega_{Pr} \approx \beta_0 k_M \dot{\bar{\alpha}}_D, \quad (4.53)$$

in terms of the Taylor-Quinney coefficient $0 < \beta_0 < 1$ and thus, consider only deviatoric deformation. Then, the evolution-field relation for the temperature is given by

$$c_0 \dot{\theta} = \beta_0 k_M \dot{\bar{\alpha}}_D - \operatorname{div}_r(\mathbf{q}_{Cr}). \quad (4.54)$$

Our model formulation is summarized as follows. Additionally to the linear momentum balance

$$-\operatorname{div}_r(\partial_{\nabla^r \chi} \psi_r) = 0, \quad (4.55)$$

we have the evolution-field equations

$$\begin{aligned} \dot{\alpha}_I &= \dot{\bar{\alpha}}_I + \operatorname{div}_r(\mathbf{q}_{Ir}), \\ \dot{d}_D + \dot{d}_H &= \dot{\bar{d}} + \operatorname{div}_r(\mathbf{q}_{dr}), \\ \omega_r &= c_0 \dot{\theta} + \operatorname{div}_r(\mathbf{q}_{Cr}), \end{aligned} \quad (4.56)$$

namely for the accumulated inelastic deformation $\bar{\alpha}_I$, for the damage \bar{d} and for the temperature θ , all defined on B_r . Here, the local source terms for the evolution of damage \bar{d} and temperature θ are calculated as

$$\begin{aligned} \dot{\bar{d}} &= r_I \langle \bar{\alpha}_I - \alpha_{Id} \rangle (s_I - \bar{d}) \dot{\bar{\alpha}}_I, \\ \omega_r &= \beta_0 k_M \dot{\bar{\alpha}}_D. \end{aligned} \quad (4.57)$$

Instead of

$$\dot{\alpha}_I = \partial_{\bar{\sigma}_I} \varphi_{Ir}, \quad (4.58)$$

we can also work with the implicit, conjugate form

$$\bar{\sigma}_I = \partial_{\dot{\alpha}_I} \chi_{Ir}, \quad (4.59)$$

$I = D, H$, with

$$\begin{aligned} \bar{\sigma}_D &= k_M + \mu_0 \ell_{E0}^2 \operatorname{div}_r(\nabla^r \bar{\alpha}_D), \\ \bar{\sigma}_H &= k_H \end{aligned} \quad (4.60)$$

and χ_{Ir} , providing the constitutive relation between $\bar{\sigma}_{\text{I}}$ and $\dot{\alpha}_{\text{I}}$. In this context, the issue of the above discussed microscopic stresses σ_{I} , becomes relevant again. Recalling relation (4.34) and assuming the same relation for the non-local thermodynamic stresses $\bar{\sigma}_{\text{I}}$, we can identify

$$\bar{\sigma}_{\text{I}} = \partial_{\dot{\alpha}_{\text{I}}} \chi_{\text{Ir}} = f_{\text{I}}(\bar{d}) \partial_{\dot{\alpha}_{\text{I}}} \chi_{\text{Im}} , \quad (4.61)$$

$\text{I} = \text{D, H}$, with χ_{Im} , providing the constitutive relation between $\bar{\sigma}_{\text{I}}$ and $\dot{\alpha}_{\text{I}}$ for $f_{\text{I}} = 1$. Neglecting any coupling between α_{D} and α_{H} for the moment, we choose the form

$$\begin{aligned} \chi_{\text{Im}}(\dots, \dot{\alpha}_{\text{I}}) &= (1 - c_{\text{jc}}) \sigma_{\text{A}} |\dot{\alpha}_{\text{I}}| \\ &+ c_{\text{jc}} \sigma_{\text{A}} \dot{\alpha}_{\text{P0}} (1 + |\dot{\alpha}_{\text{I}}|/\dot{\alpha}_{\text{P0}}) \ln(1 + |\dot{\alpha}_{\text{I}}|/\dot{\alpha}_{\text{P0}}) , \end{aligned} \quad (4.62)$$

for the microscopic dissipation potential, consistent with the Johnson-Cook model Johnson and Cook (1985) for dynamic viscoplastic deformation at the microlevel. In this particular form both, positive and negative hydrostatic stresses are considered. This latter form depends in particular on the activation stress

$$\sigma_{\text{A}}(\theta, \bar{\alpha}_{\text{D}}) := \{1 - [(\theta - \theta_0)/(\theta_{\text{m0}} - \theta_0)]^{m_{\text{jc}}}\} \{a_{\text{jc}} + b_{\text{jc}} (1 - e^{-n_{\text{jc}} \bar{\alpha}_{\text{D}}})\} , \quad (4.63)$$

for inelastic deformation at zero inelastic strain-rate modeled in saturation-Voce form. In this form we only consider deviatoric deformation, relevant to induce hardening effects. σ_{A} is determined by its initial value a_{jc} , the hardening parameters b_{jc} and n_{jc} , as well as the melting temperature θ_{m0} and thermal softening exponent m_{jc} . In particular, note that the decrease of $\sigma_{\text{A}}(\theta, \alpha_{\text{I}})$ with increasing temperature represents the effect of thermal softening in the current model. For this specific choice, note, that (4.61) is satisfied by the specific form

$$\begin{aligned} \chi_{\text{Ir}}(\dots, \dot{\alpha}_{\text{I}}) &= (1 - c_{\text{jc}}) \sigma_{\text{Am}} |\dot{\alpha}_{\text{I}}| \\ &+ c_{\text{jc}} \sigma_{\text{Am}} \dot{\alpha}_{\text{P0}} (1 + |\dot{\alpha}_{\text{I}}|/\dot{\alpha}_{\text{P0}}) \ln(1 + |\dot{\alpha}_{\text{I}}|/\dot{\alpha}_{\text{P0}}) , \end{aligned} \quad (4.64)$$

and

$$\sigma_{\text{Am}}(\theta, \bar{\alpha}_{\text{D}}) := f_{\text{I}}(\bar{d}) \{1 - [(\theta - \theta_0)/(\theta_{\text{m0}} - \theta_0)]^{m_{\text{jc}}}\} \{a_{\text{jc}} + b_{\text{jc}} (1 - e^{-n_{\text{jc}} \bar{\alpha}_{\text{D}}})\} . \quad (4.65)$$

Algorithmically equivalent to (4.61), but avoiding the calculation of the signum of $\dot{\alpha}_i$ we work with

$$|\bar{\sigma}_{\text{I}}| = f_{\text{I}}(\bar{d}) \partial_{|\dot{\alpha}_{\text{I}}|} \chi_{\text{Im}} , \quad (4.66)$$

instead of (4.61), in what follows.

With these relations at hand, our model formulation is complete and we now turn to its algorithmic implementation.

4.4 Algorithmic implementation of non-local thermo-viscoplasticity including ductile damage

Consider next the algorithmic formulation of the above model relations. To this end, consider first the time integration of (4.26) over a time interval $[t_n, t_{n+1}]$ of duration $t_{n+1, n} := t_{n+1} - t_n$.

Exponential backward-Euler integration of this relation over this interval together with the use of $\mathbf{F} = \mathbf{F}_E \mathbf{F}_P$ and the properties of the exponential map yields the general algorithmic form

$$\exp(\mathbf{A}_{Pc_{n+1},n}) \mathbf{F}_{E_{n+1}} = \mathbf{F}_{E_{n+1}}^{\text{tr}} \quad (4.67)$$

for $\mathbf{F}_{E_{n+1}}$. Here,

$$\begin{aligned} \mathbf{A}_{Pc_{n+1},n} &:= t_{n+1,n} \mathbf{L}_{Pc_{n+1}} \\ &= \frac{1}{3} \bar{\alpha}_{H_{n+1},n} n_{H_{n+1}} \mathbf{I} + \bar{\alpha}_{D_{n+1},n} \mathbf{N}_{D_{n+1}} \end{aligned} \quad (4.68)$$

follows from (4.30) in the backward-Euler context, with

$$\bar{\alpha}_{H,D_{n+1},n} := \bar{\alpha}_{H,D_{n+1}} - \bar{\alpha}_{H,D_n}, \quad (4.69)$$

and

$$\mathbf{F}_{E_{n+1}}^{\text{tr}} := \mathbf{F}_{n+1} \mathbf{F}_{P_n}^{-1} = \mathbf{F}_{n+1,n} \mathbf{F}_{E_n} \quad (4.70)$$

is the so-called trial value of $\mathbf{F}_{E_{n+1}}$.

Since (4.22), (4.30) and (4.68) imply that $\mathbf{A}_{Pc_{n+1},n}$ and $\ln \mathbf{V}_{E_{n+1}}$ commute, the relation

$$\exp(\mathbf{A}_{Pc_{n+1},n}) \mathbf{B}_{E_{n+1}} \exp(\mathbf{A}_{Pc_{n+1},n})^T = \mathbf{B}_{E_{n+1}}^{\text{tr}} \quad (4.71)$$

for $\mathbf{B}_{E_{n+1}}$ from (4.67) reduces to

$$\begin{aligned} \exp(2 \ln \mathbf{V}_{E_{n+1}}^{\text{tr}}) &= \exp(\mathbf{A}_{Pc_{n+1},n}) \exp(2 \ln \mathbf{V}_{E_{n+1}}) \exp(\mathbf{A}_{Pc_{n+1},n})^T \\ &= \exp(\mathbf{A}_{Pc_{n+1},n} + \mathbf{A}_{Pc_{n+1},n}^T + 2 \ln \mathbf{V}_{E_{n+1}}) \end{aligned} \quad (4.72)$$

via $\mathbf{B}_E = \exp(2 \ln \mathbf{V}_E)$, where

$$\ln \mathbf{V}_{E_{n+1}}^{\text{tr}} = \frac{1}{2} \ln(\mathbf{F}_{n+1} \mathbf{C}_{P_n}^{-1} \mathbf{F}_{n+1}^T) = \frac{1}{2} \ln(\mathbf{F}_{n+1,n} \mathbf{B}_{E_n} \mathbf{F}_{n+1,n}^T) \quad (4.73)$$

represents the trial value of $\ln \mathbf{V}_{E_{n+1}} = \frac{1}{2} \ln \mathbf{B}_{E_{n+1}}$. Taking the logarithm of both sides of (4.72) then yields

$$\ln \mathbf{V}_{E_{n+1}}^{\text{tr}} = \ln \mathbf{V}_{E_{n+1}} + \frac{1}{3} \bar{\alpha}_{H_{n+1},n} n_{H_{n+1}} \mathbf{I} + \bar{\alpha}_{D_{n+1},n} \mathbf{N}_{D_{n+1}} \quad (4.74)$$

via (4.68). From this, we have the updates

$$\begin{aligned} l_{H_{n+1}} &= l_{H_{n+1}}^{\text{tr}} - n_{H_{n+1}} \bar{\alpha}_{H_{n+1},n}, \\ l_{D_{n+1}} &= l_{D_{n+1}}^{\text{tr}} - \text{mag}(\mathbf{N}_{D_{n+1}}) \bar{\alpha}_{D_{n+1},n}, \end{aligned} \quad (4.75)$$

from (4.21), those

$$\begin{aligned} k_{H_{n+1}} &= \kappa_0 \{ l_{H_{n+1}}^{\text{tr}} + 3 \alpha_0 (\theta_0 - \theta_{n+1}) - n_{H_{n+1}} \bar{\alpha}_{H_{n+1},n} \}, \\ k_{D_{n+1}} &= 2 \mu_0 \{ l_{D_{n+1}}^{\text{tr}} - \text{mag}(\mathbf{N}_{D_{n+1}}) \bar{\alpha}_{D_{n+1},n} \}, \\ \text{dir}(\text{dev}(\mathbf{K}_{n+1})) &= \text{dir}(\text{dev}(\ln \mathbf{V}_{E_{n+1}}^{\text{tr}})), \end{aligned} \quad (4.76)$$

via (4.23), and so that

$$\mathbf{K}_{n+1} = k_{H_{n+1}} \mathbf{I} + k_{D_{n+1}} \text{dir}(\text{dev}(\ln \mathbf{V}_{E_{n+1}}^{\text{tr}})) \quad (4.77)$$

for the Kirchhoff stress from (4.22). Next, we turn to the calculation of the corresponding source terms, driving the evolution of the accumulated inelastic deformation $\bar{\alpha}_I$, the damage \bar{d}

and the temperature θ . Neglecting the effect of energetic hardening ($\ell_{E0} \rightarrow 0$), the combination of (4.66) with (4.60) and (4.25) together with (4.28) and (4.29) results in the local algorithmic system

$$\mathbf{r}(\boldsymbol{\epsilon}_{n+1}, \ln \mathbf{V}_{E n+1}^{\text{tr}}, \mathbf{d}_{n+1}, \mathbf{d}_{n+1}^{\text{a}}) = \begin{cases} |l_{H n+1}^{\text{tr}}| \kappa_0 \{l_{H n+1}^{\text{tr}} + 3\alpha_0(\theta_0 - \theta_{n+1}) - \bar{\alpha}_{H n+1, n}\} \\ \quad - f_H(\bar{d}) \partial_{|\dot{\alpha}_H|} \chi_{Hm}(\boldsymbol{\epsilon}_{n+1}, \mathbf{d}_{n+1}, \mathbf{d}_{n+1}^{\text{a}}) \\ \sqrt{6} \mu_0 \{l_{D n+1}^{\text{tr}} - \sqrt{\frac{3}{2}} \bar{\alpha}_{D n+1, n}\} \\ \quad - f_D(\bar{d}) \partial_{|\dot{\alpha}_D|} \chi_{Dm}(\boldsymbol{\epsilon}_{n+1}, \mathbf{d}_{n+1}, \mathbf{d}_{n+1}^{\text{a}}) \end{cases} \quad (4.78)$$

of two (scalar) equations in two (scalar) unknowns

$$\boldsymbol{\epsilon}_{n+1} = (\dot{\alpha}_{H n+1}, \dot{\alpha}_{D n+1}) . \quad (4.79)$$

Here

$$\mathbf{d}_{n+1} = \begin{pmatrix} \dot{\bar{\alpha}}_{H n+1} \\ \dot{\bar{\alpha}}_{D n+1} \\ \dot{\bar{d}}_{n+1} \\ \dot{\theta}_{n+1} \end{pmatrix} \quad (4.80)$$

are the corresponding field quantities determined via (4.56) and

$$\mathbf{d}_{n+1}^{\text{a}} = \begin{pmatrix} \bar{\alpha}_{H n+1} = \bar{\alpha}_{H n} + t_{n+1, n} \dot{\bar{\alpha}}_{H n+1} \\ \bar{\alpha}_{D n+1} = \bar{\alpha}_{D n} + t_{n+1, n} \dot{\bar{\alpha}}_{D n+1} \\ \bar{d}_{n+1} = \bar{d}_n + t_{n+1, n} \dot{\bar{d}}_{n+1} \\ \dot{\theta}_{n+1} = \frac{\theta_{n+1} - \theta_n}{t_{n+1, n}} \end{pmatrix} \quad (4.81)$$

are the algorithmic quantities calculated via Backward-Euler integration / differentiation, respectively, all fixed during the time interval $[t_n, t_{n+1}]$. The trial strain $\ln \mathbf{V}_{E n+1}^{\text{tr}}$ is calculated for a given $\mathbf{F}_{n+1, n}$ via (4.73). For fixed $\mathbf{F}_{n+1, n}$ ($\ln \mathbf{V}_{E n+1}^{\text{tr}}$) and $\dot{\mathbf{d}}_{n+1}$ (\mathbf{d}_{n+1}) (4.78) is solved via Newton-Raphson iteration via the Jacobian $\partial_{\boldsymbol{\epsilon}_{n+1}} \mathbf{r}_n$. The remaining source terms in (4.56) are calculated explicitly as

$$\begin{aligned} \dot{d}_{I n+1} &= r_I \langle \bar{\alpha}_{I n+1} - \alpha_{Id} \rangle (s_I - \bar{d}_{n+1}) \dot{\bar{\alpha}}_{I n+1} , \\ \omega_r &= \beta_0 \sqrt{6} \mu_0 \{l_{D n+1}^{\text{tr}} - \sqrt{\frac{3}{2}} \bar{\alpha}_{D n+1, n}\} \dot{\bar{\alpha}}_D . \end{aligned} \quad (4.82)$$

Besides \mathbf{K}_{n+1} via (4.76) and (4.77) the solution of (4.78) also determines the algorithmic derivatives

$$\begin{aligned} \partial_{\ln \mathbf{V}_{E n+1}^{\text{tr}}}^{\text{a}} \boldsymbol{\epsilon}_{n+1} &= -(\partial_{\boldsymbol{\epsilon}_{n+1}} \mathbf{r}_n)^{-1} (\partial_{\ln \mathbf{V}_{E n+1}^{\text{tr}}} \mathbf{r}_n) , \\ \partial_{\mathbf{d}_{n+1}^{\text{a}}}^{\text{a}} \boldsymbol{\epsilon}_{n+1} &= -(\partial_{\boldsymbol{\epsilon}_{n+1}} \mathbf{r}_n)^{-1} (\partial_{\mathbf{d}_{n+1}^{\text{a}}} \mathbf{r}_n) . \end{aligned} \quad (4.83)$$

Note, that the above formulations hold also for the case of modeling some of the field quantities \mathbf{d} as local ($\ell_{I0} \rightarrow 0, \dots$), or assuming adiabatic conditions ($\kappa_0 \rightarrow 0$). In this case, the relation for the corresponding fields given by (4.56) reduce to the local form. From these in combination with (4.82), the substitutions

$$\bar{d}_{n+1} = \bar{d}_n + t_{n+1, n} \dot{\bar{d}}_{n+1} , \quad (4.84)$$

with

$$\begin{aligned} \dot{\bar{d}}_{n+1} &= r_D \langle \bar{\alpha}_{D n+1} - \alpha_{Dd} \rangle (s_D - \bar{d}_{n+1}) \dot{\bar{\alpha}}_{D n+1} \\ &\quad + r_H \langle \bar{\alpha}_{H n+1} - \alpha_{Hd} \rangle (s_H - \bar{d}_{n+1}) \dot{\bar{\alpha}}_{I n+1} , \end{aligned} \quad (4.85)$$

$$\theta_{n+1} = \theta_n + t_{n+1,n} c_0^{-1} \beta_0 \sqrt{6} \mu_0 \{t_{D_{n+1}}^{\text{tr}} - \sqrt{\frac{3}{2}} \bar{\alpha}_{D_{n+1,n}}\} \dot{\bar{\alpha}}_D \quad (4.86)$$

and further

$$\bar{\alpha}_{I_{n+1}} = \bar{\alpha}_{I_n} + t_{n+1,n} \dot{\bar{\alpha}}_{I_{n+1}}, \quad (4.87)$$

with

$$\dot{\bar{\alpha}}_{I_{n+1}} = \dot{\alpha}_{I_{n+1}}, \quad (4.88)$$

activated in (4.78), in case of local modeling of the corresponding quantities become relevant. These substitutions have to be considered by activating the corresponding partial derivatives in context of calculating the Jacobian $\partial_{\epsilon_{n+1}} \mathbf{r}_n$ and the algorithmic derivatives (4.83). Apart from that, the local algorithm remains.

In summary, the above algorithmic relations are formulated for the time interval $[t_n, t_{n+1}]$ of duration $t_{n+1,n} := t_{n+1} - t_n$. Given are the values of the deformation gradient \mathbf{F}_n , the set of field quantities \mathbf{d}_{n+1} and the internal variables θ_n , \mathbf{B}_{E_n} , $\bar{\alpha}_{H_n}$, $\bar{\alpha}_{D_n}$ and \bar{d}_n , at the beginning of this interval. In addition, \mathbf{F}_{n+1} , and so $\mathbf{F}_{n+1,n} = \mathbf{F}_{n+1} \mathbf{F}_n^{-1}$, are determined. On this basis, we have the following algorithm.

1. calculate trial quantities:

- (a) $\mathbf{B}_{E_{n+1}}^{\text{tr}} = \mathbf{F}_{n+1,n} \mathbf{B}_{E_n} \mathbf{F}_{n+1,n}^T$, $\ln \mathbf{V}_{E_{n+1}}^{\text{tr}} = \frac{1}{2} \ln \mathbf{B}_{E_{n+1}}^{\text{tr}}$;
- (b) $l_{H_{n+1}}^{\text{tr}} = \text{tr}(\ln \mathbf{V}_{E_{n+1}}^{\text{tr}})$, $l_{D_{n+1}}^{\text{tr}} = \text{mag}(\text{dev}(\ln \mathbf{V}_{E_{n+1}}^{\text{tr}}))$;

2. local iteration:

- (a) set $\epsilon_{n+1} = \mathbf{0}$
- (b) while $r_1(\epsilon_{n+1}^{(k)}, \dots) \geq \text{tolerance}$ and $r_2(\epsilon_{n+1}^{(k)}, \dots) \geq \text{tolerance}$, solve (4.78) for ϵ_{n+1} iteratively using Newton-Raphson iteration, eventually based on substitutions (4.84)-(4.88):

$$\text{if } r_i(\epsilon_{n+1}^{(k)}, \dots) \leq \text{tolerance}, i = 1, 2, \text{ set } r_i = 0 \text{ and } (\partial_{\epsilon_{n+1}} \mathbf{r}(\epsilon_{n+1}^{(k)}, \dots))_{ij}^{-1} = 0, \\ j = 1, 2$$

$$\epsilon_{n+1}^{(k+1)} = \epsilon_{n+1}^{(k)} - (\partial_{\epsilon_{n+1}} \mathbf{r}(\epsilon_{n+1}^{(k)}, \dots))^{-1} \mathbf{r}(\epsilon_{n+1}^{(k)}, \dots), \quad k = 0, \dots; \quad (4.89)$$

- (c) in case of local modeling update $\bar{\alpha}_{I_{n+1}}$, \bar{d}_{n+1} , and θ_{n+1} via (4.84)-(4.88);
- (d) $\ln \mathbf{V}_{E_{n+1}}$ via (4.74), $\mathbf{B}_{E_{n+1}} = \exp(2 \ln \mathbf{V}_{E_{n+1}})$;
- (e) $k_{H_{n+1}}$ and $k_{D_{n+1}}$ via (4.76);
- (f) \mathbf{K}_{n+1} from (4.77);

3. return;

This algorithm is highly nonlinear in $\mathbf{F}_{n+1} = \nabla_0 \chi_{n+1}$ and \mathbf{d}_{n+1} , forcing an implicit iterative solution of the mechanical equilibrium relations for χ_{n+1} and \mathbf{d}_{n+1} at the structural level via algorithmic linearization, to which we now turn.

4.5 Algorithmic linearization

Consider again the time interval $[t_n, t_{n+1}]$ of duration $t_{n+1,n} := t_{n+1} - t_n$. For the finite-element formulation, we identify as usual the reference configuration $B \equiv B_0$ with the initial configuration ($t = t_0$) of the material and structure in question. On this basis, consider the algorithmic linearization of the model from the previous section. In the current non-local context, this is based on the algorithmic linearization $d^a \chi_{n+1}$ of the current unknown deformation field χ_{n+1} , and on the algorithmic linearization $d^a \mathbf{d}_{n+1}$ of the current unknown field quantities \mathbf{d}_{n+1} . In particular, this induces that

$$d^a \mathbf{F}_{n+1} = d^a \nabla_0 \chi_{n+1} = \nabla_0 d^a \chi_{n+1} = (\nabla_{n+1} d^a \chi_{n+1}) \mathbf{F}_{n+1} =: \mathbf{A}_{n+1} \mathbf{F}_{n+1} \quad (4.90)$$

of the corresponding deformation gradient \mathbf{F}_{n+1} , with

$$\nabla_{n+1} \chi := (\nabla_0 \chi) \mathbf{F}_{n+1}^{-1} \quad (4.91)$$

the push-forward of the referential gradient operator to the current algorithmic configuration.

Assuming there are no momentum supplies, the finite-element formulation of the mechanic part of the model from the last section is based on the weak form

$$\begin{aligned} w_{\chi}(\chi_{n+1}, \ddot{\chi}_{n+1}, \chi_*) &= \int_{B_0} \varrho_0 \ddot{\chi}_{n+1} \cdot \chi_* + \mathbf{P}_{n+1} \cdot \nabla_0 \chi_* \\ &- \int_{\partial B_0} \mathbf{p}_{n+1} \cdot \chi_* \\ &= 0 \end{aligned} \quad (4.92)$$

of referential momentum balance to solve for the unknown position field χ holding for all test deformation fields χ_* consistent with the boundary conditions. Here, \mathbf{p}_{n+1} is the prescribed referential traction field on the traction part of ∂B_0 . Depending on the type of loading environment present, of course, it may depend in general on χ_{n+1} and $\mathbf{F}_{n+1} = \nabla_0 \chi_{n+1}$. Physically, of course, boundary conditions are applied on the boundary $\partial \chi_{n+1}[B_0]$ of the current algorithmic configuration $\chi_{n+1}[B_0]$. If \mathbf{t}_{n+1} is the traction on this latter boundary, then

$$\mathbf{p}_{n+1} = \det(\mathbf{F}_{n+1}) \operatorname{mag}(\mathbf{F}_{n+1}^{-T} \mathbf{n}_0) \mathbf{t}_{n+1} \quad (4.93)$$

follows from the corresponding transformation between area elements. In the case of dead loading, which we assume here for simplicity, \mathbf{p}_{n+1} is by definition independent of χ_{n+1} and $\nabla_0 \chi_{n+1}$. In this case, \mathbf{t}_{n+1} depends on these via (4.93). In any case, on this basis, the linearization of (4.92) with respect to χ_{n+1} takes the form

$$d^a_{\chi_{n+1}} w_{\chi_{n+1}} = \int_{B_0} \chi_* \cdot \varrho_0 d^a_{\chi_{n+1}} \ddot{\chi}_{n+1} + \int_{B_0} \nabla_0 \chi_* \cdot d^a_{\chi_{n+1}} \mathbf{P}_{n+1}. \quad (4.94)$$

In addition,

$$d^a_{\chi_{n+1}} \ddot{\chi}_{n+1} = (d^a_{\chi_{n+1}} \ddot{\chi}_{n+1}) d^a \chi_{n+1} \quad (4.95)$$

holds, with $d^a_{\chi_{n+1}} \ddot{\chi}_{n+1}$ determined for example via the Newmark algorithm. Further,

$$\begin{aligned} \nabla_0 \chi_* \cdot d^a_{\chi_{n+1}} \mathbf{P}_{n+1} &= \nabla_{n+1} \chi_* \cdot (d^a_{\chi_{n+1}} \mathbf{P}_{n+1}) \mathbf{F}_{n+1}^T \\ &= \nabla_{n+1} \chi_* \cdot d^a_{\chi_{n+1}} \mathbf{K}_{n+1} - (\nabla_{n+1} \chi_*) (\nabla_{n+1} d^a \chi_{n+1}) \cdot \mathbf{K}_{n+1} \end{aligned} \quad (4.96)$$

and

$$\begin{aligned}\nabla_0 \boldsymbol{\chi}_* \cdot d^a_{\boldsymbol{\chi}_{n+1}} \mathbf{P}_{n+1} &= \nabla_0 \boldsymbol{\chi}_* \cdot \partial_{\mathbf{F}_{n+1}}^a \mathbf{P}_{n+1} [\nabla_0 d^a \boldsymbol{\chi}_{n+1}] \\ &= \nabla_{n+1} \boldsymbol{\chi}_* \cdot (\partial_{\boldsymbol{\Lambda}_{n+1}}^a \mathbf{K}_{n+1} - \mathbf{K}_{n+1} \triangle \mathbf{I}) [\nabla_{n+1} d^a \boldsymbol{\chi}_{n+1}],\end{aligned}\quad (4.97)$$

follows for the linearization of the stress term, with

$$\partial_{\boldsymbol{\Lambda}_{n+1}}^a \mathbf{K}_{n+1} := (\partial_{\mathbf{F}_{n+1}}^a \mathbf{K}_{n+1}) (\mathbf{I} \square \mathbf{F}_{n+1}) \quad (4.98)$$

the material part, and $\mathbf{K}_{n+1} \triangle \mathbf{I}$ the geometric part, of the algorithmic stress tangent. Here and in what follows, the tensor products

$$\begin{aligned}(\mathbf{A} \square \mathbf{B}) \mathbf{C} &:= \mathbf{A} \mathbf{C} \mathbf{B}, \\ (\mathbf{A} \triangle \mathbf{B}) \mathbf{C} &:= \mathbf{A} \mathbf{C}^T \mathbf{B}, \\ (\mathbf{A} \otimes \mathbf{B}) \mathbf{C} &:= (\mathbf{B} \cdot \mathbf{C}) \mathbf{A},\end{aligned}\quad (4.99)$$

on second-order tensors are employed. For the current model class we have

$$\partial_{\mathbf{F}_{n+1}}^a \mathbf{K}_{n+1} = \partial_{\ln \mathbf{V}_{E_{n+1}}^{\text{tr}}}^a \mathbf{K}_{n+1} \partial_{\mathbf{F}_{n+1}} \ln \mathbf{V}_{E_{n+1}}^{\text{tr}}, \quad (4.100)$$

with

$$\partial_{\ln \mathbf{V}_{E_{n+1}}^{\text{tr}}}^a \mathbf{K}_{n+1} = \partial_{\ln \mathbf{V}_{E_{n+1}}^{\text{tr}}} \mathbf{K}_{n+1} + \partial_{\boldsymbol{\epsilon}_{n+1}} \mathbf{K}_{n+1} \partial_{\ln \mathbf{V}_{E_{n+1}}^{\text{tr}}}^a \boldsymbol{\epsilon}_{n+1}, \quad (4.101)$$

Note, that the second term in (4.101), containing the algorithmic derivative

$$\partial_{\ln \mathbf{V}_{E_{n+1}}^{\text{tr}}}^a \boldsymbol{\epsilon}_{n+1} = -(\partial_{\boldsymbol{\epsilon}_{n+1}} \mathbf{r}_n)^{-1} (\partial_{\ln \mathbf{V}_{E_{n+1}}^{\text{tr}}} \mathbf{r}_n), \quad (4.102)$$

vanishes for $\ell_{D0} \geq 0$ and $\ell_{H0} \geq 0$. Further we have

$$\partial_{\mathbf{F}_{n+1}} \ln \mathbf{V}_{E_{n+1}}^{\text{tr}} = \frac{1}{2} \partial_{\mathbf{B}_{E_{n+1}}^{\text{tr}}} \ln \mathbf{B}_{E_{n+1}}^{\text{tr}} \partial_{\mathbf{F}_{n+1}} \mathbf{B}_{E_{n+1}}^{\text{tr}}. \quad (4.103)$$

Considering now the formulations for derivatives of isotropic tensor functions in spectral representations as described, e.g., by Silhavy (1997), the first term of (4.103) is given by

$$\partial_{\mathbf{B}_{E_{n+1}}^{\text{tr}}} \ln \mathbf{B}_{E_{n+1}}^{\text{tr}} = H_{ij} \mathbf{e}_i \otimes \mathbf{e}_j \otimes \mathbf{e}_i \otimes \mathbf{e}_j \quad (4.104)$$

with

$$H_{ij} = \begin{cases} \frac{\ln(b_i) - \ln(b_j)}{b_i - b_j} & \text{if } b_i \neq b_j \\ \frac{1}{b_i} & \text{if } b_i = b_j \end{cases} \quad (4.105)$$

and

$$\mathbf{B}_{E_{n+1}}^{\text{tr}} = b_i \mathbf{e}_i \otimes \mathbf{e}_i. \quad (4.106)$$

The second term of (4.103) is given by

$$\partial_{\mathbf{F}_{n+1}} \mathbf{B}_{E_{n+1}}^{\text{tr}} = \mathbf{I} \square (\mathbf{F}_{n+1}^{-1} \mathbf{B}_{E_{n+1}}^{\text{tr}}) + (\mathbf{B}_{E_{n+1}}^{\text{tr}} \mathbf{F}_{n+1}^{-T}) \triangle \mathbf{I}. \quad (4.107)$$

Based on this, the linearization of \mathbf{K} with respect to $d^a \boldsymbol{\chi}_{n+1}$ reduces to

$$\partial_{\boldsymbol{\Lambda}_{n+1}}^a \mathbf{K}_{n+1} := \frac{1}{2} (\partial_{\ln \mathbf{V}_{E_{n+1}}^{\text{tr}}}^a \mathbf{K}_{n+1} \partial_{\mathbf{B}_{E_{n+1}}^{\text{tr}}} \ln \mathbf{B}_{E_{n+1}}^{\text{tr}} \partial_{\boldsymbol{\Lambda}_{n+1}} \mathbf{B}_{E_{n+1}}^{\text{tr}}) \quad (4.108)$$

in combination with (4.101), (4.104) and

$$\partial_{\Lambda_{n+1}} \mathbf{B}_{E_{n+1}}^{\text{tr}} = \mathbf{I} \square \mathbf{B}_{E_{n+1}}^{\text{tr}} + \mathbf{B}_{E_{n+1}}^{\text{tr}} \triangle \mathbf{I}. \quad (4.109)$$

Here and in what follows, the superscript ‘‘a’’ on the partial derivative operator ∂^a indicates that this is an *algorithmic derivative* of the corresponding quantities. As exemplified by $\partial_{\mathbf{F}_{n+1}}^a \mathbf{K}_{n+1}$, it depends on the algorithm chosen.

Accordingly, the linearization of (4.92) with respect to the field quantities \mathbf{d}_{n+1} takes the form

$$d_{d_{a n+1}}^a w_{\chi^{n+1}} = \int_{B_0} \nabla_0 \chi_* \cdot d_{d_{a n+1}}^a \mathbf{P}_{n+1}, \quad (4.110)$$

$d_a = \dot{\hat{\alpha}}_D, \dot{\hat{\alpha}}_H, \dot{\hat{d}}, \theta$, with

$$\begin{aligned} \nabla_0 \chi_* \cdot d_{d_{a n+1}}^a \mathbf{P}_{n+1} &= \nabla_{n+1} \chi_* \cdot (d_{d_{a n+1}}^a \mathbf{P}_{n+1}) \mathbf{F}_{n+1}^T \\ &= \nabla_{n+1} \chi_* \cdot \partial_{d_{a n+1}}^a \mathbf{K}_{n+1} d^a d_{a n+1} \end{aligned} \quad (4.111)$$

and

$$\partial_{d_{a n+1}}^a \mathbf{K}_{n+1} = \partial_{\epsilon_{n+1}} \mathbf{K}_{n+1} \partial_{d_{a n+1}}^a \epsilon_{n+1}. \quad (4.112)$$

Again, note that this derivative, containing the algorithmic derivative

$$\partial_{d_{a n+1}}^a \epsilon_{n+1} = -(\partial_{\epsilon_{n+1}} \mathbf{r}_n)^{-1} (\partial_{d_{a n+1}} \mathbf{r}_n) \quad (4.113)$$

vanishes for $\ell_{D0} \geq 0$ and $\ell_{H0} \geq 0$.

Assuming no external heat supplies, a general weak form of the evolution-field equations (4.56) is given by

$$\begin{aligned} w_{d_a}(d_{a n+1}, d_{a*}) &= \int_{B_0} (\hat{d}_{a n+1} - s_{d_{a n+1}}) d_{a*} - \hat{\mathbf{q}}_{d_{a n+1}} \cdot \nabla_0 d_{a*} \\ &+ \int_{\partial B_0} \hat{\mathbf{q}}_{d_{a 0 n+1}} d_{a*}, \end{aligned} \quad (4.114)$$

$d_a = \dot{\hat{\alpha}}_D, \dot{\hat{\alpha}}_H, \dot{\hat{d}}, \theta$. Here, with

$$\hat{\mathbf{q}}_{d_{a n+1}} = -\det(\mathbf{F}_{n+1}) \mathbf{F}_{n+1}^{-1} \mathbf{F}_{n+1}^{-T} c_{d_a} \nabla_0 d_{a n+1}, \quad (4.115)$$

and

$$\begin{aligned} \hat{\dot{\alpha}}_I &= \dot{\hat{\alpha}}_{I n+1} \\ s_{\dot{\hat{\alpha}}_I n+1} &= \dot{\hat{\alpha}}_{I n+1} \\ c_{\dot{\hat{\alpha}}_I} &= \ell_{I0}^2 \\ \hat{\dot{d}} &= \dot{\hat{d}}_{n+1} \\ s_{\dot{\hat{d}} n+1} &= \dot{\hat{d}}_{D n+1} + \dot{\hat{d}}_{H n+1} \\ c_{\dot{\hat{d}}} &= \ell_{d0}^2 \\ \hat{\theta} &= c_0(\theta_{n+1} - \theta_n)/t_{n+1,n} \\ s_{\theta n+1} &= \omega_r \\ c_\theta &= k_0 \end{aligned} \quad (4.116)$$

The referential boundary flux is specified in terms of

$$\hat{q}_{d_a 0_{n+1}} = \hat{\mathbf{q}}_{d_a 0_{n+1}} \cdot \mathbf{n}_0, \quad (4.117)$$

with $\hat{q}_{d_a 0}$, the referential boundary flux vector. Further, with the flux boundary conditions given by (4.45)_{2,4,6}, we have

$$\begin{aligned} \int_{\partial B_0} \hat{\mathbf{q}}_{\hat{\alpha}_I 0} \cdot \mathbf{n}_0 \dot{\hat{\alpha}}_{I*} &:= 0, \\ \int_{\partial B_0} \hat{\mathbf{q}}_{\hat{d}0} \cdot \mathbf{n}_r \dot{\hat{d}}_* &:= 0, \end{aligned} \quad (4.118)$$

Now, using the results

$$\begin{aligned} d_{\chi_{n+1}}^a \det(\mathbf{F}) &= \det(\mathbf{F}_{n+1}) \mathbf{I} \cdot (\nabla_{n+1} d^a \chi_{n+1}), \\ d_{\chi_{n+1}}^a \mathbf{F}_{n+1}^{-1} &= -\mathbf{F}_{n+1}^{-1} (\nabla_{n+1} d^a \chi_{n+1}), \\ d_{\chi_{n+1}}^a \mathbf{F}_{n+1}^{-T} &= -(\nabla_{n+1} d^a \chi_{n+1})^T \mathbf{F}_{n+1}^{-T}, \end{aligned} \quad (4.119)$$

and restricting to the case of a constant boundary heat flux, the linearization of (4.114) with respect to χ_{n+1} takes the form

$$\begin{aligned} d_{\chi_{n+1}}^a w_{d_a} &= - \int_{B_0} \partial_{\Lambda_{n+1}}^a s_{d_a n+1} \cdot (\nabla_{n+1} d^a \chi_{n+1}) d_{a*} \\ &\quad - \int_{B_0} \left(\partial_{\Lambda_{n+1}}^a \hat{\mathbf{q}}_{d_a n+1} (\nabla_{n+1} d^a \chi_{n+1}) \right) \cdot \nabla_0 d_{a*}, \end{aligned} \quad (4.120)$$

with

$$\partial_{\Lambda_{n+1}}^a s_{d_a n+1} = \{ \partial_{\mathbf{F}_{n+1}} \ln \mathbf{V}_{E_{n+1}}^{\text{tr}} (\mathbf{I} \square \mathbf{F}_{n+1}) \}^T [\partial_{\ln \mathbf{V}_{E_{n+1}}^{\text{tr}}} s_{d_a n+1}], \quad (4.121)$$

determined via (4.103)-(4.107), (4.82) and (4.83) and

$$\begin{aligned} \partial_{\Lambda_{n+1}}^a \hat{\mathbf{q}}_{d_a n+1} &= \hat{\mathbf{q}}_{d_a n+1} \otimes \mathbf{I} - \mathbf{F}_{n+1}^{-1} \square \mathbf{F}_{n+1} \hat{\mathbf{q}}_{d_a n+1} - \mathbf{F}_{n+1}^{-1} \Delta \mathbf{F}_{n+1} \hat{\mathbf{q}}_{d_a n+1} \\ &= -\det(\mathbf{F}_{n+1}) \mathbf{F}_{n+1}^{-1} c_{d_a} \{ \nabla_{n+1} d_{a n+1} \otimes \mathbf{I} \\ &\quad - \mathbf{I} \square \nabla_{n+1} d_{a n+1} - \mathbf{I} \Delta \nabla_{n+1} d_{a n+1} \} \end{aligned} \quad (4.122)$$

Accordingly, the algorithmic linearization with respect to the field quantities d_{n+1} is given by

$$\begin{aligned} d_{d_{b n+1}}^a w_{d_a} &= \int_{B_0} (\partial_{d_{b n+1}}^a \hat{d}_{a n+1} - \partial_{d_{b n+1}}^a s_{d_a n+1}) d^a d_{b n+1} d_{a*} \\ &\quad + \delta_{ab} \int_{B_0} \det(\mathbf{F}_{n+1}) \mathbf{F}_{n+1}^{-1} \mathbf{F}_{n+1}^{-T} c_{d_a} \nabla_0 d^a d_{b n+1} \cdot \nabla_0 d_{a*}, \end{aligned} \quad (4.123)$$

with arising algorithmic derivatives determined via (4.116) in combination with (4.82) and (4.83) and δ_{ab} , the Kronecker delta.

4.6 Finite-element formulation

Let n_{dim} represent the physical dimension of B , and n_{dof} be the number of degrees-of-freedom (DOFs) characterizing B as a continuum system. In the context of the developed non-local framework, these DOFs are determined as usual by the deformation χ and the additional field quantities d . More specifically, the Cartesian components $\chi_m := \mathbf{i}_m \cdot \chi$, $m = 1, \dots, n_{\text{dim}}$, of χ represent the position DOFs of B , with $(\mathbf{i}_1, \dots, \mathbf{i}_{n_{\text{dim}}})$ the Cartesian basis. Let n_{nod}^e be the number of nodes in element e , $n_{\text{pos}}^e := n_{\text{nod}}^e \times n_{\text{dim}}$ represent the number of all position DOFs of e , and $n_{\text{dof}}^e := n_{\text{nod}}^e \times n_{\text{dof}}$ be the number of all nodal DOFs associated with element e . Further, let X_{km}^e represent the m^{th} position coordinate, and the m^{th} position DOF, of node k in element e . The array

$$\begin{aligned} \mathbf{x}^e &:= (x_1^e, \dots, x_{n_{\text{dim}}}^e, \dots, x_{(n_{\text{nod}}^e-1) \times n_{\text{dim}}+1}^e, \dots, x_{n_{\text{pos}}^e}^e), \\ &\equiv (X_{11}^e, \dots, X_{1n_{\text{dim}}}^e, \dots, X_{n_{\text{nod}}^e 1}^e, \dots, X_{n_{\text{nod}}^e n_{\text{dim}}}^e), \end{aligned} \quad (4.124)$$

contains all nodal position coordinates, and all nodal position DOFs, of element e arranged by node. Alternatively, we have the $n_{\text{nod}}^e \times n_{\text{dim}}$ matrix

$$\mathbf{X}_e := \begin{bmatrix} X_{11}^e & \cdots & X_{1n_{\text{dim}}}^e \\ \vdots & \ddots & \vdots \\ X_{n_{\text{nod}}^e 1}^e & \cdots & X_{n_{\text{nod}}^e n_{\text{dim}}}^e \end{bmatrix} \quad (4.125)$$

of all such DOFs. In what follows, we will consider \mathbf{X}_e to be a function of \mathbf{x}_e , i.e., $\mathbf{X}_e = \mathbf{X}(\mathbf{x}^e)$. On this basis, consider the polynomial approximation

$$\chi^e(\boldsymbol{\xi}, \mathbf{x}^e) = \mathbf{X}^T(\mathbf{x}^e) \mathbf{h}^e(\boldsymbol{\xi}) =: \mathbf{H}_e(\boldsymbol{\xi}) \mathbf{x}^e \quad (4.126)$$

to the element deformation field χ^e via the identification $\chi^e \equiv (\chi_1^e, \dots, \chi_{n_{\text{dim}}}^e)$. This is based on the n_{nod}^e array $\mathbf{h}^e(\boldsymbol{\xi}) := (h_1^e(\boldsymbol{\xi}), \dots, h_{n_{\text{nod}}^e}^e(\boldsymbol{\xi}))$, and the corresponding $n_{\text{dim}} \times n_{\text{pos}}^e$ matrix $\mathbf{H}_e(\boldsymbol{\xi})$, containing the shape functions for the position DOFs of element e . As usual, these represent polynomial functions of the array $\boldsymbol{\xi} := (\xi_1, \dots, \xi_{n_{\text{dim}}})$ of position coordinates on the master element $\Omega := [-1, 1] \times \cdots \times [-1, 1]$ (n_{dim} times). In particular, (4.126) determines the form

$$\mathbf{J}_e(\boldsymbol{\xi}, \mathbf{x}^e) := \partial_{\boldsymbol{\xi}} \chi^e(\boldsymbol{\xi}, \mathbf{x}^e) = \mathbf{X}^T(\mathbf{x}^e) \partial_{\boldsymbol{\xi}} \mathbf{h}^e(\boldsymbol{\xi}) \quad (4.127)$$

for the $n_{\text{dim}} \times n_{\text{dim}}$ Jacobian matrix of the transformation between physical and master element systems.

Next, let $\mathbf{x}_\tau^e := \mathbf{x}^e(t_\tau)$ be the value of \mathbf{x}^e at an arbitrary discrete time $t = t_\tau$ during $[0, d] = \bigcup_{n=0}^{n_{\text{int}}} [t_n, t_{n+1}]$. For example, we could have $\tau = 0$, i.e., the initial time, or $\tau = n$, i.e., the start of the arbitrary time interval $[t_n, t_{n+1}]$. With respect to this, we can define the element approximation

$$\nabla^e \mathbf{h}^e(\boldsymbol{\xi}, \mathbf{x}_\tau^e) = \partial_{\boldsymbol{\xi}} \mathbf{h}^e(\boldsymbol{\xi}) \mathbf{J}_e(\boldsymbol{\xi}, \mathbf{x}_\tau^e)^{-1} \quad (4.128)$$

of the spatial gradient of \mathbf{h}^e relative to \mathbf{x}_τ^e . This yields in turn element representation

$$\mathbf{F}_e(\boldsymbol{\xi}, \mathbf{x}_0^e, \mathbf{x}^e) = \mathbf{X}^T(\mathbf{x}^e) \nabla^e \mathbf{h}^e(\boldsymbol{\xi}, \mathbf{x}_0^e) \quad (4.129)$$

for the matrix of Cartesian components of the deformation gradient. For the algorithmic formulation to follow, the linearization

$$d\mathbf{F}_e(\boldsymbol{\xi}, \mathbf{x}_0^e, d\mathbf{x}^e) = \mathbf{X}^T(d\mathbf{x}^e) \nabla^e \mathbf{h}^e(\boldsymbol{\xi}, \mathbf{x}_0^e) \quad (4.130)$$

of \mathbf{F}_e and its pushed-forward form

$$\mathbf{\Lambda}_e(\boldsymbol{\xi}, \mathbf{x}^e, d\mathbf{x}^e) = \mathbf{X}^T(d\mathbf{x}^e) \nabla^e \mathbf{h}^e(\boldsymbol{\xi}, \mathbf{x}^e) \quad (4.131)$$

via $d\mathbf{F} = \mathbf{\Lambda}\mathbf{F}$, are also used in what follows. Using the row-array representation

$$\text{row}(\mathbf{A}) := (A_{11}, A_{12}, \dots, A_{n_{\text{dim}} n_{\text{dim}}}) \quad (4.132)$$

of any second-order tensor \mathbf{A} , with $n_{\text{row}} := n_{\text{dim}} \times n_{\text{dim}}$, we then have

$$\begin{aligned} \mathbf{f}^e(\boldsymbol{\xi}, \mathbf{x}_0^e, \mathbf{x}^e) &= \mathbf{G}_e(\boldsymbol{\xi}, \mathbf{x}_0^e) \mathbf{x}^e := \text{row}\{d\mathbf{F}_e(\boldsymbol{\xi}, \mathbf{x}_0^e, d\mathbf{x}^e)\}, \\ \mathbf{l}^e(\boldsymbol{\xi}, \mathbf{x}^e, d\mathbf{x}^e) &= \mathbf{G}_e(\boldsymbol{\xi}, \mathbf{x}^e) d\mathbf{x}^e := \text{row}\{\mathbf{\Lambda}_e(\boldsymbol{\xi}, \mathbf{x}^e, d\mathbf{x}^e)\}, \end{aligned} \quad (4.133)$$

in terms of the $n_{\text{row}} \times n_{\text{pos}}^e$ shape-function gradient matrix $\mathbf{G}_e(\boldsymbol{\xi}, \mathbf{x}_\tau^e)$ and \mathbf{x}^e .

Beyond the mechanical DOFs $\chi_m := \mathbf{i}_m \cdot \boldsymbol{\chi}$, $m = 1, \dots, n_{\text{dim}}$, we now have the non-local equivalent inelastic deformation $\bar{\alpha}_1$, the non-local damage field \bar{d} and the temperature θ as additional continuum DOFs. Then $n_{\text{dof}} = n_{\text{dim}} + n_{\text{dof}+}$. Let $\mathbf{d}_a^e := (d_{1a}^e, \dots, d_{n_{\text{nod}a}}^e)$ be the array of nodal values for the a^{th} additional DOF in element e , with, e.g. $d_{na}^e = \bar{\alpha}_{1n}^e, \bar{d}_n^e, \theta_n^e$. Further, let $\mathbf{d}^e := (\mathbf{d}_1^e, \dots, \mathbf{d}_{n_{\text{dof}+}}^e)$ be the array of all additional nodal values in element e (arranged by DOF). Then, based on the n_{nod}^e array $\mathbf{h}^e(\boldsymbol{\xi}) := (h_1(\boldsymbol{\xi}), \dots, h_{n_{\text{nod}}^e}(\boldsymbol{\xi}))$, the polynomial approximation to the element field quantity d_a^e is given by

$$d_a^e(\boldsymbol{\xi}, \mathbf{d}_a^e) = \mathbf{h}^e(\boldsymbol{\xi}) \cdot \mathbf{d}_a^e \quad (4.134)$$

In particular, (4.134) in combination with (4.128) determines the form

$$\nabla^e d_a^e(\boldsymbol{\xi}, \mathbf{x}_\tau^e) = \nabla^e \mathbf{h}^e(\boldsymbol{\xi}, \mathbf{x}_\tau^e)^T \mathbf{d}_a^e \quad (4.135)$$

of the spatial gradient of d_a^e relative to \mathbf{x}_τ^e , also used in what follows.

Consider next the finite-element approximation $B_0 \approx \bigcup_{e=1}^{n_{\text{ele}}} B_0^e$ of B_0 as based on n_{ele} elements. Let \mathbf{x}^s , \mathbf{d}_a^s and $\mathbf{d}^s := (\mathbf{d}_1^s, \dots, \mathbf{d}_{n_{\text{dof}+}}^s)$ represent the array of structural nodal position DOFs, the structural values for the a^{th} additional DOF and the array of all structural nodal values for the additional DOFs (arranged by DOF), respectively. Further, let $\mathbf{P}_{e\mathbf{x}}$, $\mathbf{P}_{e\mathbf{d}_a}$ and $\mathbf{P}_{e\mathbf{d}}$ represent the projection of these onto \mathbf{x}^e , \mathbf{d}_a^e and \mathbf{d}^e , respectively, determined by element connectivity, i.e., $\mathbf{x}^e = \mathbf{P}_{e\mathbf{x}} \mathbf{x}^s$. On this basis, the finite-element discretization induces the approximations

$$\begin{aligned} 0 &= w_{\boldsymbol{\chi}}(\boldsymbol{\chi}_{n+1}, \ddot{\boldsymbol{\chi}}_{n+1}, \mathbf{d}_{n+1}, \boldsymbol{\chi}_*) \approx w_{\mathbf{x}}^s(\mathbf{x}_{n+1}^s, \ddot{\mathbf{x}}_{n+1}^s, \mathbf{d}_{n+1}^s, \mathbf{x}_*) \\ 0 &= w_{d_a}(\boldsymbol{\chi}_{n+1}, \ddot{\boldsymbol{\chi}}_{n+1}, \mathbf{d}_{n+1}, d_{a*}) \approx w_{d_a}^s(\mathbf{x}_{n+1}^s, \ddot{\mathbf{x}}_{n+1}^s, \mathbf{d}_{n+1}^s, \mathbf{d}_{a*}^s), \end{aligned} \quad (4.136)$$

of the weak momentum balance (4.92) and the weak evolution-field equations (4.114), respectively, with

$$\begin{aligned} w_{\mathbf{x}}^s(\mathbf{x}_{n+1}^s, \ddot{\mathbf{x}}_{n+1}^s, \mathbf{d}_{n+1}^s, \mathbf{x}_*) &= \mathbf{f}_{\mathbf{x}}^s(\mathbf{x}_{n+1}^s, \ddot{\mathbf{x}}_{n+1}^s, \mathbf{d}_{n+1}^s) \cdot \mathbf{x}_*^s \\ w_{d_a}^s(\mathbf{x}_{n+1}^s, \ddot{\mathbf{x}}_{n+1}^s, \mathbf{d}_{n+1}^s, \mathbf{d}_{a*}^s) &= \mathbf{f}_{d_a}^s(\mathbf{x}_{n+1}^s, \ddot{\mathbf{x}}_{n+1}^s, \mathbf{d}_{n+1}^s) \cdot \mathbf{d}_{a*}^s \end{aligned} \quad (4.137)$$

and

$$\begin{aligned} \mathbf{f}_{\mathbf{x}}^s(\mathbf{x}_{n+1}^s, \ddot{\mathbf{x}}_{n+1}^s, \mathbf{d}_{n+1}^s) &= \sum_{e=1}^{n_{\text{ele}}} \mathbf{P}_{e\mathbf{x}}^T \mathbf{f}_{\mathbf{x}}^e(\mathbf{P}_{e\mathbf{x}} \mathbf{x}_{n+1}^s, \mathbf{P}_{e\mathbf{x}} \ddot{\mathbf{x}}_{n+1}^s, \mathbf{P}_{e\mathbf{d}} \mathbf{d}_{n+1}^s) \\ \mathbf{f}_{d_a}^s(\mathbf{x}_{n+1}^s, \ddot{\mathbf{x}}_{n+1}^s, \mathbf{d}_{n+1}^s) &= \sum_{e=1}^{n_{\text{ele}}} \mathbf{P}_{e\mathbf{d}_a}^T \mathbf{f}_{d_a}^e(\mathbf{P}_{e\mathbf{x}} \mathbf{x}_{n+1}^s, \mathbf{P}_{e\mathbf{x}} \ddot{\mathbf{x}}_{n+1}^s, \mathbf{P}_{e\mathbf{d}} \mathbf{d}_{n+1}^s) \end{aligned} \quad (4.138)$$

the structural nodal force arrays. In this relation,

$$\begin{aligned}
\mathbf{f}_{\mathbf{x}n+1}^e &:= \mathbf{M}_{\mathbf{xx}0}^e \ddot{\mathbf{x}}_{n+1}^e \\
&\quad + \int_{\Omega} j_0^e(\boldsymbol{\xi}) \mathbf{G}_e^T(\boldsymbol{\xi}, \mathbf{x}_{n+1}^e) \mathbf{k}_{n+1}^e dv_{\Omega} \\
&\quad - \int_{\partial\Omega} |\text{cof}(\mathbf{J}_e(\boldsymbol{\xi}, \mathbf{x}_0^e)) \mathbf{n}_{\Omega}| \mathbf{H}_e^T(\boldsymbol{\xi}) \mathbf{p}_{n+1}^e da_{\Omega}, \\
\mathbf{f}_{d_{a}n+1}^e &:= \int_{\Omega} j_0^e(\boldsymbol{\xi}) (\hat{d}_a - s_{d_a})_{n+1}^e \mathbf{h}^e(\boldsymbol{\xi}) - j_0^e(\boldsymbol{\xi}) \nabla^e \mathbf{h}^e(\boldsymbol{\xi}, \mathbf{x}_0^e) \hat{\mathbf{q}}_{d_{a}n+1}^e dv_{\Omega} \\
&\quad + \int_{\partial\Omega} \hat{q}_{d_{a}0n+1}^e |\text{cof}(\mathbf{J}_e(\boldsymbol{\xi}, \mathbf{x}_0^e)) \mathbf{n}_{\Omega}| \mathbf{h}^e(\boldsymbol{\xi}) da_{\Omega}
\end{aligned} \tag{4.139}$$

represent the element nodal force arrays in terms of the mass matrix

$$\mathbf{M}_{\mathbf{xx}0}^e := \int_{\Omega} j_0^e(\boldsymbol{\xi}) \rho_0 \mathbf{H}_e^T(\boldsymbol{\xi}) \mathbf{H}_e(\boldsymbol{\xi}) dv_{\Omega} \tag{4.140}$$

and

$$j_{\tau}^e(\boldsymbol{\xi}) := \det(\mathbf{J}_e(\boldsymbol{\xi}, \mathbf{x}_{\tau}^e)) \tag{4.141}$$

is the determinant of $\mathbf{J}_e(\boldsymbol{\xi}, \mathbf{x}_{\tau}^e)$. In (4.139) and in what follows, $\mathbf{k} := \text{row}(\mathbf{K})$ represents the row array whose components are determined by the Cartesian components of the symmetric Kirchhoff stress \mathbf{K} . For example, for $n_{\text{dim}} = 3$, we would have $\mathbf{k} = (K_{11}, K_{12}, K_{13}, K_{12}, K_{22}, K_{23}, K_{13}, K_{23}, K_{33})$. Here, and in what follows the notations ${}^e_{n+1}$ and ${}^s_{n+1}$ refer to quantities, determined at time t_{n+1} in terms of elemental $(\mathbf{x}_{n+1}^e, \ddot{\mathbf{x}}_{n+1}^e, \mathbf{d}_{n+1}^e)$ and structural DOFs $(\mathbf{x}_{n+1}^s, \ddot{\mathbf{x}}_{n+1}^s, \mathbf{d}_{n+1}^s)$, respectively. With this notation we tacitly include the dependence on further quantities, as given by the definitions above, e.g., we set $\mathbf{k}(\mathbf{f}^e(\boldsymbol{\xi}, \mathbf{x}_0^e, \mathbf{x}_{n+1}^e)) := \mathbf{k}_{n+1}^e$. Further we avoid redundant sub-/superscripts, e.g., we substitute $\mathbf{f}_{\mathbf{x}}^e(\mathbf{x}_{n+1}^e, \ddot{\mathbf{x}}_{n+1}^e, \mathbf{d}_{n+1}^e) := \mathbf{f}_{\mathbf{x}n+1}^{ee} := \mathbf{f}_{\mathbf{x}n+1}^e$. In particular, (4.139)-(4.137) follow from the results

$$\begin{aligned}
&\mathbf{x}_*^e \cdot \mathbf{f}_{\mathbf{x}n+1}^e \\
&= \int_{B_0^e} \rho_0 \ddot{\mathbf{x}}_{n+1}^e \cdot \boldsymbol{\chi}_*^e + \mathbf{K}_{n+1}^e \cdot \nabla_{n+1}^e \boldsymbol{\chi}_*^e dv_0^e \\
&\quad - \int_{\partial B_0^e} \mathbf{p}_{n+1}^e \cdot \boldsymbol{\chi}_*^e da_0^e \\
&= \mathbf{x}_*^e \cdot \left(\int_{\Omega} j_0^e(\boldsymbol{\xi}) \rho_0 \mathbf{H}_e^T(\boldsymbol{\xi}) \mathbf{H}_e(\boldsymbol{\xi}) \ddot{\mathbf{x}}_{n+1}^e + j_0^e(\boldsymbol{\xi}) \mathbf{G}_e^T(\boldsymbol{\xi}, \mathbf{x}_{n+1}^e) \mathbf{k}_{n+1}^e dv_{\Omega} \right. \\
&\quad \left. - \int_{\partial\Omega} |\text{cof}(\mathbf{J}_e(\boldsymbol{\xi}, \mathbf{x}_0^e)) \mathbf{n}_{\Omega}| \mathbf{H}_e^T(\boldsymbol{\xi}) \mathbf{p}_{n+1}^e da_{\Omega} \right)
\end{aligned} \tag{4.142}$$

for the approximation of weak momentum balance (4.92), and that

$$\begin{aligned}
&\mathbf{d}_{a*}^e \cdot \mathbf{f}_{d_{a}n+1}^e \\
&= \int_{B_0^e} (\hat{d}_a - s_{d_a})_{n+1}^e d_{a*}^e - \hat{\mathbf{q}}_{d_{a}n+1}^e \cdot \nabla_0^e d_{a*}^e dv_0^e \\
&\quad + \int_{B_0^e} \hat{q}_{d_{a}0n+1}^e d_{a*}^e da_0^e, \\
&= \mathbf{d}_{a*}^e \cdot \left(\int_{\Omega} j_0^e(\boldsymbol{\xi}) (\hat{d}_a - s_{d_a})_{n+1}^e \mathbf{h}^e(\boldsymbol{\xi}) - j_0^e(\boldsymbol{\xi}) \nabla^e \mathbf{h}^e(\boldsymbol{\xi}, \mathbf{x}_0^e) \hat{\mathbf{q}}_{d_{a}n+1}^e dv_{\Omega} \right. \\
&\quad \left. + \int_{\partial\Omega} \hat{q}_{d_{a}0n+1}^e |\text{cof}(\mathbf{J}_e(\boldsymbol{\xi}, \mathbf{x}_0^e)) \mathbf{n}_{\Omega}| \mathbf{h}^e(\boldsymbol{\xi}) da_{\Omega} \right),
\end{aligned} \tag{4.143}$$

for the approximation of the weak evolution-field equations (4.114).

In the current non-linear case, the solution of (4.136)–(4.137) in terms of the field quantities \mathbf{x}_{n+1}^s and \mathbf{d}_{an+1}^s at time t_{n+1} , is determined iteratively, e.g., using standard Newton-Rhapson iteration

$$-\begin{pmatrix} \mathbf{f}_{\mathbf{x}}^{s(k)} \\ \vdots \\ \mathbf{f}_{\mathbf{d}_{n\text{dof}+}}^{s(k)} \end{pmatrix} = \begin{pmatrix} \overline{\mathbf{K}}_{\mathbf{x}\mathbf{x}}^{s(k)} & \cdots & \mathbf{K}_{\mathbf{x}\mathbf{d}_{n\text{dof}+}}^{s(k)} \\ \vdots & \ddots & \vdots \\ \mathbf{K}_{\mathbf{x}\mathbf{d}_{n\text{dof}+}}^{s(k)} & \cdots & \mathbf{K}_{\mathbf{d}_{n\text{dof}+}\mathbf{d}_{n\text{dof}+}}^{s(k)} \end{pmatrix} \begin{pmatrix} \mathbf{x}^{s(k+1)} - \mathbf{x}^{s(k)} \\ \vdots \\ \mathbf{d}_{n\text{dof}+}^{s(k+1)} - \mathbf{d}_{n\text{dof}+}^{s(k)} \end{pmatrix} \quad (4.144)$$

This involves in particular the algorithmic linearization of $\mathbf{f}_{\mathbf{x}}^s(\mathbf{x}_{n+1}^s, \dot{\mathbf{x}}_{n+1}^s, \mathbf{d}_{n+1}^s)$ and $\mathbf{f}_{\mathbf{d}_a}^s(\mathbf{x}_{n+1}^s, \dot{\mathbf{x}}_{n+1}^s, \mathbf{d}_{n+1}^s)$

$$\begin{aligned} d_{\mathbf{x}_{n+1}^s}^a \mathbf{f}_{\mathbf{x}_{n+1}^s}^s &= \overline{\mathbf{K}}_{\mathbf{x}\mathbf{x}n+1}^s d^a \mathbf{x}_{n+1}^s \\ &= \mathbf{K}_{\mathbf{x}\mathbf{x}n+1}^s d^a \mathbf{x}_{n+1}^s + \mathbf{M}_{\mathbf{x}\mathbf{x}0}^s d^a \dot{\mathbf{x}}_{n+1}^s (d^a \mathbf{x}_{n+1}^s), \\ d_{\mathbf{d}_{an+1}^s}^a \mathbf{f}_{\mathbf{x}_{n+1}^s}^s &= \mathbf{K}_{\mathbf{x}\mathbf{d}_{an+1}^s}^s d^a \mathbf{d}_{an+1}^s \end{aligned} \quad (4.145)$$

and

$$\begin{aligned} d_{\mathbf{x}_{n+1}^s}^a \mathbf{f}_{\mathbf{d}_{an+1}^s}^s &= \mathbf{K}_{\mathbf{d}_a \mathbf{x} n+1}^s d^a \mathbf{x}_{n+1}^s, \\ d_{\mathbf{d}_{bn+1}^s}^a \mathbf{f}_{\mathbf{d}_{an+1}^s}^s &= \mathbf{K}_{\mathbf{d}_a \mathbf{d}_b n+1}^s d^a \mathbf{d}_{bn+1}^s \end{aligned} \quad (4.146)$$

with

$$\mathbf{M}_{\mathbf{x}\mathbf{x}0}^s := \partial_{\dot{\mathbf{x}}_{n+1}^s}^a \mathbf{f}_{\mathbf{x}n+1}^s = \sum_{e=1}^{n_{\text{ele}}} \mathbf{P}_{e\mathbf{x}}^T \mathbf{M}_{\mathbf{x}\mathbf{x}0}^e \mathbf{P}_{e\mathbf{x}}, \quad (4.147)$$

$$\mathbf{K}_{\mathbf{x}\mathbf{x}n+1}^s := \partial_{\mathbf{x}_{n+1}^s}^a \mathbf{f}_{\mathbf{x}n+1}^s = \sum_{e=1}^{n_{\text{ele}}} \mathbf{P}_{e\mathbf{x}}^T \mathbf{K}_{\mathbf{x}\mathbf{x}n+1}^e \mathbf{P}_{e\mathbf{x}}, \quad (4.148)$$

$$\mathbf{K}_{\mathbf{x}\mathbf{d}_{an+1}^s}^s := \partial_{\mathbf{d}_{an+1}^s}^a \mathbf{f}_{\mathbf{x}n+1}^s = \sum_{e=1}^{n_{\text{ele}}} \mathbf{P}_{e\mathbf{x}}^T \mathbf{K}_{\mathbf{x}\mathbf{d}_a n+1}^e \mathbf{P}_{e\mathbf{d}_a} \quad (4.149)$$

and

$$\mathbf{K}_{\mathbf{d}_a \mathbf{x} n+1}^s := \partial_{\mathbf{x}_{n+1}^s}^a \mathbf{f}_{\mathbf{d}_{an+1}^s}^s = \sum_{e=1}^{n_{\text{ele}}} \mathbf{P}_{e\mathbf{d}_a}^T \mathbf{K}_{\mathbf{d}_a \mathbf{x} n+1}^e \mathbf{P}_{e\mathbf{x}}, \quad (4.150)$$

$$\mathbf{K}_{\mathbf{d}_b \mathbf{d}_b n+1}^s := \partial_{\mathbf{d}_{an+1}^s}^a \mathbf{f}_{\mathbf{d}_{an+1}^s}^s = \sum_{e=1}^{n_{\text{ele}}} \mathbf{P}_{e\mathbf{d}_a}^T \mathbf{K}_{\mathbf{d}_a \mathbf{d}_b n+1}^e \mathbf{P}_{e\mathbf{d}_a} \quad (4.151)$$

via (4.138). Here, the corresponding element tangents are given by

$$\begin{aligned} \mathbf{K}_{\mathbf{x}\mathbf{x}n+1}^e &= \partial_{\mathbf{x}_{n+1}^e}^a \mathbf{f}_{\mathbf{x}n+1}^e \\ &= \int_{\Omega} j_0^e(\boldsymbol{\xi}) \mathbf{G}_e^T(\boldsymbol{\xi}, \mathbf{x}_{n+1}^e) \{ \partial_1^a \mathbf{k} - \mathbf{k} \Delta \mathbf{1} \}_{n+1}^e \mathbf{G}_e(\boldsymbol{\xi}, \mathbf{x}_{n+1}^e) dv_{\Omega}, \end{aligned}$$

$$\begin{aligned} \mathbf{K}_{\mathbf{x}\mathbf{d}_{an+1}^s}^e &= \partial_{\mathbf{d}_{an+1}^e}^a \mathbf{f}_{\mathbf{x}n+1}^e \\ &= \int_{\Omega} j_0^e(\boldsymbol{\xi}) \left((\mathbf{G}_e^T(\boldsymbol{\xi}, \mathbf{x}_{n+1}^e) (\partial_{d_a}^a \mathbf{k})_{n+1}^e \otimes \mathbf{h}_e(\boldsymbol{\xi})) \right) dv_{\Omega}, \end{aligned}$$

$$\begin{aligned} \mathbf{K}_{\mathbf{d}_a \mathbf{x} n+1}^e &= \partial_{\mathbf{x}_{n+1}^e}^a \mathbf{f}_{\mathbf{d}_{an+1}^s}^e \\ &= - \int_{\Omega} j_0^e(\boldsymbol{\xi}) \mathbf{h}_e(\boldsymbol{\xi}) \otimes (\partial_1^a s_{d_a})_{n+1}^e \mathbf{G}_e(\boldsymbol{\xi}, \mathbf{x}_{n+1}^e) \\ &\quad - j_0^e(\boldsymbol{\xi}) \nabla^e \mathbf{h}^e(\boldsymbol{\xi}, \mathbf{x}_0^e) (\partial_1^a \hat{q}_{d_a})_{n+1}^e \mathbf{G}_e(\boldsymbol{\xi}, \mathbf{x}_{n+1}^e) dv_{\Omega}, \end{aligned} \quad (4.152)$$

$$\begin{aligned} \mathbf{K}_{\mathbf{d}_a \mathbf{d}_b n+1}^e &= \partial_{\mathbf{d}_{bn+1}^e}^a \mathbf{f}_{\mathbf{d}_{an+1}^s}^e \\ &= \int_{\Omega} j_0^e(\boldsymbol{\xi}) (\partial_{d_b}^a \hat{d}_a - \partial_{d_b}^a s_{d_a})_{n+1}^e \mathbf{h}^e(\boldsymbol{\xi}) \otimes \mathbf{h}^e(\boldsymbol{\xi}) \\ &\quad + j_0^e(\boldsymbol{\xi}) \delta_{ab} c_{d_a} \nabla^e \mathbf{h}^e(\boldsymbol{\xi}, \mathbf{x}_0^e) (\mathbf{F}^{-1} \text{cof}(\mathbf{F}))_{n+1}^e \nabla^e \mathbf{h}^e(\boldsymbol{\xi}, \mathbf{x}_0^e)^T dv_{\Omega}. \end{aligned}$$

In particular, these follow from the results

$$\begin{aligned}
& \mathbf{x}_*^e \cdot \mathbf{K}_{\mathbf{xx}n+1}^e d^a \mathbf{x}_{n+1}^e \\
&= \int_{B_0^e} \nabla_{n+1}^e \boldsymbol{\chi}_*^e \cdot (\partial_{\mathbf{A}}^a \mathbf{K} - \mathbf{K} \triangle \mathbf{I})_{n+1}^e [\nabla_{n+1}^e d^a \boldsymbol{\chi}_{n+1}^e] dv_0^e \\
&= \mathbf{x}_*^e \cdot \left\{ \int_{\Omega} j_0^e(\boldsymbol{\xi}) \mathbf{G}_e^T(\boldsymbol{\xi}, \mathbf{x}_{n+1}^e) \{ \partial_1^a \mathbf{k} - \mathbf{k} \triangle \mathbf{1} \}_{n+1}^e \mathbf{G}_e(\boldsymbol{\xi}, \mathbf{x}_{n+1}^e) dv_{\Omega} \right\} d^a \mathbf{x}_{n+1}^e, \\
& \mathbf{x}_*^e \cdot \mathbf{K}_{\mathbf{xd}_an+1}^e d^a \mathbf{d}_{an+1}^e \\
&= \int_{B_0^e} \nabla_{n+1}^e \boldsymbol{\chi}_*^e \cdot (\partial_{d_a}^a \mathbf{K})_{n+1}^e d^a d_{an+1}^e dv_0^e \\
&= \mathbf{x}_*^e \cdot \left\{ \int_{\Omega} j_0^e(\boldsymbol{\xi}) \left((\mathbf{G}_e^T(\boldsymbol{\xi}, \mathbf{x}_{n+1}^e) (\partial_{d_a}^a \mathbf{k})_{n+1}^e \otimes \mathbf{h}_e(\boldsymbol{\xi})) \right) dv_{\Omega} \right\} d^a \mathbf{d}_{an+1}^e, \\
& \mathbf{d}_{a*}^e \cdot \mathbf{K}_{\mathbf{d}_a \mathbf{x}n+1}^e d^a \mathbf{x}_{n+1}^e \\
&= - \int_{B_0^e} (\partial_{\mathbf{A}}^a s_{d_a})_{n+1}^e \cdot (\nabla_{n+1}^e d^a \boldsymbol{\chi}_{n+1}^e) d_{a*}^e \\
&\quad - \left((\partial_{\mathbf{A}}^a \hat{\mathbf{q}}_{d_a})_{n+1}^e (\nabla_{n+1}^e d^a \boldsymbol{\chi}_{n+1}^e) \right) \cdot \nabla_0^e d_{a*}^e dv_0^e \\
&= \mathbf{d}_{a*}^e \cdot \left\{ - \int_{\Omega} j_0^e(\boldsymbol{\xi}) \mathbf{h}_e(\boldsymbol{\xi}) \otimes (\partial_1^a s_{d_a})_{n+1}^e \mathbf{G}_e(\boldsymbol{\xi}, \mathbf{x}_{n+1}^e) \right. \\
&\quad \left. - j_0^e(\boldsymbol{\xi}) \nabla^e \mathbf{h}^e(\boldsymbol{\xi}, \mathbf{x}_0^e) (\partial_1^a \hat{\mathbf{q}}_{d_a})_{n+1}^e \mathbf{G}_e(\boldsymbol{\xi}, \mathbf{x}_{n+1}^e) dv_{\Omega} \right\} d^a \mathbf{x}_{n+1}^e, \\
& \mathbf{d}_{a*}^e \cdot \mathbf{K}_{\mathbf{d}_a \mathbf{d}_b n+1}^e d^a \mathbf{d}_{bn+1}^e \\
&= \int_{B_0^e} (\partial_{d_b}^a \hat{d}_a - \partial_{d_b}^a s_{d_a})_{n+1}^e d^a d_{bn+1}^e d_{a*}^e \\
&\quad + \delta_{ab} (\mathbf{F}^{-1} \text{cof}(\mathbf{F}))_{n+1}^e c_{d_a} \nabla_0^e d^a d_{bn+1}^e \cdot \nabla_0^e d_{a*}^e dv_0^e \\
&= \mathbf{d}_{a*}^e \cdot \left\{ \int_{\Omega} j_0^e(\boldsymbol{\xi}) (\partial_{d_b}^a \hat{d}_a - \partial_{d_b}^a s_{d_a})_{n+1}^e \mathbf{h}^e(\boldsymbol{\xi}) \otimes \mathbf{h}^e(\boldsymbol{\xi}) \right. \\
&\quad \left. + j_0^e(\boldsymbol{\xi}) \delta_{ab} c_{d_a} \nabla^e \mathbf{h}^e(\boldsymbol{\xi}, \mathbf{x}_0^e) (\mathbf{F}^{-1} \text{cof}(\mathbf{F}))_{n+1}^e \nabla^e \mathbf{h}^e(\boldsymbol{\xi}, \mathbf{x}_0^e)^T dv_{\Omega} \right\} d^a \mathbf{d}_{bn+1}^e,
\end{aligned} \tag{4.153}$$

via (4.97), (4.110), (4.120) and (4.123), respectively. The $n_{\text{row}} \times n_{\text{row}}$ matrix $\mathbf{k} \triangle \mathbf{1}$ is defined by

$$\begin{aligned}
\text{row}(\boldsymbol{\Lambda}_*) \cdot (\mathbf{k} \triangle \mathbf{1}) \text{row}(\boldsymbol{\Lambda}) &:= \boldsymbol{\Lambda}_* \cdot (\mathbf{K} \triangle \mathbf{I}) \boldsymbol{\Lambda} \\
&= \boldsymbol{\Lambda}_* \cdot \mathbf{K} \boldsymbol{\Lambda}^T \\
&= \text{sym}(\boldsymbol{\Lambda}_* \boldsymbol{\Lambda}) \cdot \mathbf{K}.
\end{aligned} \tag{4.154}$$

Again, in (4.139) and this latter relation, \mathbf{k} represents the row array whose components are determined by the Cartesian components of the symmetric Kirchhoff stress \mathbf{K} .

4.7 Kinematics in context of adaptive remeshing

Performing an analysis with adaptive remeshing, we face the problem of a reference configuration B_0 changing with every remeshing step. In this context, consider the relations between the involved different configurations, as illustrated in Fig. 4.1.

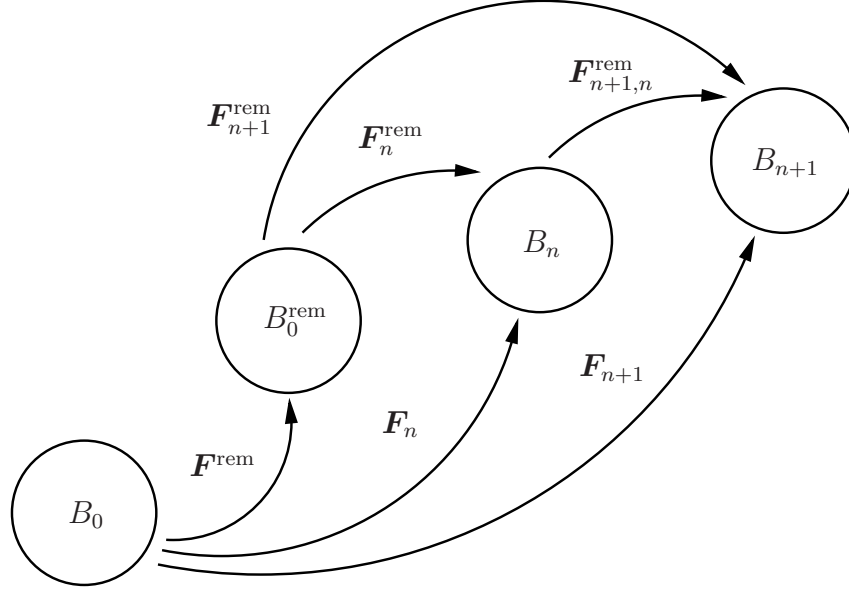


Figure 4.1: Relations between different configurations in context of adaptive remeshing.

The deformation gradient, mapping the original reference configuration B_0 to the configuration B_τ , is given by

$$\mathbf{F}_\tau = \mathbf{F}_\tau^{\text{rem}} \mathbf{F}^{\text{rem}}. \quad (4.155)$$

Here, $\mathbf{F}_\tau^{\text{rem}}$ is the deformation gradient, mapping the new reference configuration B_0^{rem} to the configuration B_τ . The relation between the original reference configuration B_0 and the new reference configuration B_0^{rem} is given by \mathbf{F}^{rem} . From the algorithmic point of view the determination of \mathbf{F}_{n+1} via

$$\mathbf{F}_\tau = \mathbf{F}_{n+1,n}^{\text{rem}} \mathbf{F}_n. \quad (4.156)$$

is preferable. Making use of this formulation \mathbf{F}_n is simply updated as an internal variable and is transferred by the mapping process. Beyond \mathbf{F}_{n+1} the above finite element approximations of the weak momentum balance and the weak evolution-field equations, as well as the corresponding element tangents require the information about the reference coordinates \mathbf{x}_0^s . As will be shown in the following, a mapping of this information can be avoided, by transformation of the corresponding expressions. In this context, note that making use of

$$j_0^e(\boldsymbol{\xi}) dv_\Omega = \det(\mathbf{F}_{n+1})^{-1} j_{n+1}^e(\boldsymbol{\xi}) dv_\Omega \quad (4.157)$$

and

$$\nabla^e \mathbf{h}^e(\boldsymbol{\xi}, \mathbf{x}_0^e) = \nabla^e \mathbf{h}^e(\boldsymbol{\xi}, \mathbf{x}_{n+1}^e) \mathbf{F}_{n+1} \quad (4.158)$$

in combination with (4.115) and (4.135), the element nodal force arrays of the corresponding finite element discretization of the weak momentum balance (4.139)₁ and the weak field-evolution equations (4.139)₂ can be transformed to

$$\begin{aligned} \mathbf{f}_{\mathbf{x}n+1}^e &:= \mathbf{M}_{\mathbf{xx}n+1}^{e\text{rem}} \ddot{\mathbf{x}}_{n+1}^e \\ &+ \int_{\Omega} j_{n+1}^e(\boldsymbol{\xi}) \mathbf{G}_e^T(\boldsymbol{\xi}, \mathbf{x}_{n+1}^e) (\det(\mathbf{F})^{-1} \mathbf{k})_{n+1}^e dv_{\Omega} \\ &- \int_{\partial\Omega} |\text{cof}(\mathbf{J}_e(\boldsymbol{\xi}, \mathbf{x}_0^{e\text{rem}})) \mathbf{n}_{\Omega}| \mathbf{H}_e^T(\boldsymbol{\xi}) \mathbf{p}_{n+1}^{e\text{rem}} da_{\Omega} \end{aligned} \quad (4.159)$$

and

$$\begin{aligned} \mathbf{f}_{d_a n+1}^e &:= \int_{\Omega} j_{n+1}^e(\boldsymbol{\xi}) \left(\det(\mathbf{F}_{n+1})^{-1} (\hat{d}_a - s_{d_a})_{n+1}^e \mathbf{h}^e(\boldsymbol{\xi}) \right. \\ &\quad \left. - c_{d_a} \nabla^e \mathbf{h}^e(\boldsymbol{\xi}, \mathbf{x}_{n+1}^e) \nabla^e \mathbf{h}^e(\boldsymbol{\xi}, \mathbf{x}_{n+1}^e)^T \mathbf{d}_{a n+1}^e \right) dv_{\Omega} \\ &+ \int_{\partial\Omega} \hat{q}_{d_a 0 n+1}^{e\text{rem}} |\text{cof}(\mathbf{J}_e(\boldsymbol{\xi}, \mathbf{x}_0^{e\text{rem}})) \mathbf{n}_{\Omega}| \mathbf{h}^e(\boldsymbol{\xi}) da_{\Omega} \end{aligned} \quad (4.160)$$

respectively, with

$$\mathbf{M}_{\mathbf{xx}n+1}^e := \int_{\Omega} j_{n+1}^e(\boldsymbol{\xi}) \det(\mathbf{F}_{n+1})^{-1} \varrho_0 \mathbf{H}_e^T(\boldsymbol{\xi}) \mathbf{H}_e(\boldsymbol{\xi}) dv_{\Omega}. \quad (4.161)$$

Here, $\mathbf{x}_0^{e\text{rem}}$ is the array of element reference coordinates, referring to the new reference configuration B_0^{rem} . $\mathbf{p}_{n+1}^{e\text{rem}}$ and $\hat{q}_{d_a 0 n+1}^{e\text{rem}}$ are the referential traction field and boundary flux, respectively, both prescribed on the corresponding part of $\partial B_0^{\text{rem}}$. Correspondingly, the transformations of the element tangents (4.152) are given by

$$\begin{aligned} \mathbf{K}_{\mathbf{xx}n+1}^e &= \int_{\Omega} j_{n+1}^e(\boldsymbol{\xi}) \mathbf{G}_e^T(\boldsymbol{\xi}, \mathbf{x}_{n+1}^e) \det(\mathbf{F}_{n+1})^{-1} \{ \partial_1^a \mathbf{k} - \mathbf{k} \Delta \mathbf{1} \}_{n+1}^e \mathbf{G}_e(\boldsymbol{\xi}, \mathbf{x}_{n+1}^e) dv_{\Omega}, \\ \mathbf{K}_{\mathbf{xd}_a n+1}^e &= \int_{\Omega} j_{n+1}^e(\boldsymbol{\xi}) \left((\mathbf{G}_e^T(\boldsymbol{\xi}, \mathbf{x}_{n+1}^e) \det(\mathbf{F}_{n+1})^{-1} (\partial_{d_a}^a \mathbf{k})_{n+1}^e \otimes \mathbf{h}_e(\boldsymbol{\xi})) \right) dv_{\Omega}, \\ \mathbf{K}_{d_a \mathbf{x} n+1}^e &= - \int_{\Omega} j_{n+1}^e(\boldsymbol{\xi}) \mathbf{h}_e(\boldsymbol{\xi}) \otimes (\det(\mathbf{F})^{-1} \partial_1^a s_{d_a})_{n+1}^e \mathbf{G}_e(\boldsymbol{\xi}, \mathbf{x}_{n+1}^e) \\ &\quad - j_{n+1}^e(\boldsymbol{\xi}) \nabla^e \mathbf{h}^e(\boldsymbol{\xi}, \mathbf{x}_{n+1}^e) (\det(\mathbf{F})^{-1} \mathbf{F} \partial_1^a \hat{q}_{d_a})_{n+1}^e \mathbf{G}_e(\boldsymbol{\xi}, \mathbf{x}_{n+1}^e) dv_{\Omega}, \\ \mathbf{K}_{d_a d_b n+1}^e &= \int_{\Omega} j_{n+1}^e(\boldsymbol{\xi}) (\det(\mathbf{F})^{-1} \partial_{d_b}^a \hat{d}_a - \det(\mathbf{F})^{-1} \partial_{d_b}^a s_{d_a})_{n+1}^e \mathbf{h}^e(\boldsymbol{\xi}) \otimes \mathbf{h}^e(\boldsymbol{\xi}) \\ &\quad + j_{n+1}^e(\boldsymbol{\xi}) \delta_{ab} c_{d_a} \nabla^e \mathbf{h}^e(\boldsymbol{\xi}, \mathbf{x}_{n+1}^e) \nabla^e \mathbf{h}^e(\boldsymbol{\xi}, \mathbf{x}_{n+1}^e)^T dv_{\Omega}. \end{aligned} \quad (4.162)$$

Note, that based on relations (4.108) and (4.122), $\partial_1^a \mathbf{k}$ and $\det(\mathbf{F})^{-1} \mathbf{F} \partial_1^a \hat{q}_{d_a}$ are independent of \mathbf{F}_{n+1} . Further, the local algorithm to determine the current stress state \mathbf{k}_{n+1} as well as the source terms $s_{d_a n+1}$ are based on $\ln \mathbf{V}_{E n+1}^{\text{tr}}$ and thus on $\mathbf{B}_{E n}$ and $\mathbf{F}_{n+1, n}$. Then, in the transformed relations above, the current deformation gradient is present only in terms of

$$\begin{aligned} \det(\mathbf{F}_{n+1}) &= \det(\mathbf{F}_{E n+1}) \det(\mathbf{F}_{P n+1}) \\ &= \det(\mathbf{B}_{E n+1})^{\frac{1}{2}} \exp(\bar{\alpha}_{H n+1}). \end{aligned} \quad (4.163)$$

The latter expression is based on the form

$$\overline{\ln(\det(\dot{\mathbf{F}}_{\mathbf{P}_{n+1}}))} = \text{tr}(\mathbf{L}_{\mathbf{P}_c}) , \quad (4.164)$$

in combination with (4.30). Consequently, in context of the above model formulation, the set of state dependent variables, that have to be transferred reduces to $(\mathbf{B}_{E_n}, \bar{\alpha}_{D_n}, \bar{\alpha}_{H_n}, \bar{d}_n)$. In case of an adiabatic analysis, we have the additional state dependent variable θ_n . With these definitions at hand, our adaptive finite element framework is complete and we now turn to its application in context of metal cutting.

Chapter 5

Local and non-local modeling of the cutting process

Abstract– In this chapter, the finite element framework, consisting of the adaptive remeshing scheme and the extended thermodynamic formulation, is applied to the simulation of the high speed cutting process and results are discussed. Here, we start with the discussion of heat conduction excluding damage. As will be shown, thermal softening alone leads to a delayed chip segmentation and furthermore to unrealistic high temperatures inside the main deformation zone. Improvements are demonstrated in terms of an additional damage formulation. As will be shown, due to lack of any dependence on time- or lengthscale for local damage development, as, e.g., given for the development of temperature in terms of the heat balance equation, simulation results show a dependence on the local element edge length for such a local formulation. In this context improvements by a non-local formulation of damage as well as the implementation of the non-local formulation in a commercial code are discussed. Additionally, we present the issue of non-isochoric plasticity and the related pressure dependent damage development. This chapter closes with the presentation of simulation results, calculated in context of a benchmark study.

5.1 Implementation of local, thermo-viscoplasticity including heat conduction

In what follows, we apply our developed adaptive finite element framework to the modeling and simulation of orthogonal cutting. For that purpose, our material model is implemented in ABAQUS/Standard, in particular in terms of the user subroutine UMAT. Starting our investigation on the process of cutting we do not consider any damage development at the moment and further, restrict ourselves to the simple case of local thermo-viscoplasticity, including heat conduction ($\ell_{I0} = 0$, $I = D, H$, $\ell_{d0} = 0$ and $k_0 > 0$). In particular, the development of damage is deactivated by setting the saturation rates r_I , $I = D, H$ in (4.82)₁ to zero. Now, in combination with (4.38) in (4.78) and $D_2 > 0$, isochoric plasticity is enforced. As discussed above, local modeling of the field quantities \bar{d} and $\bar{\alpha}_I$, $I = D, H$ is established in terms of the substitutions (4.84), (4.85) and (4.87), (4.88), respectively. Consequently, the remaining evolution-field equation is the heat balance equations as given by (4.56)₃. Here, we make use of a temperature dependent description of the thermal conductivity as given in Pottlacher et al. (2002). In particular k_0 varies linearly between $k_0(\theta = 300K) = 10.85$ [$\text{Wm}^{-1}\text{K}^{-1}$] and $k_0(\theta = 1570K) = 31.85$ [$\text{Wm}^{-1}\text{K}^{-1}$]. As documented in the ABAQUS Theory Manual (ABAQUS-Manual (2008)), the weak forms of the corresponding balance equations are formulated in terms of the current configuration B_{n+1} . As gradients of the corresponding quantities are also calculated with respect to the current coordinates, the ABAQUS implementation and our formulation, as given in terms

of the transformed element nodal force arrays (4.159), (4.160) and corresponding element tangents (4.162), respectively, correspond. (For further details, the interested reader is referred to ABAQUS-Manual (2008), Theory Manual, 1.51 (Equilibrium and virtual work), 2.11 (Heat transfer)). The implementation in ABAQUS-UMAT is generally achieved by passing the quantities and corresponding derivatives, which depend on the constitutive formulation of the material to the user subroutine. As documented in the Abaqus User Subroutines Reference Manual (ABAQUS-Manual (2008), User Subroutines Reference Manual, 1.1.34 (UMAT)), these are defined as

$$\begin{aligned}
\text{STRESS} &:= (\det(\mathbf{F})^{-1} \mathbf{k})_{n+1}^e \\
\text{RPL} &:= (\det(\mathbf{F})^{-1} \omega_r)_{n+1}^e \\
\text{DDSDDE} &:= (\det(\mathbf{F})^{-1} \partial_{\text{sym}(1)}^a \mathbf{k})_{n+1}^e \\
\text{DDSDDT} &:= (\det(\mathbf{F})^{-1} \partial_{\theta}^a \mathbf{k})_{n+1}^e \\
\text{DRPLDE} &:= (\det(\mathbf{F})^{-1} \partial_{\text{sym}(1)}^a \omega_r)_{n+1}^e \\
\text{DRPLDT} &:= (\det(\mathbf{F})^{-1} \partial_{\theta}^a \omega_r)_{n+1}^e
\end{aligned} \tag{5.1}$$

Here, the linearization of the Kirchhoff stress \mathbf{K} with respect to the symmetric part of \mathbf{A}_{n+1} , stems from a linearization, based on the Jaumann-rate of \mathbf{K} (see ABAQUS-Manual (2008), User Subroutines Reference Manual, 1.1.34 (UMAT) for further details). Note, that the determination of the above quantities follows from (4.159), (4.160) and (4.162) in terms of $d_a = \theta$. The simulation results to follow are based on the material parameter values given in Table 5.1. For all simulations to follow, the allowable error is set to $\|\mathbf{e}_{\epsilon_p}\|_{\max} = 0.05$. Additionally, we apply the equivalent deviatoric plastic deformation $\bar{\alpha}_D$ and the deviatoric plastic rate $\dot{\bar{\alpha}}_D$, in particular normalized to the mean value, as additional refinement indicators. Here, the element size varies linearly between $\bar{\alpha}_{D1} = 0.7$ and $\bar{\alpha}_{D2} = 0.9$ for the deviatoric plastic deformation and between $\dot{\bar{\alpha}}_{D1} = 1.0$ and $\dot{\bar{\alpha}}_{D2} = 1.3$ for the normalized deviatoric plastic rate. To study the

θ_0 [K]	λ_0 [GPa]	μ_0 [GPa]	α_0 [K ⁻¹]	ρ_0 [kg/ m ³]	$c_0 \rho_0$ [J/kg K]		
300.	110.5	80.	4.3×10^{-6}	8.19325×10^3	435		
a_{jc} [MPa]	b_{jc} [MPa]	n_0	θ_{M0} [K]	m_0	c_{jc}	$\dot{\alpha}_0$ [s ⁻¹]	β_0
450	2012.7	1.6332	1570	1.3	0.017	0.001	0.9

Table 5.1: Johnson-Cook model parameters for Inconel 718 (partly from Sievert et al. (2003)) determining the model relations (4.62) and (4.63).

influence of heat conduction on the development of chip formation, we choose three different cutting speeds v_c at two different tool rake angles γ . The tool edge radius is fixed at $r=20 \mu\text{m}$. The cutting depth is chosen as $t_c=150 \mu\text{m}$. The different cutting conditions for the different cases, discussed in the following are summarized in Table 5.2.

The simulation results generally confirm, that the decreasing influence of heat conduction with increasing cutting speeds favors the formation of localized deformation patterns, up to shear banding. The change from a continuous, to a segmented chip at a cutting speed of $v_c=200 \text{ mmin}^{-1}$, as reported, e.g., by Hoffmeister and Wessels (2005) is, at least for the given cutting conditions, not being reproduced. Further, the decrease of the specific cutting forces, generally observed in practice, is confirmed only for $\gamma=-7^\circ$ (see Figure 5.1). As reported in the work of Clos et al. (2003) the maximum temperatures inside the main deformation zone for

heat conduction	γ [°]	v_c [mmin ⁻¹]
h 0 100	0	100
h 0 200	0	200
h 0 1000	0	1000
h -7 100	-7	100
h -7 200	-7	200
h -7 1000	-7	1000

Table 5.2: Cutting conditions for the local model with heat conduction.

$v_c=1000\text{mmin}^{-1}$ have been detected with approximately 1000 K. In our simulation, we detect temperatures of 1200 K and higher (see Figure 5.3). The deviation between the experimentally detected and simulated temperatures suggests an additional softening effect, which decreases the yield strength and thus, plastic heating inside these highly deformed areas. In literature, this additional softening effect is often modeled in terms of ductile damage (see e.g. Sievert et al. (2003)).

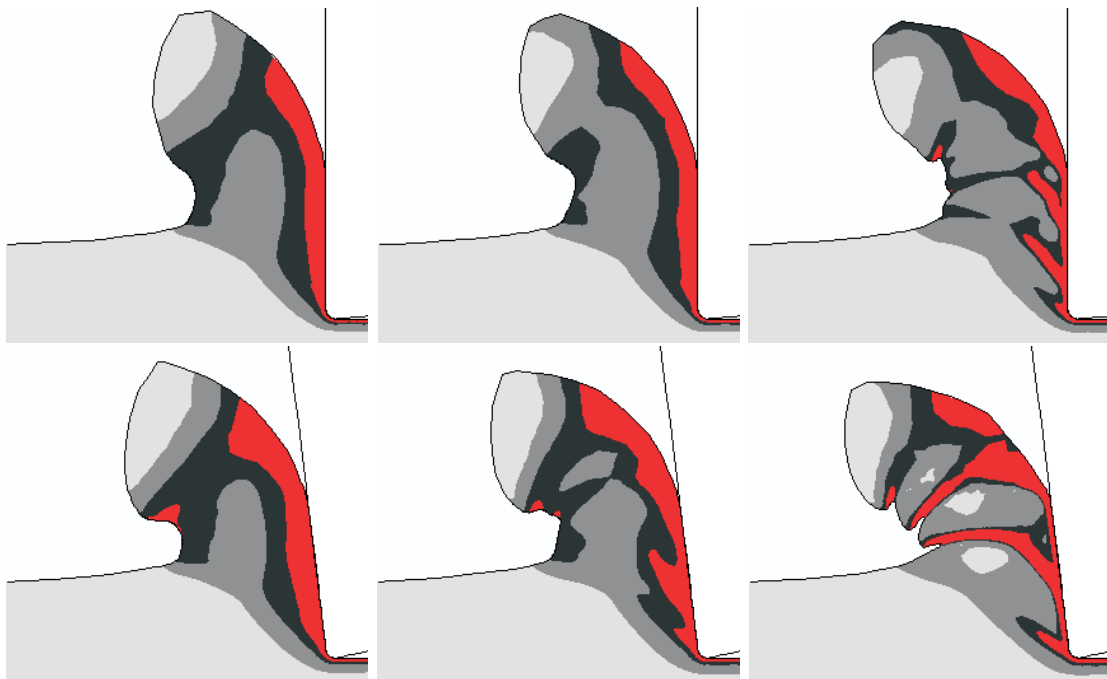


Figure 5.1: Chip formation for the local model with heat conduction for different tool rake angles (above: $\gamma=0^\circ$ below: $\gamma=-7^\circ$) at different cutting speeds (left: 100mmin^{-1} , middle: 200mmin^{-1} , right: 1000mmin^{-1}). The contour plots show the distribution of accumulated inelastic deformation.

5.2 Local, thermo-viscoplasticity including heat conduction and ductile damage

Based on the above results, we will now activate the development of damage. In what follows, we assume that damage development or more generally spoken, isotropic softening, induced

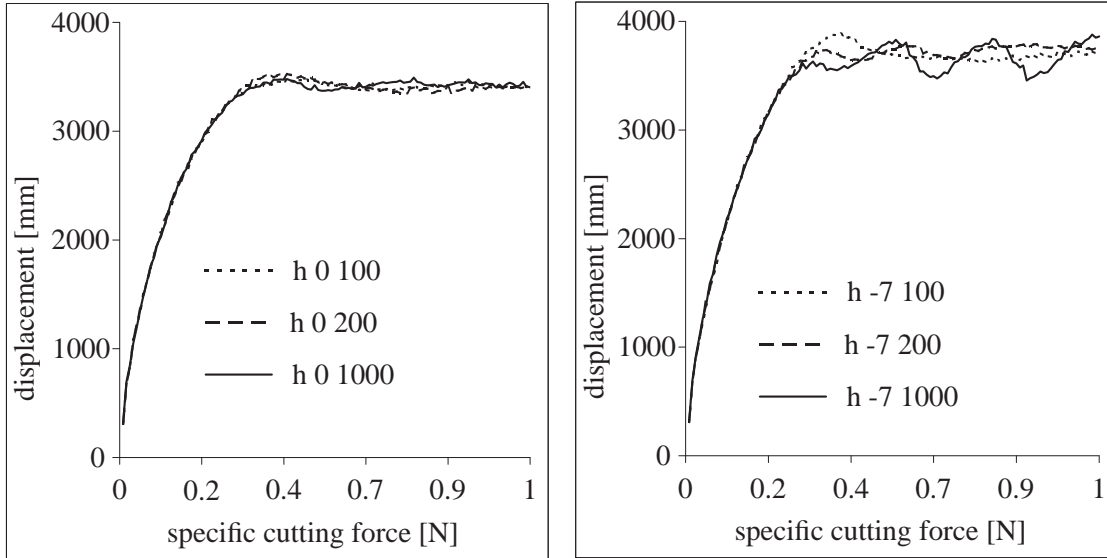


Figure 5.2: Cutting forces for the cutting simulation with local modeling and heat conduction for different tool rake angles γ and different cutting speeds v_c , as specified in Table 5.2.

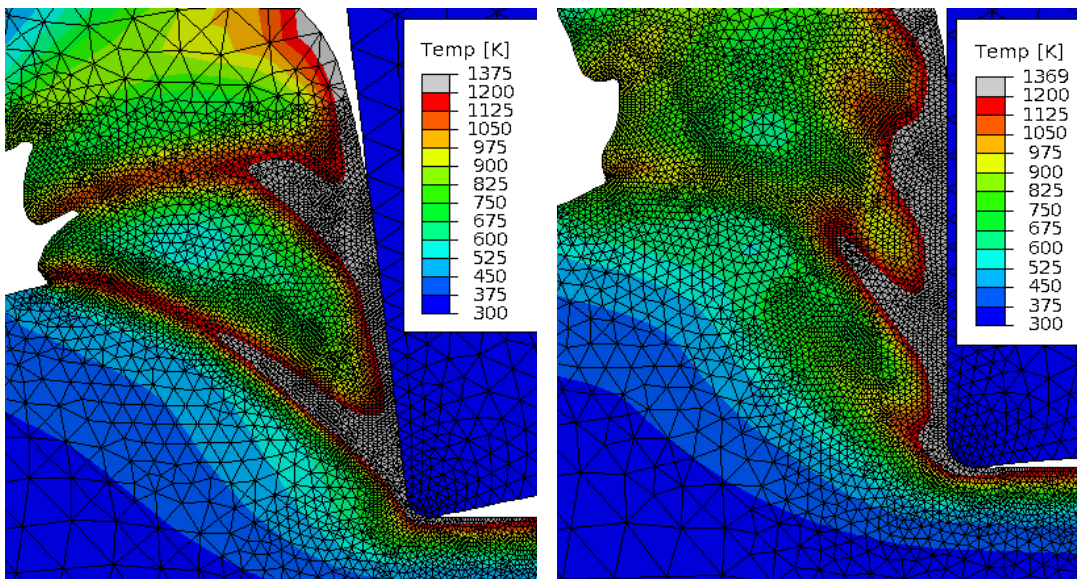


Figure 5.3: Distribution of temperature for the cutting simulation at $v_c = 1000 \text{ mm min}^{-1}$. Left: $\gamma = -7^\circ$. Right: $\gamma = 0^\circ$. Contrary to experimental observations (see e.g. Clos et al. (2003)), the temperatures inside the main deformation zone are above 1000 K.

by purely deviatoric plastic deformation d_D is activated beyond a critical value of plastic deformation ($\alpha_{Dd} > 0$). A similar behavior (rapidly increased development of damage beyond a specific point) is modeled in Sievert et al. (2003) by describing the development of the softening quantity in terms of an exponential function. Damage, related to spherical processes d_H is interpreted as growth and coalescence of voids and thus, starts parallel with the development of α_H , which enforces $\alpha_{Hd} = 0$. Currently lacking any detailed experimental data, we fit the saturation rate to the area of increased damage production, described by the model of Sievert et al. (2003).

In particular we set $r_D=5.0$. Rather than (4.36) for d_H , we work with the simplified form

$$\dot{d}_H = r_H (1 - d_H) \dot{\alpha}_H, \quad (5.2)$$

Now, setting $r_H = 1$ simply identifies d_H as void volume fraction. For the moment, we recognize the void volume fraction as the only softening quantity induced by $\dot{\alpha}_H$. Incorporating other effects (e.g., spreading of microcracks) can generally be expressed by setting $r_H > 1$. Assuming that pressure dominates in the primary deformation zone, we restrict to the simple case of isochoric plasticity, for the moment. This is actually enforced by choosing a sufficiently high activation stress, in particular we set $D_1 = 10^6$ in (4.38). In context of simulating the process of machining, the vanishing influence of heat conduction with increasing cutting speed, results in enhanced thermal softening, shear banding and a change from a continuous to a segmented chip at a critical cutting speed. Performing a series of thermo-mechanical simulations with heat conduction at the desired critical cutting speed allows the identification of the onset of deviatoric damage triggered by α_{Dd} . Although this parameter should be identified in terms of an appropriate experiment in general, this method gives valuable hints for its lower boundary. As presented in the previous section, the cutting conditions, here in particular the tool rake angle, has a significant influence on the chip formation. Consequently, we have to restrict to a specific set of cutting conditions, when performing such parameter studies. Lacking any detailed experimental data, we restrict to a tool rake angle of $\gamma = 0^\circ$ for the moment. The set of parameters for the local damage model (4.36) and for the cutting conditions used in the following study are summarized in Table 5.3

heat conduction with deviatoric damage	γ [°]	v_c [mmmin ⁻¹]	r_D	α_{Dd}
h d 0 100 2.0	0	100	5	2.0
h d 0 200 2.0	0	200	5	2.0
h d 0 1000 2.0	0	1000	5	2.0
h d 0 100 1.5	0	100	5	1.5
h d 0 200 1.5	0	200	5	1.5
h d 0 1000 1.5	0	1000	5	1.5

Table 5.3: Parameters for local damage model (4.36).

As can be seen from the contour plots for the chip formation (Figure 5.4), the minimum value for the onset of deviatoric damage can be approximated with $\alpha_{Dd} = 1.5$. At this value, we detect the onset of shear banding for the chosen critical cutting velocity $v_c = 200 \text{mmmin}^{-1}$. Shear banding is just repressed for $v_c = 100 \text{mmmin}^{-1}$. For $\alpha_{Dd} = 2$ shear band formation is not detected for both cutting speeds, $v_c = 200 \text{mmmin}^{-1}$ and $v_c = 100 \text{mmmin}^{-1}$, respectively. Again, this result is strictly related to the given cutting parameters in combination with the given parameters for the discussed material model. Comparing the plots for the specific cutting force (Figure 5.5), we observe an decrease with activated damage development. Additionally to the periodic stress drops, induced by localized plastic deformation, we detect a decrease of the peak values as well. The temperature plot for the main deformation zone shows a reduction of the maximum temperatures to approximately 1100 K, which is still higher than the temperatures, observed in experimental investigations. A further reduction can generally be obtained by modeling an earlier onset of softening, which implies a lower value of α_{Dd} . In context of our current model

formulation this is unprofitable as this would also lead to an earlier onset of segmented chip formation for lower cutting speeds. To resolve this conflict, the model can be enhanced by, e.g., introducing a rate dependent formulation of α_{Dd} . Lacking any detailed experimental data and on a detailed micro mechanical motivation, we keep this in mind for future work but restrict to the constant value of α_{Dd} for the moment.

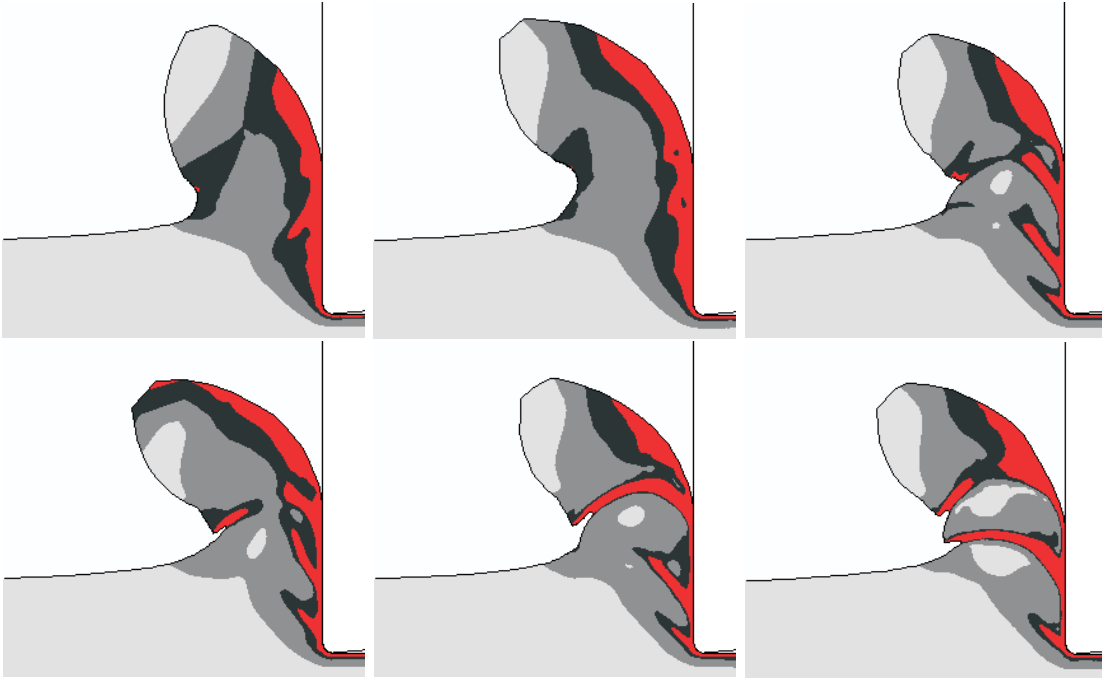


Figure 5.4: Chip formation for the local model with heat conduction and damage for different triggering of deviatoric damage (above: $\alpha_{Dd} = 2.0$ below: $\alpha_{Dd} = 1.5$) at different cutting speeds (left: 100mmmin^{-1} , middle: 200mmmin^{-1} , right: 1000mmmin^{-1}). The contour plots show the distribution of accumulated inelastic deformation.

5.3 Non-local formulation in combination with a commercial code

Recalling the set of governing equations given by the linear momentum balance (4.55) and the additional evolution field equations (4.56), note that the mechanical boundary value problem alone (4.55) is generally lengthscale independent. Working with a rate dependent constitutive model for our material as we do, a dependence on the timescale is introduced at least. In the above simulations with heat conduction, the model is enriched with an additional length- and timescale dependence. In our simulations this additional dependence on the timescale shows in the dependence of chip formation on the cutting speed (see Figure 5.1 and Figure 5.4). Moreover, due to the inherent dependence of the heat flux on the dimension of length, we also have a lengthscale dependence. Considering, e.g., the case of adiabatic heating ($k_0 \rightarrow 0$) in combination with a rate independent material model, the dependence on the cutting speed as well as on the dimension of our model would actually vanish. In terms of the heat balance equation, both, time- and lengthscale dependence are given for $k_0 \geq 0$. Corresponding to $k_0 \rightarrow 0$, the influence on both time- and lengthscale vanishes and the mechanical boundary value problem

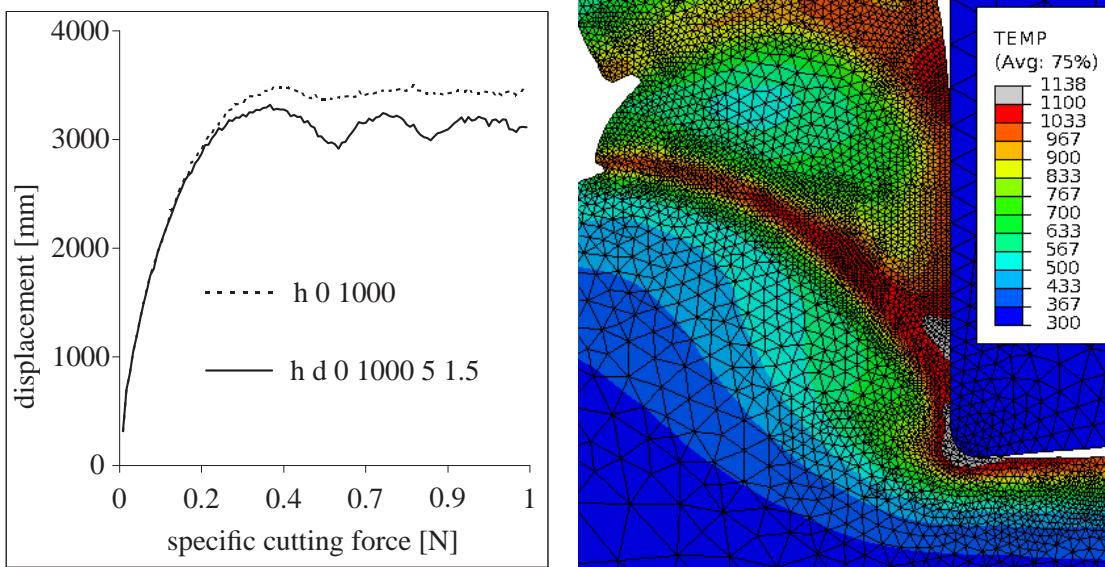


Figure 5.5: Influence of ductile damage on the specific cutting force and on the development of temperature inside the main deformation zone.

is again independent on the lengthscale for local modeling of the plastic rates and local modeling of the damage (e.g., $\ell_{H0} \rightarrow 0$, $\ell_{D0} \rightarrow 0$, $\ell_{d0} \rightarrow 0$). Under the assumption of non-local interaction of voids in terms of damage development or non-local interaction of dislocation activation in terms of plastic processes, however, we would actually expect a dependence on the dimension (lengthscale) of our boundary value problem. In context of a finite element solution of the boundary value problem given by (4.55) and (4.56), the following lengthscales are significant. As discussed above we have the set of quantities describing non-local processes like heat conduction, interaction of voids and interaction of dislocation processes, in particular the thermal conductivity k_0 and the internal length parameters ℓ_{da0} , respectively. Additionally, we have the characteristic lengthscale of the boundary value problem ℓ_s (structural lengthscale, e.g., cutting depth) and in context of a finite element solution the characteristic element edge length ℓ_h given, e.g., by the minimum element edge length h_{\min} . The ratio ℓ_{da0}/ℓ_h is important in context of mesh dependence. This issue will also be discussed in what follows. As shown in Chapter 2, the onset of shear banding, and thus the segmentation frequency, is strongly related to the minimum element edge length of the finite element discretization for local modeling of the quantities governing the effect of softening. This so-called pathological mesh dependence is deeply rooted in the local character of the governing equations and can thus not be eliminated by adaptive remeshing. Starting with the discussed local formulation with heat conduction, this effect becomes obvious. As can be seen in terms of the contour plots for the accumulated inelastic deformation in Figure 5.6 further mesh refinement leads to a sharper localization of plastic deformation and moreover, to completely different deformation patterns. Motivated by the successful application of a non-local formulation of the damage in previous works (see e.g. Reusch et al. (2008)), here in terms of a non-local Gurson model, in context of crack propagation in metal matrix composites, we will now apply such a non-local damage formulation in context of simulating the process of cutting. In particular we make use of the model formulation discussed in the previous chapter and, as in the discussion for the case of heat conduction,

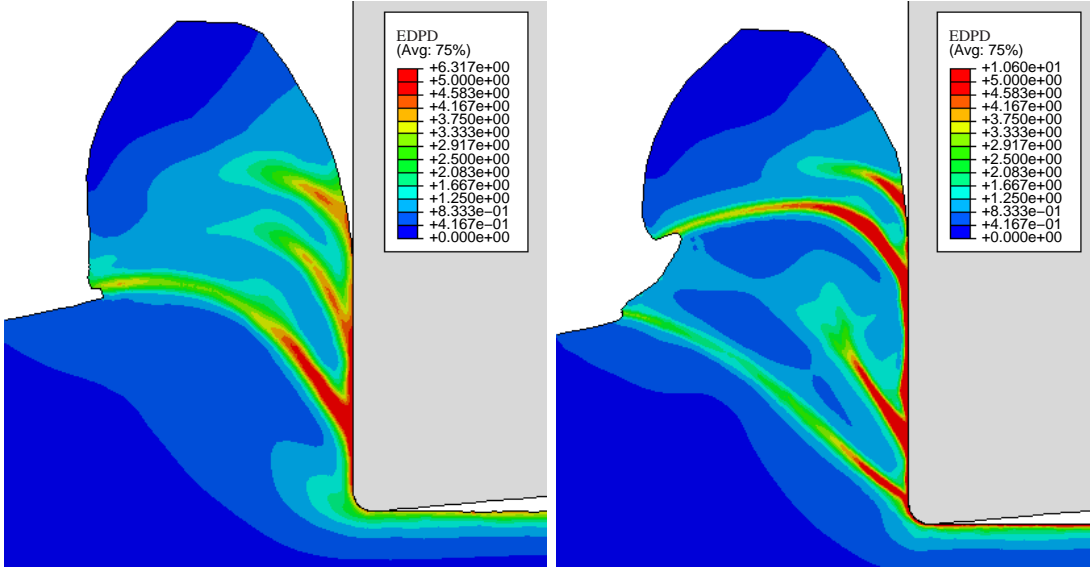


Figure 5.6: Demonstration of pathological mesh dependence. The reduction of the minimum edge length causes sharper localization resulting in different deformation patterns. Here, the minimum element edge length are set to $h_{\min}=0.1/16\text{mm}$ (left) and $h_{\min}=0.1/32\text{mm}$ (left). The figures show the distribution of equivalent deviatoric plastic deformation.

restrict to the case of isochoric plasticity for the moment. The non-local damage formulation as given in terms of (4.56)₂ in combination with (4.66) and (4.37) is analogous to the non-local class, applied in Reusch et al. (2008). Contrary to this work, the local development of damage, induced by deviatoric processes \dot{d}_d , to which we restrict in case of isochoric plasticity for the moment, is described by (4.33). As in contrast to nonlocal damage or nonlocal plasticity, heat conduction is a standard implementation in commercial finite element codes, we will now make an attempt to adapt our formulation to this implementation. For this purpose, recall the weak evolution-field equations, as given in terms of (4.114). In this context note that making use of the substitutions

$$\begin{aligned}
 \hat{\alpha}_I &= c_0(\dot{\alpha}_{In+1} - \dot{\alpha}_{In})/t_{n+1,n} \\
 s_{\dot{\alpha}_{In+1}} &= c_0(\dot{\alpha}_{In+1} - \dot{\alpha}_{In})/t_{n+1,n} \\
 c_{\hat{\alpha}_I} &= (c_0 \ell_{I0}^2)/t_{n+1,n} \\
 \hat{d} &= c_0(\dot{d}_{n+1} - \dot{d}_n)/t_{n+1,n} \\
 s_{\dot{d}_{n+1}} &= c_0(\dot{d}_{Dn+1} + \dot{d}_{Hn+1} - \dot{d}_n)/t_{n+1,n} \\
 c_{\hat{d}} &= (c_0 \ell_{d0}^2)/t_{n+1,n} \\
 \hat{\theta} &= c_0(\theta_{n+1} - \theta_n)/t_{n+1,n} \\
 s_{\theta_{n+1}} &= \omega_r \\
 c_{\hat{\theta}} &= k_0
 \end{aligned} \tag{5.3}$$

instead of (4.116) yields the identical formulation for the evolution-field equations, but now the algorithmic formulation for the equivalent plastic deformation and damage correspond to that for the temperature. Practically, the implementation of the non-local description is established by setting the temperature DOF as d_a and returning the rate of plastic heating and corresponding derivatives as s_{d_a} and corresponding derivatives of s_{d_a} , respectively. The local algorithm

remains untouched and the adaption of the corresponding derivatives is straightforward by following the general framework developed above. Working, e.g., with the finite element code ABAQUS, the adaption of the heat conduction coefficient in terms of the time increment $t_{n+1,n}$ becomes possible by making use of the user subroutine USDFLD (user defined field) in combination with a field dependent heat conduction coefficient. In particular, we make use of the linear relation

$$c_{0(d_a)}(q_f) = c_0 \ell_{d_0}^2 q_f \quad , \quad (5.4)$$

with the field quantity simply calculated as

$$q_f = t_{n+1,n}^{-1} \quad . \quad (5.5)$$

Note, that the information passed to the user subroutine is now given by the adapted terms

$$\begin{aligned} \text{STRESS} &:= (\det(\mathbf{F})^{-1} \mathbf{k})_{n+1}^e \\ \text{RPL} &:= (\det(\mathbf{F})^{-1} s_{d_a})_{n+1}^e \\ \text{DDSDDE} &:= (\det(\mathbf{F})^{-1} \partial_{\text{sym}(\mathbf{I})}^a \mathbf{k})_{n+1}^e \\ \text{DDSDDT} &:= (\det(\mathbf{F})^{-1} \partial_{d_a}^a \mathbf{k})_{n+1}^e \\ \text{DRPLDE} &:= (\det(\mathbf{F})^{-1} \partial_{\text{sym}(\mathbf{I})}^a s_{d_a})_{n+1}^e \\ \text{DRPLDT} &:= (\det(\mathbf{F})^{-1} \partial_{d_a}^a s_{d_a})_{n+1}^e \end{aligned} \quad (5.6)$$

with corresponding s_{d_a} given by (5.3). The user subroutine UMAT only offers the degrees of freedom displacement and temperature, which enforces one to model the development of the temperature as adiabatic. As θ is now treated as an internal variable we have to make use of substitution (4.86).

To investigate the behavior of the non-local damage formulation separated from thermal softening we start with a simple numerical example without adaptive remeshing. Here, we apply the example of a notched tensile specimen as introduced by Sievert et al. (2003) and later also applied in the work of Flatten (2007). The specimen with dimensions and boundary conditions as given in Figure 5.7 is elongated quasi-static, which allows isothermal conditions. Further, the onset of damage is triggered at $\alpha_{\text{Dd}} = 0$ to allow a pronounced development of damage at early stages of elongation. This avoids distorted elements as expected in case of a required long elongation of the specimen with $\alpha_{\text{Dd}} = 1.5$. The simulation results given in Figure 5.8 and Figure 5.9 demonstrate the influence of the above introduced lengthscales ℓ_{d_0} , ℓ_s and ℓ_h . The structural lengthscale is arbitrarily fixed at $\ell_s := 1$ mm. As stated above, we are mainly interested in resolving lengthscale effects, but in terms of a numerical solution of the boundary value problem also the issue of mesh dependence is important (see Figure 5.6). The simulations have been carried out with three different meshes ($\ell_h=0,25\text{mm}$, $\ell_h=0,125\text{mm}$, $\ell_h=0,0625\text{mm}$) at two different material lengthscales ($\ell_{d_0}=0,1\text{mm}$, $\ell_{d_0}=0,5\text{mm}$). As can be seen from both, the force-displacement diagrams (Figure 5.8) and the corresponding contour plots (Figure 5.9), the tendency of converging solutions can be observed for sufficiently large ratios ℓ_{d_0}/ℓ_h . For small values of this ratio, the well known pathological mesh dependence is observed. For the given problem, adequate results are detected for $\ell_{d_0}/\ell_h > 2$. Generally spoken, the local mesh size should be smaller than the material lengthscale, to resolve the underlying BVP. The effect of different ratios ℓ_{d_0}/ℓ_s is emphasized in Figure 5.10. As can be observed, higher values of ℓ_{d_0}/ℓ_s

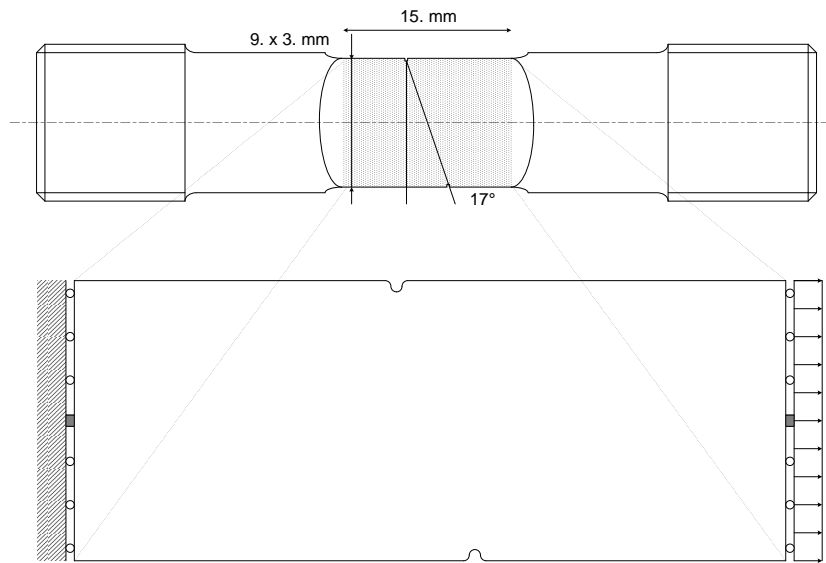
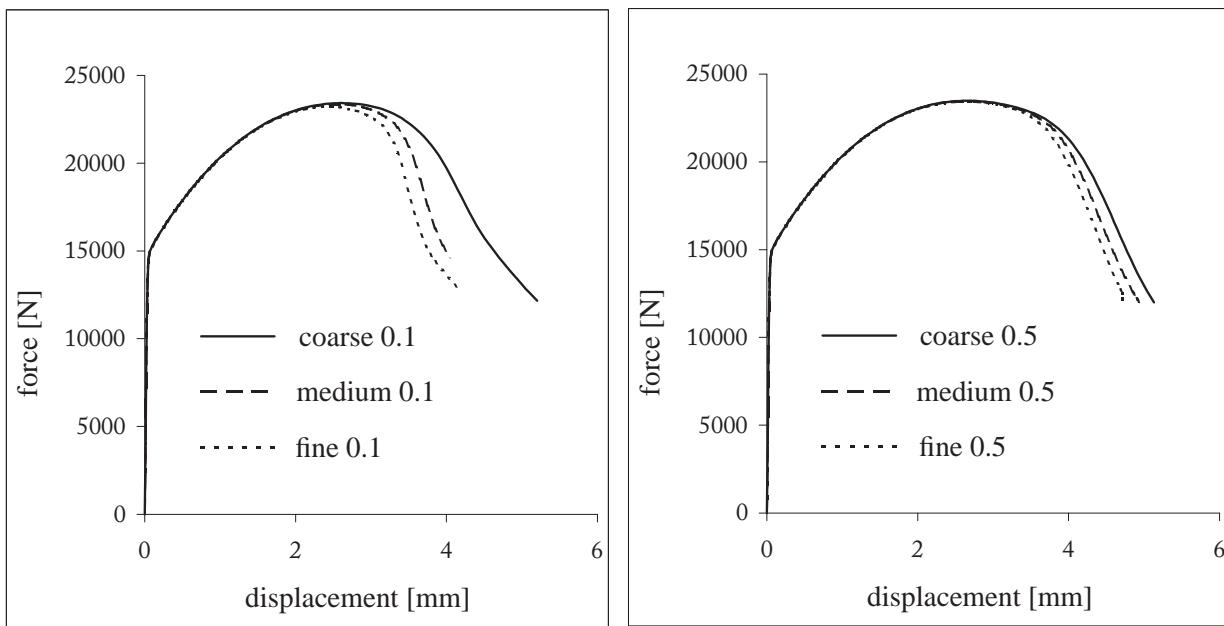


Figure 5.7: Notched tensile specimen as introduced by Sievert et al. (2003) and later also applied in the work of Flatten (2007).



non-local damage	ℓ_{d0} [mm]	ℓ_h [mm]	ℓ_{d0}/ℓ_h
coarse 0.1	0.1	0.25	0.4
medium 0.1	0.1	0.125	0.8
fine 0.1	0.1	0.0625	1.6
coarse 0.5	0.5	0.25	2.0
medium 0.5	0.5	0.125	4.0
fine 0.5	0.5	0.0625	8.0

Figure 5.8: Force-displacement diagrams for the notched tensile specimen as given in Figure 5.7. The specimen is elongated quasi-static, which allows isothermal conditions. The tendency of converging solutions can be observed for sufficiently large ratios ℓ_{d0}/ℓ_h

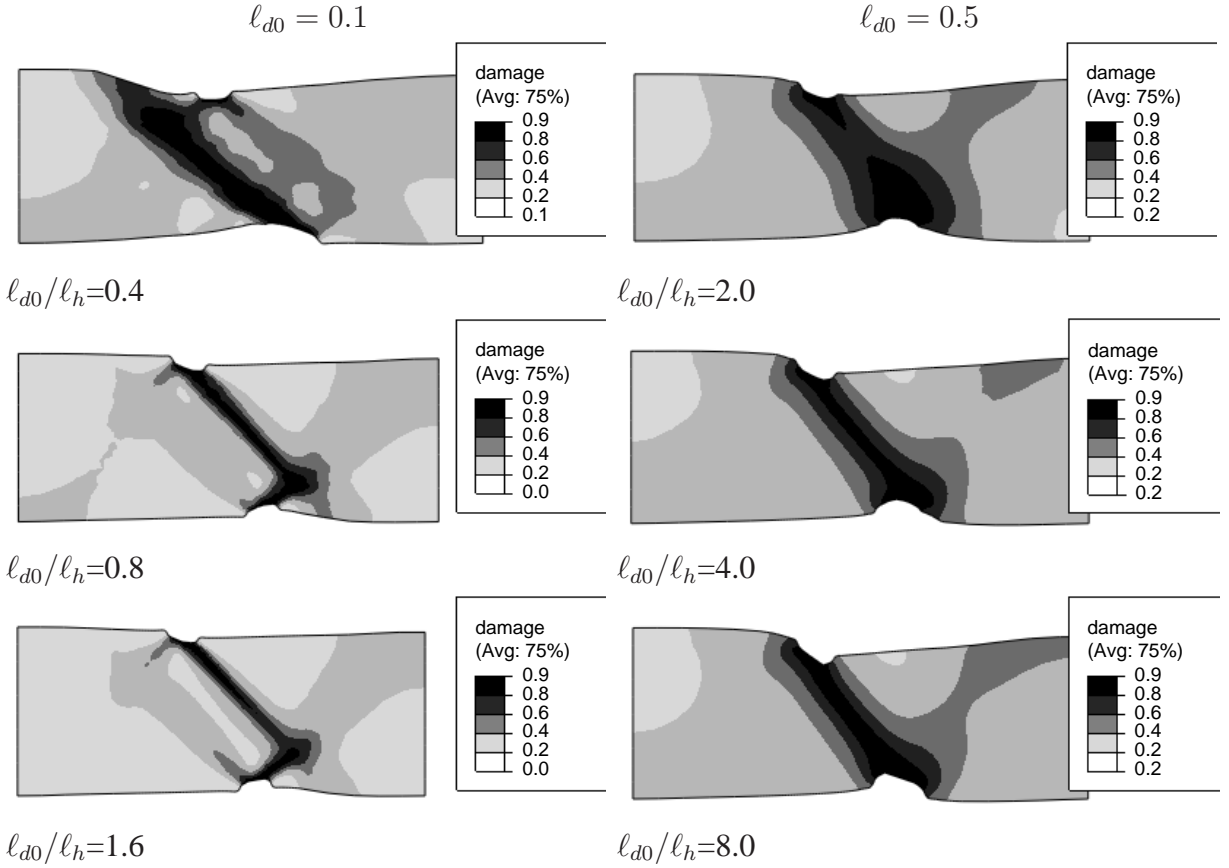


Figure 5.9: Contour plots showing the distribution of damage for the notched tensile specimen as given in Figure 5.7. The specimen is elongated quasi-static, which allows isothermal conditions. Simulations are carried out for $l_{d0} = 0.1$ (left column) and $l_{d0} = 0.5$ (right column), with element edge lengths $l_h = 0.25$ mm (above), $l_h = 0.125$ mm (middle) and $l_h = 0.0625$ mm (below). The structural scale is fixed at $l_s := 1$ mm. See text for further details.

lead to a broadened area of the softening quantity causing the specimen to fail at a later point. Different values of l_{d0} are generally related to different materials (microstructures). Note, that for quasistatic, isothermal loading, increasing of l_{d0} and thus increasing of l_{d0}/l_s is corresponding to decreasing l_{d0}/l_h , e.g., downsizing the structure. Restricting here and in what follows to ratios $l_{d0}/l_h > 2$, we now demonstrate the behavior of the non-local damage formulation in terms of a cutting simulation. Again, starting with an exclusion of thermal softening, which is purely academic in case of cutting, we set the Taylor-Quinney coefficient to $\beta_0 \rightarrow 0$ (isothermal formulation). In the above investigations, we set the onset of damage to a high value to keep the influence of thermal softening dominant, in particular, we found $\alpha_{Dd} = 1.5$. Now, to allow the onset of localized plastic deformation patterns without thermal softening, we work with $\alpha_{Dd} = 0.75$ for this specific situation and keep all other parameters fixed. The first simulation is calculated with a characteristic element edge length of $l_h = l_h^{\text{ref}} = h_{\text{min}} = 0.1/16$ mm. The characteristic length of the structure is given by $l_s = l_s^{\text{ref}} = t_c = 0.15$ mm. Further, lacking on any detailed information for the specific microstructure we set the internal length, describing the non-local damage effects arbitrarily to the determined minimum value $l_{d0} := 2 l_h^{\text{ref}}$. Now, increasing the internal length to $l_{d0} = 8 l_h^{\text{ref}}$ we detect results corresponding to those for

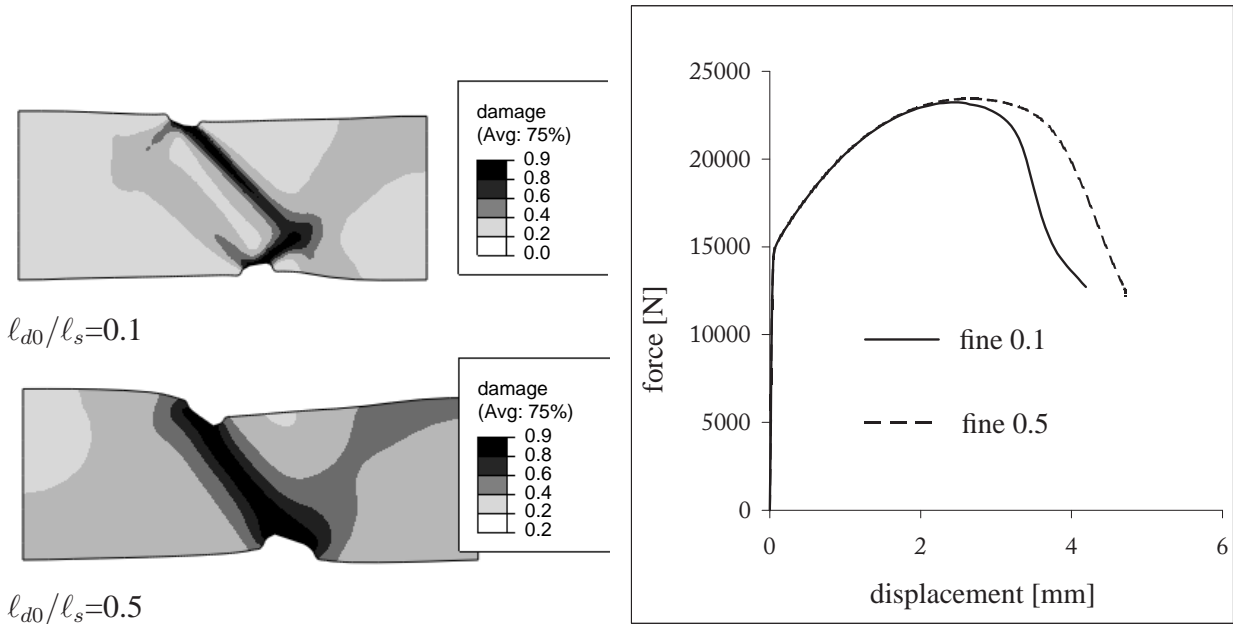


Figure 5.10: Force-displacement diagrams and corresponding contour plots showing the distribution of damage for the notched tensile specimen as given in Figure 5.7. The figures show the effect of different ratios ℓ_{d0}/ℓ_s . The structural scale is fixed at $\ell_s := 1$ mm.

the simulation of the tensile specimen above. In contrast to the simulation with $\ell_{d0} := 2 \ell_h^{\text{ref}}$ (Figure 5.11_a) the simulation with $\ell_{d0} := 2 \ell_h^{\text{ref}}$ (Figure 5.11_b) does not show any segmentation of the chip. Again, increasing the effect of non-local interaction or decreasing the structure, respectively, leads to a broadened area of damage, resulting in a delocalization of plastic deformation. As observed above, decreasing of the element edge length from $\ell_h = \ell_h^{\text{ref}}$ (Figure 5.11_a) to $\ell_h = \ell_h^{\text{ref}}/2$ (Figure 5.11_c) does not show any prominent effects of mesh dependence. However, this is not the case when having the additional effect of thermal softening. In this case, the development of temperature is independent from any lengthscale resulting again in pathological mesh dependence (Figure 5.12_a, Figure 5.12_c). Also the lengthscaling effect is less distinct (Figure 5.12_a, Figure 5.12_b). These results, as well as the results for the variation of the cutting speed, as presented above suggest a formulation and implementation with a non-local description for all involved softening quantities, e.g., a combination of heat conduction and a non-local formulation of damage. As the current UMAT-based implementation allows only one additional degree of freedom, the presented formulation should be implemented in the more flexible user element environment (UEL).

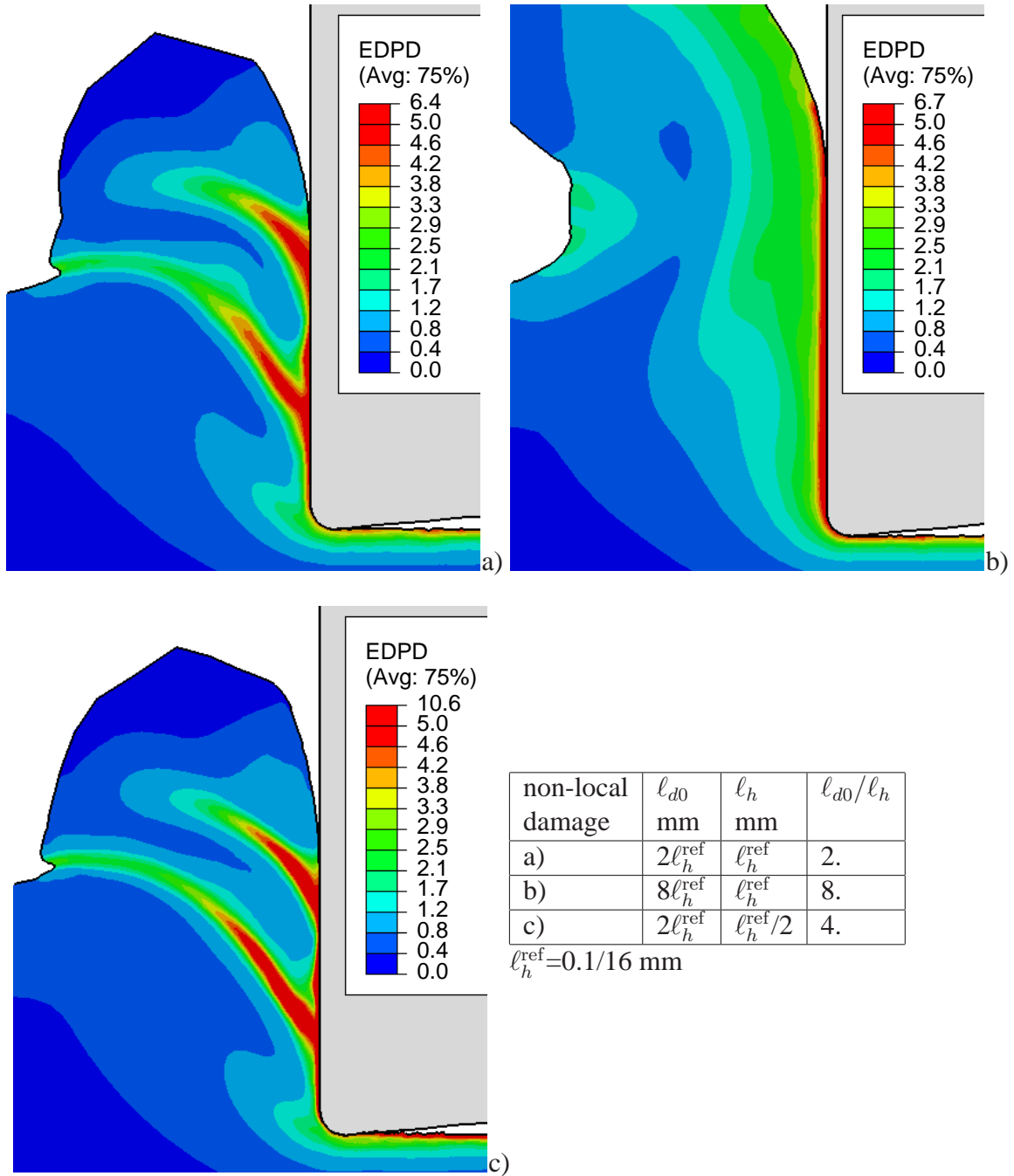


Figure 5.11: Cutting simulation with non-local formulation of the damage at isothermal conditions. Increasing the effect of non-local interaction leads to a broadened area of damage resulting in a delocalization of plastic deformation (a,b). Decreasing of the element edge length from $\ell_h = \ell_h^{\text{ref}}$ (a) to $\ell_h = \ell_h^{\text{ref}}/2$ (c) does not show any prominent effects of mesh dependence.

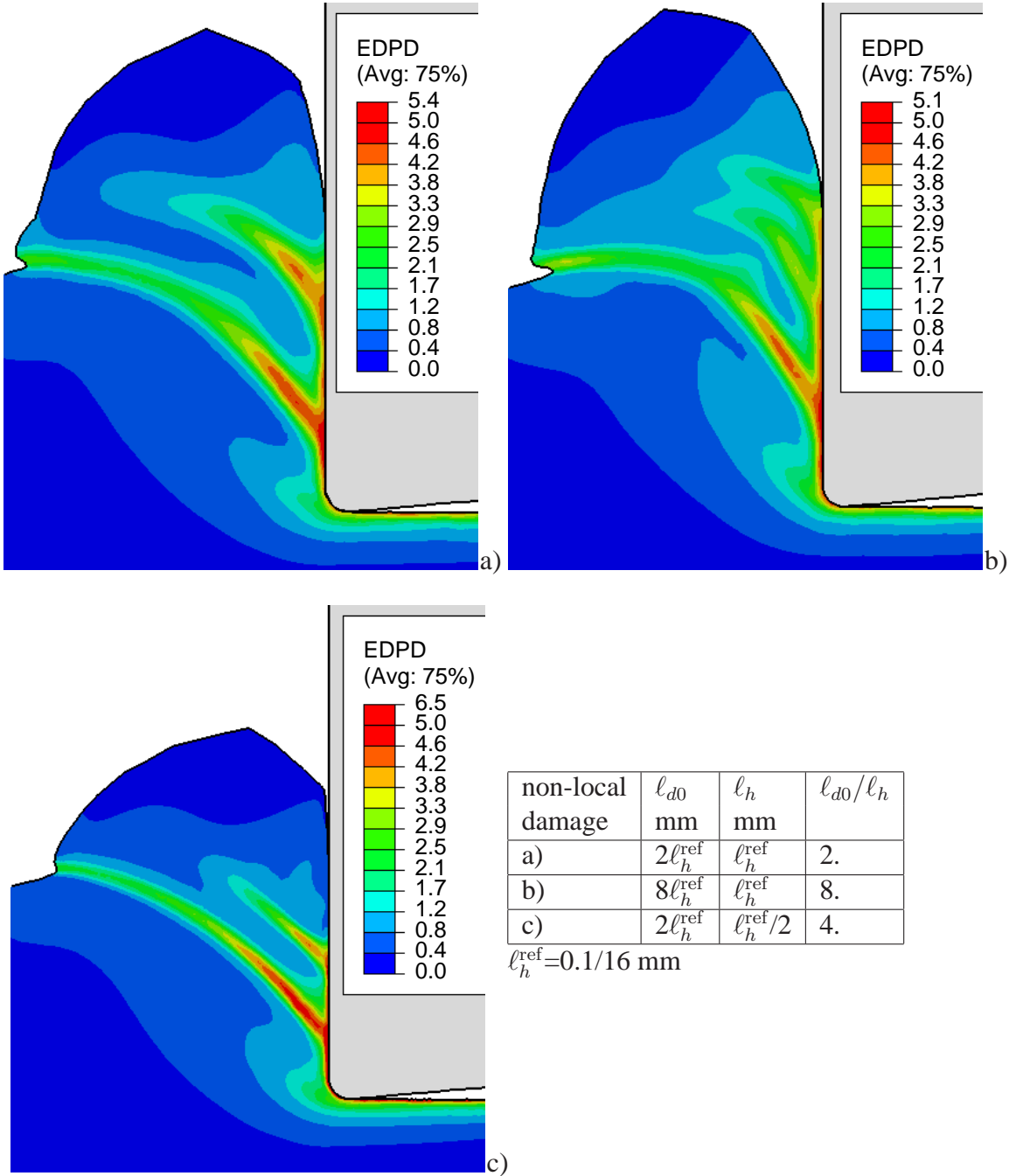


Figure 5.12: Cutting simulation with non-local formulation of the damage and adiabatic heating. In this case, the development of temperature is independent from any lengthscale resulting again in pathological mesh dependence (a,c). The lengthscaling effect is weakly distinct (a,b)

5.4 Outlook hydrostatic/deviatoric coupling

As an outlook on future work, we present the modeling of non-isochoric plasticity. In contrast to modeling the influence of the hydrostatic stress state on the development of damage indirectly, in terms of some scalar value describing the level of triaxiality, as introduced, e.g., in the work of Singh et al. (2003), we favor the approach of modeling this influence directly in terms of hydrostatic activation and deformation processes. Corresponding to the work of Gurson (1977), this approach is open to adjustments, motivated by micromechanical observations. These observations can be supported by, e.g., detailed finite element modeling and simulation of specific microstructures. In the above formulation, $\bar{\sigma}_H = k_H$ and $\bar{\sigma}_D = k_M$ are generally uncoupled at the microlevel. Assuming that both, the hydrostatic and deviatoric parts of macroscopic stress states, will activate and drive inelastic deformation at the level of the microstructure, they become coupled. The stress-state coupling is based on a combined effective microscopic stress $\sigma_{Pm}(\sigma_{Dm}, \sigma_{Hm})$ with $\sigma_{Pm}(\sigma_{Dm}, \sigma_{Hm} = 0) = \sigma_{Dm}$ and $\sigma_{Pm}(\sigma_{Dm} = 0, \sigma_{Hm}) = \sigma_{Hm}$. These are satisfied for example by the form

$$\sigma_{Pm}(\sigma_{Dm}, \sigma_{Hm}) = \sqrt{\sigma_{Dm}^2 + \sigma_{Hm}^2} \quad (5.7)$$

which we work with for simplicity here. As discussed above the microscopic stresses σ_{Im} , $I = D, H$ are related to the macroscopic ones via

$$\sigma_{Im} = \bar{\sigma}_I / f_I(\bar{d}), \quad (5.8)$$

in terms of $f_I(\bar{d})$ representing the influence of the microstructure (e.g. voids, microcracks etc.), given by (4.37) and (4.38). Defining next an effective microscopic deformation rate $\dot{\alpha}_{Im}$ by

$$\sigma_{Im} \dot{\alpha}_{Im} = \bar{\sigma}_I \dot{\alpha}_I, \quad (5.9)$$

here in terms of the conjugate pair $\bar{\sigma}_I$ and $\dot{\alpha}_I$, the relations (5.7), (5.8) and (5.9) yield

$$\sigma_{Pm}^2 = \bar{\sigma}_D^2 \dot{\alpha}_D^2 / \dot{\alpha}_{Dm}^2 + \bar{\sigma}_H^2 \dot{\alpha}_H^2 / \dot{\alpha}_{Hm}^2 = f_D^2 \dot{\alpha}_D^2 \sigma_{Dm}^2 / \dot{\alpha}_{Dm}^2 + f_H^2 \dot{\alpha}_H^2 \sigma_{Hm}^2 / \dot{\alpha}_{Hm}^2. \quad (5.10)$$

Assuming next, that the effective microscopic flow behavior is the same with respect to hydrostatic and deviatoric loading, we have $\sigma_{Dm} / \dot{\alpha}_{Dm} = \sigma_{Hm} / \dot{\alpha}_{Hm}$, and so

$$\sigma_{Pm}^2 = \{f_D^2 \dot{\alpha}_D^2 + f_H^2 \dot{\alpha}_H^2\} \sigma_{Im}^2 / \dot{\alpha}_{Im}^2. \quad (5.11)$$

This can be rearranged to obtain an expression for σ_{Im} , and so that

$$\bar{\sigma}_I = g_I(\dot{\alpha}_D, \dot{\alpha}_H, \bar{d}) f_I(\bar{d}) \sigma_{Pm} \quad (5.12)$$

via (4.34), with

$$g_I(\dot{\alpha}_D, \dot{\alpha}_H, \bar{d}) := \dot{\alpha}_I f_I(\bar{d}) / \sqrt{f_D(\bar{d})^2 \dot{\alpha}_D^2 + f_H(\bar{d})^2 \dot{\alpha}_H^2} \quad (5.13)$$

representing the effect of coupling. Based on (4.66) in combination with (4.62) and (4.63), we choose

$$\sigma_{Pm} := \{1 + c_{jc} \ln(1 + |\dot{\alpha}_P| / \dot{\alpha}_{P0})\} \{1 - [(\theta - \theta_0) / (\theta_{m0} - \theta_0)]^{m_{jc}}\} \{a_{jc} + b_{jc} (1 - e^{-n_{jc} \bar{\alpha}_P})\}. \quad (5.14)$$

In this constitutive relation the accumulated plastic deformation and its corresponding rate is a composite of $\bar{\alpha}_D$ and $\bar{\alpha}_H$, in general. Assuming, that spherical plastic deformation is small in comparison to deviatoric plastic deformation, we work with

$$\begin{aligned}\dot{\bar{\alpha}}_P &:= \dot{\bar{\alpha}}_D \\ \bar{\alpha}_P &:= \bar{\alpha}_D\end{aligned}\quad (5.15)$$

for simplicity. Again, having $\bar{\sigma}_H = k_H$ and $\bar{\sigma}_D = k_M$, the above relation represents the implicit relation to determine $\dot{\bar{\alpha}}_I$. For the moment we abstain from deriving the corresponding rate and dissipation potentials and simply work with the implicit constitutive relation given by (5.12), instead of (4.66). Note that a corresponding uncoupled form is obtained for $g_1:=1$ (5.13). Lacking of any detailed information about the specific microstructure, the parameters for the relation moderating the transformation between macroscopic and microscopic hydrostatic stresses (4.38) are set to $D_1 := 2/3$ and $D_2 := 1/2$. These values actually stem from a comparison between our model formulation and the well known model of Gurson (1977). This issue will be illustrated in the following. The established model of Gurson (1977), here in the form introduced by Tvergaard (1981), considers the influence of the hydrostatic stress in terms of a yield surface given by

$$\phi = \frac{k_D^2}{\sigma_{Pm}^2} + 2 q_1 \bar{d} \cosh\left(q_2 \frac{3 k_H}{2 \sigma_{Pm}}\right) - (q_1 \bar{d})^2 - 1 = 0 \quad (5.16)$$

Slight rearranging leads in a first step to the relation between the macroscopic deviatoric and spherical stresses k_D and k_H , respectively and the microscopic stress σ_{Pm} causing plastic yielding inside the matrix material.

$$\left(\frac{1}{1 - q_1 \bar{d}} k_D\right)^2 + \sigma_{Pm}^2 \left(\frac{(2 q_1 \bar{d})^{\frac{1}{2}}}{1 - q_1 \bar{d}}\right)^2 \left(\cosh\left(q_2 \frac{3 k_H}{2 \sigma_{Pm}}\right) - 1\right) = \sigma_{Pm}^2 \quad (5.17)$$

In this form, the maximum deviatoric and hydrostatic stresses $k_{D_{max}}$ and $k_{H_{max}}$, respectively, can be identified by simply setting k_H or k_D to zero (see also Figure 5.13).

$$k_{D_{max}} = f_D(\bar{d}) \sigma_{Pm} = (1 - q_1 \bar{d}) \sigma_{Pm} \quad (5.18)$$

$$k_{H_{max}} = f_H(\bar{d}) \sigma_{Pm} = \frac{2}{3 q_2} \operatorname{arccosh}\left(\left(\frac{(1 - q_1 \bar{d})}{(2 q_1 \bar{d})^{\frac{1}{2}}}\right)^2 + 1\right) \sigma_{Pm} \quad (5.19)$$

Note that in general, spherical tension is not arbitrarily high, e.g., in case of a quasistatic simple tension test

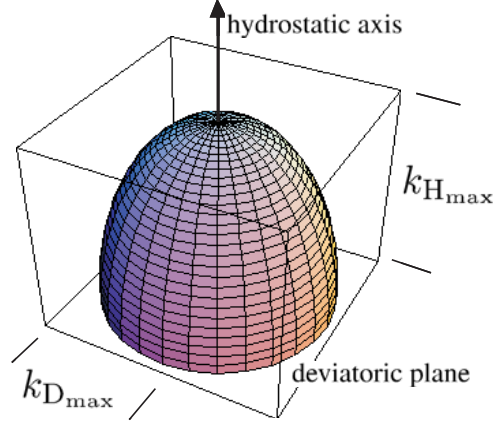
$$k_H = \frac{1}{3} \sigma_{Pm} \quad (5.20)$$

This motivates an approximation in terms of the series expansion of

$$\cosh(x) = 1 + \frac{x^2}{2!} + R \quad (5.21)$$

in equation (5.17). This leads to

$$\left(\frac{1}{1 - q_1 \bar{d}} k_D\right)^2 + \sigma_{Pm}^2 \left(\frac{(2 q_1 \bar{d})^{\frac{1}{2}}}{1 - q_1 \bar{d}}\right)^2 \left(\frac{1}{2} \left(q_2 \frac{3 k_H}{2 \sigma_{Pm}}\right)^2 + R\right) = \sigma_{Pm}^2 \quad (5.22)$$

Figure 5.13: Gurson yield surface at a fixed damage \bar{d} .

Again, for $R := 0$ this relation allows to identify the maximum stresses

$$k_{D_{\max}} = f_D(\bar{d}) \sigma_{Pm} = (1 - q_1 \bar{d}) \sigma_{Pm} \quad (5.23)$$

$$k_{H_{\max}} = f_H(\bar{d}) \sigma_{Pm} = \frac{2}{3} \frac{1 - q_1 \bar{d}}{q_2 (q_1 \bar{d})^{\frac{1}{2}}} \sigma_{Pm} \quad (5.24)$$

In Reusch et al. (2008) and other works the parameters for the Gurson yield surface are assumed with $q_1=1.5$ and $q_2=1$. Noting that the above comparison with a rate independent formulation is just a first approach to have at least a qualitative determination of our parameters D_1 and D_2 , we make use of the approximation $q_1 = q_2 = 1$. This identifies a transformation between macroscopic and microscopic stresses similar to our model formulation in terms of (4.37) and (4.38) with $D_1 := 2/3$ and $D_2 := 1/2$.

Starting with these parameters we will now again make use of the notched tensile specimen to demonstrate the effect of additional hydrostatic-stress driven damage. Here we compare the purely deviatoric formulation ($D_1 = 10^6$, $D_2=1/2$.) with i) the uncoupled formulation ($g_I := 1$, $D_1=2/3$, $D_2=1/2$) and ii) with the coupled formulation ($D_1=2/3$, $D_2=1/2$). To avoid an infinite hydrostatic activation stress and thus, to allow hydrostatic activity from the beginning, we work with an initial damage of $\bar{d} = 10^{-3}$. Both, the uncoupled and the coupled formulation are computed for $r_H=1$ and $r_H=4$ (increased hydrostatic-stress driven damage). The development of deviatoric-stress driven damage is characterized by $\alpha_{Dd}=1.5$ (see discussion Section 5.2) and $r_D=5$. Comparing the corresponding force-displacement diagrams and the corresponding contour plots for the distribution of damage, given in Figure 5.14 and Figure 5.15, respectively, we observe that for both the uncoupled formulation, as well as for the coupled formulation failure occurs at an earlier point in time, compared to the purely deviatoric formulation. Also the stress drop is more distinct for the non-isochoric formulation. The difference between the coupled and the uncoupled formulation becomes strongly distinct for an increased hydrostatic-stress driven damage ($r_H=4$). This is explained by the following facts. In the decoupled case, depending on the specific form of $f_H(\bar{d})$, the point of activation of spherical plastic deformation is, in general, related to high values of \bar{d} . Thus, the onset of damage is still triggered by α_{Dd} . The additional hydrostatic-stress driven damage merely leads to an increased rate of damage production. In the coupled case, both hydrostatic and deviatoric processes are active, simultaneously. This

leads to earlier damage initiation, as d_H develops parallel to α_H . A comparison between the

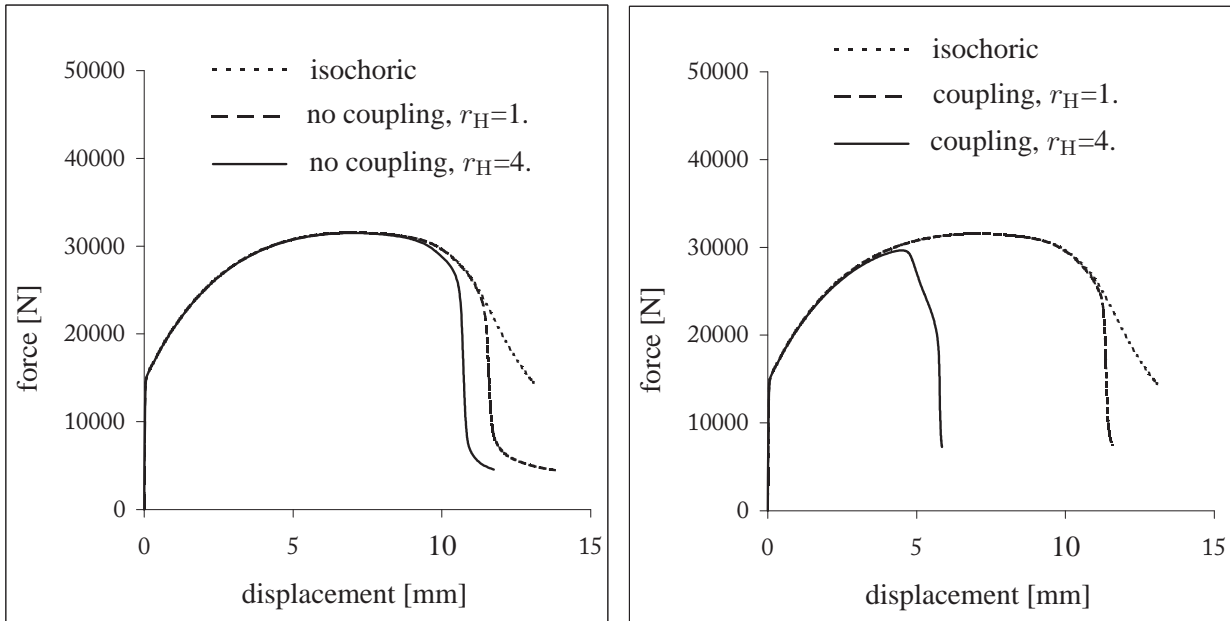


Figure 5.14: Force-displacement diagrams for the notched tensile specimen for different cases of combined hydrostatic-deviatoric coupling, as based on (4.36), (5.2) and (5.12). The onset of deviatoric driven damage is triggered at $\alpha_{Dd}=1.5$ with a saturation rate of $r_D=5$. The uncoupled formulation is yielded with $g_I=1$. The simulations have been carried out with $r_H=1$ and with increased hydrostatic-stress driven damage ($r_H=4$). See text for details.

results for the purely deviatoric formulation and the coupled formulation with an increased influence of hydrostatic-stress driven damage ($D_1=2/3$, $D_2=1/2$, $r_H=4$), now in terms of a cutting simulation is shown in Figures 5.16-5.18. Similar to the notched tensile specimen the additional hydrostatic-stress driven damage leads to an earlier development of the localized shear band (see Figure 5.16) and thus, to an earlier stress drop for the specific cutting forces (see Figure 5.17). In contrast to the above results for the notched tensile specimen, the effect of hydrostatic stress is only weakly present. This is explained by the small hydrostatic stresses inside the main deformation zone (see Figure 5.18, left). More distinct is the stress drop of specific cutting forces in comparison to the purely deviatoric formulation. Obviously, the additional mode of spherical plastic deformation (see Figure 5.18, right) leads to a softer response of the structure (chip). Again, the above results have been calculated with estimated parameters and thus, can only reflect qualitative tendencies.

5.5 CIRP Benchmark

We close the presentation of our adaptive finite element framework with a result for a cutting simulation generated in context of a benchmark study organized by the College International pour la Recherche en Productique (CIRP, engl.: The International Academy for Production Engineering). Besides other parameters, such as cutting velocity and tool rake angle, which influence has already been discussed above, the influence of the tool edge radius on cutting forces

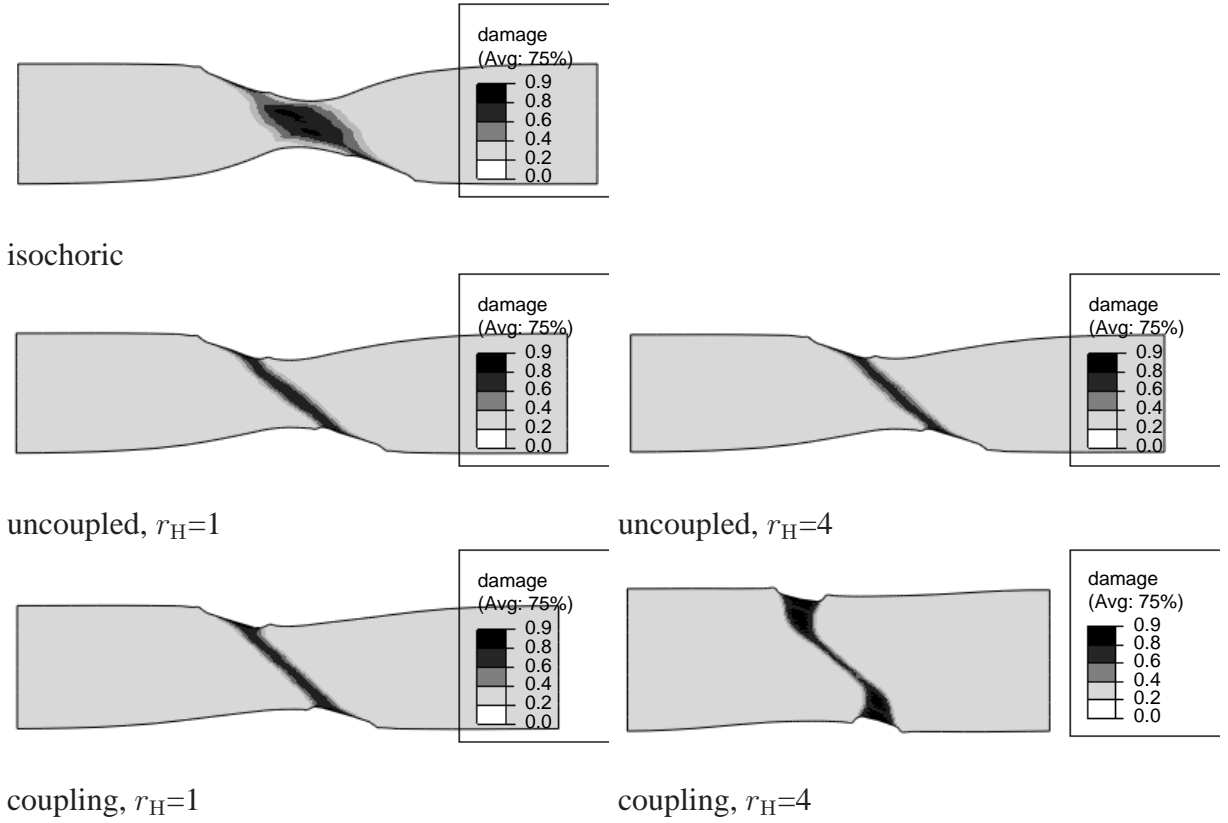


Figure 5.15: Development of ductile damage for the notched tensile specimen for different cases of combined hydrostatic-deviatoric coupling, as based on (4.36), (5.2) and (5.12). The onset of deviatoric driven damage is triggered at $\alpha_{Dd}=1.5$ with a saturation rate of $r_D=5$. The uncoupled formulation is yielded with $g_I=1$. The simulations have been carried out with $r_H=1$ and with increased hydrostatic-stress driven damage ($r_H=4$). See text for details.

and resulting surface has been investigated. In fact, this investigation is predestined for the developed adaptive approach as here the accurate resolution of the deformation field in front of the cutting tool edge becomes extremely relevant. The following simulations have been carried out with the above developed formulation, based on the Johnson-Cook formulation for viscoplastic flow. Here, we applied the purely deviatoric formulation without damage production. The development of the temperature is modeled with heat conduction ($k_0=43$ [Wm⁻¹K⁻¹]). The cutting speed and cutting depth are given by $v_c=175$ m/min⁻¹ and $t_c=0.05$ mm, respectively. The set of Johnson-Cook parameters for the material AISI1045, used in the following study, is summarized in Table 5.4.

θ_0 [K]	λ_0 [GPa]	μ_0 [GPa]	α_0 [K ⁻¹]	ρ_0 [kg/ m ³]	$c_0 \rho_0$ [J/kg K]		
300.	110.5	80.	4.3×10^{-6}	7.88×10^3	533		
a_{jc} [MPa]	b_{jc} [MPa]	n_0	θ_{M0} [K]	m_0	c_{jc}	$\dot{\alpha}_0$ [s ⁻¹]	β_0
553	543.686	8.5757	1733	1.	0.0134	1.	0.9

Table 5.4: Johnson-Cook model parameters for AISI 1045, determining the model relations (4.62) and (4.63)

Comparing the results for the forces for the tool edge radii of $r=15\mu\text{m}$ and $r=55\mu\text{m}$ the influ-

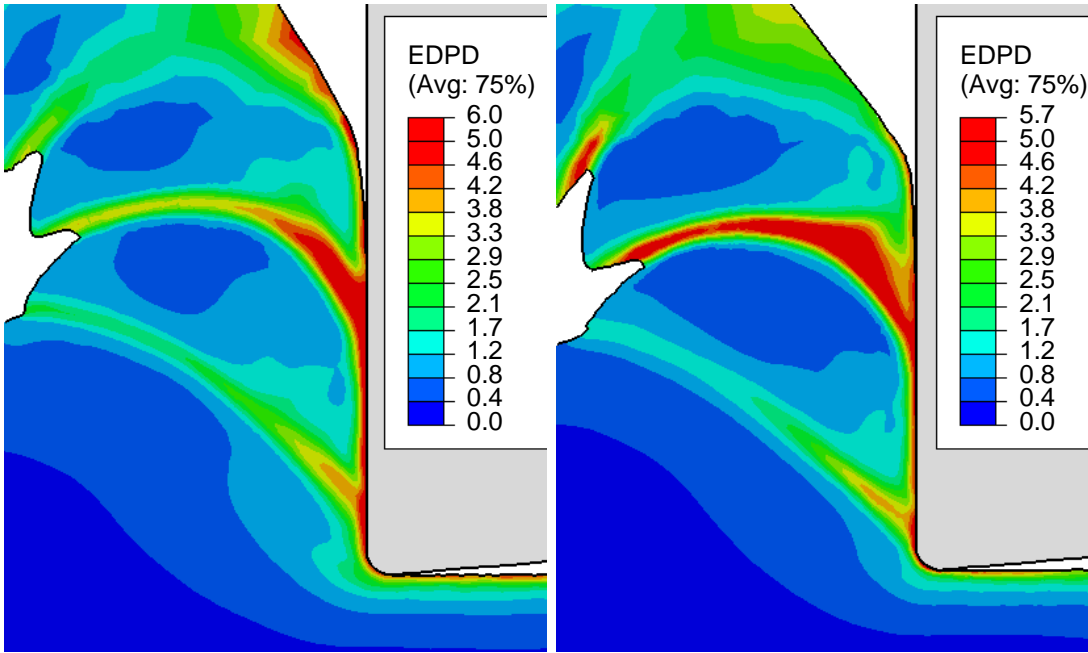


Figure 5.16: Distribution of equivalent deviatoric plastic deformation for the cutting simulation with non-local damage. Curves show the results for the simulation with isochoric plastic deformation (left) and deviatoric/hydrostatic coupling (right).

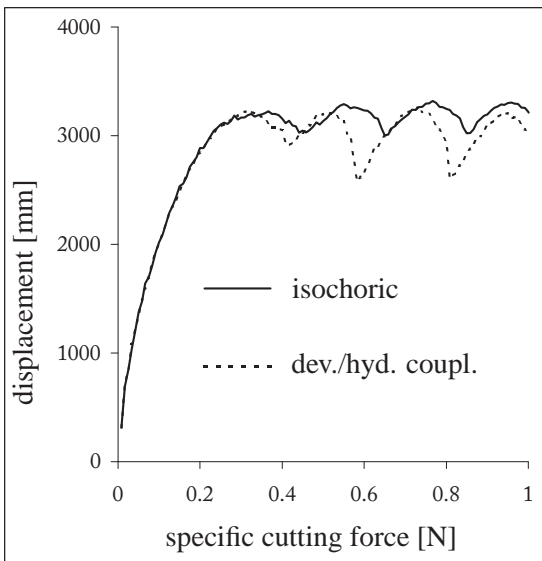


Figure 5.17: Specific cutting forces for the cutting simulation with non-local damage. Curves show the results for the simulation with isochoric plastic deformation and deviatoric/hydrostatic coupling.

ence of the tool edge radius is small, at first sight (Figure 5.19). Contrary, the effect on the corresponding thrust forces is immense. This issue is clearly explained in terms of the material flow in front of the cutting tool edge, as shown in Figure 5.20. As can be observed, in a small distance to the tool tip the material flow is comparable for different tool edge radii. Now, as the cutting force is mainly dependent on the shear and corresponding stresses inside the main deformation zone, we observe comparable results for this quantity. In contrast, the

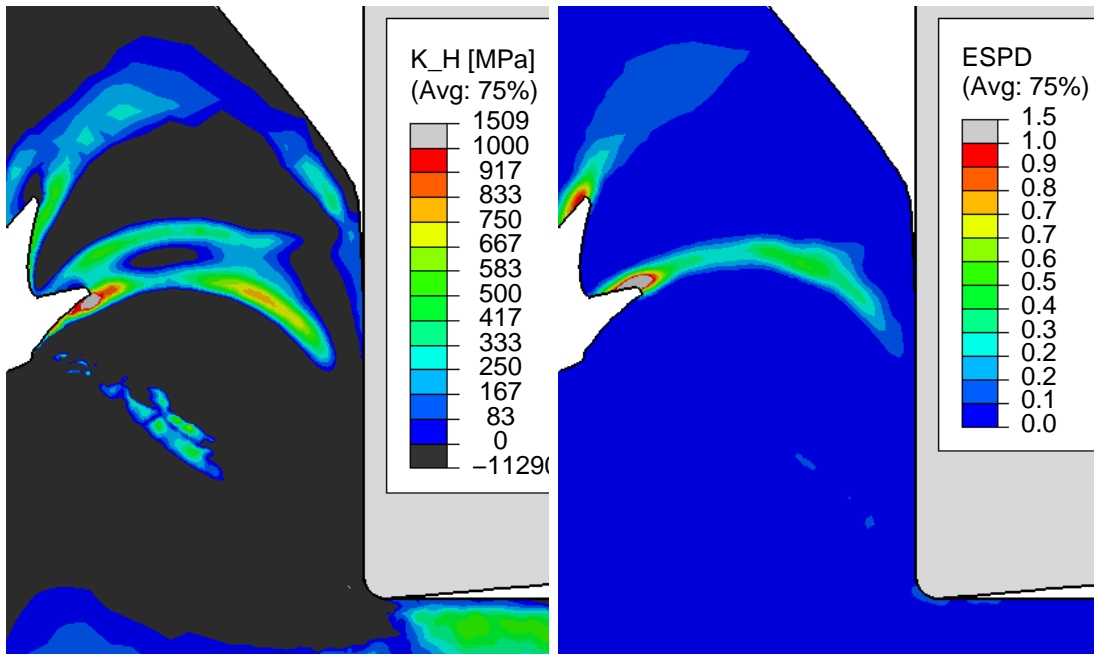


Figure 5.18: Hydrostatic stress (left) and distribution of equivalent spherical plastic deformation (right) for the cutting simulation with non-local damage. and deviatoric/hydrostatic coupling. Due to the small hydrostatic stresses inside the main deformation zone the effect of hydrostatic stress is only weakly present. Obviously, the additional mode of spherical plastic deformation is needed, which leads to a softer response of the structure (chip). See also Figure 5.17.

thrust force is mainly dependent on the deformation below the tool tip. This deformation is characterized by the stagnation point. As is clearly reflected in terms of the material flow, this stagnation point, where the material separates into the chip and the resulting surface, is located much higher for the larger tool edge radius (Figure 5.20, right). In effect, a higher amount of material has to be deformed below the tool tip, resulting in higher thrust forces. This and the increased contact time for the material forming the new surface is also reflected in terms of higher temperatures inside the resulting surface (see Figure 5.21, left). Another effect is the smoother trend of the cutting force and the thrust force for the larger tool edge radius (Figure 5.19). Considering the distribution of temperature and the distribution of equivalent plastic deformation as given in Figure 5.22 and Figure 5.23, respectively, we observe that a smaller tool edge radius leads to a more localized plastic deformation. In effect, this leads to an inhomogeneous hardening/softening, causing stronger oscillations of the corresponding forces. As an additional example to the distribution of temperature, we show the distribution of the von Mises residual stress inside the resulting surface (see Figure 5.21, right). In accordance to the higher plastic deformations inside the surface (see Figure 5.23), we detect higher residual stresses for the larger tool edge radius, in general. The stress drop, directly below the surface is assumed to stem from a complex mix of thermal softening and thermal residual stresses, induced by subsequent cooling. However, this example demonstrates the complexity of the process of cutting, which suggests interesting research topics for future work.

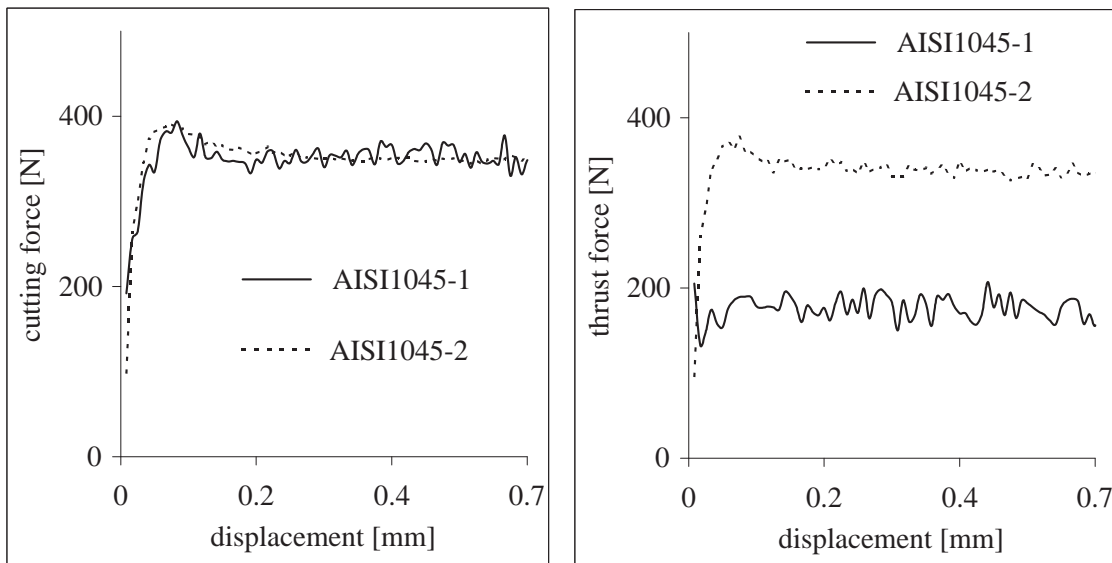


Figure 5.19: Cutting force and thrust force for the cutting simulation with tool edge radii $r=15\mu\text{m}$ (AISI1045-1) and $r=55\mu\text{m}$ (AISI1045-2).

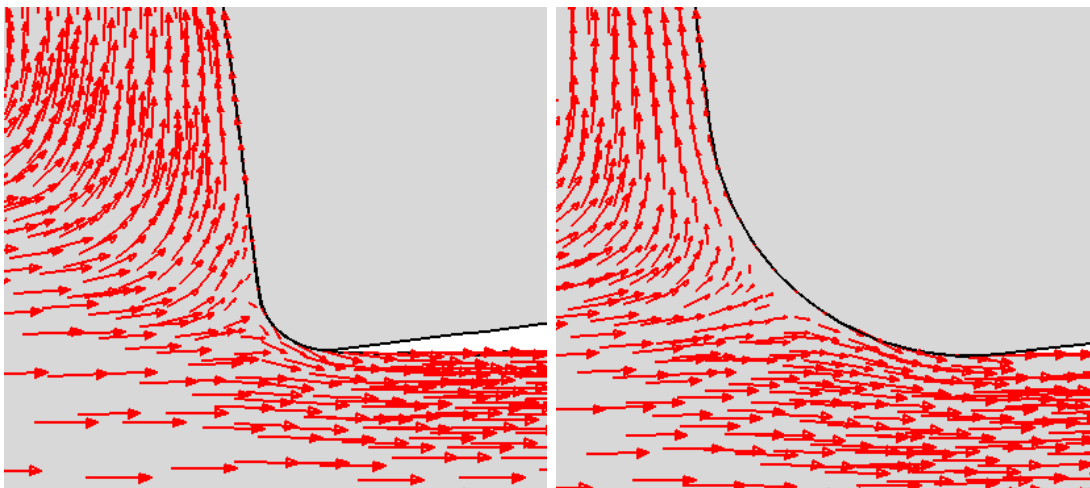


Figure 5.20: Material flow in front of the cutting tool edge for the cutting simulation with tool edge radii $r=15\mu\text{m}$ (left) and $r=55\mu\text{m}$ (right).

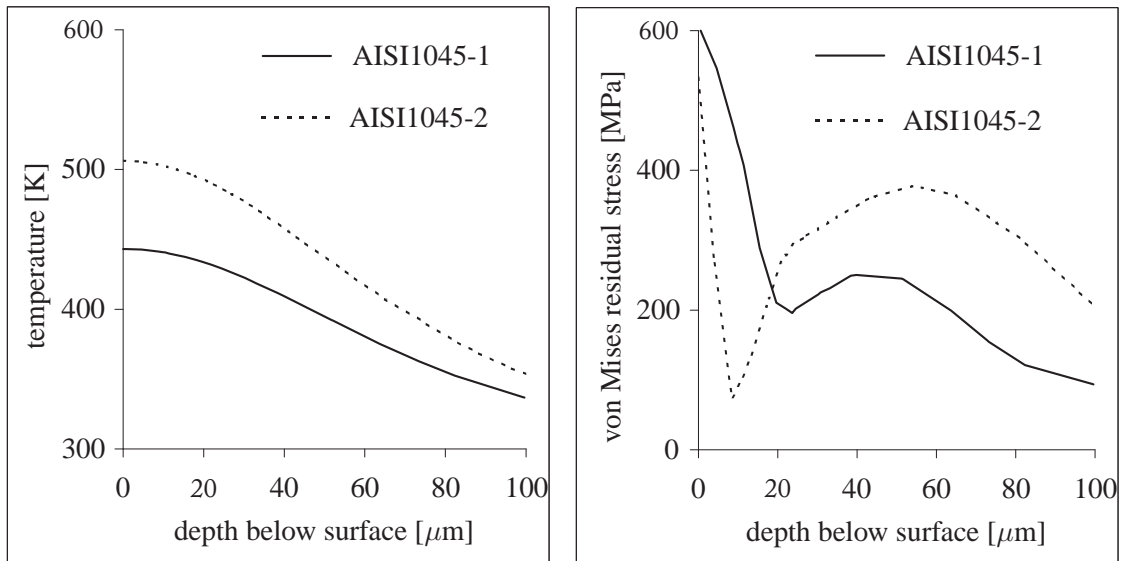


Figure 5.21: Distribution of temperature and von Mises residual stress for the resulting surface. The distribution for both quantities was taken along a vertical path, 0.2 mm behind the tool tip.

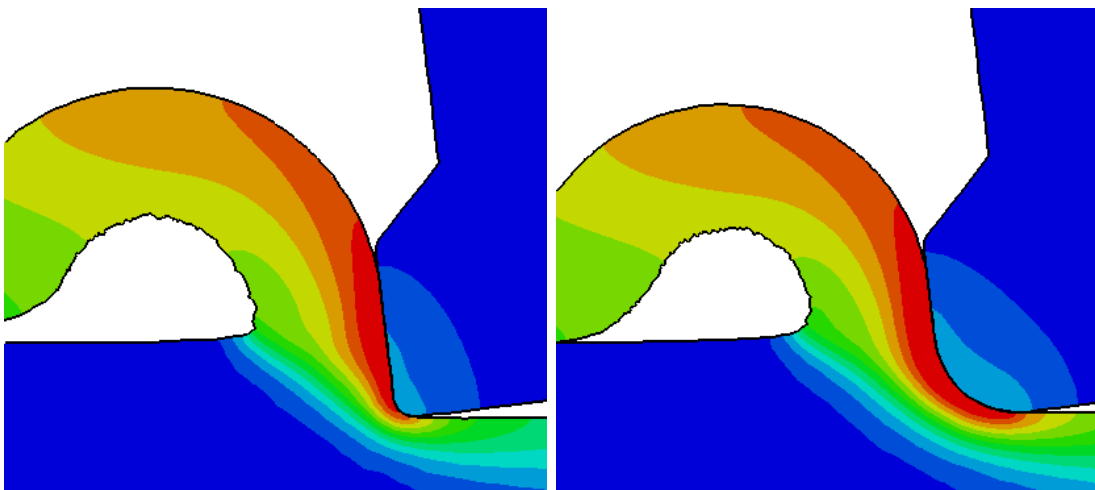


Figure 5.22: Distribution of temperature for the cutting simulation with tool edge radii $r=15\mu\text{m}$ (left) and $r=55\mu\text{m}$ (right).

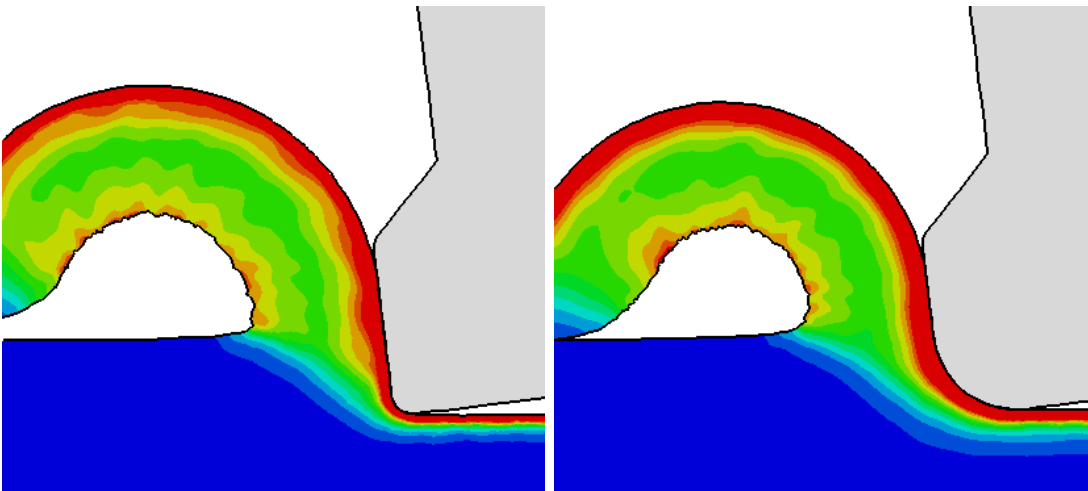


Figure 5.23: Distribution of equivalent plastic deformation for the cutting simulation with tool edge radii $r=15\mu\text{m}$ (left) and $r=55\mu\text{m}$ (right).

Chapter 6

Conclusion and Outlook

6.1 Conclusion

The current work contributes to an enhanced modeling and simulation of high speed cutting and related processes by the following issues. The developed adaptive finite element framework allows a robust and accurate modeling of the complex deformation processes, taking place during metal cutting. Based on a combination of error estimation, refinement indication and remeshing, an adequate resolution of the underlying boundary value problem with a prescribed accuracy can be ensured at any time. In this context, the adaptive scheme has also proven its capability to reduce the influence of mesh orientation. The presented method of point wise error estimation is robust, easy implemented and is capable of identifying the magnitude of gradients with a minimum of numerical cost. The physical meaning of the accumulated plastic deformation in context of localization phenomena has been shown and a possible application as a refinement indicator has been demonstrated on numerical examples. Additionally, in context of detecting material instabilities, the rate of equivalent plastic strain as well as the plastic power have turned out to work very well. Here, in contrast to the accumulated plastic deformation, these parameters for the refinement strategy are problem-dependent and cannot be determined in advance. For the mapping of internal variables it has been shown that the classical finite element projection of the recovered values leads to numerical diffusion. Here, a separated, direct transfer has been established. In contrast to standard models, based on, e.g. a predefined separation of the chip from the workpiece, the adaptive approach ensures a reasonable resolution of the complex deformation patterns and moreover allows the modeling of the resulting surface. The latter issue is highly important in context of production engineering, as the state of the resulting surface is decisive for the quality of the whole product. The presented adaptive framework is implemented in a modular fashion and is thus open for further improvements. The simulation results for the cutting process, presented in this work show, that thermal softening only explains the effect of segmented chip formation in general. A detailed investigation on the resulting temperatures, however, suggests additional softening effects. Thus, the author developed an extended thermodynamic framework, with a general non-local description of several thermodynamic quantities, including the additional softening effect of damage. Contrary to standard isochoric formulations, the current work is based on both hydrostatic stress- and deviatoric stress-driven inelastic deformation, damage, and failure. This separated approach, allows further investigations and specifications of microstructural effects and their influence on, e.g., the development of damage. The presented form for the development of damage is capable of representing the effect of pronounced localization patterns, up to shear banding and chip segmentation for increased cutting speeds. Also the change from a continuous to a segmented chip at a critical cutting speed

has been reproduced. Further, the effect of hydrostatically driven damage has been demonstrated in terms of a notched tension specimen, as well as in terms of a cutting simulation. As has been shown, the extended non-local description allows the modeling of lengthscale effects, in general. This issue may become relevant when decreasing the structural lengthscale of the problem as, e.g., in terms of micro-cutting. The additional benefit of further reduction of mesh dependence is also prominent and has been discussed.

6.2 Outlook

The simulation results presented in the current work are essentially academic in nature, at this time. Excepting the parameters for the thermo-viscoplastic part of the material model, which are available in literature, the parameters for the presented damage formulation have not yet been properly identified. In the present work the influence of the microstructure has been introduced by a relation, moderating the transfer between macroscopic and microscopic stresses, based on micromechanical assumptions. For starting, the parameters of this relation have been fit to the specific form of the well known Gurson-model. In future work, further investigations should start by determining the specific form of these microstructural relations. Here, we could start by solving boundary value problems with an explicit representation of a specific microstructure (e.g. voids), corresponding to the original boundary value problem introduced by Gurson. Additionally, material testing with varying influence of hydrostatic stress must supplement such investigations. Related to this are microstructural investigations and simulations with the aim of identifying the interaction radius of voids. In the current work, we restricted to the application of the general form of non-local damage and thus considered only non-local interaction of, e.g., voids and microcracks. Assuming non-locality for the non-local rates of deviatoric and spherical accumulated inelastic deformation and assuming further, that these quantities drive the development of damage, the damage production is inherently non-local. In this context a detailed investigation on the different involved lengthscales has to follow. The presented simulation results suggest a formulation and implementation with a non-local description for all involved softening quantities, e.g., a combination of heat conduction and a non-local formulation of damage. The current, UMAT-based implementation allows only one additional degree of freedom. Thus, the presented formulation should be implemented in the more flexible user element environment (UEL). This is already work in progress. In context of metal cutting, the adaptive framework allows further investigations not possible with standard models. As has been shown, the detailed resolution of the deformation field allows access to detailed information about the state in the contact zone between workpiece and tool (pressure, relative velocities, temperatures). This information is indispensable when investigating, e.g., the effect of tool wear which will be future work.

References

- ABAQUS-Manual, Version 6.8, 2008.
- Aifantis, E. C., On the microstructural origin of certain inelastic models, *J. Engrg. Mater. Technol.*, Volume 106, pp. 326–330, 1984.
- Aifantis, E. C., On the role of gradients in the localization of deformation and fracture, *International Journal of Engineering Science*, Volume 30, pp. 1279–1299, 1992.
- Babuska, I., Rheinboldt, W. C., A-posteriori error estimates for the finite element method, *Int. J. Numer. Methods Engrg.*, Volume 12, pp. 1597–1615, 1978.
- Babuska, I., Rheinboldt, W. C., Analysis of optimal finite element method in R^1 , *Math. Comp.*, Volume 30, pp. 1597–1615, 1979.
- Babuska, I., Upadhyay, C. S., Gangaraj, S. K., Copps, K., Validation of a posteriori error estimators by numerical approach, *Int. J. Num. Meth. Engineering*, Volume 37, pp. 1073–1123, 1994.
- Bäker, M., An investigation of the chip segmentation process using finite elements, *Tech. Mech.* Volume 23, pp. 1–9, 2003.
- Bäker, M., Finite element simulation of high-speed cutting forces, *Journal of Materials Processing Technology*, Volume 176, pp. 117–126, 2006.
- Bäker, M., Rösler, J., Siemers, C., A finite element model of high speed metal cutting with adiabatic shearing, *Comput. Struct.* Volume 80, pp. 495–513, 2002.
- Bazant, Z. P., Lin, F.-B., Nonlocal yield-limit degradation, *International Journal for Numerical Methods in Engineering*, Volume 26, pp. 1805–1823, 1988.
- Bazant, Z. P., Oh, B.-H., Crack band theory for fracture of concrete, *Materials and Structures*, Volume 16, pp. 155–177, 1983.
- Bazant, Z. P., Pijaudier-Cabot, G., Nonlocal continuum damage, localization instability and convergence, *Journal of Applied Mechanics*, Volume 115, pp. 755–767, 0148-9062 doi: DOI: 10.1016/0148-9062(89)90740-7, 1988.
- Behrens, A., Westhoff, B., Kalisch, K., Application of the finite element method at the chip forming process under high speed cutting conditions, in Tönshoff, H. K., Hollmann, F. (editors), *Hochgeschwindigkeitsspanen*, 112–134, Wiley-vch, 2005.
- Boroomand, B., Zienkiewicz, O. C., Recovery procedures in error estimation and adaptivity. Part II: Adaptivity in nonlinear problems of elasto-plasticity behaviour, *Computer Methods in Applied Mechanics and Engineering*, Volume 176, pp. 127–146, 1999.
- Boussetta, R., Coupez, T., Fourment, L., Adaptive remeshing based on a posteriori error estimation for forging simulation, *Computer Methods in Applied Mechanics and Engineering*, Volume 195, pp. 6626–6645, 2006.
- Bugeda, G., A comparison between new adaptive remeshing strategies based on point wise stress error estimation and energy norm error estimation, *Commun. Numer. Meth. Engng.*

- Volume 18, pp. 469–482, 2002.
- Chambon, R., Caillerie, D., El Hassan, N., One-dimensional localisation studied with a second grade model, *European Journal of Mechanics - A/Solids*, Volume 17, pp. 637–656, 1998.
- Clos, R., Schreppel, U., P., V., Temperature, microstructure and mechanical response during shearband-formation in different metallic materials, in *Int. Conf. Mech. Phys. Behav. Mat. Under Dynamic Loading (DYMAT2003)*, 541–547, Porto, Portugal, 2003.
- Comi, C., Perego, U., Criteria for mesh refinement in nonlocal damage finite element analyses, *European Journal of Mechanics - A/Solids*, Volume 23, pp. 615–632, 2004.
- El-Magd, E., Treppmann, C., Mechanical behaviour of materials at high strain rates, in Schulz, H. (editor), *Scientific Fundamentals of High-Speed Cutting*, 113–122, Hanser, 2001.
- El-Wardany, T., Elbestawi, M., Effect of material models on the accuracy of high-speed machining simulation, in Schulz, H. (editor), *Scientific Fundamentals of High-Speed Cutting*, 77–91, Hanser, 2001.
- Engelen, R. A., Geers, M. G., Baaijens, F. P., Nonlocal implicit gradient-enhanced elasto-plasticity for the modelling of softening behaviour, *International Journal of Plasticity*, Volume 19, pp. 403–433, 2003.
- Eringen, A. C., A unified theory of thermomechanical materials, *International Journal of Engineering Science*, Volume 4, pp. 179–202, 0020-7225 doi: DOI: 10.1016/0020-7225(66)90022-X, 1966.
- Eringen, A. C., On nonlocal plasticity, *International Journal of Engineering Science*, Volume 19, pp. 1461–1474, 0020-7225 doi: DOI: 10.1016/0020-7225(81)90072-0, 1981.
- Flanagan, D., Belytschko, T., A Uniform Strain Hexahedron and Quadrilateral with Orthogonal Hourglass Control, *International Journal for Numerical Methods in Engineering*, Volume 17, pp. 679–706, 1981.
- Flatten, A., Lokale und nicht-lokale Modellierung und Simulation thermomechanischer Lokalisierung mit Schädigung und Stabilitätsuntersuchung für metallische Werkstoffe unter Hochgeschwindigkeitsbeanspruchung, *Fakultät Maschinenbau*, 192, 2007.
- Fleck, N. A., Hutchinson, J. W., Strain gradient plasticity, *Advances in Applied Mechanics*, Volume 33, Academic Press, New York, 1997.
- Gao, H., Huang, Y., Nix, W. D., Hutchinson, J. W., Mechanism-based strain gradient plasticity - I. Theory, *Journal of the Mechanics and Physics of Solids*, Volume 47, pp. 1239–1263, 1999.
- Geers, M. G. D., Ubachs, R. L. J. M., Engelen, R. A. B., Strongly non-local gradient enhanced finite strain elastoplasticity, *International Journal for Numerical Methods in Engineering*, Volume 49, pp. 1–53, 2000.
- Gurson, A. L., Continuum theory of ductile rupture by void nucleation and growth, 1. Yield criteria and flow rules for porous ductile media, *Journal of Engineering Materials and Technology-Transactions of the ASME*, Volume 99, pp. 2–15, 1977.
- Hinton, E., Campbell, J. S., Local and global smoothing of discontinuous finite element func-

- tions using a least square method, *International Journal for Numerical Methods in Engineering*, Volume 8, pp. 461–480, 1974.
- Hoffmeister, H.-W., Wessels, T., Thermomechanische Wirkmechanismen bei der Hochgeschwindigkeitszerspannung von Titan- und Nickelbasislegierungen, in Tönshoff, H. K., Hollmann, F. (editors), *Hochgeschwindigkeitsspannen metallischer Werkstoffe*, 470–491, Wiley-vch, 2005.
- Hortig, C., Svendsen, B., Simulation of chip formation during high-speed cutting, *Journal of Materials Processing Technology*, Volume 186, pp. 66–76, 2007.
- Huang, Y., Gao, H., Nix, W. D., Hutchinson, J. W., Mechanism-based strain gradient plasticity - II. Analysis, *Journal of the Mechanics and Physics of Solids*, Volume 48, pp. 99–128, 2000.
- Huerta, A., Pijaudier-Cabot, G., Discretization influence on regularization by two localization limiters, *Journal of Engineering Mechanics*, Volume 120, pp. 1198–1218, 1994.
- Huerta, A., Rodriguez-Ferran, A., Diez, P., Error Estimation and Adaptivity for Nonlinear Fe Analysis, *Int. J. Appl. Math. Comput. Sci.*, Volume 12, pp. 59–70, 2002.
- Johnson, G. R., Cook, W. H., A constitutive model and data for metals subjected to large strain, high strain-rates and high temperatures, in *Proceedings of the 7th International Symposium on Ballistics*, 541–547, The Hague, The Netherlands, 1983.
- Johnson, G. R., Cook, W. H., Fracture characteristics of three metals subjected to various strains, strain rates, temperatures and pressures, *Engineering Fracture Mechanics*, Volume 21, pp. 31–48, 1985.
- Lee, E. H., Shaffer, B. W., The theory of plasticity applied to a problem of machining, *J. Appl. Phys.* Volume 18, pp. 405–413, 1951.
- Levine, N., Superconvergent recovery of the gradient from piecewise linear finite element approximations, *IMA J. Numer. Anal.*, Volume 5, pp. 407–427, 1985.
- Mabrouki, T., Rigal, J. F., A contribution to a qualitative understanding of thermo-mechanical effects during chip formation in hard turning, *Journal of Materials Processing Technology*, Volume 176, pp. 214–221, 2006.
- Marusich, T., Ortiz, M., Modelling and simulation of high speed machining, *Int J. Num. Meth. Engineering*, Volume 38, pp. 3675 – 3694, 2005.
- Maugin, G. A., Internal Variables and Dissipative Structures, *Journal of Non-Equilibrium Thermodynamics*, Volume 15, pp. 173–192, 1990.
- Merchant, M., Mechanics of the metal cutting process, I. Orthogonal cutting and a type 2 chip, *J. Appl. Phys.*, Volume 16, pp. 267–275, 1945.
- Mindlin, R. D., Micro-structure in linear elasticity, *Archive for Rational Mechanics and Analysis*, Volume 16, pp. 51–78, 1964.
- Onate, E., Bugeda, G., A study of mesh optimality criteria in adaptive finite element analysis, *Engineering Computations*, Volume 10, pp. 307–321, 2007.

- Ortiz, M., Quigley, J. J., Adaptive mesh refinement in strain localization problems, *Computer Methods in Applied Mechanics and Engineering*, Volume 90, pp. 781–804, 1991.
- Özel, T., Altan, T., Process simulation using finite element method – prediction of cutting forces, tool stresses and temperatures in high-speed flat end milling, *International Journal of Machine Tools and Manufacture*, Volume 40, pp. 713–738, 2000.
- Özel, T., Zeren, E., Determination of work material flow stress and friction for FEA of machining using orthogonal cutting tests, *Journal of Materials Processing Technology*, Volume 153-154, pp. 1019–1025, 2004.
- Peerlings, R., de Borst, R., Brekelmans, W., de Vree, J., Gradient-enhanced damage for quasi brittle materials, *Internat. J. Numer. Methods Engrg*, Volume 39, pp. 3391–3403, 1996.
- Peerlings, R. H. J., Geers, M. G. D., de Borst, R., Brekelmans, W. A. M., A critical comparison of nonlocal and gradient-enhanced softening continua, *International Journal of Solids and Structures*, Volume 38, pp. 7723–7746, 0020-7683 doi: DOI: 10.1016/S0020-7683(01)00087-7, 2001.
- Pietruszczak, S., Mroz, Z., Finite element analysis of deformation of strain-softening materials, *International Journal for Numerical Methods in Engineering*, Volume 17, pp. 327–334, 10.1002/nme.1620170303, 1981.
- Pottlacher, G., Hosaeus, H., Wilthan, B., Kaschnitz, E., Seifert, A., Thermophysikalische Eigenschaften von festem und flüssigem Inconel 718, *Thermochimica Acta*, Volume 382, pp. 255–267, 2002.
- Qiu, X., Huang, Y., Wei, Y., Gao, H., Hwang, K. C., The flow theory of mechanism-based strain gradient plasticity, *Mechanics of Materials*, Volume 35, pp. 245–258, 2003.
- Reusch, F., Hortig, C., Svendsen, B., Nonlocal Modeling and Simulation of Ductile Damage and Failure in Metal Matrix Composites, *J. Eng. Mater. Technol.*, Volume 130, p. 14, 2008.
- Reusch, F., Svendsen, B., Klingbeil, D., Local and non local gurson based ductile damage and failure modelling at large deformation, *Europ. J. Mech. A/Solid*, Volume 22, pp. 779–792, 2003.
- Rodriguez-Ferran, A., Huerta, A., Error estimation and adaptivity for nonlocal damage models, *International Journal of Solids and Structures*, Volume 37, pp. 7501–7528, 2000.
- Rogula, D., Introduction to nonlocal theory of material media, in Rogula, D. (editor), *Nonlocal Theory of Material Media*, Volume 286, pp. 125–222, Springer, Wien and New York, 1982.
- Rosakis, P., Rosakis, A. J., Ravichandran, G., Hodowany, J., A thermodynamic internal variable model for the partition of plastic work into heat and stored energy in metals, *Journal of the Mechanics and Physics of Solids*, Volume 48, pp. 581–607, 2000.
- Sievert, R., Hamann, A., Noack, H. D., Löwe, P., Singh, K. N., Künecke, G., Clos, R., Schrepel, U., Veit, P., Uhlmann, E., Zettler, R., Simulation of chip formation with damage during high-speed cutting (in German), *Tech. Mech.* Volume 23, pp. 216–233, 2003.
- Silhavy, M., *The mechanics and thermodynamics of continuous media*, Springer Verlag, 1997.

- Singh, K. N., Clos, R., Schreppel, U., Veit, P., Hamann, A., Klingbeil, D., Sievert, R., Künecke, G., Versagenssimulation dynamisch belasteter Proben mit unterschiedlichen Mehrachsigekeitszustnden unter Verwendung des Johnson-Cook-Versagensmodells fr eine Nickelbasislegierung, *Tech. Mech.* Volume 23, pp. 205–215, 2003.
- Svendsen, B., Phase field extension of crystal plasticity with application to herdening modeling, in Raabe, D., Chen, L.-Q., Barlat, F., Roters, F. (editors), *Continuum Scale Simulation of Engineering Materials: Fundamentals - Microstructures - Process Applications*, Wiley-VCH Verlag, 2004.
- Tönshoff, H. K., Denkena, B., Ben Amor, R., Ostendorf, A., Stein, J., Hollmann, C., Kuhlmann, A., Chip formation and temperature development at high cutting speeds (in german), in Tönshoff, H. K., Hollmann, F. (editors), *Hochgeschwindigkeitsspanen*, 1–40, Wiley-vch, 2005.
- Topping, B., Muylle, J., Ivnyi, P., Putanowicz, R., Cheng, B., *Finite Element Mesh Generation*, Saxe-Coburg Publications, 2004.
- Toupin, R. A., Micro-structure in linear elasticity, *Archive for Rational Mechanics and Analysis*, Volume 11, pp. 385–414, 1962.
- Tvergaard, V., Influence of voids on shear band instabilities under plane strain conditions, *Int. J. Fracture*, Volume 17, pp. 389–407, 1981.
- Tvergaard, V., Needleman, A., Effects of non-local damage in porous plastic solids, *International Journal of Solids and Structures*, Volume 32, pp. 1063–1077, 1995.
- Yang, Q., Mota, A., Ortiz, M., A class of variational strain-localization finite elements, *International Journal for Numerical Methods in Engineering*, Volume 62, pp. 1013–1037, 2005.
- Zienkiewicz, O. C., Zhu, J. Z., A simple error estimator and adaptive procedure for practical engineering analysis, *Int J. Num. Meth. Engineering*, Volume 24, pp. 337–357, 1987.
- Zienkiewicz, O. C., Zhu, J. Z., The superconvergent patch recovery and a posteriori error estimates. part 1: the recovery technique, *Int J. Num. Meth. Engineering*, Volume 33, pp. 1331–1364, 1992a.
- Zienkiewicz, O. C., Zhu, J. Z., The superconvergent patch recovery and a posteriori error estimates. part 2: error estimates and adaptivity, *Int J. Num. Meth. Engineering*, Volume 33, pp. 1365–1382, 1992b.

Acknowledgements

The work presented in this thesis was carried out between 2005 and 2010 during my time as a Ph.D. student at the Institute of Mechanics, Technical University of Dortmund. Having come to the end, I would like to express my thanks to all the people here who gave me tremendous support and help in the last five years.

First of all, I would like to express my thanks to my academic advisor Professor Bob Svendsen for his scientific support and seasoned guidance. Without his work in the fields of material modeling and computational mechanics, this thesis could not have been achieved.

My special thanks also go to the previous chief engineers of our group Dr. Fredrik Reusch and Dr. Vladislav Levkovitch for their help with all aspects of the work, willingness to answer my questions and for their friendship.

Further, I would like to thank Professor Dirk Biermann for his interest in my work and willingness to act as examiner of this thesis. Special thanks goes to Prof. Andreas Menzel for enabling joined research activities in nearby future.

Next I want to thank my fellow workers responsible for the friendly atmosphere in the group. Especially, I would like to express my gratitude to Mr. Farhad Parvizian for his great support, help and the many discussions we had on various computational issues. Furthermore, I would like to thank Mr. Tobias Kayser for his continuous support in the area of computational hardware and software facilities. I also appreciate Dr. Björn Kiefer, Mr. Richard Ostwald, Mr. Tobias Waffenschmidt, Dr. Jayabal Kaliappan, Dr. Thorsten Bartel, Dr. Vadim Palnau, Dr. Ralf Denzer, Dr. Svantje Bargmann and Dr. Clemens Barthel for sharing their ideas concerning mechanical and computational issues throughout the years. Thanks to Mr. Till Clausmeyer and Mr. Benjamin Klusemann for their support and friendship throughout the years.

Special thanks would go to Mrs. Kerstin Walter for her years of warm help for my research, business travelling issues and solving my daily inconveniences. Thanks to Miss Christine Vu and Miss Daria Walenczyk for their excellent language correction of the thesis and papers.

Finally, I want to thank my wife Tanja for giving me so much moral support and for her love. She dealt with our everyday-life problems for me, freeing me to pursue my research activities. Special thanks also goes to my children's grandparents Monika and Christoph, who supported me so much. Last but not least I would like to extend my heartfelt thanks to my children Fin and Charlotte for their love.

Curriculum Vitae

Personal

Name: Christian Hortig
Date of Birth: September 8, 1978
Place of Birth: Lippstadt, Germany
Nationality: German

Education and Experience

2005-2010 Phd. study, Institute of Mechanics, Technical University of Dortmund, Germany
1999-2005 Diploma study, Department of Mechanical Engineering, Technical University of Dortmund, Germany
1989-1998 High School, Ostendorf-Gymnasium Lippstadt, Germany